

NASA-CR-199695


(NASA-CR-199695) CENTER FOR SPACE
TRANSPORTATION AND APPLIED RESEARCH
FOURTH ANNUAL SYMPOSIUM PROCEEDINGS
Final Report (Tennessee Univ. -
Calspan) ~~210~~ p
225 p.

N96-70521
--THRU--
N96-70535
Unclas

Z9/20 0083104

The University of Tennessee-Calspan

Center for Space Transportation and Applied Research



FOURTH ANNUAL
SYMPOSIUM
PROCEEDINGS

CSTAR

NOVEMBER 11-12, 1992

ATTACHMENT H
NAGW-1195
CSTAR-FINAL REPORT



The University of Tennessee-Calspan
**Center for Space Transportation
and Applied Research**

UTSI RESEARCH PARK

TULLAHOMA, TN 37388-8897

FAX (615) 455-6167

November 11, 1992

Welcome to the Fourth Annual Technical Symposium sponsored by the UT-Calspan Center for Space Transportation and Applied Research (CSTAR).

CSTAR, one of the 17 NASA Centers for the Commercial Development of Space, has just completed its fifth year of operation. In conjunction with 12 industrial and 8 university partners, the Center is engaged in 17 projects, with active participation by 50 faculty, staff and graduate students. NASA's Marshall Space Flight Center, Lewis Research Center and AMES Research Center support several projects. The CSTAR investigators deserve significant recognition and all the credit for the Center's accomplishments and continued growth.

This Technical Symposium is organized to provide an overview of the technical accomplishments during the past year in the Center's five Research and Technology focus areas:

Advanced Chemical Propulsion
Electric Propulsion
Space Transportation
Computational Methods
Laser Materials Processing

The Center broadened its scope of responsibility two years ago when it accepted management of the COMmercial Experiment Transporter (COMET) program. The development of commercial transportation infrastructure is a growing emphasis area for the Center. Two significant flight experiments continue to be developed; an Electric Propulsion Orbital Platform, and a cooperative effort between CSTAR, Lumonics and the University of Waterloo for laser materials processing in space.

Ms. Paula Reed deserves considerable recognition and credit for assimilating the proceedings and organizing this symposium. Ms. Sandy Shankle and her staff in the UTSI Short Course Office have efficiently handled the registration and logistics. Copies of the proceedings were made by the UTSI Print Shop. To all of you, thank you for your dedication and assistance.

We believe the CSTAR Technical Symposium will be a helpful and rewarding experience. While here, please feel free to talk to the investigators and visit the facilities and laboratories at The University of Tennessee Space Institute, at AEDC and at the new CSTAR Building.

Sincerely,

George W. Garrison, Ph.D.
Executive Director

ptr

INTRODUCTION

These proceedings continue the series of quarterly technical reports as the Annual Report which summarizes the progress of the Center for Space Transportation and Applied Research (CSTAR). These comprehensive proceedings include all active research and technology projects as well as a status report on COMET, the Commercial Experiment Transporter ELV project.

The technical reports focus on progress made during the previous year. They are designed to inform CSTAR investigators and industrial partners about general progress in all areas. Additional technical papers are presented at national conferences during the year.

TABLE OF CONTENTS

CSTAR
FOURTH ANNUAL
SYMPOSIUM PROCEEDINGS
NOVEMBER 11-12, 1992

	<u>PAGE</u>
<u>COMMERCIAL SPACE TRANSPORTATION:</u>	
COMMERCIAL EXPERIMENT TRANSPORTER	1
WESTAR	9
<u>ELECTRIC PROPULSION:</u>	
ELECTRIC PROPULSION ORBITAL PLATFORM	15
ION THRUSTER NUMERICAL MODELING	22
ION THRUSTER DIAGNOSTICS	26
ARCJET PLUME DIAGNOSTICS	40
<u>LASER MATERIALS PROCESSING:</u>	
THE SPACE APPLICATIONS INDUSTRIAL LASER SYSTEM	52
LASER INDUSTRIAL PARTNERSHIP PROGRAM	65
WELDER-LWP: A FAST-TRANSIENT, THREE DIMENSIONAL COMPUTATIONAL MODEL FOR CONTINUOUS AND PULSED HIGH-ENERGY-DENSITY WELDING PROCESSES	71
<u>CHEMICAL PROPULSION:</u>	
ADVANCED NOZZLE CONCEPTS	73
SPACE SHUTTLE MAIN ENGINE PROPELLANT PATH LEAK DETECTION USING SEQUENTIAL IMAGE PROCESSING	109
OXYGEN-RICH COMBUSTION DEVICES	119
LIQUID ROCKET SPRAY COMBUSTION STABILITY ANALYSIS	139
A NUMERICAL SIMULATION OF AXISYMMETRIC, STEADY-STATE PLASMA FLOW THROUGH MPD-TYPE THRUSTERS WITH APPLIED MAGNETIC FIELDS	157
COMPUTATION OF TWO-PHASE FLOW IN SOLID ROCKET MOTORS	169
<u>COMPUTATIONAL METHODS:</u>	
ANOMALY DETECTION OF TURBOPUMP VIBRATION IN SPACE SHUTTLE MAIN ENGINE USING STATISTICS AND NEURAL NETWORKS	179
AN INTEGRATED KNOWLEDGE SYSTEM FOR THE SPACE SHUTTLE HAZARDOUS GAS DETECTION SYSTEM	189
FLUID MECHANICS COMPUTER BASED LAB SIMULATOR	196

CSTAR FOCUS AREA:

COMMERCIAL SPACE TRANSPORTATION

·COMmercial Experiment Transporter (COMET)

Mr. Joe Pawlick, Program Manager, CSTAR

·WESTAR

Mr. Thomas Wonder, Westinghouse Electric Corporation

COMET: First Mission Progress¹J. F. Pawlick², E. G. Allee³, and C. H. Myers⁴

University of Tennessee - Calspan
 Center for Space Transportation and Applied Research (CSTAR)
 UTSI Research Park
 Tullahoma, TN 37388

NDB
 5939
 P-8

Abstract

The COMmercial Experiment Transporter (COMET) is a set of hardware and related infrastructure used to support orbital experiments of the CCDS's and their industrial partners. During the nineteen months since the program started, contracts have been signed, design reviews conducted on all components, experiments selected for the first mission, almost all hardware has been manufactured, and a majority of components have completed testing. The Program Office and CCDS Monitors took an active role in the development, planning, and conduct of the actions leading to the first flight of COMET scheduled in the first quarter of 1993. The Recovery System/Site has been exercised, and the Launch Facility is well on its way toward completion. As October came to a close, most of the major components of the COMET FreeFlyer have come together in League City, TX for an integrated test.

This report deals primarily with the programmatic issues which were resolved as the program matured. At times it is impossible to disassociate the technical from the programmatic and, in such cases, the technical material is presented to provide insight into the path selected by both the CCDS and Contractor Management.

COMET Overview

The COMET FreeFlyer will be launched with
 CCDS payloads aboard both the Service Module

and Recovery System into a 300 nm circular orbit
 from the Conestoga Launch Vehicle. The non-
 recoverable Service Module will contain about 15

¹ This work is supported by the Center for Space Transportation and Applied Research (CSTAR) under NASA Grant NAGW-1195.

² CSTAR/UTSI, Manager of Space Transportation

³ CSTAR/Calspan, COMET Chief Engineer

⁴ CSTAR/Calspan, Operations Analyst

Other Contributors Include:

Dr. F. Wessling, CMDS, University of Alabama, Huntsville

Dr. M. Robinson, BioServe, University of Colorado

Mr. R. Martinez, CSP, Texas A & M University

Mr. T. Gallimore, CMC, University of Alabama, Birmingham

Mr. N. Combs, SVEC, University of Houston

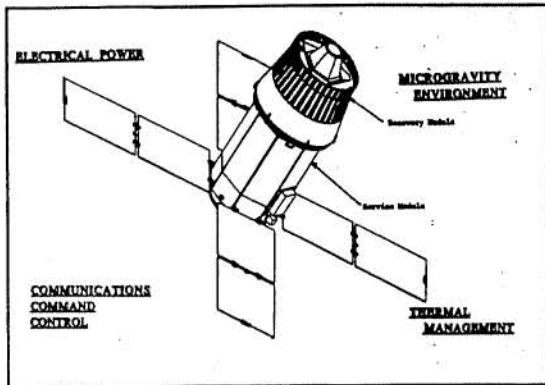


Figure 1 COMET's FreeFlyer

cubic feet of payload volume while the Recovery System will have about ten cubic feet. Command and control of the FreeFlyer and experiment data communications will be controlled through a Commercial Payloads Operations Control Center (COMPOCC) in League City, TX.

The Recovery System will separate from the FreeFlyer after about a month in orbit to be recovered near the Great Salt Lake Desert in the Utah Test and Training Range (UTTR).

Programmatic Overview

During the period of April 8, 1991, through October 30, 1992, the COMmercial Experiment Transporter progressed from Authorization to Proceed for the Contractors, Preliminary Design Reviews, Critical Design Reviews, Fabrication of almost all components, and testing of a majority of those components.

The Service Module has developed from original design, through fabrication of all components, and has undergone extensive testing, which has culminated in its arrival in League City, TX, for Integrated Testing. The Recovery System has followed almost the same path, however, with some perturbations in the spin table design, avionics/software design, and de-spin mechanisms. It has completed most of its testing and is currently ready for Integration Testing with the Service Module in League City, TX. The Commercial Payload Operations Control Center (COMPOCC) has developed into a fully operational control center, ready for operational status. Payloads have been selected, and the majority of them have completed unit testing and are being integrated into the Recovery System and Service Module. The Launch Vehicle has matured through its design process, with the Star 48V ready for installation, the Castor IV's being manufactured, the avionics ready for testing, and almost all mechanical items completed and being integrated. The Flight and Ground Software has been completed and is undergoing testing. The Launch Pad started in July 1992 and is ready for installation of the mechanical structures. The Recovery Site has been tested, and operational tests of the Recovery System have taken place.

The COMET System, as a total, is coming together partially in League City, and appears to be heading for an on-time launch in the first quarter of 1993.

COMET STATUS UPDATE

Following is an update in the status of the COMET Program.

Payloads:

Following are the payloads manifested for COMET Mission #1:

Recovery System

[1] Biomodule	(Penn State)
[2] Non Linear Organic Thin Films and Crystals	(UAH)
[3] MDA Minilab	(UAH)
[4] Animal Autonomous Space Support Module	(BioServe)
[5] Plant Autonomous Space Support Module	(BioServe)
[6] Protein Crystal Growth-Batch (PCG-M)	(UAB)
Utility - Acceleration Measurement System (AMS)	(UAH)

Service Module

[7] Oxygen Atom Flux Monitors for Spacecraft(SURSAT)	(CMDS)
[8] * Autonomous Rendezvous and Docking (ARD)	(SpARC)
* Requires COMET Mission #2 for docking.	
[9] Frozepipe (Frozen Heat Pipe Experiment)	(Texas A&M - CSP)
[10] LEOEX (Low Earth Orbit Communications)	(Florida Atlantic)

The Payloads have all been delivered to the Integration Contractor (SII) in League City, TX, and have undergone extensive testing in anticipation of Integrated Systems Testing with the Service Module, the Recovery System, and the COMPOCC.

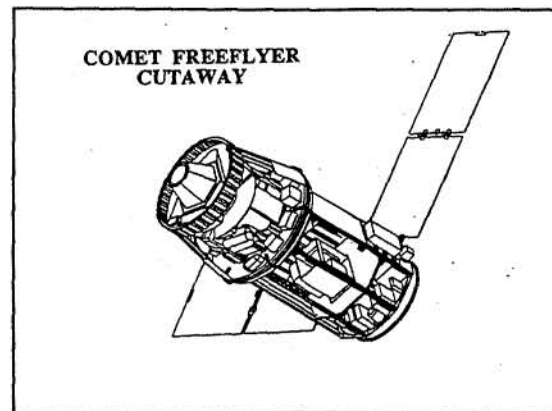


Figure 2 Payload Location

The Autonomous Rendezvous and Docking Experiment (ARD) was delivered early to Space Industries, where it underwent fit checks and basic communication checks. ARD will remain on board the Service Module well past the 130 day mission with regular communication checks. It is only after the second COMET Service Module has been launched that this experiment will start its operation, being the target for the COMET #2 chase module. The chase module will target, operate, thrust, and observe the target vehicle without intervention from the ground, with an ultimate link-up and transfer of material.

SURSAT is an atomic oxygen flux monitoring experiment desiring proximity to the atomic oxygen present in Low Earth Orbit. It will be placed on the outside face of the Service Module, in the ram direction, and will remain in operation for the duration of the spacecraft's orbital lifetime.

Frozepipe is an experiment measuring the performance of heat pipes during extreme

temperature variations. It is manifested to be installed on one of the outside experiment panels.

LEOEX is a communications experiment testing various communication configurations in anticipation of future communications satellites.

Biomodule, MDA, NLO, and PCG-M are all experiments dealing with the growing of crystals in a microgravity environment.

AMASS and PMASS deal with plant and small animal tissue changes that occur in a microgravity environment.

One other component on the Recovery System is being provided by a CCDS, but is being flown as a utility on COMET. UAH is providing microgravity measurement equipment, similar to that flown on the Consort missions, to quantize the microgravity disturbances during the mission. This is of particular importance to the crystal growing experimenters, who need to know the environmental conditions fairly accurately in order to assess the success of their experiments.

The Payload Integrators have integrated all experiments into their respective mockups, have communicated with simulators where applicable, and at the time of this writing are in the stage of being integrated into the Service Module, and Recovery System for communication with the FreeFlyer command and telemetry system, as well as the COMPOCC.

Launch Vehicle

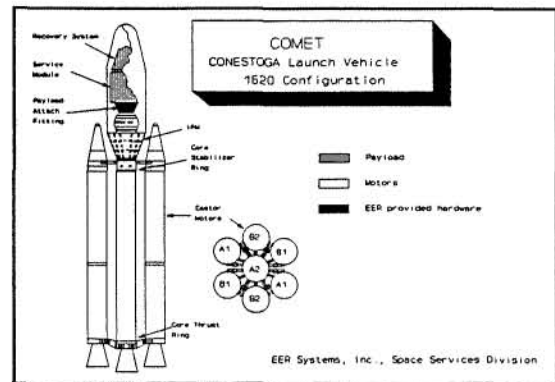


Figure 3 Conestoga Launch Vehicle

The Launch Vehicle has progressed from the initial design stage into the Conestoga 1620 depicted in figure 3. The core motor is a Castor IVB with thrust vector control. Attached to the core motor are four Castor IVA's and two Castor IVB's. On top of the core motor is a Star 48V, also with thrust vector control. Wind tunnel tests were conducted on the Conestoga 1620, with the results feeding into the thermal design, as well as the trajectory design.

Coordination of the launch vehicle launch complex requirements with NASA has completed intense discussions, and on July 31, 1992, site construction commenced. The design of the Launch complex completed earlier this year; earthwork was finished in August, and pile driving/pile capping and structural concrete finished in mid October. The mechanical structures are nearing completion of fabrication and should start erection in November.

The Launch Vehicle Flight Software CDR was held in July, and Flight Software is undergoing the final

stages of testing. There have been some interface issues concerning the IMU, but all appears to be reaching a mutually agreeable solution. EER has elected to develop a state-of-the-art, AI based, Ground Control Software to relieve the burden on the launch control team from sifting through the myriad of status information provided shortly before launch. The system will be able to make intelligent choices on what data is important to the launch control team, and rapidly flag any out-of-nominal condition, as well as conditions where groups of data taken together indicate problems. The Ground Control Software will be ready for installation in December.

All mechanical and electrical Launch vehicle assemblies are in fabrication, testing, or are being integrated with the launch vehicle. Most avionics assemblies are in testing.

The Launch Vehicle appears to be on track for a first quarter launch.

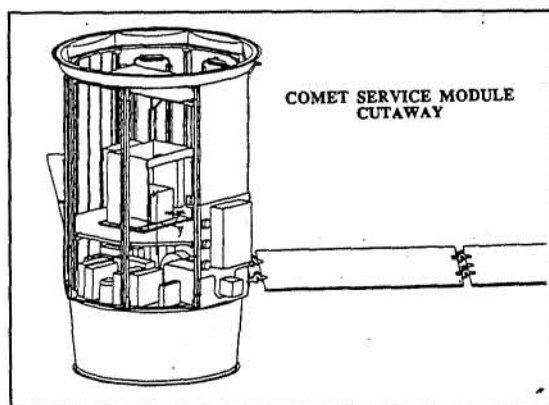


Figure 4 Service Module

Service Module

The Service Module has progressed completely through all phases of design, manufacturing, and testing, and is currently involved in Integration & Test in League City, TX. The design and manufacture has progressed very smoothly, with only minor problems with power controllers and some specialized electronics equipment.

One of the largest integration efforts on the COMET program involves the Capillary Pump Loop (CPL) - Thermal Control System that was provided to the COMET Service Module and Recovery System by OAO Corporation of Greenbelt, MD, under the supervision of Defense Systems Incorporated and Westinghouse. This effort took the technology from heat pipes, and some preliminary spaceflight results from OAO, and applied it to an engineering effort to develop a microgravity adaptable thermal control system. The OAO CPL system utilizes no mechanical pumps except for priming the system; therefore, there are no mechanical disturbances to interfere with the microgravity environment, and in particular, the crystal growth experiments. What was even more demanding of this integration effort, was the fact that the system is designed to operate in low gravity, and the passive-evaporation pumps do not work well in a one-gravity environment that they are tested in here on Earth. The program had a number of setbacks in fabricating and characterizing the system, but in the end, the OAO/DSI/Westinghouse team has delivered a unique system specifically adapted for the

requirements of COMET. The Recovery System is also incorporating the OAO CPL system.

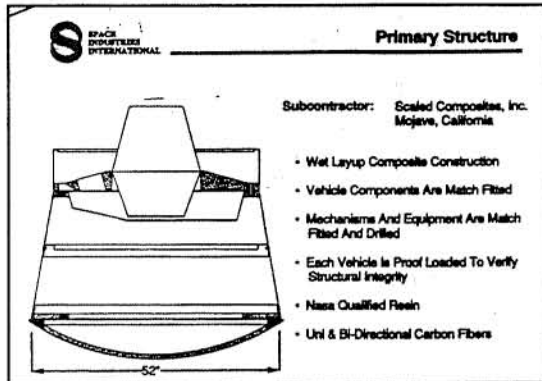


Figure 5 Recovery System Structure

Recovery System

The Recovery System is nearing completion, with most of the major components currently undergoing Integration and Test in League City, TX. The Avionics supplied by the SouthWest Research Institute have been integrated into the flight system along with SII supplied software, have undergone testing, and are being tested with the Recovery System experiments.

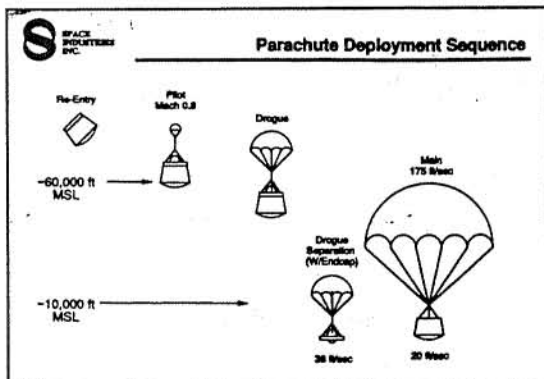


Figure 6 Recovery System Parachute Deployment

The Parachute & Airbag systems have been extensively tested, starting with a 20-ft drop test to check the operation of the airbag. The next test involved dropping a protoflight model of the recovery system from a privately-owned Canberra from 20,000 feet. This test successfully tested the limits of the main chute and the deployment of the airbag. The most recent test involved dropping the protoflight unit from the Canberra in excess of 50,000 feet to test the deployment of the drogue chutes, as well as the main chute and airbag. This test was conducted at UTTR and exercised the UTTR & SII Recovery Teams. The test was completed successful, with complete recovery and disassembly in less than four hours.

Space Industries has studied the re-entry aerodynamics extensively, and determined that in order to meet the landing range dispersion requirements, the Recovery System will have to spin up before the retro-motor fires in order to compensate for off-axis thrust of the retro-motor. This, in turn, entails a de-spin mechanism be incorporated. SII has successfully designed, built, and tested a Yo-Yo de-spin system in record time in order to meet this required change.

Another area of concern for SII has been the design of the spin table/spin bearing that mates the Recovery System to the Service Module and allows for the spin-up of the Recovery System just prior to separation. This item has been plagued by a number of engineering anomalies, and Space

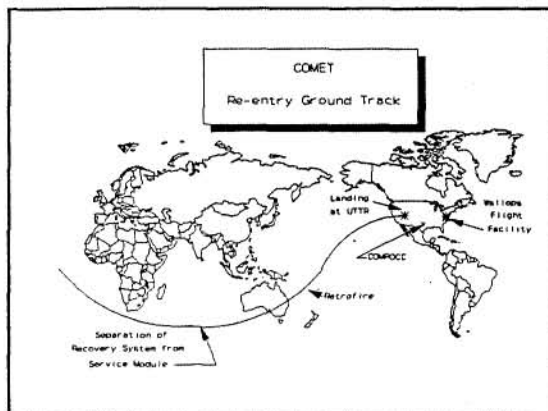


Figure 7 Landing Sequence

Industries appears to have solved all of the major problems associated with the thermal expansion of the bearings and associated race-ways.

Overall, the Recovery System appears to be ready for launch after Integration & Test.

Orbital Operations

The COMPOCC has evolved into a fully functional Satellite Control Center with fully operational

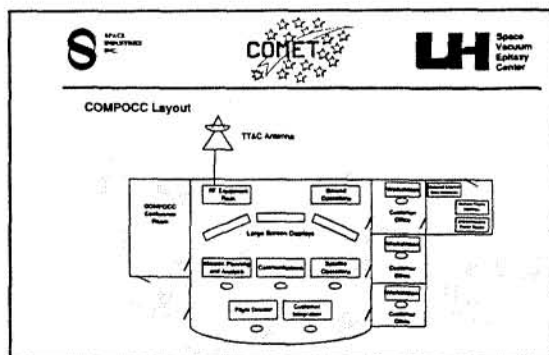


Figure 8 COMPOCC Layout

workstations, computer networks, data storage facilities, and an operational command and control

software system. They have installed a fully operational Tracking, Telemetry, and Command system consisting of a Scientific Atlanta antenna and receiving station and have fully tested it with satellites on orbit and the COMET FreeFlyer in League City.

Other Programmatic Issues

Gunn Report

In May, 1992, Mr. C. Gunn of NASA Code SV was asked to provide a non-advocate program review of COMET. On May 27 & 28, 1992, the COMET Management Team and the CCDS Monitors presented a technical overview of the complete COMET program, from contracts & finance to ordnance system design. Overall, the review team was favorably impressed, and forwarded a set of 18 recommendations to Code C and the COMET Team. All the recommendations have been reviewed and feedback provided to the Gunn Committee.

SUMMARY

The COMET Program is in the midst of Integrating a myriad of different components from suppliers and contractors scattered across the U.S., and has just started the testing of this collection of highly-technical components. To date, only minor problems have occurred, and the COMET Team has responded with one voice and quickly vanquished those marauding gremlins of doom. COMET nears its first launch, and from software,

to hardware, to launch pad, the whole COMET team is pointing in the right direction, and it appears that we'll have a some real COMET carrier waves coming from 300 miles up before the end of March.

List of Major COMET

Contractors and Suppliers

Service Module

Westinghouse - Prime Contractor

Defense Systems Inc. - Service Module
Manufacturer

OA0 Inc. - Thermal Control System Supplier

Space Sciences Corp. - Attitude Control Systems

Kearfott-Siegler - IMU

Recovery System

Space Industries Inc. - Prime Contractor

Pioneer - Parachute Systems

Scaled Composites - RS Structure

SouthWest Research Institute - Avionics

Launch Vehicle

EER Systems, Inc. - Prime Contractor

Morton Thiokol - Motors

Logicon Control Dynamics - Flight Software

Altair Aerospace Corporation - Ground Control
Software

Tracor - Fairing

Orbital Operations

Space Industries Inc. - Prime Contractor

Space Applications Corporation - Software
Development

Payload Integration

Space Industries Inc. - Prime Contractor

SouthWest Research Institute - Environmental
Testing



5770
p.6
**WESTAR: AMERICA'S FIRST FULLY COMMERCIAL
RECOVERABLE SPACE SERVICE**

Thomas Wonder
Westinghouse Electric Corporation, Huntsville, Alabama
September 24, 1992

ABSTRACT

The WESTAR service -- Westinghouse Space Transportation and Recovery -- is a fully integrated, commercially operated service to fly payloads into low-Earth orbit for extended duration missions, and return payloads safely to Earth in a Recovery System. After recovery, other payloads on the same mission can continue operating in a Service Module bus providing satellite services. The system to provide this service is currently being built for the first of three orbital missions for the COMmercial Experiment Transporter (COMET) Program. The first flight using this system will be launched from Wallops Flight Facility, Virginia during the first quarter of 1993, with recovery 30 days later at the Utah Test and Training Range.

INTRODUCTION

For those who require low-cost, fast-turnaround access to space, Westinghouse is providing WESTAR (Westinghouse Space Transportation and Recovery), a fully integrated service which offers a "ticket to space" for users, either one-way or round trip. While in orbit, the WESTAR service provides basic utilities as required, such as electric power, cooling, pressurized air, data management, and communications.

WESTAR is designed to launch on a small expendable launch vehicle, so flights can be scheduled with reliable frequency to accommodate a wide range of research and production programs. The WESTAR service provides flexible payload accommodations by means of a two-part spacecraft, consisting of a Recovery System and a Service Module. Access to payloads is possible up to 6 hours before launch for installation of degradable materials, and for the Recovery System, payloads can be accessed on the ground within 4 hours of separation from the Service Module.

This paper provides a brief background on WESTAR and its forerunner program, COMET (COMmercial Experiment Transporter). Technical details of launch/orbital parameters and payload accommodations for a nominal WESTAR mission are provided.

BACKGROUND

Until now, the commercial development of space in the United States -- especially requiring recoverable payloads -- has been mainly tied to Space Shuttle flights. The number of experimenters who have used the Shuttle, compared to those who would like to place experiments in space, is relatively small for various reasons, including high cost, lack of man-rating, or less-than-the-highest priority. Also, there are numerous arguments why the Shuttle is not an ideal vehicle for many experimenters: (1) man-rating an experimenter's payload imposes delay and additional cost on the experimenter, (2) the microgravity environment is not good enough, and (3) the time in space is too short.

At a meeting of Directors for the NASA-sponsored CCDSs (Centers for Commercial Development of Space) in Houston, in early 1990, Mr. James R. Rose, NASA Office of Commercial Programs (Code C) put forward a challenge: *establish a program to encourage the development of a commercial space industry that is not linked to the Shuttle or that requires extensive government involvement.* Included in the rationale:

- The CCDSs and their industrial partners require long duration flights - longer than the Shuttle will allow.

- Shuttle flight opportunities are becoming increasingly more limited.
- Studies revealed an existing market for commercial space.

The COMET (COMmercial Experiment Transporter) Program came into being as a result of that challenge. The Program Plan was approved by NASA Code C in May 1990 with Mr. Joseph Pawlick, Program Manager, of the Center for Space Transportation and Applied Research in Tullahoma taking the lead. The primary aim of the COMET Program is to buy access to space and related services -- but not the associated hardware and systems -- from qualified contractors. Highlights of the Program Plan:

- Statements of Work are written for performance, not for hardware.
- Recoverability (required in 75% of payloads) is built into the system.
- Design is the responsibility of the contractor team.
- No Mil Standards or NASA Standards need to be followed.
- Quality is responsibility of the contractor team.
- Hardware and systems are property of the contractors.

A draft RFP was released in July, 1990, with the final RFP issued August 22, 1990 covering six contract areas. Contractor selection was completed March 8, 1991: The work areas, their respective CCDS monitors, and contractors selected (*italicized*) are shown:

Systems Engineering: Center for Space Transportation and Applied Research, University of Tennessee Space Institute / Calspan Operations; *Westinghouse Electric Corporation*.

Payload Integration: Center for Macromolecular Crystallography, University

of Alabama at Birmingham; *Space Industries Inc.*

Launch Vehicle: Consortium for Materials Development in Space, University of Alabama in Huntsville; *EER Systems*.

Service Module: Center for Space Power, Texas A&M University, College Station; *Westinghouse Electric Corporation*.

Recovery System: Bioserve Space Technologies, University of Colorado, Boulder; *Space Industries, Inc.*

Orbital Operations: Space Vacuum Epitaxy Center, University of Houston; *Space Industries, Inc.*

The authority to proceed was given on April 8, 1991, and initial payloads' selection was completed June 24, 1991. The contracts call for three missions during 1993, 1994, and 1995, with two optional missions in 1996 and 1997. All Preliminary Design Reviews (PDRs) were accomplished by September 1991, with all Critical Design Reviews (CDRs) completed by November 1991.

STATUS

Most of the flight hardware for the first COMET flight has been built and tested, including high altitude drop tests of the Recovery System. A Commercial Payload Operation and Control Center (COMPOCC) has been completed in Houston and is operational, currently tracking satellites for calibration purposes. Experiment payload integration and test will commence in October, 1992 at Houston. The first mission will be launched during the first quarter of 1993 from Wallops Island, Virginia, with recovery 30 days later at the Utah Test and Training Range west of Salt Lake City.

Parallel to the COMET Program, which is only available to the CCDSs and their associates, Westinghouse established the privately financed WESTAR service, which is available to any user with a need to access space. A similar spacecraft design, and the same facilities for launch, payload

integration, orbital operations, and recovery are available from Westinghouse as a single point of contact. The first WESTAR mission is scheduled for the first quarter of 1994, with a potential of 10 missions per year by 2000. Negotiations are currently underway with potential users.

Descriptions of the mission and payload accommodations which follow are for the WESTAR service.

MISSION DESCRIPTION

WESTAR is a fully integrated space transportation and recovery service that can

carry payloads to the environment of space, leave some there, and return with others. Basic utilities such as electric power, controlled temperature and pressure, spacecraft orientation, data management and communications are provided while in orbit.

Each mission is capable of launching a two-part spacecraft - carrying payloads into a 300 nautical mile circular orbit - consisting of a Recovery System which returns to land after 30+ days by parachute, and a non-recoverable Service Module which stays in orbit for 2+ years (Figure 1). Payloads run the gamut from material studies to communications to life sciences.

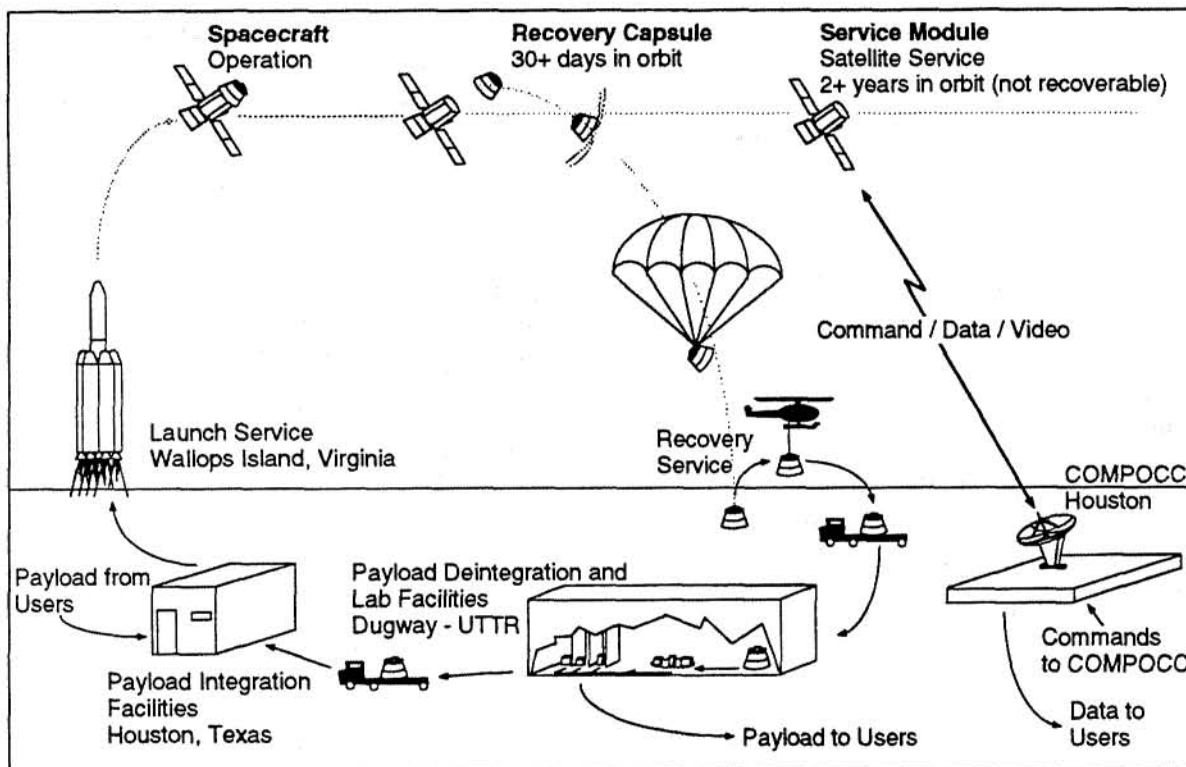


Figure 1 - WESTAR Service Concept

The WESTAR service concept consists of the following major elements:

Payload Integration - Payloads are integrated into the Recovery Capsule and the Service Module through an extended period of interface with the user. This interface includes the exchange of appropriate interface documentation, face-to-face meetings to work out integration issues, required preflight testing and mockups, and

subsequent delivery of the payload(s) for final integration into the Recovery System and Service Module. The Recovery System and Service Module are then integrated into a single spacecraft, and preflight testing of the spacecraft is completed. Late access to payloads is provided up to approximately 6 hours before launch.

Launch - The spacecraft is mated to the launch vehicle, the fairing is secured over the

spacecraft, final testing is completed, and all other preparations for launch are completed. The launch vehicle with spacecraft aboard is then launched and monitored to orbital insertion. A CAD representation of the WESTAR spacecraft is shown in Figure 2.

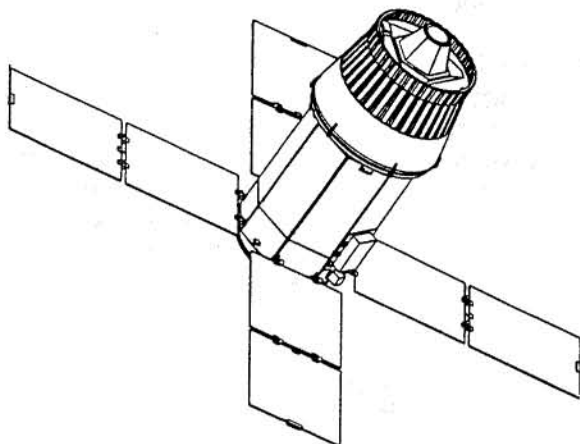


Figure 2 - WESTAR Spacecraft

On-orbit Operation - After the spacecraft is placed in orbit, solar arrays on the Service Module are deployed and initial operational testing of the spacecraft is completed. Operation of payloads then begins, and continues for a few days up to several years, depending on the requirements of the payload.

Acquisition of Payload Data While On-orbit - During on-orbit operation, data downlinked from payloads is received at the COMPOCC and provided to the user either at the COMPOCC or via a communication link to a remote location.

Recovery Operation - When orbital operation of a recoverable payload is completed after 30+ days after launch, the Recovery System is spin-stabilized, pointed for the re-entry maneuver, and separated from the Service Module. A deorbit motor aboard the Recovery System is fired and the capsule re-enters the atmosphere. A parachute system slows the capsule for landing, and a shock attenuation system absorbs the final impact with the ground.

Payload Deintegration and Return to User - The Recovery System is immediately transported to nearby facilities where the

payload is removed. An early access capability of 4 hours is achievable. Users may work on their payloads in the recovery site facilities, or the payloads can be shipped to the user's choice of destination.

Continued Operation of the Service Module - Payloads in the Service Module can continue operating long after the Recovery System has separated and re-entered. Payloads not requiring recovery, for example, astronomical observation, earth observation, atmospheric monitoring, navigation, search and rescue, and communications operations can all be accomplished aboard the Service Module during this time.

WESTAR missions can be accommodated on either a dedicated or shared basis. With a dedicated mission, the user has full control over scheduling of the launch date, selection of orbital parameters, and scheduling of system resources such as electric power. Dedicated missions also offer a significant reduction in cost per pound of payload. On shared missions, scheduling of launch date and use of resources are allocated to accommodate all users.

Standard WESTAR missions are scheduled for launch from the Wallops Flight Facility (WFF) in Virginia, and recovered at the Utah Test and Training Range (UTTR) near Bonneville, Utah. Both locations are at approximately 40° inclination from the equator, offering the maximum number of passes over the recovery area for a given mission. Both have ground facilities to conduct required payload integration and de-integration activities, and can provide laboratory and other support to the user.

Alternate launch, landing, and orbital operations sites can be accommodated based on the user's requirements.

PAYLOAD ACCOMMODATIONS AND SUPPORT SYSTEMS

The two-part WESTAR spacecraft design is modular, providing maximum flexibility for payload accommodations.

This modularity and reconfigurability allows users to send a wide range of materials, equipment, and systems into space. Figure 3 provides a graphic representation of the payload accommodation spaces for both the Recovery System and Service Module, which offer payload volumes of 10 and 15 cubic feet respectively, and a total of 550 lbs allocated between the two carriers. Payload volume in the Recovery System can be increased to 12 cubic feet, allowing an additional 50 lbs for a total of 600 lbs, if the pressurized container is eliminated and the

payload is exposed to the vacuum of space.

Thermal Control - The Service Module and Recovery System are independently cooled, each using a capillary pump loop (CPL) two-phase ammonia system. The CPL system is capable of maintaining the payloads at $72 \pm 5^\circ \text{F}$ with a heat input of up to 400 watts. The advantage of the CPL system is the lack of mechanical pumps, valves, and relays which can create microgravity disturbances to the payload environment.

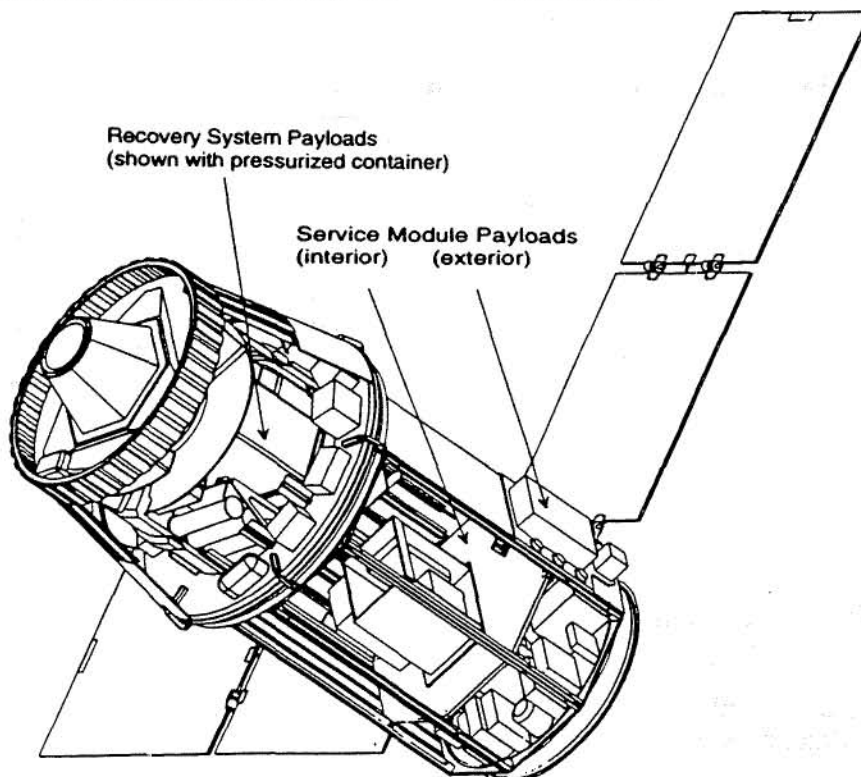


Figure 3 - Payload Accommodation Spaces

Attitude Control - The attitude control system (ACS) onboard the Service Module is a 3-axis system with 4 major operational modes: (1) alignment for orbit insertion, (2) solar-pointing, (3) earth-pointing, and (4) reentry pointing for the Recovery System. A microgravity environment of 10 to the minus 5 g is maintained during the solar and earth-pointing modes using a combination of reaction wheels and 3-axis torque coils. Solar-pointing of $\pm 0.5^\circ$ is assisted by a fine sun sensor, and earth-pointing of $\pm 1^\circ$ is controlled by a reaction wheel in a momentum bias mode. Orientation during

both solar and earth-pointing is supplied by a horizon scanner. Cold gas thrusters are used for the orbit insertion maneuver, reentry alignment, and for off-setting the spin table torque during the Recovery System spin balance prior to reentry release. Orbit insertion and reentry alignment are controlled by a 3-axis inertial measurement unit.

Power - The Service Module power system provides 28 ± 4 volts DC for all payloads and housekeeping. Four solar panels, in combination with rechargeable

batteries, generate sufficient power to allocate 350 watts continuous and 400 watts for up to 200 hours to the payloads.

Payload Data - The spacecraft has provisions for a total of twelve ports, each providing a data, power and video interface. In addition, each port can be multiplexed to ten locations, thus accommodating up to 120 payload components. A command and data handling processor has an allocated memory of 1 Mb for Service Module telemetry and 3 Mb for payloads. Data interface is RS422 with X-modem protocol. Also available is a

standard NTSC video format. The RF data downlink is 250 kbps and uplink command is 9.6 kbps. At the downlink data rate, the 4 Mb memory can be downloaded in just over 2 minutes of 50 minutes per day available for two-way communications. During the mission, command uplink and payload downlink telemetry is managed through the COMPOCC in Houston. The COMPOCC also supports remote user's requirements via modem data transfer.

A summary of WESTAR integrated payload capabilities is presented in Table 1.

Table 1 - WESTAR Integrated Payload Capabilities

		Recovery System	Service Module
Payload Mass		up to 600 / 550 lbs*	up to 550 lbs*
Payload Volume		12 / 10 ft ³	15 ft ³
Environment	• Microgravity	1 x 10 ⁻⁵ g	
	• Pressure	vacuum / 1 atm	vacuum
	• Baseplate Temp.	72 ± 5° F	72 ± 5° F
Power	• Voltage	28 ± 4 VDC	
	• Continuous	350 watts	
	• Peak (200 hours)	400 watts	
	• Transient	1000 watts	
Heat Rejection		400 watts	400 watts
Communication	• Downlink (& Video)	250 Kbps	
	• Uplink	9.6 Kbps	
	• Time	Five 10-minute periods per day	

*Combined payload mass in the Service Module and Recovery System.

SUMMARY

Westinghouse Electric Corporation has developed a new way for users to access space through a commercial initiative, the WESTAR service, a derivative of the CCDS COMET Program. With WESTAR, users can reliably fly recoverable payloads and non-recoverable payloads - up to a total of 600 lbs - on the same mission by means of a separable Recovery System mated to a Service Module, a three-axis stabilized spacecraft bus powered by solar arrays and

rechargeable batteries. A nominal mission is launched to a 300 nautical mile circular orbit at an inclination of 40°. A nominal mission length is 30 days in orbit for the Recovery System and up to 2+ years for the Service Module.

The first flight using this system will be launched from Wallops Island, Virginia during the first quarter of 1993, with recovery 30 days later at the Utah Test and Training Range.

CSTAR FOCUS AREA:

ELECTRIC PROPULSION

·Electric Propulsion Orbital Platform

Mr. Verlin Friedly
Dr. George W. Garrison
Dr. Wim Ruyten

·Ion Thruster Numerical Modeling

Dr. Xiaohang (Jeff) Peng
Dr. Wim Ruyten
Dr. Dennis Keefer

·Ion Thruster Diagnostics

Dr. Wim Ruyten
Mr. Verlin Friedly
Dr. Xiaohang (Jeff) Peng
Ms. Julia A. Celenza
Dr. Dennis Keefer

·Arcjet Plume Diagnostics

Dr. Wim Ruyten
Dr. Dennis Keefer

Electric Propulsion Orbital Platform

V. J. Friedly*, G. W. Garrison†, and W. M. Ruyten‡

University of Tennessee—Calspan
Center for Space Transportation and Applied Research
UTSI Research Park, Tullahoma, Tennessee 37388-8897

ABSTRACT

This paper describes the status of the Electric Propulsion Orbital Platform (EPOP), the primary objective of which is to provide an instrumented platform for testing electric propulsion devices in space. It is anticipated that the first flight, EPOP-1, will take place on the Shuttle-deployed Wake Shield Facility in 1996, and will be designed around a modified version of a commercial 1.8 kW hydrazine arcjet system, to be operated on gaseous hydrogen propellant. Specific subsystems are described, including the arcjet system, the propellant and power systems, and the diagnostics systems.

INTRODUCTION

In January of 1992, a feasibility study was completed for the test of a 1.8 kW hydrazine arcjet system on the Wake Shield Facility [1]. This flight, EPOP-1, was envisioned as the first flight of the Electric Propulsion Orbital Platform (EPOP). EPOP is conceived as a space platform upon which NASA and U.S. industry can perform necessary space demonstrations of electric propulsion devices. As is well known, electric propulsion offers specific impulses which are significantly higher than those which can be obtained with conventional chemical systems. For example, the propellant exit velocity from arcjets is typically 50% larger than can be achieved by traditional chemical systems.

While the basic concept of the EPOP program has remained the same, significant changes have occurred. McDonnell-Douglas Space Systems Company has joined the EPOP-1 consortium, and will assume the technical lead. As before, Rocket Research Company and Boeing Defense & Space Group will be involved also, and the Space Vacuum Epitaxy Center (SVEC) will serve as the interface for integration of EPOP-1 on the Wake Shield Facility. Instead of hydrazine, gaseous hydrogen will be used as the propellant. This sets EPOP-1 apart as the only planned flight experiment involving a hydrogen arcjet, both in the U.S. and abroad. The immediate commercial motivation for the hydrogen arcjet flight experiment is to

develop a Solar Electric Orbital Transfer Vehicle (SEOTV). Such an SEOTV would serve to provide the McDonnell-Douglas Delta-2 launch vehicle with orbit-raising capability. A study by McDonnell-Douglas has shown that there is a substantial market for such an application, with an estimated 41 launches over the next twelve years.

EPOP will provide the following benefits to such commercialization of space: (1) A realistic demonstration of electric propulsion systems in the actual space environment; (2) The development of a national test facility that can be configured to user needs; and (3) The development of an infrastructure for the systematic advancement of electric propulsion technology.

In this regard, EPOP also enhances CSTAR's mission of reducing the cost of accessing space. Specifically, the knowledge gained from EPOP will contribute to improved thruster design and improved components for electric propulsion systems. Also, the EPOP program is laid out such that the knowledge and experience of each flight can be used for the further development of diagnostics for space applications of electric propulsion systems.

In this paper, we review the program concept and objectives for the EPOP program as a whole. Also, for the 1.8 kW hydrogen arcjet system demonstration of EPOP-1, we describe the top-level constraints imposed by the experiment carrier, and their implementation. The arcjet system, propellant system, the diagnostics systems, and mission aspects are also discussed. Previous descriptions of the EPOP program may be found elsewhere [2-4].

* Research Engineer

† CSTAR Executive Director and Professor of Mechanical Engineering

‡ Senior Research Engineer

PROGRAM CONCEPT AND OBJECTIVES

The objectives of the EPOP program are to develop a universal facility as a payload on several carriers for demonstrating electric propulsion devices in space; and, thereby, to develop a capability for characterizing the in-space operation of electric propulsion systems. In particular, the program will strive to increase the confidence of the satellite community in electric propulsion and promote commercial applications of electric propulsion systems by assembling data bases for the benefit of potential users, manufacturers, and integrators of electric propulsion systems.

The EPOP program will make maximum use of existing or planned NASA flight programs, such as Shuttle experiments, the Wake Shield Facility (WSF), COMET [5; p. 213], and Space Station Freedom (SSF). The program flight plan defined by the consortium is shown in Fig. 1, which strives for an initial gaseous hydrogen arcjet flight on WSF-03, to be followed by an ion thruster flight on WSF-04, a prototype orbit transfer vehicle mission based on a liquid hydrogen arcjet experiment on COMET, and, finally, a high-power, long-duration test of an arcjet or ion-thruster system on SSF. In addition to the demonstration of the electric propulsion systems themselves, EPOP enables the development and demonstration of specific subsystems, such as solar arrays, batteries, power conditioners, and diagnostics instrumentation.

This paper describes the first of these flight experiments, EPOP-1, a gaseous hydrogen experiment on

the Wake Shield Facility. Mission objectives that have been established for EPOP-1 are:

- To demonstrate a complete hydrogen arcjet propulsion system;
- To develop and demonstrate an in-space electric propulsion test capability;
- To determine whether significant variations exist between ground-based and space-based operation of this arcjet system, including: electromagnetic characteristics, effects on the spacecraft, plume characteristics, and other operating characteristics.

Below, we address the specific implementation of these objectives, assuming Wake Shield to be the EPOP-1 carrier.

RATIONALE FOR AN IN-SPACE TEST

Many of the performance characteristics of an electric propulsion system can be characterized in ground tests. Even so, there is an inherent advantage to performing a demonstration in the actual space environment. This advantage stems both from the general demonstration of a completely integrated propulsion system, and the specific demonstration of specific components of this system.

A primary element of EPOP-1 will be the demonstration of a complete hydrogen feed system. Thus EPOP-1 will serve to reduce the risk of using new feed system components on a more expensive spacecraft. Also, as a result, critical components of the feed system will have already been tested before they are to be incorporated into a complete cryogenic storage system.

Another critical aspect of the flight experiment will be operation of the arcjet system itself. Specifically, ground tests have suggested that the operating voltage of the arcjet may be higher for the lower vacuum levels in the space test. This effect needs to be quantified so that the power conditioning unit can be designed accordingly.

Finally, since the arcjet is an electrothermal device, there is a question about the compatibility of the electromagnetic characteristics of the system with those of the spacecraft. EPOP-1 will attempt to address this compatibility issue. We anticipate that the space demonstration will prove to commercial users that hydrogen arcjet technology will be a highly desirable alternative to conventional chemical propulsion.

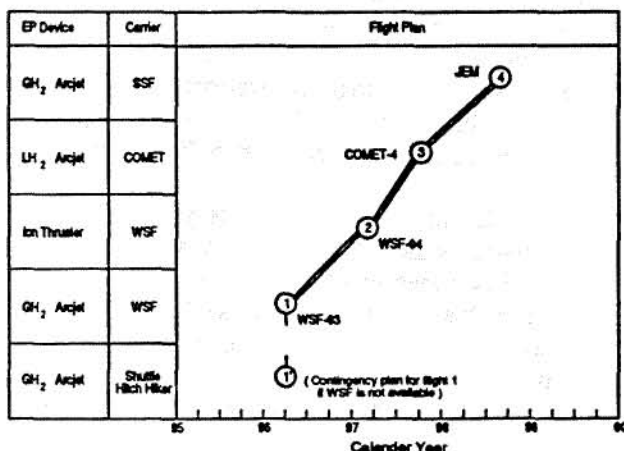


Fig. 1: Program plan for first four EPOP flights.

ARCJET SYSTEM

The decision to fly a 1.8 kW gaseous hydrogen arcjet experiment on EPOP-1 was based on maturity of the technology; specific interests on the part of the industrial consortium members; anticipated cost and funding figures; and consideration of other electric propulsion flight programs. Missions that will ultimately utilize hydrogen arcjets, for instance orbit transfer missions, will use arcjets that will require input powers of up to 30 kW. These higher power arcjets have been demonstrated in ground-testing to perform at specific impulses of up to 1500 s, at efficiencies of up to 40 percent [6].

However, a number of optimization and technical issues remain. These include performance optimization, establishment of the optimum voltage-current characteristic and mass flowrate for operation in a low-vacuum environment, heat dissipation, and electrode lifetime. We believe that operation of a lower power arcjet will allow some of these technical issues to be addressed along with a demonstration of a complete gaseous hydrogen arcjet.

It is intended to fly, on EPOP-1, a modified version of the 1.8 kW hydrazine arcjet system that has been developed at Rocket Research Company under a NASA Lewis Research Center grant [7]. A flight qualified version of this system [8] has been built by Rocket Research Company (see Fig. 2) for AT&T's Telstar 4 satellite, to be launched in 1993. This RRC 1.8 kW hydrazine arcjet (model MR 508) has a demonstrated Isp in excess of 500 s, and achieves a propellant savings of 200 kg over traditional chemical thrusters for a typical geosynchronous

communication satellite. This mass savings is exclusive of further mass savings in other areas, such as propellant tanks, support structure and launch vehicle.

The three components of the envisioned arcjet system include the arcjet thruster, the power cable, and the power conditioning unit (PCU). The latter may need to be reconfigured for the higher operating voltage for hydrogen. The hydrazine arcjet, shown in Fig. 2, would be stripped of the catalyst bed, gas generator, valve heater, propellant valve, and fluid resistor. This hardware is used when hydrazine is the propellant to decompose and control the flow of the liquid propellant. Otherwise, it is not anticipated that significant modifications will be required to the design. Total mass of the system should be less than 6 kg.

Thermal considerations regarding integration of the arcjet system with the Wake Shield would center primarily around the PCU, which rejects less than 10 percent of the input power, or typically 160 to 165 W, to the spacecraft mounting interface. By contrast, typical heat rejection to the spacecraft from the arcjet body itself is less than 5 W, because most excess energy is radiated away from the nozzle tip, which is sprayed with a high emissivity coating.

In addition to actively conditioning the power to the arcjet, the PCU contains electrical interfaces to the data acquisition and control subsystem, the power supply, and the arcjet thruster. Also, the PCU is programmed to refire automatically in the case of misfirings of the arc. Once the arc is established, the PCU maintains constant power output (rather than constant voltage or constant current) to the arcjet.

PROPELLANT SYSTEM

EPOP-1 will store and deliver gaseous hydrogen to the arcjet. A schematic of the proposed propellant system is shown in Fig. 3. Gaseous hydrogen, stored at a maximum pressure of 1900 psia, will be supplied to the system through a pyrotechnic valve that will be opened at the beginning of the experiment. A 10 micron filter will be used to insure the gas is devoid of particles, and a pressure regulator will be used to lower the pressure from tank pressure to 15 psia. This low pressure was chosen to simulate the pressure that would be present if a cryogenic storage system were used — the storage method an actual transfer vehicle would use for reduced storage tank mass and volume. A compressor will be used to increase the line pressure to ~100 psia, the pressure required by the arcjet, with the actual pressure being regulated by a pressure regulator near the arcjet. The operation of this

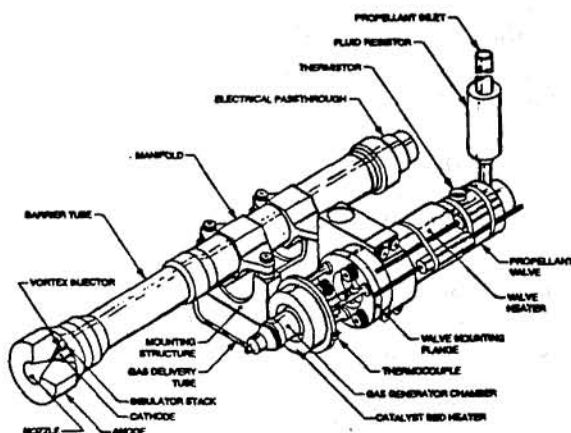


Fig. 2: Schematic of a 1.8 kW arcjet, which is to be modified for EPOP-1. The hardware from the catalyst bed to the fluid resistor (foreground) will be removed.

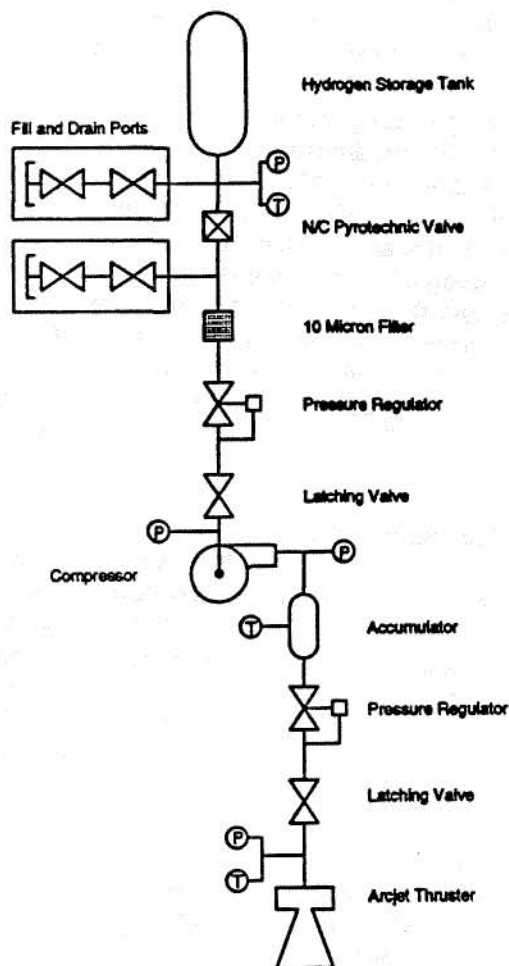


Fig. 3: Schematic of the gaseous hydrogen propellant system for EPOP-1.

flow control in a low-gravity environment is an important objective of demonstrating the operation of a complete hydrogen arcjet system. Temperature and pressure sensors are employed to help determine flowrates into the arcjet. Thus the actual flowrate will be calculated based on calibration measurements made before the flight.

EPOP-1 CARRIER

The Wake Shield Facility, being developed by the Space Vacuum Epitaxy Center (SVEC) at the University of Houston [5; p. 161], has been baselined as the carrier for EPOP. The primary aim of the WSF program is to utilize the vacuum environment of low Earth orbit (LEO) for materials processing in an ultra-clean environment; specifically, for epitaxial film growth experiments.

As shown in Fig. 4, the WSF is a circular stainless steel disk, 3.7 m in diameter. It is released from the

Table I: Top-level constraints for EPOP-1.

Constraint	Value
Maximum experiment mass	350 kg (770 lbm)
EPOP experiment time	24 hrs
Arcjet operation time	150 min. (cum.)
Peak power requirement	2 kW
WSF power available	< 500 W
Environmental constraints	1) Ultra-High vacuum 2) Shuttle constraints
Safety	Meet shuttle specs.
Telemetry	16 kbps Telemetry 64 kbps Video
Schedule	Launch June 96, WSF-03

Shuttle by the remote manipulator system (RMS) such that the axis normal to the surface is orientated along its orbital flight path. The EPOP experiment will be mounted (see Fig. 4), along with WSF's avionics, batteries, grapple fixture, and attitude control system on the ram side. Telemetry and control of WSF will be through an S-band RF link with the Shuttle. This link also allows for transmission of compressed video data. An obvious advantage of using WSF as the carrier for EPOP is the availability of these data links.

The use of WSF imposes several constraints on the EPOP experiment, specifically with regard to experiment time, experiment mass, available power, and telemetry. These are summarized in Table I. The goals and mission schedule for WSF necessitate that any arcjet firings be conducted after completion of all crystal growth experiments, leaving a period of about 24 hours until retrieval of the WSF by the Shuttle.

Insufficient power levels are available from WSF for a 1.8 kW experiment, so that EPOP must carry its own batteries. Due to a total mass limitation of 350 kg, the maximum net firing time of the arcjet system becomes limited to about 150 minutes. While this time is long enough to benchmark general performance of the arcjet system, it is too short to perform contamination studies.

DIAGNOSTICS SYSTEMS

To monitor the operation of the arcjet, and to enable a comparison between space- and ground-based operation, a number of diagnostics systems are under consideration for EPOP-1. These include systems that are EPOP-

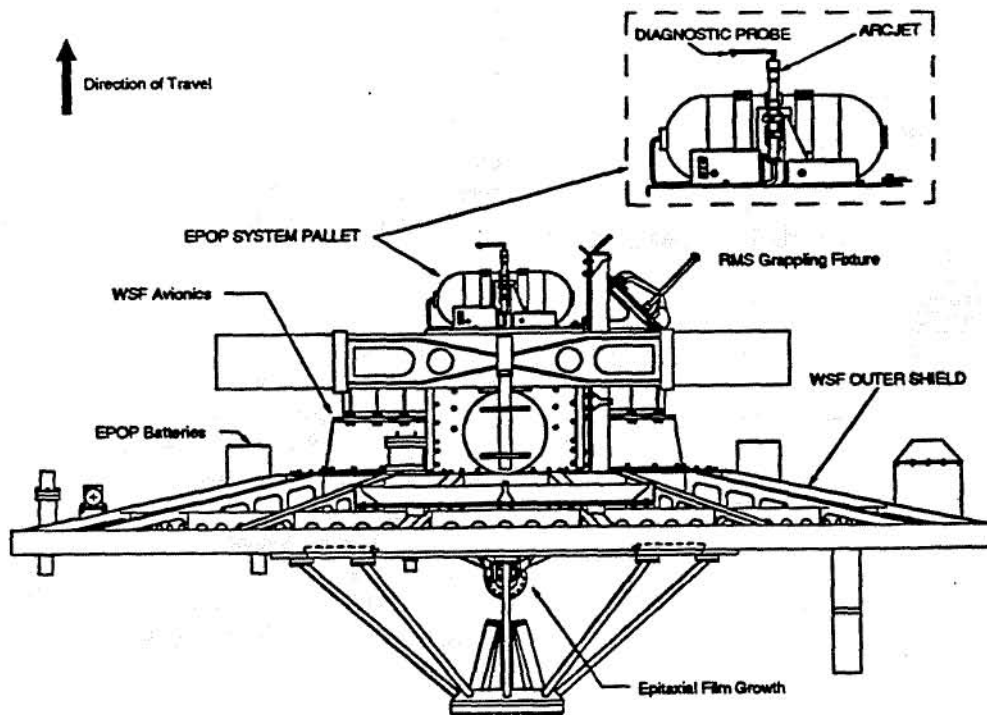


Fig. 4: Schematic of the Wake Shield Facility and the EPOP-1 experiment package.

specific, as well as systems that are available from Wake Shield and the Shuttle. Systems from the first category are shown schematically in Fig. 5. These are:

(1) Electronics to measure output voltage and output current from the PCU to the arcjet, during steady-state operation as well as during the initial transient when the arc is initiated. In particular, the arc voltage is a sensitive indicator of arcjet performance. For example, it reflects fluctuations in propellant flow rate, and there is indication that the arc voltage for a given current and flowrate may be higher than for operation in a terrestrial vacuum chamber;

(2) Electronics to measure battery voltage and input current to the PCU. These measurements would serve primarily to allow for an unambiguous diagnosis of any unexpected arcjet behavior;

(3) Pressure and temperature transducers at several locations in the propellant feed system, to allow for calculation of the propellant mass flow of the thruster;

(4) Thermocouples and thermistors to measure temperatures at various points on the arcjet and the PCU. These measurements would be performed, for example, to

estimate the radiative heat loss from the thruster, and to determine if heat losses from the PCU are dissipated adequately into the WSF structure;

(5) A camera and filter wheel assembly to obtain video data of the arcjet plume at different wavelengths. Video data can be used to analyze the stability of the plume, as well as to perform estimates of its core temperature, namely by comparing narrowband images taken at the hydrogen balmer-alpha and balmer-beta spectral lines, at 656.3 nm and 486.1 nm, respectively;

(6) A Langmuir probe to characterize the plasma properties of the arcjet plume. Specifically, measurements of the voltage-current characteristic of the probe would allow the calculation of electron density, electron temperature, plasma potential, and floating potential of the plume; if possible, a maneuverable probe will be used, so that radial sweeps of the plume can be performed.

In addition to these EPOP-specific diagnostics systems, a number of systems from the Wake Shield and the Shuttle would be available:

(7) Accelerometers, to determine the thrust of the arcjet system. Because the mass of the WSF is ~3000 kg,

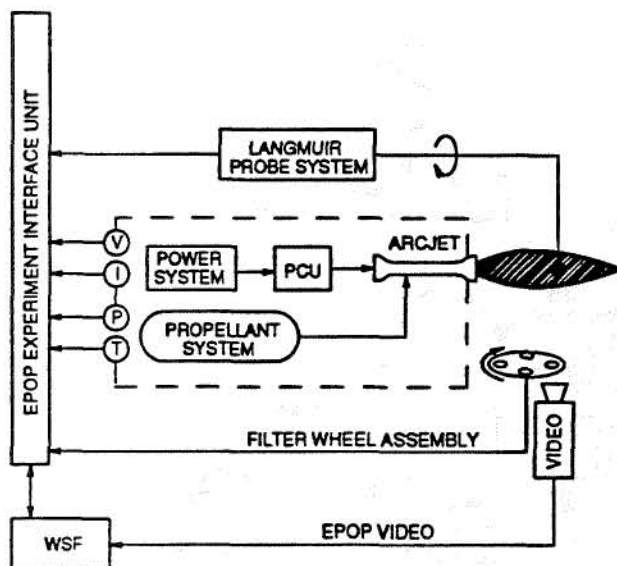


Fig. 5: Schematic of the EPOP-specific diagnostics systems.

and arcjet thrust will be on the order of 0.2 N, the expected acceleration will be on the order of $7 \mu g$. Thus the thrust measurement will only have a 15% accuracy. This in conjunction with the mass flow measurements above, would enable the calculation of a bracketed specific impulse that could serve to determine if measurements made on the ground are within this bracket. It should be noted that these acceleration measurements will be made independent of the EPOP demonstration.

(8) Use of the WSF communications link to perform additional electromagnetic interference characterization. This would be performed by error checking and noise analysis on the standard communication channel employed by WSF during firing of the arcjet system. Increased noise levels would constitute proof for electromagnetic characteristics at the frequency of the communication band (S-band). However, even a null result could be used to set upper limits on any noise from the arcjet system;

(9) If available, Phillips Laboratories' CHAWS plasma diagnostics package. In particular, coordination with this experiment would allow additional plasma characterization on both the ram and wake sides of the spacecraft, away from the arcjet thruster.

Finally, if Shuttle safety consideration would allow for thruster firings immediately prior to or during retrieval of the Wake Shield by the Shuttle's RMS, plume photography and video of the arcjet plume would be possible from the orbiter bay. One important diagnostic, namely characterization of contamination of spacecraft

surfaces as a result of arcjet operation, has been deemed too difficult, because of the relatively short operating time of the experiment.

Final selection of diagnostics subsystems and components for EPOP-1 will depend on funding and further analysis. It may not be practical to implement both types of electromagnetic characteristics diagnostics.

EPOP CONSORTIUM

A responsibility matrix for providing certain tasks for EPOP-1 is given in Table II. The table presents a general outline of responsibilities over the 5 year project. Although CSTAR is listed as having the lead in the EPOP program, technical and management decisions are made with complete consensus of the partners: McDonnell-Douglas Space Systems Company (MDC); Rocket Research Company (RRC); and Boeing Defense & Space Group (BD&SG). CSTAR has also taken the lead in developing and implementing the diagnostics to be used on EPOP.

McDonnell Douglas Space Systems Company will be the systems integrator for EPOP and will be the responsible partner for the areas that will support this role. They will also take the lead for the propellant and power supply subsystems, using their experience in this area.

Rocket Research Company will be responsible for production of the arcjet system. The arcjet system consists of three major subsystems: the arcjet thruster, the PCU and the triaxial power cable assembly connecting the

Table II: Responsibility matrix for EPOP-1.

	CSTAR	MDC	BD&SG	RRC	SVEC
Program Management	✓				
Diagnostics	✓				
System Engineering and Integration		✓			
Flight Operations		✓			
Power Supply		✓			
Propellant Subs.		✓			
Exp't Control & Data Acquisition			✓		
Arcjet and PCU				✓	
WSF Support and Modifications					✓

arcjet and PCU. The arcjet thruster is manufactured at RRC, while the PCU is manufactured at RRC's sister company Pacific Electro Dynamics, also located in Redmond, Washington. The power cable assembly is manufactured by Reynolds Industries, located in Los Angeles, California. Rocket Research Company is the arcjet system integrator, and performs project management and all integration and subsystem-level testing for the arcjet.

Boeing Defense & Space Group will be responsible for the experiment control and data acquisition subsystem. Finally, the Space Vacuum Epitaxy Center (SVEC) will be responsible for integration of the EPOP package on the Wake Shield Facility.

SUMMARY

We have explored the possibility of promoting the commercial use of electric propulsion systems in the U.S., namely by providing a flexible flight-testing capability for electric propulsion systems that would be funded jointly by NASA's Office of Commercial Programs and industry. In particular, we have performed a feasibility study for the flight of a 1.8 kW hydrogen arcjet experiment — EPOP-1 — aboard the Wake Shield Facility, a Shuttle-deployed free-flyer. At this point, it is envisioned that EPOP-1 will be manifested for a 1996 launch date.

Maximum cumulative thruster firing time for the experiment will be 2.5 hours. During this time, operating characteristics of the arcjet system will be monitored, including thrust, electrical efficiency, specific impulse, plasma properties of the plume, arcjet and plume temperatures, radio-frequency noise, and interference with spacecraft communications. Because of the small amount of hydrogen required, a simple gaseous storage system can be used. EPOP will draw supplemental power from the WSF bus, but primary power will be provided by a dedicated battery system. Thus, experiment time is limited by the maximum battery mass.

Responsibilities for the EPOP-1 experiment will be shared between CSTAR, which is a NASA-OCP-sponsored Center for the Commercial Development of Space, and industrial partners. At present, these partners are McDonnell Douglas Space Systems Company, Rocket Research Company, and Boeing Defense & Space Group. Also, as the responsible organization for the Wake Shield Facility, SVEC, another CCDS, will be involved.

ACKNOWLEDGMENTS

This work was funded by NASA Office of Commercial Programs under grant NAGW-1195 (EPOP supplement). We gratefully acknowledge inputs from other contributors and members of the EPOP consortium, present and past. These are: D. E. Hedges and J. S. Meserole at Boeing Defense & Space Group; K. Armbruster, R. D. Smith, R. J. Cassady, and W. W. Smith at Olin Rocket Research Company; E. C. Cady, R. S. Bell, and T. Miller at McDonnell Douglas Company; and A. Ignatiev and M. Sterling at the Space Vacuum Epitaxy Center. We appreciate greatly the many contributions by Dr. F. A. Speer, former Director of CSTAR.

REFERENCES

1. "EPOP Technical Feasibility Study," submitted to NASA Office of Commercial Programs, January 1992; copies available upon request.
2. Friedly, V. J., Garrison, G. W., and Ruyten, W. M., "EPOP: Toward the realization of an Electric Propulsion Orbital Platform," AIAA paper 92-3201, Nashville, Tennessee, July 1992.
3. Friedly, V. J., and Ruyten, W. M., "EPOP: the Electric Propulsion Orbital Platform," Proceedings of the CSTAR Thirs Annual Technical Symposium, Tullahoma, Tennessee, January 1992, pp. 62-73.
4. Ruyten, W. M., and Friedly, V. J., "EPOP diagnostics and data acquisition," Proceedings of the CSTAR Third Annual Technical Symposium, Tullahoma, Tennessee, January 1992, pp. 74-82.
5. "Accessing Space: A Catalogue of Process, Equipment, and Resources for Commercial Users," NP-133, written for the Office of Commercial Programs, NASA Headquarters, Code CCL, December 1990.
6. Haag, T., and Curran, F., "High Powered Hydrogen Arcjet Performance," AIAA 91-2227, 27th AIAA/SAE/ASME/ASEE Joint Propulsion Conference, Sacramento, CA, June 1991.
7. Smith R. D., Roberts C. R., Davies K., and Vaz J., "Development and Demonstration of a 1.8 kW Hydrazine Arcjet Thruster," AIAA paper 90-2547, Orlando, FL, July 1990.
8. Knowles S. C., Yano S. E., and Aadland R. S., "Qualification and Life Testing of a Flight Design Hydrazine Arcjet System," AIAA paper 90-2576, Orlando, FL, July 1990.

ION THRUSTER NUMERICAL MODELING

Xiaohang(Jeff) Peng*, Wilhelmus M. Ruyten**, and Dennis Keefer†

University of Tennessee-Calspan
Center for Space Transportation and Applied Research
University of Tennessee Space Institute
Tullahoma, Tennessee 37388

ABSTRACT

We present further numerical results of our particle-in-cell/Monte Carlo calculations of accelerator grid erosion in an ion thruster. Comparison between numerical and experimental results suggests that the accelerator grid impingement is primarily due to ions created far downstream from the accelerator grid. In particular, for the same experimental conditions as those of Monheiser and Wilbur at Colorado State University, we find that a downstream plasma density of $2 \times 10^{14} \text{ m}^{-3}$ is required to give the same ratio of 5% of accelerator grid impingement current to beam current. For this condition, we find a potential hill in the downstream region of 2.5 V.

I. Introduction

Accelerator grid erosion is one of the remaining issues for space applications of ion propulsion. Serious accelerator grid erosion was observed in several ground lifetests on xenon ion thrusters [1,2,3]. It is thought that the accelerator grid erosion is caused by charge-exchange ions, although there has recently been some speculation that it may also be a result of ionization of the background neutral gas by electron impact. Charge-exchange ion production is proportional to the sum of the neutral density due to propellant loss from the thruster and the neutral density in the vacuum chamber. It is very important to know what role the neutral gas plays in the vacuum chamber in terms of the grid erosion in order to interpret ground test results and to predict the engine lifetime in space operation conditions. In the past two years, we have developed a PIC simulation model to simulate the ion optics and accelerator grid erosion induced by

charge-exchange collisions [4,5]. However, if only those charge-exchange ions created near the accelerator region are considered, the calculated impingement current is about one order of magnitude less than the experimentally observed value.

The accelerator grid erosion rate and erosion pattern largely depend on the downstream plasma condition and the downstream electric field. It was believed and observed in the past that there was a potential hill near the accelerator grid. By assuming a certain downstream plasma density, our previous calculations did give a potential hill in the downstream region near the accelerator grid [4,5]. However, in recent experiments no significant electric potential gradient was observed in the region downstream from the accelerator grid [1,6]. Therefore, the motivation for this study is to see what downstream plasma density is required to predict the same ratio of the accelerator grid impingement current to the beam current as observed in the experiment conducted at Colorado State University [1], and to calculate the downstream electric potential field.

This work was supported by NASA Lewis Research Center under Grant NAG3-1315 and Boeing Defense & Space Group, Seattle Washington (Grant Monitor Dr. J.S. Meserole).

* CSTAR/UTSI, Research Engineer

** CSTAR/Calspan, Research Physicist

+ UTSI/CSTAR, B.H. Goethert Professor ES&M

The difference between these calculations and the previous ones is that ions are allowed to be extracted from the downstream plasma. By assuming a downstream plasma density, calculations for accelerator grid impingement current were made to include the contribution of ions extracted from the downstream plasma. Beyond this study, a detailed analysis of the downstream plasma effects on the accelerator grid erosion and the neutralization process are needed to simulate the downstream plasma by following both individual electrons and ions.

II. Simulation Model

Our Particle-In-Cell (PIC) and Monte Carlo simulation model for studying the ion optics and charge-exchange grid erosion is described in [4,5]. In this model, the PIC method is used to simulate the ion flow, and the Monte Carlo method is used to simulate the charge-exchange collisions.

The difference with our previous calculations is that in the present study ions can also be extracted from the downstream plasma. The reason for this is that if there are ion sources in the downstream region, ions can be extracted continuously from the plasma. The downstream plasma could result from the charge-exchange collisions between fast beam ions and neutral atoms and/or electron-neutral ionization collisions. Since, at this point, the electron density is not determined by tracking individual electron simulation particles, it is impossible to differentiate between these processes, and the calculation assumes a fixed plasma density.

Instead of tracking individual electron particles, it is assumed that the electron density n_e is in a Boltzmann equilibrium with the ion density n_0 in the downstream neutral plasma according to:

$$n_e = n_0 \exp \left[- \frac{e(\Phi - \Phi_0)}{kT} \right]$$

where e is the electron charge, k is Boltzmann's constant, T_e is the electron temperature, Φ_0 is the plasma potential, and Φ is the local potential.

III. Example Calculation

The calculations were performed for operation of the thruster on xenon propellant. The computational domain was chosen to correspond to the experimental configuration used by Monheiser and Wilbur [1]. It is assumed that a neutral plasma exists at the upstream boundary of the computational domain, with an ion temperature of 1000 K and an electron temperature of 1.5 eV. The screen grid is at a potential of 1000 Volt and the accelerator grid is at a potential of -500 Volt. The discharge voltage is assumed to be 30 Volt. The neutral density in the code is chosen to correspond to a vacuum chamber pressure of 7×10^{-6} Torr, and the beam current is 0.5 mA. Both screen and accelerator grid hole diameters are 1 cm. The separation of the two grids is 0.4 cm; the thicknesses of the grids are 1.5 cm. The center-to-center distance between two adjacent apertures is 1.5 cm. Calculations were performed for different downstream plasma densities, namely in the range 10^{13} to 10^{15} m^{-3} . The electron temperature of the downstream plasma was set equal to those inside the thruster, namely 1.5 eV.

Our two-dimensional, axisymmetric PIC/Monte Carlo code has been ported to run on a PC. Although we have shown that a three-dimensional code is necessary to calculate the pitted erosion patterns that are observed in ground tests, the two-dimensional code, which is less time-consuming, is particularly well suited to modeling the ion optics. An especially attractive feature of the new, PC-based, code is that of added graphics capability, which allows the operator to monitor continuously the flow of both the beam and charge exchange ions as the calculation is progressing. An example of this graphical output is shown in Figure 1. The upper portion of the plot shows the electric potential contours and the lower portion shows ion particles. The graphical simulation now clearly shows how these charge exchange ions (outside of the primary ion beam) proceed toward the accelerator grid.

Energy distribution of erosion ions

Figure 2 shows the energy distribution of ion particles which strike the accelerator grid. For both upstream and downstream surfaces of the accelerator grid, it can be seen that most ion particles have

energies of about 500 eV. This indicates that most of them are created in the downstream plasma region. In Figure 2b, those ions which have energies much less than 500 eV are charge-exchange ions created near the accelerator grid region. For the interior surface of the accelerator grid shown in Figure 2c, most ions have energies less than 200 eV. The impingement current reaching the downstream surface of the accelerator grid is more than 98% of the total accelerator grid impingement current. Therefore, it is concluded that the accelerator grid erosion is caused by those ions created far downstream from the accelerator grid inside the plasma.

Electric potential field

Electric potential contours are shown in Figure 3. In order to have a 5% ratio of the accelerator grid impingement current to the beam current, as found in Ref. 1, it was necessary to assume a downstream plasma density of about $2 \times 10^{14} \text{ m}^{-3}$, with an assumed electron temperature of 1.5 eV (for these values we actually find a ratio of 4.7%). Under these conditions, the calculated downstream electric potential peak value is about 2.5 Volt. The plasma density of $2 \times 10^{14} \text{ m}^{-3}$ implies that the fraction of the background gas that is ionized is about 0.1 percent.

IV. Conclusion and Recommendations

Based on this study, it is confirmed that the accelerator grid erosion is caused by the ions created far downstream from the accelerator grid. To obtain about the same ratio of the accelerator grid impingement current to the beam current as observed at Colorado State University [1], we find that a downstream plasma density of about $2 \times 10^{14} \text{ m}^{-3}$ is required, with an assumed electron temperature of 1.5 eV.

To fully understand the role of the downstream plasma on accelerator grid erosion, several questions must be answered by the experiments: What is the downstream plasma density? What is the downstream electron temperature? How does the downstream plasma density vary as a function of the vacuum chamber pressure? And finally, does the formation of the downstream plasma result from charge-exchange collisions and/or electron-neutral ionization collisions?

From the numerical simulation side, it appears that electron particles also need to be tracked individually in order to simulate the neutralization process and provide insight into the formation of the downstream plasma.

ACKNOWLEDGMENTS

This work was jointly supported by NASA Lewis Research Center under grant NAG3-1315 and Boeing Defense & Space Group in Seattle, Washington (grant monitor Dr. J. S. Meserole).

References:

- [1] Monheiser, J. and Wilbur, P., "An Experimental Study of Impingement-Ion-Production Mechanisms," AIAA paper 92-3826, Nashville, Tennessee, July 1992.
- [2] Patterson, M. J. and Verhey, T. R., "5-kW Xenon Ion Thruster Lifetest," AIAA paper 90-2543, Orlando, Florida, July 1988.
- [3] Rawlin, V. K., "Internal Erosion Rates of a 10-kW Xenon Ion Thruster," AIAA paper 88-2912, Boston, Massachusetts, July 1988.
- [4] Peng, X., Keefer, D., and Ruyten, W. M., "Plasma Particle Simulation of Electrostatic Ion Thrusters," *J. of Propulsion and Power*, Vol. 8, No. 2, pp. 361-366, March-April 1992.
- [5] Peng, X., Ruyten, W. M., and Keefer, D., "Three-Dimensional Simulation of Grid Erosion in Ion Thrusters," IEPC paper 91-119, 22nd International Electric Propulsion Conference, Viareggio, Italy, October 1991.
- [6] Beattie, J. R. and Matossian, J. N., "High Power Ion Thruster Technology," NASA Contract Report CR-187161, February 1992.

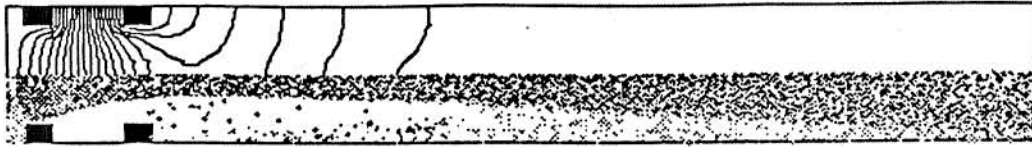


Figure 1: Typical snapshot during the simulation of the ion dynamics in the ion acceleration region of an ion thruster. Shown are electric potential contours and the positions of beam and charge-exchange ions.

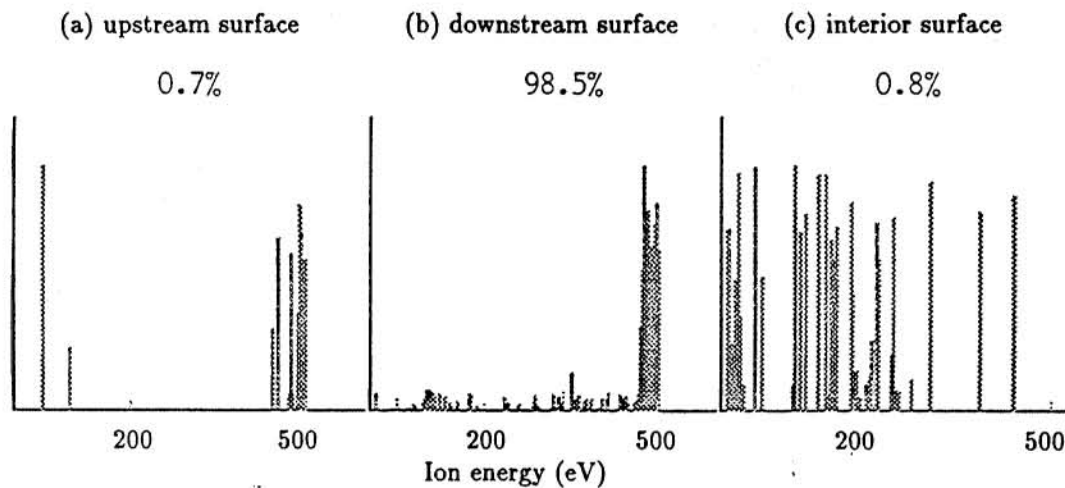


Figure 2: Energy distributions of the ions which impact the accelerator grid: (a) upstream surface, (b) downstream surface, and (c) interior surface.

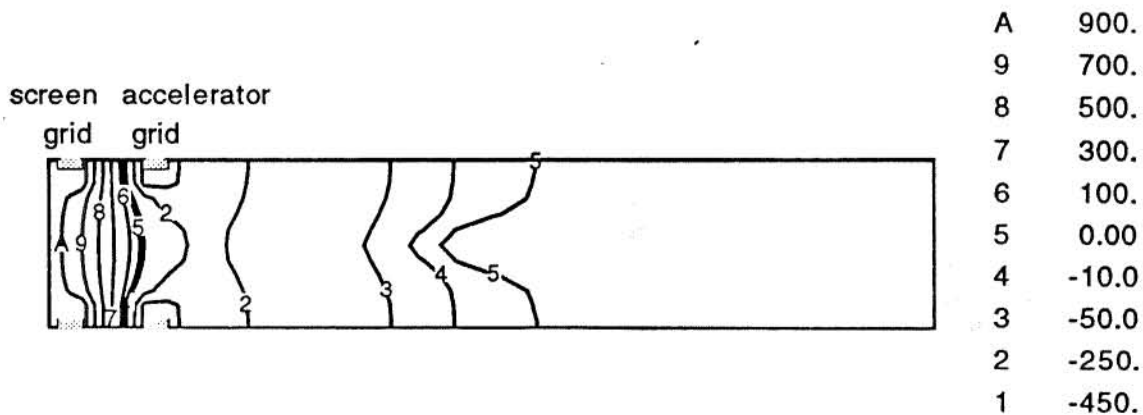


Figure 3: Electric potential contours.

ION THRUSTER DIAGNOSTICS

W. M. Ruyten*, V. J. Friedly**, X. Peng**, J. A. Celenza†
University of Tennessee-Calspan
Center for Space Transportation and Applied Research
Tullahoma, Tennessee 37388-8897

and

D. Keefer‡
Center for Laser Applications
University of Tennessee Space Institute
Tullahoma, Tennessee 37388-8897

Abstract

We report the results of spectroscopic investigations of beam-plasma interactions in the plume from a 3 cm ion source operated on argon. Ion-electron, ion-neutral, and electron-neutral scattering are identified by studying the dependence of neutral and ion emission intensities on chamber pressure and mass flow rate, and by analyzing the emission lineshapes at a non-orthogonal angle to the plume axis. Through the Doppler shift, we are able to separate contributions from fast beam ions and fast charge-exchange neutrals on the one hand, and of slow neutrals and slow ions on the other. We discuss the application of this new technique to the characterization of beam plasma interactions in the downstream region of ion thruster engines, and its potential for identifying the processes which lead to grid erosion.

1. Introduction

It has been suspected for a long time that one of the important mechanisms of accelerator grid erosion in ion thrusters is the production of charge-exchange ions in the downstream region of the plume. These ions are created at relatively small velocities. Thus they are accelerated back to the thruster grid, causing sputtering of the accelerator grid. We have performed extensive numerical studies of this process using particle-in-cell and Monte-Carlo techniques, and a number of papers on this work have been presented [1-8].

The numerical models are especially successful in calculating the pitted erosion patterns which develop

during extended life testing of the grids. It appears that the models are also capable of yielding correct quantitative erosion rates. However, this requires knowledge of several experimental parameters which are not easily measured. One of these is the density distribution of neutral atoms near the grids, and the resulting production rate of charge-exchange ions as a function of position. Direct-Simulation-Monte-Carlo calculations are in progress to model the neutral efflux from the thruster in detail.

Most recently, it has been called into question whether the production of charge-exchange ions, by itself, can account for the observed impingement currents in ground tests [9]. It appears that even an ionization level as low as 0.01 percent of the background gas surrounding the thruster may be sufficient to provide the balance of the ion current on the accelerator grids, after charge-exchange is accounted for [8]. To model this extraction of ions from the plasma surrounding the thruster, it is necessary to know such properties as ion and electron temperatures, and the location and spatial extent of the plasma sheath which separates the thruster from its surroundings.

A standard technique for analyzing the above processes is through the use of electrical probes [10-13], and we

This work was supported jointly by Boeing Defense & Space Group of Seattle, Washington, and by the Center for Space Transportation and Applied Research.

* Principal Investigator; Calspan, Senior Engineer

** Research Engineer

† Graduate Student

‡ UTSI/CLA, B. H. Goethert Professor of ES&M

have reported the results of such measurements [14]. Here we investigate an alternative technique, based on spectroscopic measurements of line emissions from the ion plume. Similar types of optical studies have been performed previously [13,15-16]. However, an important innovation of our work is the use of a spectrometer with sufficient resolution (better than 0.1 \AA fwhm) to study the Doppler shapes of the emission lines at a nonorthogonal observation angle to the plume axis.

All experiments were performed on the plume from a 3 cm ion source, operated on argon. We show that the production of charge-exchange neutral atoms can be identified unambiguously from the emission lineshapes. We are also able to identify the effects of ion-neutral scattering and electron excitation of beam ions, by studying the dependence of the emission intensities of both ion and neutral lines on source flow rate and facility background pressure. The results of the optical measurements appear to be consistent with the Langmuir probe studies, reported earlier [14].

We discuss the importance of the new spectroscopic technique to the characterization of plume plasma properties and beam-plasma interactions in ion thruster plumes. In particular, we identify possible ways in which the technique could be used to pinpoint the boundary conditions which are needed for a correct numerical simulation of the beam-plasma interactions and the resulting grid erosion in ion thrusters.

2. Experimental setup and procedure

Experimental measurements were performed on the plume from a commercial 3 cm ion source, operated on argon. A photograph of the source, Ion Tech model 3-1500-100, is shown in Fig. 1. A high-resolution spectrometer, a 1.25 m focal length SPEX with an 1800 gr/mm grating, was used to record line emissions from both neutral and singly ionized argon in the plume. Figure 2 shows a diagram of the optical setup. The ion source is mounted on a computer-controlled xyz stage inside the test facility. Plume emission is observed through a large optical access port.

Light from the plume is focused into the spectrometer by a large-aperture ($f/6$) Cassegrain telescope, mounted outside of the vacuum facility. The spectrometer was aligned either perpendicular to the plume, or at an angle of 71.4 degrees to the plume centerline (as shown in Fig. 2). A red-sensitized photo multiplier tube (PMT) served as the detector. The PMT signal was amplified and read out by the PC-based data acquisition system. Also, the signal was recorded simultaneously by a stripchart recorder.

For some of the experiments, the external neutralizer filament of the ion source was moved about 80 mm downstream from the grids. In this manner, it was possible to observe argon line emissions close to the source without picking up the strong continuum emission from the brightly glowing filament. Typical flow rates for the source were 4 to 12 sccm argon. Also, for a number of experiments the tank pressure was raised intentionally by flowing additional gas, also argon, into the facility through a bypass valve. Using a Balzers cryo pump, the resulting tank pressures were in the range 0.0013 to 0.04 Pa, or 1×10^{-5} to 3×10^{-4} Torr.

Discharge, beam, and accelerator voltages for the source were typically 50 V, 300 V to 1100 V, and -500 V, respectively. Typical beam currents were in the range 40 to 100 mA. These correspond to rather low propellant utilization efficiencies, especially for the higher flow rates. On the other hand, the large neutral loss from the source and the bypass flow into the chamber assured strong optical emissions from the plume, thereby simplifying the experimental measurements.

Horizontal slit widths of 10 to 100 microns were used on the spectrometer. These values correspond to spectral resolutions of 0.038 to 0.38 \AA . Slit heights were 1 to 10 mm. An absolute calibration of the detection system was performed using a standard tungsten filament lamp. Measurements could be performed over the range 3300 to 8600 \AA , with maximum sensitivity around 4500 \AA . Wavelengths below 3300 \AA are not transmitted by the optical access port of the vacuum chamber. Above 8600 \AA , the quantum efficiency of the PMT falls off rapidly. Further details of the optical setup may be found in an accompanying paper on arcjet plume diagnostics [17].

3. Results of survey measurements

A broad survey scan of the plume revealed a rich spectrum of neutral (Ar I) and singly ionized argon (Ar II) emissions, superimposed on the continuum background from the filament. A small part of this spectrum is shown in Fig. 3. Using an atlas of argon lines [18], it was straightforward to identify the various lines. Moreover, it appears that all of the lines listed in the atlas were present in the plume spectrum.

It is important to note that the radiative lifetime for all observed lines is on the order of several nanoseconds. Thus, even for a 1000 eV ion, moving with a velocity of 70 km/sec, the "lifepath" of the excited state is less than 1 mm. This implies that any excited species created in the source have already decayed by the time they reach the observation region, some 20 to 100 mm downstream from

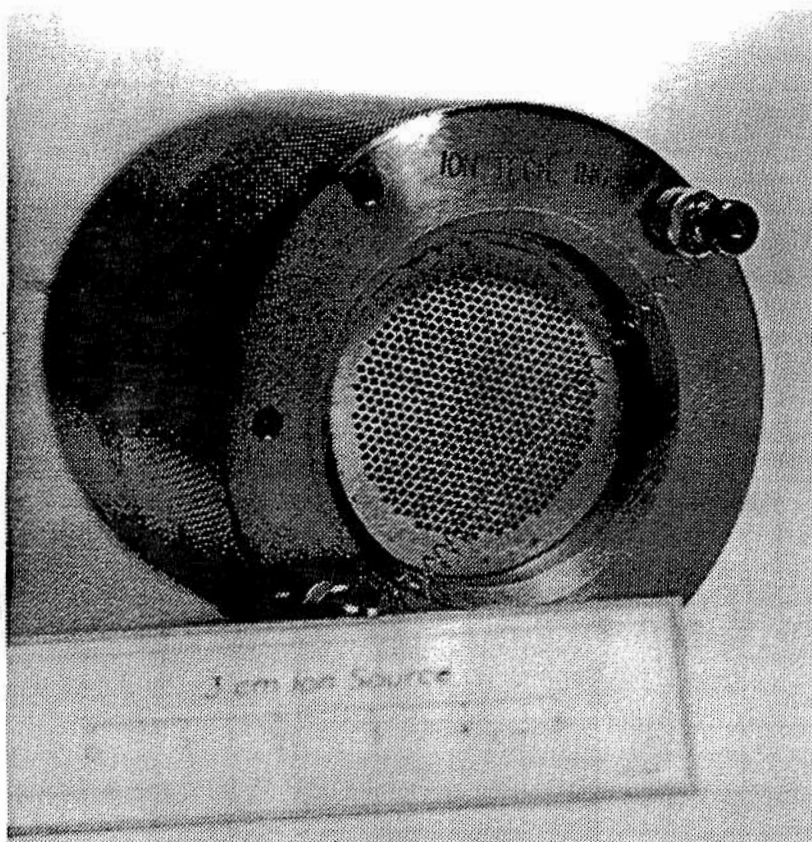


Figure 1: Photograph of the 3 cm ion source.

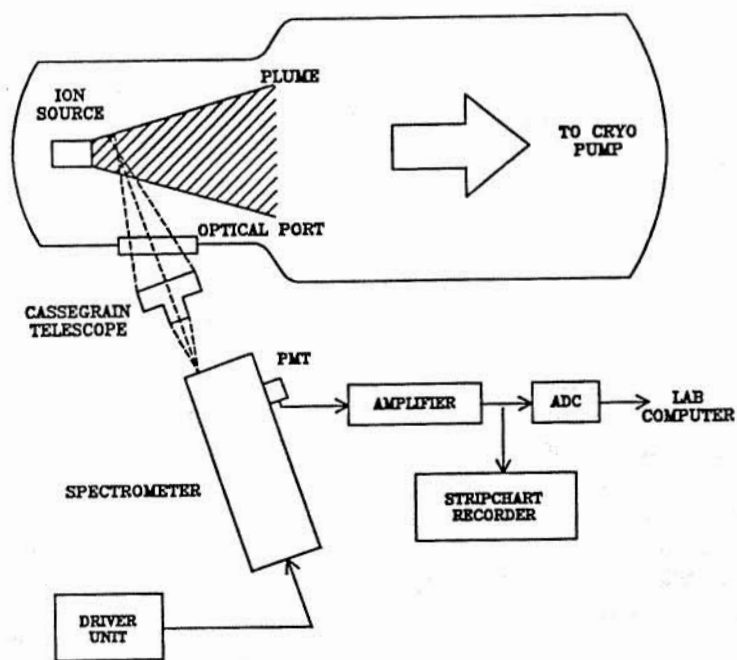


Figure 2: Schematic of the optical setup.

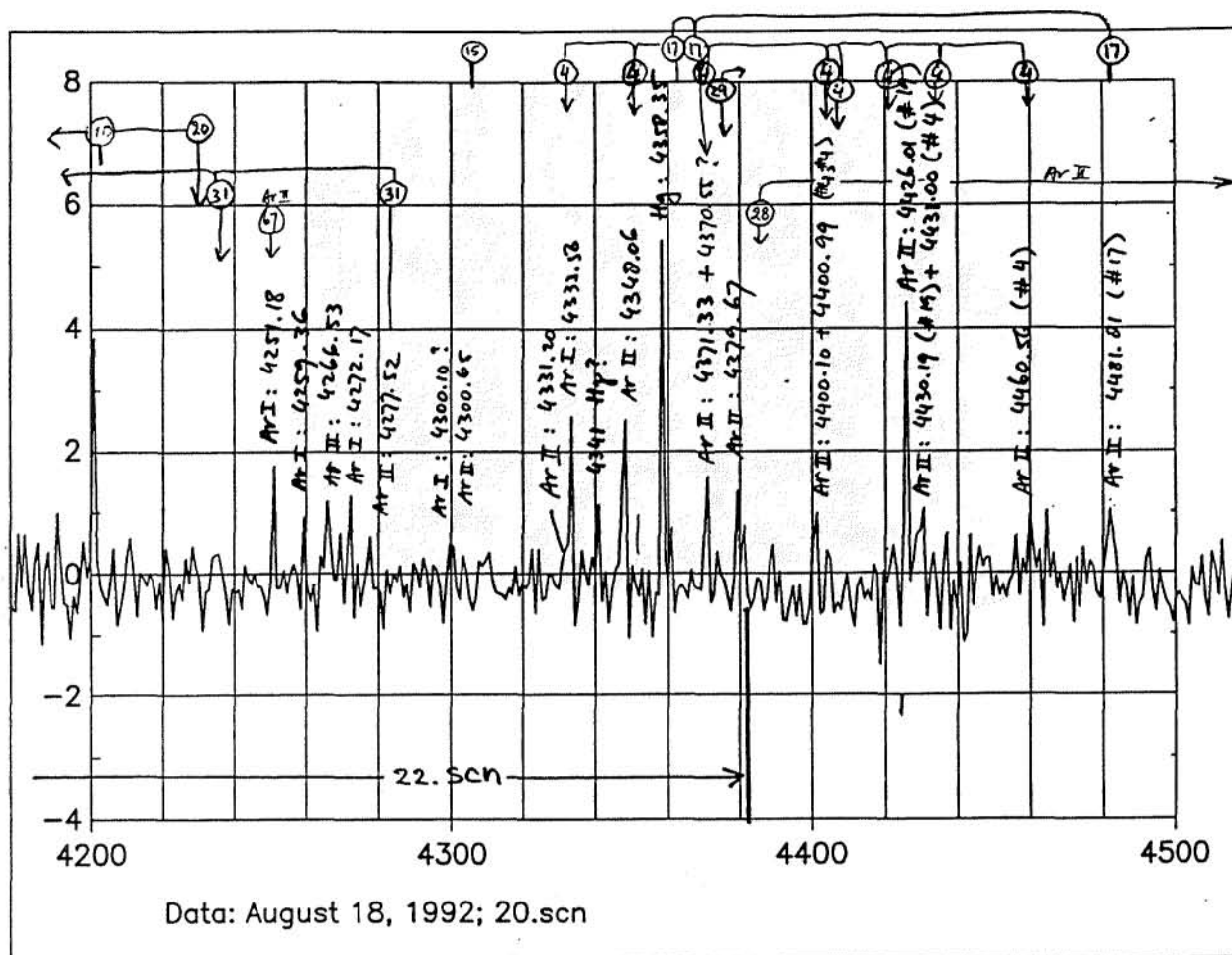


Figure 3: Small section of a coarse survey scan, covering the range 4200 Å to 4500 Å of the argon plume spectrum. The baseline has been corrected for filament emission. Line designations and multiplet numbers from Ref. [18] are indicated, both for neutral (Ar I) and ion lines (Ar II). Many more lines can be identified by scanning smaller portions of the spectrum at slower rates.

the accelerator grid. Thus all measured emissions must be the result of scattering and/or excitation processes which occur within the field of view of the optical system.

For a few selected spectral lines, the spatial variation of the plume emissions was established. Figure 4 shows the emission signals for a neutral line and a nearby ion line as a function of axial distance from the source. Clearly, the spatial variation of the two emission features is very similar. For reference, the emission from the filament is shown as well (these data were obtained before the filament was moved 80 mm downstream).

The decrease in emission intensity of the argon lines appears to be consistent with the observed divergence of the ion plume: Namely, because the observation region has a finite height, the fraction of the plume which is imaged onto the detector decreases as the plume expands. Also,

the decrease in emission intensity in Fig. 4 follows the same pattern as the decrease in electron current at plasma potential obtained with a Langmuir probe (see Fig. 4 of Ref. [14]).

Figure 5 shows similar results for radial scans of the plume, performed at two axial locations. Again, the spatial variation of ion and neutral signals is essentially identical. From Fig. 5, we estimate that the plume diameters (enclosing 95 percent of the ion flux) are 25 mm at $x = 0$ mm and 44 mm at $x = 60$ mm, respectively. These values imply a 9 degree half-angle for the plume divergence. This value is larger than the calculated value of 5.5 degrees (see Fig. 13 in Section 7). As is pointed out in Section 7, this is probably due to beam broadening as a result of elastic and/or inelastic scattering off the fairly high density neutral gas in the facility.

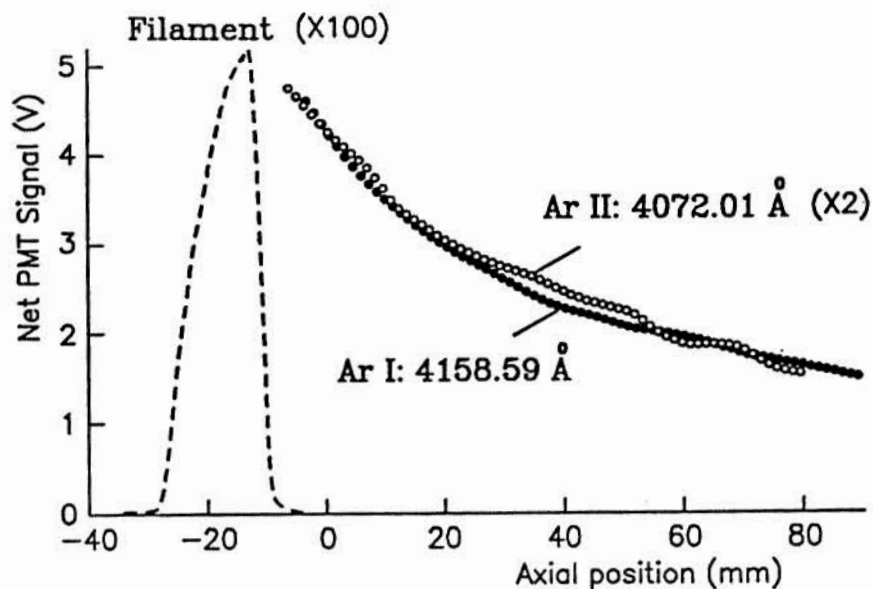


Figure 4: Axial variation of emission intensity for an argon neutral line (Ar I), an argon ion line (Ar II), and the filament background. The coiled filament is located at about $z = -15$ mm; the accelerator grid is located at about $z = -25$ mm. Data taken with $V_B = 500$ V.

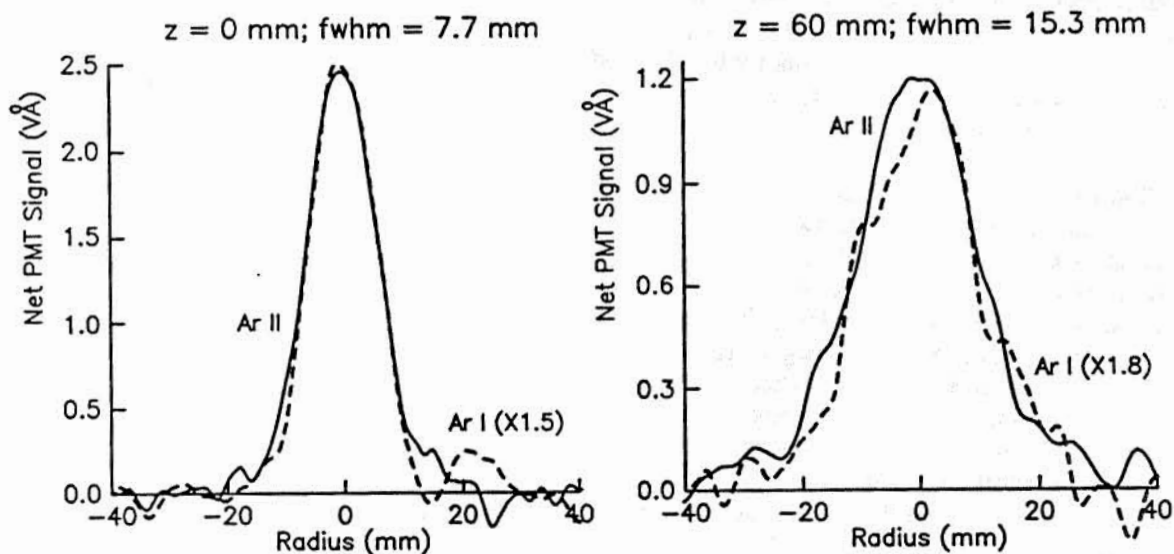
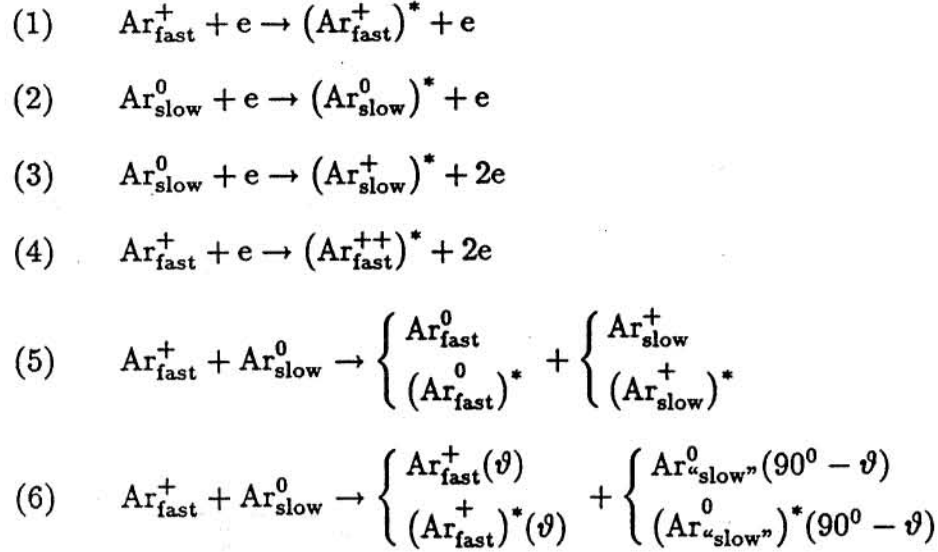


Figure 5: Radial variation of emission intensity at two axial positions, for the same conditions as in Fig. 4.

Table I: Beam-plasma interactions which we consider in this study. Asterisks indicate excited states.



4. Identification of interaction mechanisms

In the absence of beam-plasma interactions, the only heavy species in the plume would be fast beam ions (ions with kinetic energies of at least several hundred electron volts) and slow neutral atoms (atoms with no more than several electron volts of kinetic energy). Both would either be in the ground state or a metastable state, and no emission would be observed. To account for the observed plume emissions it is necessary to identify the different excitation mechanisms.

In Table I we list the interactions which we believe to be most important [19]. The first two are: (1) electron impact of beam ions; and (2) electron impact of slow neutrals. The second pair is: (3) ionization of slow neutrals by electron impact; and (4) production of doubly-charged ions by electron impact of singly charged beam ions. We did not find any evidence of doubly charged ions in the broad survey spectra. However, no concentrated effort was made to identify such doubly charged ions, so we cannot rule out their existence. Neither of the reactions (1) through (4) are accompanied by significant momentum transfer to the heavy collision partner. Thus the velocity vectors of the ions and neutrals are unchanged during the excitation process.

The remaining two processes in Table I involve interactions between fast beam ions and slow neutrals. They are: (5) charge-exchange collisions; and (6) elastic or inelastic scattering. Figure 6 illustrates the two

processes. In the first one (5) a fast beam ion exchanges an electronic charge with a slow neutral atom, leaving behind a slow ion and a fast neutral atom. Little momentum transfer takes place, so the resulting fast neutral has essentially the same vector velocity as the original beam ion. The charge-exchange ion picks up a small (but superthermal) velocity, perpendicular to the path of the beam ion.

In the other process (6) from Fig. 6, both the beam ion and the thermal neutral maintain their identities (ion and

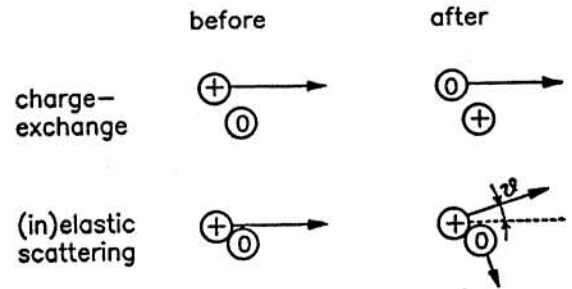


Figure 6: Schematic representation of charge-exchange and (in)elastic scattering processes between fast beam ions and slow neutral atoms. In an inelastic collision, one or both of the scattering partners are left in an excited state after the collision.

neutral, respectively). However, depending on the impact parameter of the collision, both are scattered. For small impact parameters, the scattering angles can be large. Thus the velocity vector of the incident beam ion can be modified significantly (both in magnitude and direction), and the thermal neutral atom can pick up a significant velocity. Conservation of momentum implies that the velocity vectors after the collision are orthogonal.

Both processes (5) and (6) may give rise to plume emission directly. This occurs when one of the scattering partners is left in an excited state after the collision. This is the case in an *inelastic* collision. Alternatively, it is possible that excitation of the scattering product does not occur until *after* the collision, namely upon electron impact of the elastically scattered product by one of the reactions (1) through (4) from Table I. We cannot distinguish between these two scenarios on the basis of the present set of experiments.

However, the above description of the relevant beam-plasma interactions invites several conjectures which may be verified experimentally. These concern the dependence of emission intensities on neutral densities; the interpretation of the emission lineshape as a measure of the velocity distribution of the emitting species through the Doppler effect; and the broadening of the plume with increasing neutral density. These conjectures, with supporting experimental data, are discussed in Sections 5, 6, and 7.

5. Dependence of emission on neutral density

Among the six interactions identified in Table I, processes (1) and (4) stand out as the only ones which should be independent of the neutral density in the plume. By contrast, the rates of all other processes in Table I should be linearly proportional to the neutral density. This leads to the following conjectures:

Conjecture 1: The emission intensity from neutral atoms should be proportional to the neutral density and extrapolate to zero in the limit of zero neutral density. This is because all neutral emissions involve either the neutral atom itself, or a neutral collision partner in the case of a charge-exchange reaction.

Conjecture 2: The emission intensity from singly ionized ions should vary linearly with neutral density. However, unlike for neutral emissions, emissions from ions should contain a signal component which is independent of the neutral density, namely that which is associated with electron excitation of beam ions.

Conjecture 3: The emission intensity from doubly charged ions should be independent of the neutral density, because only beam ions and electrons are involved.

To test the first two conjectures, a series of experiments was performed in which the spectrometer was scanned repeatedly across a particular spectral line. The neutral density in the plume was varied either by flowing gas into the chamber through the bypass valve, or by increasing the flow rate through the source. However, all electrical parameters of the ion source were kept constant. In particular, the beam current was kept constant. Emission intensities were calculated by curve-fitting the recorded spectral lines with a gaussian model function. This procedure was found to be quite adequate to calculate the area under the spectral line, even though the fit did not always approximate the data very well.

Figures 7 and 8 show some of the results. In Figure 7, the emission signal of the argon neutral line at 4159 Å is plotted as a function of chamber pressure for different flow rates. Figure 8 shows similar data for the argon ion line at 4880 Å. To test conjectures 1 and 2, bilinear curve fits were performed to the data from Figs. 7 and 8, according to:

$$S_{\text{PMT}} = A + B \times P + C \times \dot{m}^* \quad (1)$$

where S_{PMT} is the emission signal, P is the chamber pressure, and \dot{m}^* is the net neutral flow through the source. This net flow is the actual flow rate through the source, corrected for the flow equivalent of the ionized fraction of the plume (1 sccm of flow per 64 mA of current for argon).

The solid lines in Figs. 7 and 8 represent the results of the bilinear curve fits. They are found to approximate the data quite well, thereby verifying the conjecture of a linear dependence of emission intensity on neutral density. The dashed lines represent the extrapolated pressure dependence in the limit of zero net neutral flow through the source. This limit corresponds to 100 percent propellant utilization efficiency, and cannot be achieved experimentally with our source.

To distinguish between conjectures 1 and 2, we need to identify the signal contribution in the limit of zero neutral density. This limit is given by the intercept of the dashed curves with the vertical axes in Figs. 7 and 8, given by the parameter A from Eq. (1). In Fig. 7, this intercept is given by $A = 0.064 \pm 0.051$, where the standard deviation is calculated from the bilinear curve fit. That is, the neutral signal extrapolated to zero neutral density is negligible, in agreement with conjecture 1.

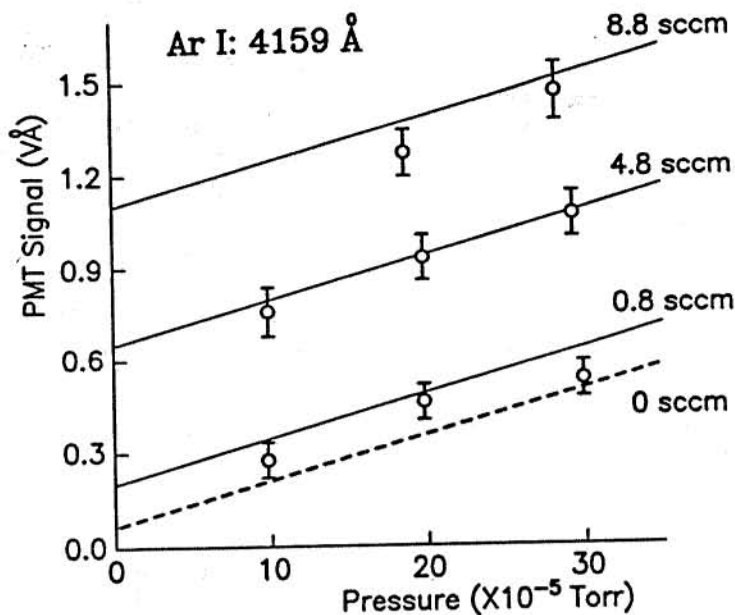


Figure 7: Dependence of emission intensity on chamber pressure and net neutral flow rate (in sccm) for the argon neutral line at 4159 Å. Experimental conditions were as follows: $V_D = 50$ V; $V_B = 900$ V; $V_A = -500$ V; $J_B = 80$ mA; $\alpha = 71.4^\circ$. Solid and dashed lines represent the results of a bilinear curve fit.

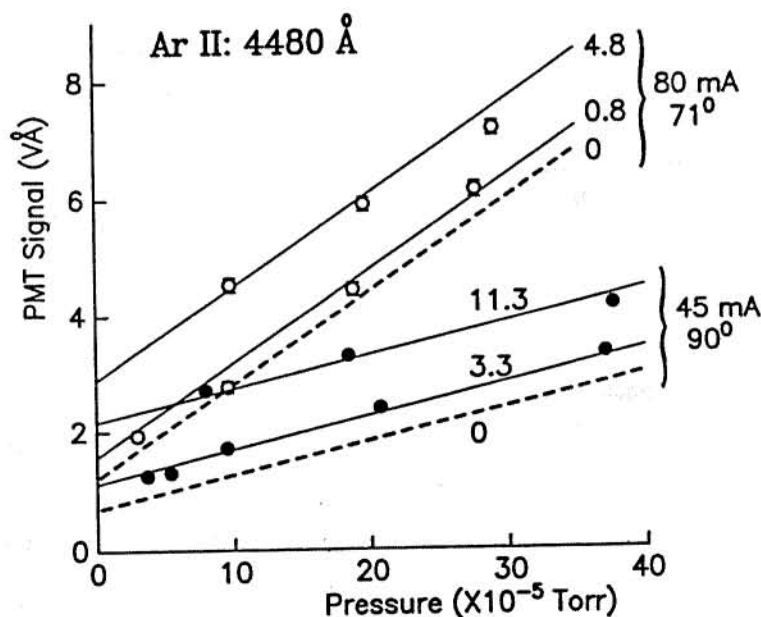


Figure 8: As Fig. 7, for the argon ion line at 4880 Å. Conditions were $V_D = 50$ V; $V_B = 900$ V; $V_A = -500$ V; $J_B = 80$ mA; $\alpha = 71.4^\circ$ for upper set of data, and $V_D = 50$ V; $V_B = 500$ V; $V_A = -500$ V; $J_B = 45$ mA; $\alpha = 90^\circ$ for the other.

On the other hand, both sets of data in Fig. 8 yield a non-vanishing contribution for the emission of an ion line in the limit of zero neutral density, namely $A = 1.20 \pm 0.20$ for the set of data taken with a beam current of 80 mA, and $A = 0.683 \pm 0.095$ for a beam current of 45 mA. Both of these values are statistically significant at the level of six standard deviations. Thus, they are convincing proof that part of the emission signal is due to electron excitation of the ion plume, as stated in conjecture 2.

So far, no systematic effort has been made to identify emissions from doubly charged ions. Thus conjecture 3 can neither be verified nor rebutted at this point.

In principle, it should be possible to establish, in similar fashion, the dependence of the emission intensity on the ion flux. We have found that, indeed, the strength of the emission signals increases with beam current. However, it is not clear a priori whether this dependence should be linear. In particular, we expect that the electron density in the plume is strongly correlated with the ion density, so as to maintain a charge-neutral beam. Thus it is conceivable that even processes which do not involve beam ions (electron excitation or ionization of slow neutrals) should show a dependence on beam current. Similarly, electron excitation of beam ions might depend nonlinearly on the beam current as a result of the coupling between positive and negative charge. For these and other reasons, a systematic study of the dependence of emission intensity on beam current is rather complicated, and we have not undertaken such a study here.

6. Lineshape measurements

In order to clarify the role of the different contributions to the observed emission lines, we performed detailed measurements of the emission lineshapes. One of the primary mechanisms to determine lineshape is Doppler broadening. Namely, let the non-Doppler shifted wavelength of an emission line be given by λ_0 . If the emitting atom has a velocity component v_1 along the observation direction, the observed emission wavelength is Doppler shifted by an amount $\Delta\lambda_D$, given by

$$\Delta\lambda_D = \lambda_0 \times (v_1 / c), \quad (2)$$

where c is the speed of light. The shift is toward lower wavelength for an atom moving toward the detector. This Doppler shift can be substantial for the beam ions excited by electron impact [process (1) from Table I] and for charge-exchange neutrals [process (5) from Table I], which continue traveling at beam velocities. For a beam voltage V_B , a discharge voltage V_D , and an observation angle α (either 90° or 71.4° in our experiments), the

projected velocity for a beam atom moving along the centerline of the source is given by:

$$v_1 = [(2e/m) \times (V_D + V_B)]^{1/2} \times \cos\alpha, \quad (3)$$

where e/m is the charge-to-mass ratio of the beam ion. As an example, for $V_D = 900$ V, $V_B = 50$ V, $\alpha = 71.4^\circ$ and $\lambda_0 = 8115$ Å (a strong argon neutral line), Eqs.(2) and (3) yield a negative shift of 0.58 Å. Given the spectrometer resolution of 0.1 Å or better, it should be straightforward to resolve this shift. This leads to the following conjecture:

Conjecture 4: Through the Doppler shift, it should be possible to separate the emissions from fast beam ions and fast charge-exchange neutrals on the one hand, and of slow ions and neutrals on the other.

To test this conjecture, we have measured a number of emission lineshapes for both ion and neutral lines. Typical results are shown in Figs. 9 and 10. Figure 9 shows the recorded emission lineshape for the conditions of the example above (circles are experimental data; the curve fits are discussed in Section 7). These data were obtained with 25 micron slits on the spectrometer. The instrument line width at this setting is 0.10 Å at full-width-half-maximum (fwhm).

The lineshape in Figure 9 clearly consists of two peaks, separated exactly by the calculated Doppler shift of -0.58 Å. Thus, the left component of the line can be identified unambiguously as the charge-exchange neutral contribution. By inference, the right component must be due to excited neutrals, excited either by inelastic scattering with the ion beam [process (6) in Table I] or by electron impact of slow neutrals [process (2) of Table I]. Neutral atoms excited in either process are predominantly slow-moving, so that they are centered at zero Doppler shift. In fact, the origin of the Doppler shift scale in Figure 9 is chosen such that it coincides exactly with the center of the right emission peak.

Measurements were also performed on the same spectral line for a different beam voltage ($V_B = 500$ V), and on a different neutral line (7635 Å, $V_B = 900$ V). In both cases, the separation of the two peaks was consistent with the Doppler shifts calculated from Eqs.(2) and (3). Further discussion of the observed lineshapes is given in Section 7. We conclude that conjecture 4 has been verified for neutral lines.

For ion lines, the situation is slightly different. This is clear from Fig. 10 which shows the lineshape of the argon ion line at 4880 Å. This measurement was performed with the same instrument resolution as the data from Fig. 9. However, because of the lower emission wavelength, the

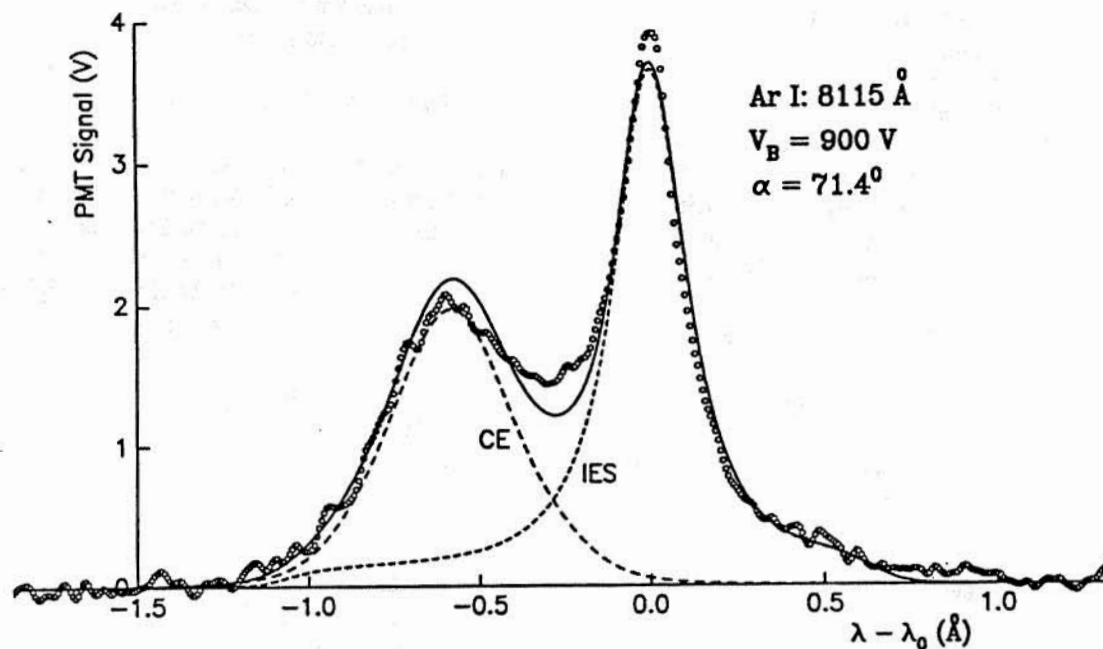


Figure 9: Observed emission lineshape of the 8115 Å argon neutral line, at an observation angle of 71.4°. Circles represent experimental data. Dashed lines are based on the model calculations discussed in Section 7. The solid line is the sum of the two dashed lines.

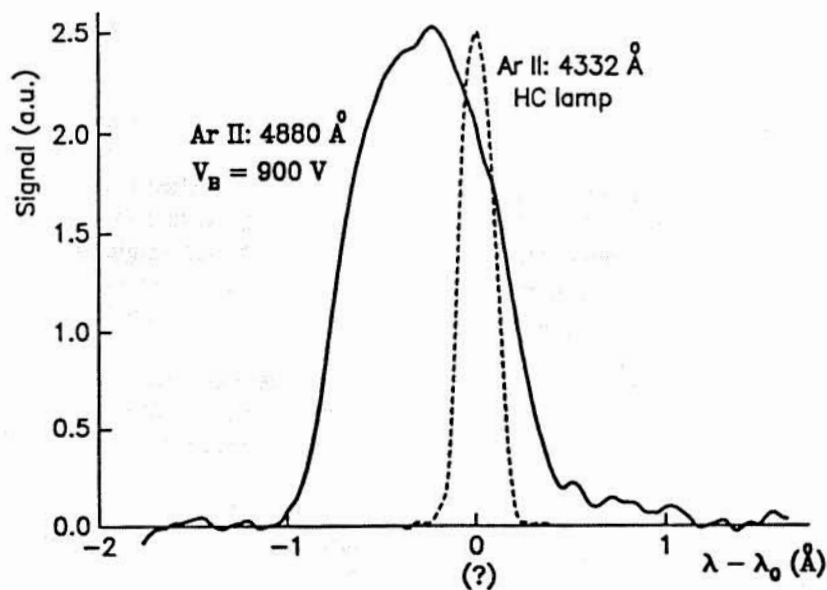


Figure 10: Observed emission lineshape of the 4880 Å argon ion line, for the same conditions as in Figure 9. The origin of the Doppler shift scale has been fixed at an arbitrary position. For comparison, the scan of an argon ion line from a hollow cathode lamp is shown also.

Doppler shift between the fast and slow components is smaller than in Fig. 9. Primarily as a result of this, we believe, the double peak structure of the emission line is obscured, so that conjecture 4 has not been verified for an ion line.

Unfortunately, no strong argon ion emission occurs at significantly larger wavelengths. To resolve this situation, we intend to repeat the measurements at a larger observation angle α . Also we plan to check if sufficient signal can be collected on one of the "reddest" argon ion lines tabulated in Ref. [18], around 6800 Å.

Because no clear two-peaked structure is evident in the ion lineshape from Fig. 10, we were unable to locate the origin of the Doppler shift scale unambiguously. Even without being able to resolve the double-peaked structure for the ion line, this situation could be improved by recording a simultaneous reference signal. For example, the emission from a low power argon discharge could be used for this purpose. As an example, a typical scan of such a spectral line from a hollow cathode lamp is shown in Fig. 10 along with the emission lineshape from the ion plume.

Even in the absence of a good absolute wavelength calibration, an attempt was made to measure the shift of the center of the argon ion line from Fig. 10 as a function of the beam voltage. Figure 11 displays the measured line

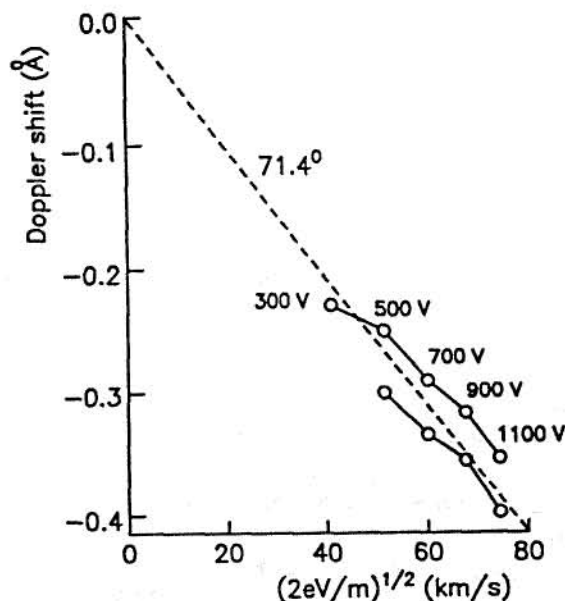


Figure 11: Measured (circles) versus calculated line positions (dashed) of the argon ion line from Fig. 10 for beam voltages of 300, 500, 700, 900, and 1100 V; $J_B = 40$ mA; $\dot{m} = 4$ sccm. The vertical scale has been fixed arbitrarily.

positions along with the theoretical prediction from Eqs.(2) and (3). The precision of the wavelength determination was limited to about 0.015 Å, as determined by the procedure for setting the marker signal on the spectrometer. Also, the two series of data did not reproduce well. Nevertheless, it is evident from Fig. 11 that the center of the line (arbitrarily defined as the point of gravity of the lineshape) shifts in agreement with the predictions from Eqs.(2) and (3).

7. Further analysis of the lineshapes

Of course, one important factor which determines the width of the measured spectral lines is the spectrometer resolution. Even at best, this resolution is insufficient to allow a determination of the true width of the emission signals from slow neutrals and slow ions. On the other hand, the widths of the emission lines associated with emissions from beam ions and from charge-exchange neutrals should reflect the distribution of plume angles for the respective species. These distributions of plume angles are primarily determined by the ion optics of the ion source. However, especially at high background densities, additional beam broadening may result due to elastic and/or inelastic scattering of beam ions, as is illustrated in the lower diagram of Fig. 6.

An intermediate case is provided by neutrals which have been scattered through a large angle as a result of a collision with a beam ion at small impact parameter. Such neutrals may have a substantial velocity after the collision, giving rise to broadening of the slow peak of a neutral emission line. In this case, the associated lineshape is determined in large part by the differential scattering cross-section for the elastic or inelastic collision.

The above arguments can be formulated in terms of specific conjectures for each of the components of the ion and neutral lines. We refrain from this because the analysis to support these conjectures is as yet incomplete. However, we discuss several results which elucidate the principles involved.

Figure 12 shows the measured line widths of the argon ion lines which form the basis for the data from Fig. 11. It is evident that the observed line widths increase dramatically as the beam energy is increased. This is consistent with the interpretation that the line width of the fast component of the emission lineshape is determined in large part by the divergence of the plume. The dotted lines in Fig. 12 correspond to points of equal plume divergence as indicated. It follows that the plume divergence increases slightly as the beam energy is increased.

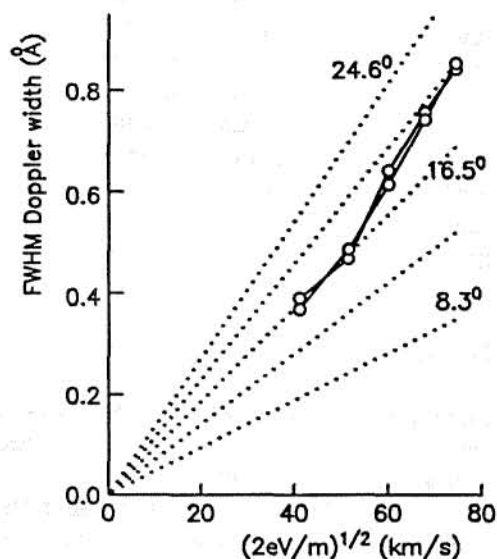


Figure 12: Measured line widths, corresponding to the data from Fig. 11. The dotted lines indicate points of equal beam divergence, measured as the enclosed angle at full-width half-maximum of the beam profile.

This effect was verified by a numerical simulation of the ion optics of the 3 cm source, using our previously developed code. Figure 13 shows the resulting distribution of plume half-angles (defined as the angle of a given beam ion to the axis of the source), for the same conditions as in the experiment. Specifically, Fig. 13 shows that, indeed, the distribution of plume half-angles widens as the beam voltage is increased (we do not have an explanation for the bimodal distributions of plume angles for $V_B \geq 900$ V). The measured divergences in Fig. 12 are actually somewhat larger than the calculated values. This can be explained by the combination of instrument broadening and beam broadening as a result of elastic scattering.

Figure 14 shows the effect of beam broadening as a result of elastic or inelastic scattering explicitly. Namely, as the chamber pressure is raised by flowing additional gas into the chamber through the bypass valve, the width of the 4880 Å ion line increases significantly. For a high neutral flow rate through the source (the curve marked 12 sccm in Fig. 14), the effect is even more serious, and even larger line widths result.

Finally, we have performed a series of calculations to reproduce the measured emission lineshapes explicitly. The calculations are similar to those in Ref. [20]. They are rather involved, and we discuss them here only briefly. The calculated distribution of plume angles from Fig. 13

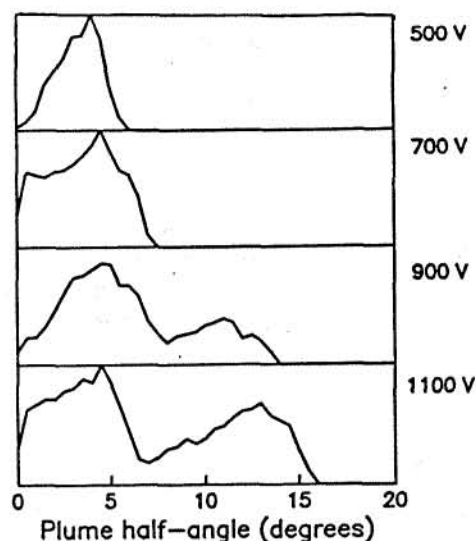


Figure 13: Calculated distribution of beam angles corresponding to the conditions from Figs. 11 and 12 for values of beam voltage as indicated. No elastic or inelastic scattering was taken into account.

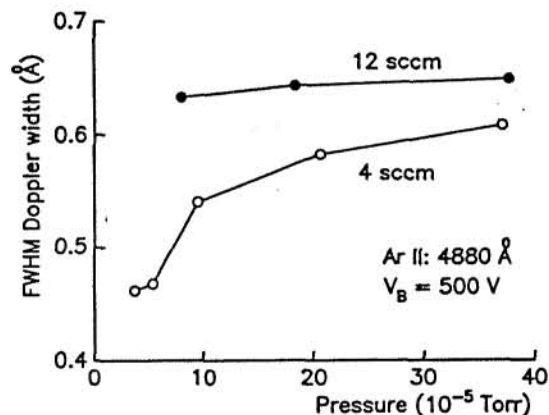


Figure 14: Measured line width of the argon ion line at 4880 Å as a function of chamber pressure and total mass flow rate through the source.

is used as a starting point. By integration over the polar angles ϑ_i and φ_i from Fig. 15, the projections v_i of the beam ions (or charge-exchange neutrals) along the observation direction are calculated. The resulting distribution of projected velocities is then converted to a distribution of Doppler shifts, and convolved with the instrument profile. As an example, the fast component of the neutral line from Fig. 9 was modeled.

The resulting curve is shown in Fig. 9 as a dashed curve, marked 'CE' to indicate that it corresponds to charge-exchange neutrals. The agreement between the

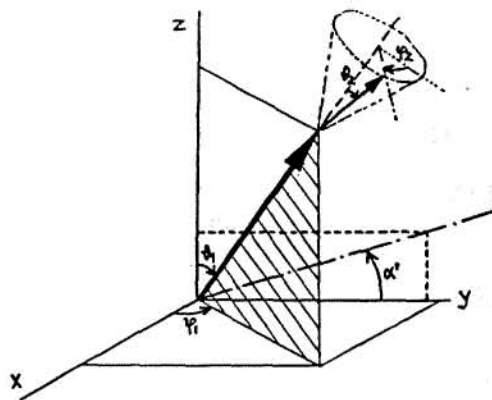


Figure 15: Polar scattering diagram used to compute the projections of beam and scattered ion velocities onto the observation direction, taken to lie in the yz -plane at an angle $\alpha' = 90^\circ - \alpha$ to the y -axis.

theoretical curve and the experimental data is quite impressive for the left side of the fast peak, where the contribution from the slow peak is small. This agreement is even more remarkable when considering that only one adjustable parameter was needed to match the theoretical curve to the data, namely the amplitude of the peak.

We have also attempted to account for the "left-over" part of the lineshape from Fig. 9, given by the difference of the experimental data and the dashed curve marked 'CE'. This "slow" peak, centered at zero Doppler shift, consists of slow neutrals excited by electron impact, and of neutrals scattered by elastic and/or inelastic collisions with beam ions. To model the latter process, it was necessary to perform an integration over a second set of polar angles (ϑ_2 and φ_2 in Fig. 15) for each beam angle, to account for the scattering process. Furthermore, it was necessary to assume a particular form for the differential scattering cross-section for the corresponding process. As is illustrated by the dashed curve marked 'IES' in Fig. 9, it was indeed possible to model the peak at zero Doppler shift in this way, including the relatively broad wings which result from large-angle scattering at small-impact parameters. Although the results are still rather tentative, they indicate that it may be possible to model the emission lineshapes accurately even for such complicated interactions.

8. Discussion and conclusions

It is generally assumed that the measurement of velocity distributions of plasma species through exploitation of the Doppler effect is only possible in experiments in which a narrowband laser is used as the

wavelength-selective element. For example, we have previously shown how the technique of laser induced fluorescence can be used to measure exit velocities in arcjet plumes [21-22].

Here we have shown that, actually, high-resolution emission spectroscopy *can* be used to characterize the beam-plasma interactions in the plume from an ion source. Much information can be gained from the analysis of the emission lineshapes of both neutral and ion lines. Specifically, because of their large plume velocities, it is possible to measure the Doppler shifts of fast beam ions and fast charge-exchange neutrals directly. Also, it is possible to distinguish these emissions from those arising from electron impact of slow neutrals, elastically and/or inelastically scattered neutrals, and slow charge-exchange ions.

We propose that the new technique be employed to study various processes in the downstream plasma region of ion thruster engines. Specifically, we have shown that it is possible to identify charge-exchange collisions between beam ions and slow neutral atoms, as well as electron impact excitation of beam ions. Indirect evidence for electron impact ionization of background neutral atoms has been found as well.

Other diagnostic applications of this spectroscopic technique can be envisioned as well. Among these are: estimation of electron temperatures in the plume by analyzing the ratio of ion-to-neutral emission intensities [13]; measurement of beam broadening as a result of the interaction of the plume with the background gas; and further use of the optical measurements to verify the numerical codes. Finally, the spectroscopic measurements serve as a valuable stepping stone toward more sophisticated experiments based on the technique of laser induced fluorescence.

Acknowledgements

This work was supported by Boeing Defense & Space Group, Seattle, Washington, and by NASA grant NAGW-1195. We are especially indebted to N. Wright for his technical support.

References

- [1] X. Peng, W. M. Ruyten, and D. Keefer, "Plasma particle simulation of electrostatic ion thrusters," AIAA paper 90-2647, 21st International Electric Propulsion Conference, Orlando, Florida, July 18-20, 1990.

- [2] X. Peng, W. M. Ruyten, V. J. Friedly, and D. Keefer, "Plasma particle simulation of electrostatic ion thrusters," Proceedings of the 2nd Annual Technical Symposium, CSTAR, Tullahoma, Tennessee, November 1-2, 1990, pp. 73-78.
- [3] X. Peng, W. M. Ruyten, and D. Keefer, "Monte Carlo simulation of ion-neutral charge exchange collisions and grid erosion in an ion thruster," AIAA paper 91-0607, 29th Aerospace Sciences Meeting, Reno, Nevada, January 7-10, 1991.
- [4] X. Peng, W. M. Ruyten, and D. Keefer, "Particle simulation of grid erosion in ion thrusters," AIAA paper 91-2120, 27th Joint Propulsion Conference, Sacramento, California, June 24-26, 1991.
- [5] X. Peng, W. M. Ruyten, and D. Keefer, "Three-dimensional particle simulation of grid erosion in ion thrusters," Paper 91-119, 22nd International Electric Propulsion Conference, Viareggio, Italy, October 14-17, 1991.
- [6] X. Peng, D. Keefer, and W. M. Ruyten, "Plasma particle simulation of electrostatic ion thrusters," *AIAA Journal of Propulsion and Power*, Vol. 8, No. 2, March-April 1992, pp. 361-366.
- [7] X. Peng, W. M. Ruyten, and D. Keefer, "Ion thruster modeling," Proceedings of the 3rd Annual Technical Symposium, CSTAR, Tullahoma, Tennessee, January 14-15, 1992, pp. 91-97.
- [8] X. Peng, W. M. Ruyten, and D. Keefer, "Further study of the effect of the downstream plasma condition on accelerator grid erosion in an ion thruster," paper AIAA-92-3829, 28th AIAA Joint Propulsion Conference, Nashville, Tennessee, July 6-8, 1992.
- [9] J. Monheiser and P. Wilbur, "An experimental study of impingement-ion-production mechanisms," paper AIAA-92-3826, Nashville, Tennessee, July 6-8, 1992.
- [10] N. Hershkowitz, "How Langmuir probes work," in "Plasma Diagnostics, Volume 1," edited by O. Auciello and D. L. Flamm, Academic Press, Boston, 1989, pp. 113-183.
- [11] P. M. Chung, L. Talbot, and K. J. Touryan, "Electrical probes in stationary and flowing plasmas: theory and applications," Springer-Verlag, New York, 1975.
- [12] Y. Hayakawa, K. Miyazaki, and S. Kitamura, "Measurements of electron energy distributions in an ion thruster," *J. Propulsion and Power*, Vol. 8, No. 1, pp. 118-126, 1992.
- [13] T. I. Cox, et al., "The use of Langmuir probes and optical emission spectroscopy to measure electron energy distribution functions in RF-generated argon plasmas," *J. Phys. D: Appl. Phys.*, Vol. 20, No. 7, pp. 820-831, 1987.
- [14] D. Keefer, W. Ruyten, V. Friedly, and J. Meserole, "Ion propulsion: experimental work," CSTAR Quarterly Report, January 1, 1992 - March 31, 1992, pp. 34-39.
- [15] P. M. Latham, A. R. Martin, and M. T. Cresdee, "Optical emission spectrum of the UK-10 ion thruster operating on xenon," paper 88-112, Proceedings of the 20th International Electric Propulsion Conference, Garmisch-Partenkirchen, October 1988, pp. 627-633.
- [16] R. Goldstein and K. M. Monagan, "Optical properties of mercury ion thruster exhaust plumes; significance for candidate SEP science instruments," paper AIAA-75-362, New Orleans, Louisiana, March 1975.
- [17] W. M. Ruyten and D. Keefer, "Arcjet plume diagnostics," these proceedings.
- [18] Wiese, Smith, and Miles, "Atomic Transition Probabilities: Sodium through Calcium," National Bureau of Standards, publication No. 22.
- [19] J. B. Hasted, "Physics of atomic collisions," Butterworths, London, 1964.
- [20] F. J. Morgan, A. Marcuzzi, and C. H. Dugan, "Shapes of optical emission lines from atoms excited by fast ion impact: I. calculated results," *Can. J. Phys.*, Vol. 52, 2525-2533, 1975.
- [21] W. M. Ruyten and D. Keefer, "Laser fluorescence velocimetry of an arcjet exhaust plume," Paper 91-093, 22nd International Electric Propulsion Conference, Viareggio, Italy, October 14-17, 1991; also to appear in *AIAA J.*
- [22] W. M. Ruyten and D. Keefer, "Characterization of electric thruster plumes using multiplexed laser induced fluorescence measurements," AIAA paper 92-2965, 23rd AIAA Plasma Dynamics and Lasers Conference, Nashville, Tennessee, July 6-8, 1992.

ARCJET PLUME DIAGNOSTICS

W. M. Ruyten*

University of Tennessee-Calspan
Center for Space Transportation and Applied Research
Tullahoma, Tennessee 37388-8897

and

D. Keefer**

Center for Laser Applications
University of Tennessee Space Institute
Tullahoma, Tennessee 37388-8897

Abstract

We report the results of spectroscopic measurements on the exhaust plume from a 1 kW NASA Lewis arcjet, operated on simulated ammonia. The strongest emission features consist of the Balmer lines of atomic hydrogen and a number of vibration-rotation bands of the NH radical. From the spectral data, we calculate a heavy particle temperature of about 3000 K at the exit plane, and an electron temperature of 0.30 eV. Measurements of the spatial distribution of these emission features are presented also. We discuss the importance of the measurements to planned laser induced fluorescence experiments.

1. Introduction

With the upcoming deployment of hydrazine arcjets on the 1993 launch of Telstar 4, arcjets have reached the point of commercial viability. Still, a strong interest remains in improving their performance. To a significant extent, this effort is hampered by the limited understanding of the basic physical processes in the device. This accounts for the continuing interest in experimental diagnostics and numerical modeling.

Different techniques have been used to characterize arcjet plumes. These include Langmuir probes [1-2], emission spectroscopy [3-8], absorption [9-10], and laser induced fluorescence (LIF) [8,11-15]. Emission spectroscopy has also been used to monitor the arc region itself [16]. At the same time, there have been several modeling efforts [17-19]. The combined experimental and numerical work is providing greater insight into the

mechanisms of arc physics, the generation of thrust, and the factors determining electrical efficiency of the device.

We have previously demonstrated the LIF technique on a locally-built arcjet, operated on argon [13-15]. The main goal of the present effort is to perform similar measurements on the plume from a 1 kW benchmark thruster from NASA Lewis Research Center [20], operated on simulated ammonia (a mixture of three parts hydrogen to one part nitrogen by volume). The excitation line that will be used for these LIF studies is the Balmer-alpha line of atomic hydrogen at 6563 Å.

Because of scheduling conflicts, we have not yet been able to perform the LIF studies themselves. However, spectroscopic investigations of the plume were performed in preparation for the LIF work. Although these measurements were intended primarily as a stepping stone toward the more complicated LIF experiments, they are interesting in their own right. In particular, these measurements were not restricted to the hydrogen Balmer-alpha line. Strong emissions were also observed from other members of the hydrogen Balmer series, and several strong vibrational-rotational bands of the NH radical were detected.

This work was supported jointly by Rocket Research Company of Redmond, WA; the Air Force Office of Scientific Research; and by the Center for Space Transportation and Applied Research.

* Principal Investigator; Calspan, Senior Engineer

** UTSI/CLA, B. H. Goethert Professor of ES&M

Here we demonstrate how these emissions can be used to map the spatial distributions of H and NH in the plume,

and to determine plume temperatures. We report the results of three different temperature determinations. The first is analysis of the Doppler width of the hydrogen Balmer-alpha line. This yielded a temperature of 3150 ± 80 K at the nozzle exit plane. The second is determination of the electron temperature from the intensity ratios of the hydrogen Balmer-beta through Balmer-epsilon lines. This resulted in a temperature of 0.300 ± 0.003 eV, or 3470 ± 35 K. Finally, the rotational temperature of the NH $c^1\Pi \rightarrow b^1\Sigma^+$ (0-0) band was determined to be 2680 ± 60 K.

The close agreement between these three independent temperature determinations is striking. However, this situation may be peculiar to the high chamber background pressure in this work (500 Pa, or 4 Torr). At the time of the LIF measurements, additional pumping will be available, resulting in an estimated chamber pressure of about 50 Pa. It should be worthwhile to repeat the spectroscopic measurements at that time.

The outline of this paper is as follows: Section 2 describes the experimental setup and procedures for the spectroscopic work. In Section 3 we describe the measurements on the hydrogen Balmer lines, including line shape analysis of the Balmer-alpha line and the determination of electron temperature from the Balmer-beta through Balmer-epsilon lines. In Section 4 we present measurements of the rotational bands of the NH radical, and the determination of the rotational temperature of the $c^1\Pi \rightarrow b^1\Sigma^+$ (0-0) band. In Section 5, we discuss measurements of the spatial distributions of excited H and NH emissions. In Section 6 we conclude with a summary and a discussion of the relevance of the data to future arcjet plume studies.

2. Experimental

All experimental work was performed in the large vacuum facility of the Center for Laser Applications at the University of Tennessee Space Institute. The vacuum tank consists of a cylindrical chamber, 6.0 m long by 2.7 m wide, with a bell-shaped section on one end. This is where the arcjet was mounted, namely on a computer-controlled xyz stage (see Fig. 1). For these experiments, only a single Stokes pump equipped with blower was available, with a pumping speed of 110 l/s. Typical vacuum levels during thruster operation were 400 to 670 Pa (3 to 5 Torr), at flow rates of 5 to 7 sl/min.

Figure 2 shows the arcjet, which is on loan from NASA Lewis Research Center. A description of the arcjet may be found, for example, in Ref. [20]. Typical power dissipation was 10 Amps at 80 Volts, for a flow rate of 7 sl/min. The 3:1 hydrogen-nitrogen mixture was premixed.

The mixture was chosen to avoid dealing with the corrosive properties of ammonia itself. A comparison with operation on actual ammonia may be undertaken at a future date. Based on experiments performed at Aerospace Corporation [8] we expect only minor differences between operation on actual versus simulated ammonia.

The emission measurements were performed with a 1.25 meter SPEX spectrometer with an 1800 gr/mm grating. Typical slit widths were 10 μ m and 25 μ m, with corresponding resolutions of 0.038 Å and 0.095 Å, measured as full-width-half-maximum (fwhm) values on an assumed gaussian instrument line profile. Emissions from the plume were collected through a large optical access port in the chamber, and focused onto the spectrometer entrance slit with a wide-aperture (f/6) Cassegrain telescope.

A red-sensitized photo multiplier tube (PMT) was used as the detector. The quantum efficiency of this tube falls off sharply above 8600 Å. Light below 3300 Å is not transmitted by the optical access port of the chamber. Figure 3 shows the combined detection efficiency of the optical setup. This calibration was performed with a standard filament source, which was placed at the position of the arcjet plume for this purpose.

The dominant spectral features in the emission spectra of the arcjet plume were those of atomic hydrogen (Section 3) and the NH radical (Section 4). Also, weak emissions from the molecular nitrogen ion (N_2^+) were present, with a bandhead at 3914 Å, stretching to the blue. No emissions from atomic nitrogen could be detected.

A drawback of the use of the Cassegrain telescope turned out to be its use of a diffractive element. This resulted in a net shift of the effective observation point in the plume as a function of observation wavelength. This effect is particularly noticeable in the spatial plume measurements of Section 5. However, it may also be that because of this effect the calibration curve from Fig. 3 is slightly in error, as is discussed at the end of Section 3.

3. Analysis of hydrogen Balmer emissions

One of the strongest emission features in the plume was the series of lines corresponding to the Balmer series of atomic hydrogen. As is illustrated in Fig. 4, this is the series of lines which terminate on the level with principal quantum number equal to two ($n=2$). The most prominent of these is the Balmer-alpha line at 6563 Å, which corresponds to the $n=3$ to $n=2$ transition. Also observed were the beta ($4 \rightarrow 2$), gamma ($5 \rightarrow 2$), delta ($6 \rightarrow 2$), epsilon ($7 \rightarrow 2$), and zeta ($8 \rightarrow 2$) members of this series.

Figure 5 shows a scan of the Balmer-alpha line. This measurement was performed about 2 mm downstream from the exit nozzle, with slit settings of 25 μm . The asymmetry of the line shape is a result of the fine structure of the line. Due to this fine structure, the Balmer-alpha line actually consists of five non-overlapping components, with relative positions of -0.144, -0.036, 0.0, 0.220, and 0.328 cm^{-1} , and corresponding intensity ratios of 0.05 : 0.28 : 2.50 : 0.31 : 1.96 [12, 21, p.223].

We were able to fit the lineshape from Fig. 5 (solid line) almost perfectly by a multi-component gaussian curve fit (dotted line), in which each component (dashed lines in Fig. 5) represents one of the five non-overlapping fine structure transitions. The relative positions and relative amplitudes are as specified above, and the width of each of the components is the same. The fitted value of this width at fwhm is 0.2807 ± 0.0002 Å. Correcting for the spectrometer width of 0.095 Å, we find that the Doppler width of the transition, Δ_D , is 0.2641 Å fwhm. Substituting this value into the expression for Doppler broadening:

$$8 k T \ln 2 = m c^2 (\Delta_D / \lambda)^2, \quad (1)$$

where k is Boltzmann's constant, λ is the transition wavelength, and m is the mass of atomic hydrogen, we find a value of the Doppler temperature, T , of 3150 K. The main uncertainty in this value is due to the correction for the instrument width. Estimating this uncertainty to be 10 percent, it follows that the uncertainty in the Doppler temperature is 80 K.

We have also performed scans of the Balmer-beta through Balmer-zeta lines. No fine structure analysis was performed for these lines. However, Table I lists the calculated areas and widths of these lines, as well as several other quantities. Also, the corresponding quantities for the Balmer-alpha line are shown. From these data, it is possible to estimate the electron temperature in the plume [3].

This is illustrated in Fig. 6, in which the log of the ratio S_i^*/S_∞ is plotted versus the upper state energy E_i of the transition, where S_∞ is a measure (in arbitrary units) of the line intensity in the limit of infinite temperature [21, p.129], and $S_i^* = S_i/\eta_i$ is the measured line intensity S_i corrected for the detection efficiency η_i from Fig. 3 at the specified wavelength. From the expression

$$S_i^* \propto S_\infty \exp(-E_i / kT_e), \quad (2)$$

it follows that the data in Fig. 6 should fall on a straight line whose slope is inversely proportional to the electron temperature T_e .

It is clear from Fig. 6 that the data from the Balmer-beta through Balmer-epsilon lines fall on a straight line indeed. The slope of this line yields an electron temperature of 3470 ± 35 K, or 0.300 ± 0.003 eV. The data point for the Balmer-zeta line was not included in the linear fit because we believe that this line overlaps with a rotational line from the molecular nitrogen ion, which was present in small amounts. Neither was the data point for the Balmer-alpha line included in the fit, due to its evidently anomalous behavior relative to the other lines from the Balmer series.

One possible explanation for the anomalous behavior of the Balmer-alpha line is that the sensitivity calibration from Fig. 3 is in error as a result of the diffractive effects of the Cassegrain telescope. As discussed at the end of Section 2, such diffractive effects might have been responsible for focusing different portions of the standard-lamp-filament onto the entrance slit of the spectrometer. This would affect the Balmer-alpha point in Fig. 6 in particular, because its sensitivity factor ($\eta_i = 2.841$) differs so much from the factors for the Balmer-beta through Balmer-epsilon lines (each equal to 80 within a few percent - see Table I).

The measured value of 0.30 eV for the electron temperature is in good agreement with electron temperature measurements in arcjet plumes obtained with Langmuir probes [1-2]. Also, it is in excellent agreement with the value of 0.33 eV obtained in Ref. [3], obtained using the same method as that employed here. Interestingly, the Balmer-alpha point was excluded in Ref. [3] as well, where it fell significantly below the straight line fitted through the other data points.

We conclude this section by reiterating that the hydrogen Balmer-alpha line was found to be the most prominent emission feature in the plume spectrum. Thus we are confident that the population of the $n=2$ level in Fig. 4 will be sufficient to excite the Balmer-alpha transitions in an LIF experiment as well.

4. Analysis of NH molecular bands

In addition to the strong series of lines of the hydrogen Balmer series, strong emissions from the NH radical were found. The most prominent, and perhaps most characteristic, of these are those of the $A^3\Pi \rightarrow X^3\Sigma$ band. Figure 7 shows a partial scan of this band system. The Q-branches of the 0-0 and 1-1 vibrational transitions are identified in the left part of Fig. 7. The remaining part of the scan reveals the interwoven P-branch transitions of the 0-0 and 1-1 systems.

The NH A→X band has been studied previously by Crofton et al., namely in the plume from an ammonia arcjet, similar to the one used in our work [8]. Both emission and excitation measurements were performed. A surprising finding of Ref. [8] was that the rotational temperatures calculated from the emission spectra, around 4500 K, were significantly higher than those of the excitation spectra, which were only about 2000 K. Also, the vibrational temperature, estimated from the ratio of 1-1 to 0-0 emissions, was significantly lower, namely 2500 K. However, it is also stated in Ref. [8] that these temperature determinations have a considerable uncertainty, due to an apparent violation of Boltzmann equilibrium among the rotational levels.

Similar analyses could be performed on the data from Fig. 7, yielding rotational temperatures for both the 0-0 and 1-1 bands. Also it should be possible to estimate a vibrational temperature from the 0-0 to 1-1 emission ratios. We have the resources to perform this type of analysis, but have not done so yet. However, from a mere comparison of the spectrum from Fig. 7 with the spectra shown in Ref. [8], it appears that the vibrational temperature must be higher than 2500 K (the 1-1 transitions have larger relative amplitudes in Fig. 7 than in the corresponding figures from Ref. [8]). Similarly, the significant representation of transitions with large rotational quantum numbers (the lines above about 343 nm in Fig. 7) appears to indicate that the rotational temperature is probably not much lower than the value of 4500 K found in Ref. [8].

Other band systems of NH were observed in our work as well. These include the (0-1) band of the $A^3\Pi \rightarrow X^3\Sigma$ system between 370 and 381 nm; the (0-1) band of the $c^1\Pi \rightarrow a^1\Delta$ system between 363 and 367 nm; and the (0-0) band of the $c^1\Pi \rightarrow b^1\Sigma^+$ system between 450 and 474 nm. A comprehensive discussion of these various band systems may be found in Ref. [22], which shows spectra obtained in an ammonia-argon arcjet plume.

We did perform an analysis of the $c^1\Pi \rightarrow b^1\Sigma^+$ band. A scan of the main part of this band is shown in Fig. 8. Because the band involves singlet transitions, the line structure is much more open than that of the triplet $A^3\Pi \rightarrow X^3\Sigma$ band. This simplifies the analysis considerably. In particular, it is straightforward to measure the intensities of individual rotational transitions and to obtain the rotational temperature, T_R , of the plume. This is accomplished in a similar fashion as for the above analysis of the hydrogen Balmer series. In particular, the expression which corresponds directly to Eq.(2) is given by

$$S^*(J') \propto S_{J,J'} \exp (-E(J') / kT_R), \quad (3)$$

where $S^*(J')$ is the line intensity of the line with rotational quantum number J' , corrected for the optical detection efficiency; $S_{J,J'}$ is the Hönl-London line strength factor; and $E(J')$ is the energy of the upper rotational level. Expressions for the line strength factors were taken from Ref. [23]. They are given by $S_{J,J'} = \frac{1}{2}J'$ for the P-branch; $S_{J,J'} = J' + \frac{1}{2}$ for the Q-branch; and $S_{J,J'} = \frac{1}{2}(J'+1)$ for the R-branch transitions.

The resulting Boltzmann plot for the $c^1\Pi \rightarrow b^1\Sigma^+$ band is shown in Fig. 9. The line intensities were measured directly off the stripchart output from the survey scan of the spectrum. A total of 41 isolated transitions were identified, namely 10 from the P-branch, 17 from the Q-branch, and 14 from the R-branch. A linear fit to the data yields a rotational temperature of $T_R = 2680 \pm 60$ K, and is seen to approximate all data reasonably well. Based on this observation, we conclude that the assumption of Boltzmann equilibrium is well justified for these data (the opposite conclusion was drawn in Ref. [8]).

5. Spatial distribution of emission intensities

Several experiments were performed to characterize the spatial distribution of emission intensities in the plume. For this purpose, the spectrometer was tuned to a particular emission line, and a scan was performed by moving the arcjet thruster either parallel or perpendicular to the plume axis. The entrance and exit slits of the spectrometer were opened to 200 μm and 400 μm , respectively, to include most of the area under the emission lineshape.

Figure 10 shows the variation in emission signal for the alpha, beta, and gamma lines of the hydrogen Balmer series. Also shown is the signal at 336 nm, given by the (0-0) Q-branch of the A→X band of NH. All data were scaled to unit amplitude. It appears that the spatial behavior of all components is different. In part, this is due to the refractive distortion of the Cassegrain telescope, which resulted in wavelength-dependent relative shifts of the emission profiles. Thus, unfortunately, the value of the data from Fig. 10 is limited.

One unambiguous conclusion from Fig. 10 is that NH emission persists long after the hydrogen Balmer emissions have subsided. Also, the width of the Balmer-alpha profile is less than that of the Balmer-beta profile. In turn, its width is less than that of the Balmer-gamma profile. In principle, it should be possible to calculate from this the axial variation of the electron temperature, using Eq.(2). However, this will not be possible until the wavelength-dependent distortion of the Cassegrain telescope is remedied or accounted for.

Similarly, Figure 10 shows the radial variations of the Balmer-alpha emission and the NH Q-branch emission, several millimeters downstream from the exit nozzle. In these measurements, the optical distortion is even more evident: Clearly, there is no reason why the two emissions should be centered differently around the plume axis. Figure 10 also points out another difficulty in obtaining good spatial measurements with the Cassegrain system: the asymmetry of the radial Balmer-alpha profile. In a modest effort it was established that the profile is quite sensitive to the alignment of the optical system.

We conclude that it is straightforward to get a rough idea of the spatial distribution of emitting plume species from the axial and radial scans. However, a very careful optical alignment will be required for quantitative measurements. Moreover, it will be desirable to replace the present Cassegrain system with one without diffractive optics. Because it is likely that the spatial distributions of emitting plume species will be affected to a significant extent by the lower background pressure that we anticipate for future experiments, we did not perform any further spatial distribution measurements.

6. Discussion and summary

We have performed spectroscopic measurements on the plume from a 1 kW arcjet, operated on simulated ammonia. The resolution of these measurements was better than 0.1 Å. Thus, three independent plume temperature determinations could be performed. These were based on the Doppler width of the hydrogen Balmer-alpha line; the intensity ratios of the hydrogen Balmer-beta through Balmer-epsilon lines; and the rotational line intensities of the (0-0) branch of the $c^1\Pi \rightarrow b^1\Sigma^+$ band of the NH radical. The respective temperatures at the exit plane, 3150 ± 80 K, 3470 ± 35 K, and 2680 ± 60 K are in close agreement.

It must be kept in mind that these values are averaged quantities along the line-of-sight. Thus it is difficult to extract local values of temperatures and concentrations from them, although such could be accomplished by Abel inversion of radial emission profiles [3]. However, the method of choice for obtaining such point data is laser induced fluorescence (LIF). We plan to perform such LIF experiments in the near future, using the hydrogen Balmer-alpha line.

Because of its prominence as an emission feature, we are confident that the hydrogen Balmer-alpha line can be used as a valuable diagnostic line in LIF experiments as well. However, the emission measurements also point out a concern in this regard, namely the apparently anomalous behavior of the emission intensity of the hydrogen

Balmer-alpha line relative to the higher members of the Balmer series.

Such anomalous behavior has been reported elsewhere as well [3]. It appears that the population of the $n=3$ state (the upper level of the Balmer-alpha transition in emission) is *not* in thermal equilibrium with the other members of the Balmer series. However, its Doppler temperature seems to agree both with the distribution of higher-level quantum states of the H atom as well as with the distribution of rotational levels of the $c^1\Pi$ $v=0$ branch of the NH radical.

Because excitation of the Balmer-alpha line in an LIF scheme involves an even lower level (the $n=2$ level), the possibility for anomalous behavior is even greater. Moreover, the observed non-equilibrium effects in this work may have been mitigated by the rather high background pressure in the experiments. An upgrade of the vacuum facility is almost complete. Thus future experiments will be carried out at lower background pressures. For these, it will be even more important to compare the results from excitation measurements obtained with LIF to results obtained with emission spectroscopy.

Only one of the molecular bands of the NH radical was analyzed in this work, namely the $c^1\Pi \rightarrow b^1\Sigma^+$ (0-0) band. Its singlet structure allows for a simpler analysis than the triplet $A^3\Pi \rightarrow X^3\Sigma^-$ system, studied in Refs. [4] and [8]. In particular, it was easy to measure the intensities of individual rotational lines. Thus it was possible to obtain the rotational temperature from a Boltzmann plot which included all three branches (P, Q, and R) of the band system. The resulting temperature agrees well with the two temperatures obtained from the hydrogen Balmer emissions, and is roughly equal to that obtained from the emission measurements from Ref. [8].

An interesting feature of the NH emissions is that they persist at least 10 mm further downstream from the exit nozzle than the Balmer emissions from atomic hydrogen. This information may be useful to validate models of the plume chemistry. Also, weak emissions from the molecular nitrogen ion were detected. No emission from atomic nitrogen was found. Thus it seems very unlikely that excitation of atomic nitrogen using LIF could be used as a valuable diagnostic.

Finally, our experiments indicate that some modifications to the optical setup would be required to perform precise measurements of the spatial distributions of emission intensities. In particular, the wavelength-dependent distortion of the Cassegrain telescope would have to be eliminated or accounted for. However, the

measurements also indicate that, having made such a modification, it should be possible to measure the dependence of the electron temperature and Doppler temperature of the Balmer-alpha line as a function of downstream position from the exit nozzle.

Acknowledgments

This work was supported by grants from Rocket Research Company of Redmond, Washington; the Air Force Office of Scientific Research under grant AFOSR-91-0200; and by the Center for Space Transportation and Applied Research under NASA grant NAGW-1195. We gratefully acknowledge the loan of the arcjet system from NASA Lewis Research Center. Finally, we thank N. Wright for his expert technical assistance.

References

- [1] Sankovic, J. M., "Investigation of the arcjet near field using electrostatic probes," NASA TM 103638, Washington, D.C., 1990.
- [2] Carney, L. C., and Keith, T. G., "Langmuir probe measurements of an arcjet exhaust," *J. Propulsion and Power*, Vol. 5, No. 3, pp. 287-294, May-June 1989.
- [3] Hoskins, W. A., Kull, A. E., and Butler, G. W., "Measurement of population and temperature profiles in an arcjet plume," AIAA paper 92-3240, Nashville, TN, July 1992.
- [4] Janson, S. W., Welle, R. P., Schulthess, D. R., and Cohen, R. B., "Arcjet plume characterization part II: optical diagnostics results," AIAA paper 90-2643, Orlando, FL, July 1990.
- [5] Manzella, D. H., Curran, F. M., Myers, R. M., and Zube, D. M., "Preliminary plume characteristics of an arcjet thruster," AIAA paper 90-2645, Orlando, FL, 1990.
- [6] Tosti, E., Deininger, W. D., Mazzacurati, V., and Ruocco, G. C., "Arcjet plume analysis using emissions spectroscopy," paper 91-092, 22nd IEPC, Viareggio, Italy, October 1991.
- [7] Cemogora G., et al., "Rotational temperature measurements of N_2^+ in an arcjet at low pressure," AIAA 92-2967, Nashville, TN, July 1992.
- [8] Crofton, M. W., Welle, R. P., Janson, S. W., and Cohen, R. B., "Temperature, velocity, and density studies in the 1 kW ammonia arcjet plume by LIF," AIAA paper 92-3241, Nashville, TN, July 1992.
- [9] Pollard, J. E., "Arcjet diagnostics by XUV absorption spectroscopy," AIAA paper 92-2966, Nashville, TN, July 1992.
- [10] Manzella, D. H., and Cappelli, M. A., "Vacuum ultraviolet absorption in a hydrogen arcjet," AIAA paper 92-3564, Nashville, TN, July 1992.
- [11] Erwin, D. A., Pham-Van-Diep, G. C., and Deininger, W. D., "Laser induced fluorescence measurements of flow velocities in high-power arcjet thruster plumes," *AIAA Journal*, Vol. 29, No. 8, 1991, pp. 1298-1303.
- [12] Liebeskind, J. G., Hanson, R. K., and Cappelli, M. A., "Flow diagnostics of an arcjet using laser induced fluorescence," AIAA paper 92-3243, Nashville, TN, July 1992.
- [13] Ruyten, W. M., and Keefer, D., "Characterization of electric thruster plumes using laser induced fluorescence measurements," AIAA paper 92-2965, Nashville, TN, July 1992.
- [14] Ruyten, W. M., and Keefer, D., "Laser fluorescence velocimetry of an arcjet exhaust plume," paper 91-093, 22nd IEPC, Viareggio, Italy, October 1991.
- [15] Ruyten, W. M., Friedly, V. J., and Keefer, D., "Electric propulsion: experimental research," Proceedings of the 3rd Annual Technical Symposium, Center for Space Transportation and Applied Research, Tullahoma, Tennessee, January 14-15, 1992, pp. 83-90.
- [16] Zube, D. M., and Myers, R. M., "Techniques for spectroscopic measurements in an arcjet nozzle," *J. Propulsion and Power*, Vol. 8, No. 1, pp. 254-256, Jan.-Feb. 1992.
- [17] Moeller, T., Rhodes, R., Keefer, D., Sedghi-Nasab, A., and Ruyten, W., "Comparison of experimental and numerical results for an argon arcjet," AIAA paper 92-3105.
- [18] Rhodes, R. P., and Keefer, D., "Modeling of a hydrogen arcjet thruster," AIAA paper 91-1994, Sacramento, CA, June 1991.

- [19] Tanaka, K., Tschia, K., Kaita, K., and Nishida, M., "Computational simulation of arcjet thruster flow fields," paper A90-25826, 3rd International Symposium on Computational Fluid Dynamics, Nagoya, Japan, August 1989.
- [20] Curran, F. M., and Sarmiento, C. J., "Low power arcjet performance characterization," AIAA paper 90-2578, Orlando, FL, July 1990.
- [21] Kuhn, H. G., "Atomic Spectra," 2nd Ed., Academic Press, New York, 1969.
- [22] Lents, J. M., "An evaluation of molecular constants and transition probabilities for the NH free radical," *J. Quant. Spectrosc. Radiat. Transfer*, Vol. 13, 1973, pp. 297-310.
- [23] Kovacs, I., "Rotational structure in the spectra of diatomic molecules," American Elsevier, New York, 1969, p. 123.

Table I: Data obtained from scans of the hydrogen Balmer-alpha through Balmer-zeta lines. Listed from left to right are: (1) line designation and wavelength; (2) line width, Δ , at fwhm; (3) integrated signal, S_i , under line profile; (4) intensity calibration factor, η_i , from Fig. 3; (5) corrected line intensity, $S_i^* = S_i/\eta_i$; (6) line intensity, S_∞ , in limit $T \rightarrow \infty$; (7) log ratio, $\ln(S_i^*/S_\infty)$, from Eq.(2); and (8) upper state energy, E_i . Numbers in parentheses indicate estimated standard deviations in the last digits.

(1) Line	(2) Δ (Å)	(3) S_i (mVÅ)	(4) η_i	(5) S_i^* (mVÅ)	(6) S_∞	(7) $\ln(S_i^*/S_\infty)$	(8) E_i (eV)
H α : 6563Å	0.3320(3)	26601(35)	2.841	9363(12)	11.8	6.676(2)	12.089
H β : 4861Å	0.2451(8)	3656(17)	82.75	44.2(2)	5.38	2.106(5)	12.750
H γ : 4341Å	0.2343(37)	682.1(1.4)	80.08	8.52(2)	2.87	1.088(2)	13.056
H δ : 4102Å	0.241(11)	205(12)	79.16	2.59(15)	1.50	0.546(56)	13.222
H ϵ : 3970Å	0.281(32)	99(14)	78.51	1.25(18)	1.04	0.184(13)	13.322
H ζ : 3889Å†	0.238(38)	63(13)	53.94	1.16(24)	0.73	0.47(18)	13.388

† Line thought to be coincident with rotational line from N_2^+ spectrum.

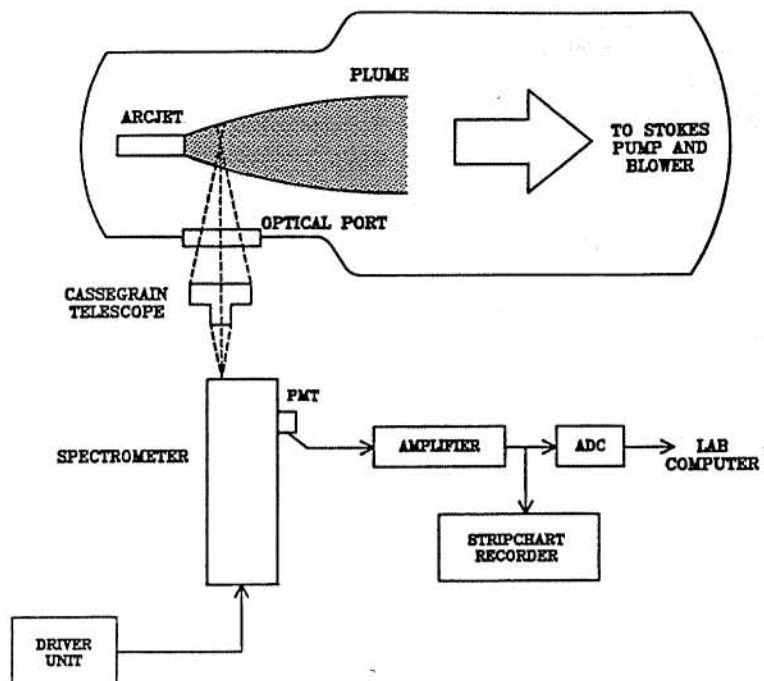


Figure 1: Schematic of the optical setup.

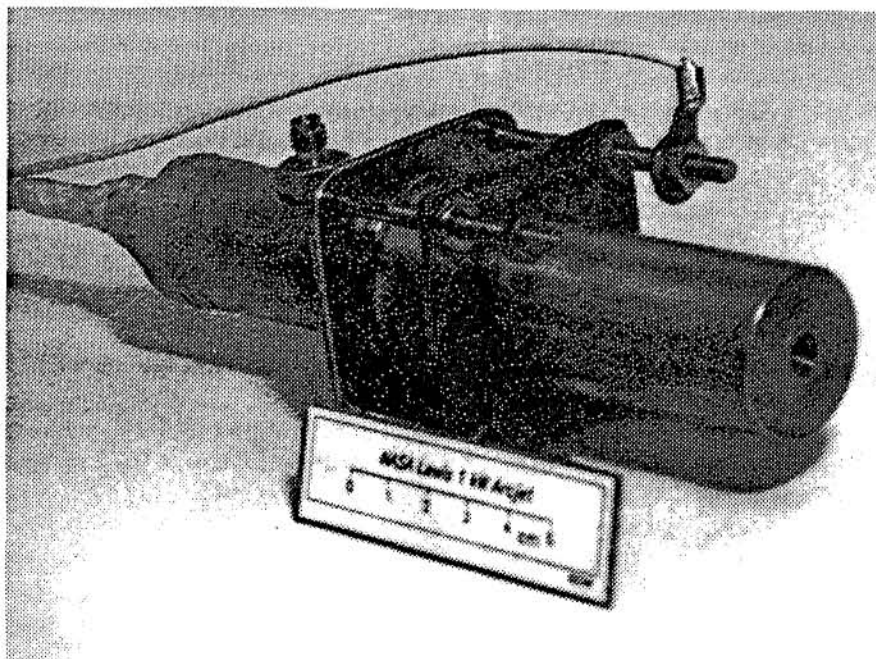


Figure 2: Photograph of the NASA Lewis arcjet. Length of displayed scale is 5 cm.

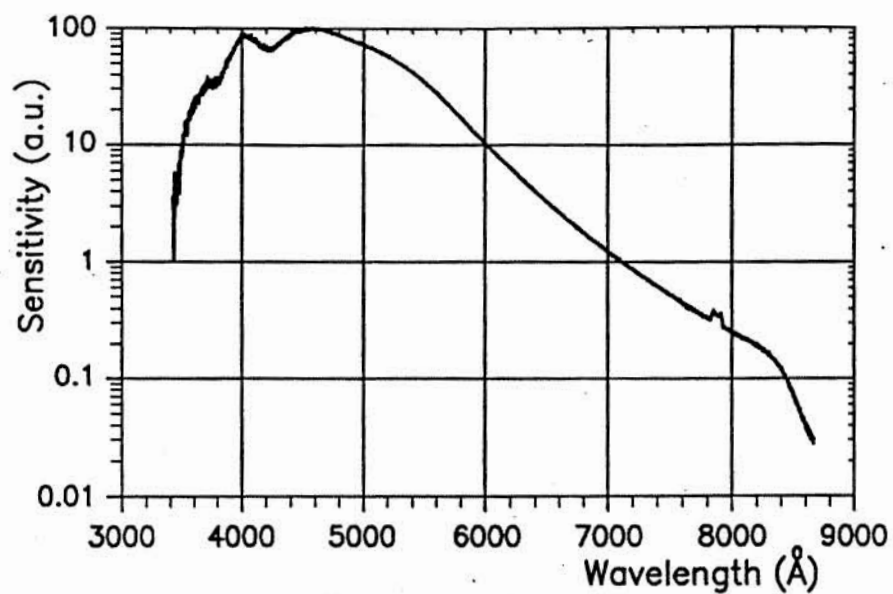


Figure 3: Measured sensitivity curve of the combined optical detection system, in arbitrary units.

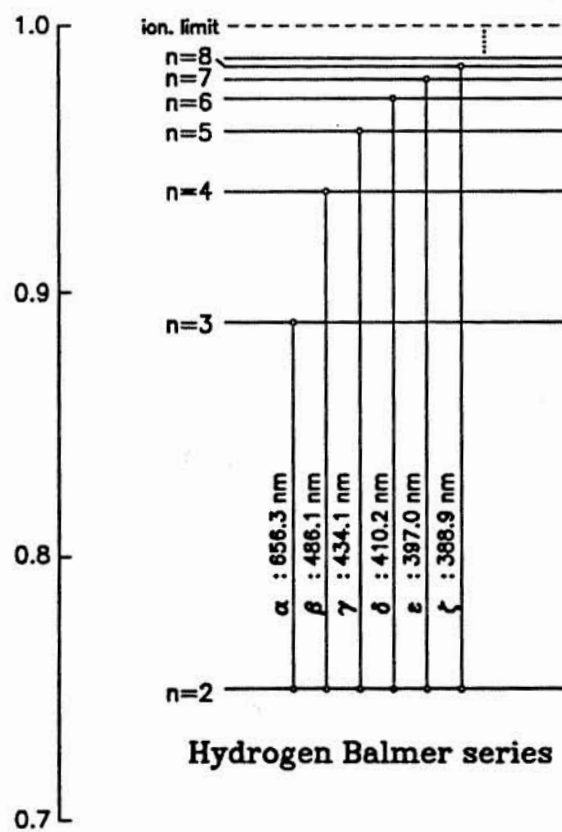


Figure 4: Schematic energy level diagram of atomic hydrogen, indicating the transitions of the Balmer series. Numbers along the vertical scale are in units of the ionization potential (13.6 eV).

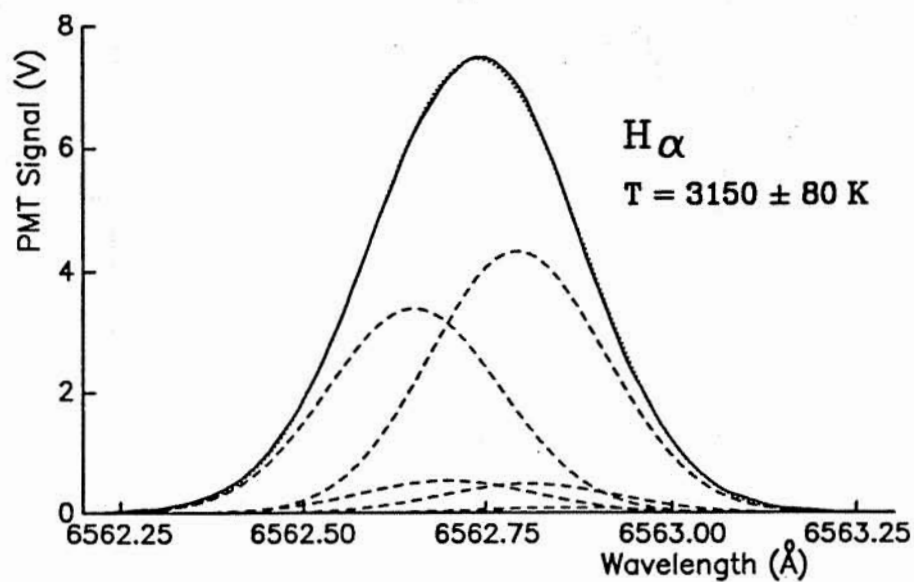


Figure 5: Measured emission lineshape of the hydrogen Balmer-alpha line (solid curve). Also shown is a multi-component gaussian curve fit (dotted curve). The individual fine structure components of the fit are shown as dashed curves.

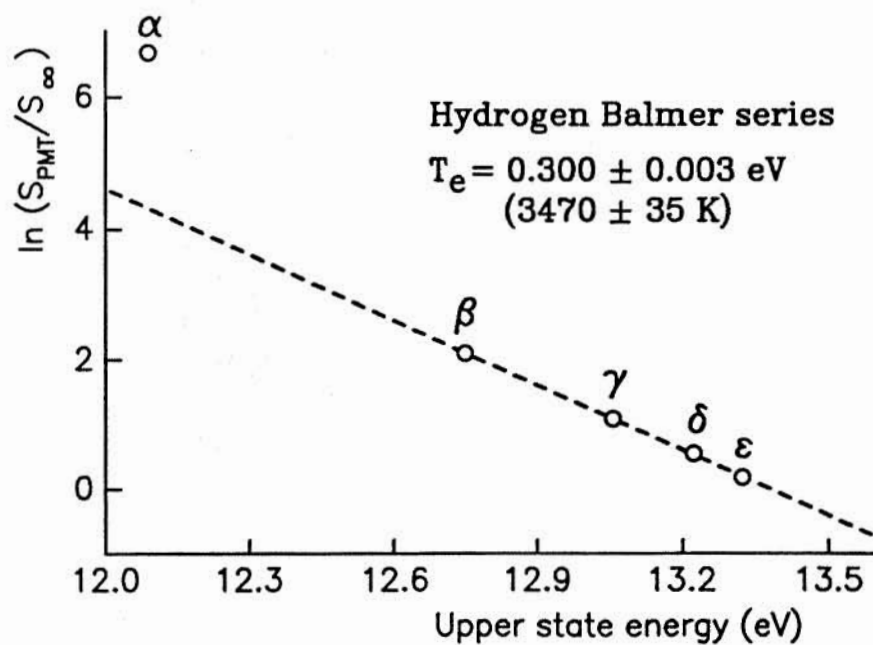


Figure 6: Boltzmann plot for the hydrogen Balmer-alpha through Balmer-epsilon lines.

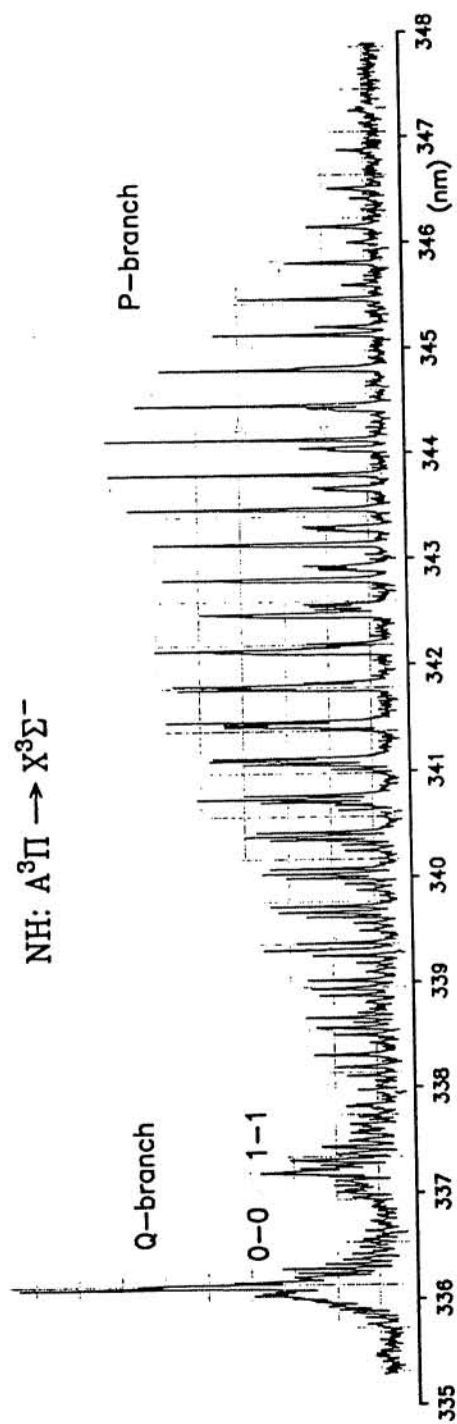


Figure 7: Emission scan of the $\text{NH } A^3\Pi \rightarrow X^3\Sigma^-$ band, performed about 2 mm downstream from the exit nozzle. Both 0-0 and 1-1 vibrational bands are present.

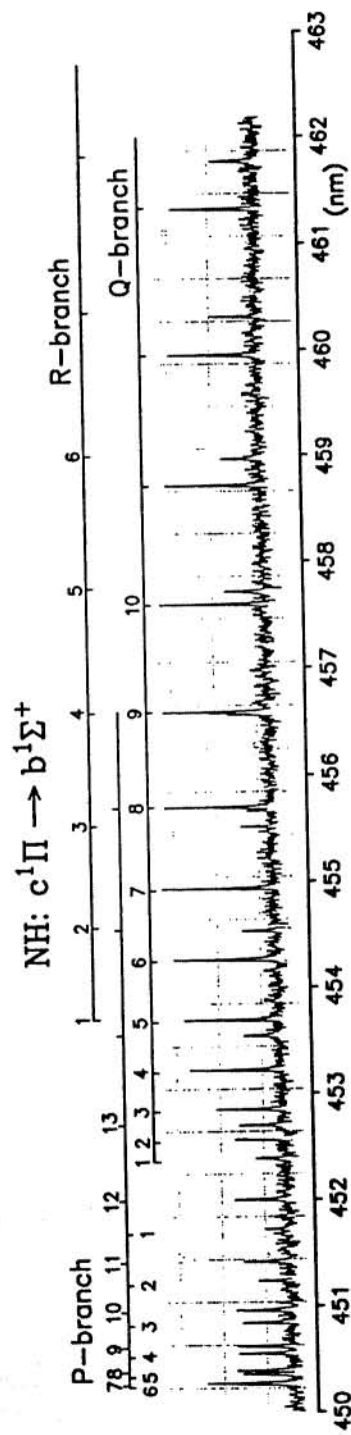


Figure 8: Part of the $\text{NH } c^1\Pi \rightarrow b^1\Sigma^+$ band, for the same conditions as in Fig. 7. Line designations are indicated.

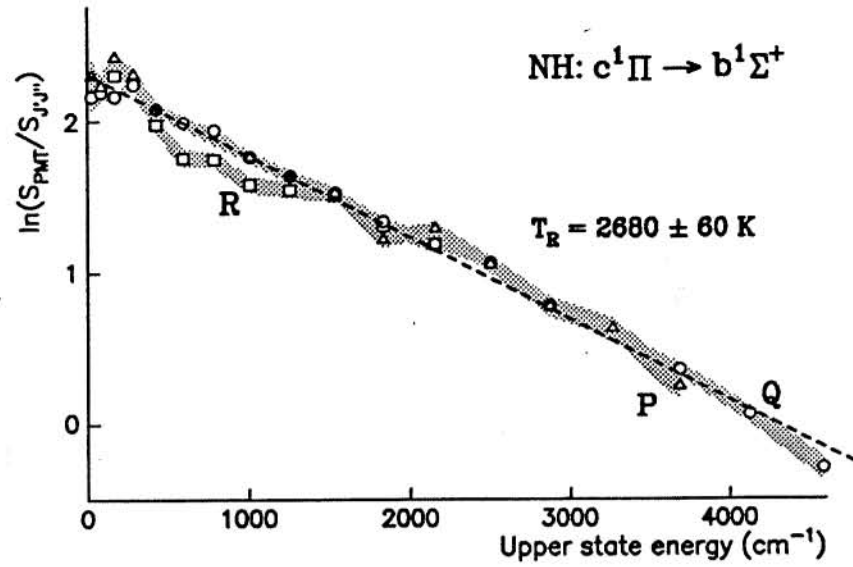


Figure 9: Boltzmann plot for the rotational lines of the NH $c^1\Pi \rightarrow b^1\Sigma^+$ band from Fig. 8. Triangular, round, and square data points represent P, Q, and R-branch transitions, respectively. The shaded bands indicate estimated uncertainties of the individual data points.

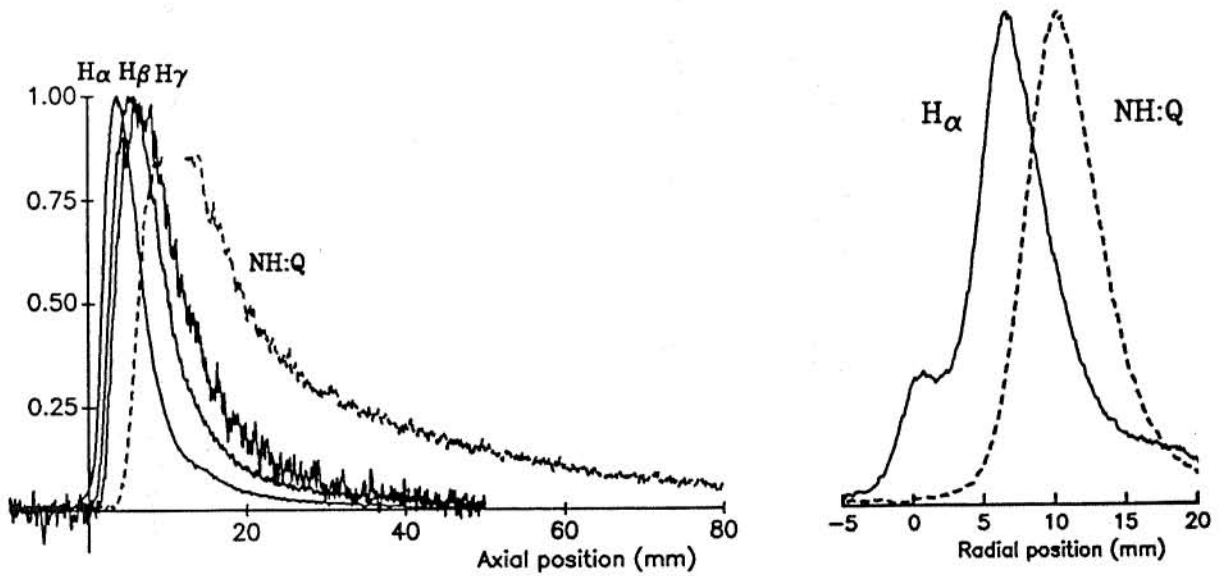


Figure 10: Measured axial (left) and radial variation (right) in emission intensity of several plume species. See text for a discussion of the effects of optical distortion.

The Space Applications Industrial Laser System

Robert Mueller¹, Brice Bible², Mary Helen McCay³, Michael Sharp⁴, and Dwayne McCay⁵
Center for Space Transportation and Applied Research (CSTAR)
Tullahoma, Tennessee, USA 37388

5945
p-9

Abstract

A joint program (Center for Space Transportation and Applied Research, University of Tennessee Space Institute, University of Waterloo, and Lumonics Corporation) is underway to develop a YAG laser based materials processing workstation to fly in the cargo bay of the Space Shuttle. The system will be capable of cutting and welding steel, aluminum and Inconel alloys of the type planned for use on the space station Freedom. As well as demonstrating the ability of a YAG laser to perform remote (fiber-optic delivered) repair and fabrication operations in space, fundamental data will be collected on these interactions for comparison with terrestrial data and models.

The flight system, scheduled to fly in 1995, will be constructed as two modules to fit into standard Get Away Special (GAS) canisters. The first can holds the laser and its power supply, to be constructed by the industrial partner, Lumonics Industrial Processing Division. The second canister has the materials processing workstation and the command and data acquisition subsystems. These components will be provided by the groups at UTSI and the University of Waterloo. The cans are linked by a fiber-optic cable which transmits the flight from the laser head to the workstation.

This paper delineates the activities, requirements and accomplishments for the SAILS project to date.

Introduction

The UT-Calspan Center for Space Transportation and Applied Research (CSTAR) is one of 17 NASA Centers for the Commercialization of Space (CCDS). The mission of CSTAR is to team with industry and academia in the development of new and innovative space technologies. The SAILS program has been developed under this mission because of its broad potential to benefit industry, academia, and government through advanced laser materials processing technology.

The long term space missions planned by NASA will require some form of machining and repair capability. The proof-of-concept flight in 1995 will firmly establish the YAG laser as a viable materials processing tool for space applications. Follow-on phases to the program will develop the infrastructure necessary for implementation on long term space structures by the end of the century.

As the lifetime and complexity of space structures increase, the ability to construct, maintain and repair these structures in space must also be improved. The industrial laser represents a possible solution to the problem of conducting multiple task manufacturing and repair operations at remote, hostile locations such as an orbiting platform.

The purpose of the Space Applications Industrial Laser System (SAILS) project is to demonstrate the capability to employ a YAG laser processing facility in space and to perform practical laser materials processing operations under microgravity conditions. The objectives of this project may be grouped under the following categories:

Science: Determine the effects of gravity on welding, drilling, cutting, brazing, and soldering. Compare experimental results with models to improve predictions of process behavior in Earth's gravity and microgravity.

Space Engineering: Demonstrate viability of laser technology to perform repair and fabrication type operations in space. Applications include a laser repair kit for Space Station, manned Mars missions, and a Moon base, and a laser-based factory in space.

¹Research Engineer

²Program Manager

³Associate Professor

⁴Applications Engineer

⁵Professor

Laser Engineering: Design refinement and demonstration of the industrial YAG laser to show that it has become a simple, compact, efficient and rugged tool capable of operating in any environment; in particular show the advantages of fibre optic beam delivery, including ruggedness and the ability to operate in remote and harsh environments. The Lumonic's Luxstar Laser has been chosen as the prototype from which the flight laser will be developed.

Program Status

The SAILS program, initiated in 1990, continues to progress toward a 1995 Space Shuttle flight. During FY92, NASA assigned SAILS to STS-72 with a tentative launch date of June 6, 1995. The following gives the status of several other program challenges.

Payload Flight Plan

The payload flight plan which describes in detail how the flight will be accomplished for the SAILS program was originally submitted to NASA in 1991 and received approval from the NASA Level I Payload Review Board (PRB) in March 1992. This review was primarily to evaluate the commercial merit of the program. Following Level I approval, SAILS was submitted to the NASA Level II PRB for technical evaluation. This board awarded conditional approval to the program in August 1992 subject to evaluation by each of the appropriate NASA Centers.

NASA Payload Integration

The lead for integration of the SAILS hardware has been assigned to the NASA Small Payloads Flight Division at Goddard Space Flight Center (GSFC). After a preliminary meeting between CSTAR and GSFC in September 1992, SAILS was designated as a Complex Autonomous Payload (CAP) due to its unique fiber optic interconnection requirement. The CAP also allows for an additional 1/2 canister (15") addition to the standard GAS can which may be beneficial in integrating the Lumonics LUXSTAR laser.

GSFC also has the responsibility to furnish the canisters and support services to be used for the experiment and to deliver the system to JSC for safety inspection prior to flight. One document GSFC submits to JSC is the Payload Accommodations Requirements (PAR) which defines all necessary experiment requirements and identifies all potential hazards. GSFC will work with CSTAR in development and submittal of this document to JSC

for flight manifesting. A draft PAR was completed in FY92 with the final document scheduled for submittal to JSC in early 1993.

Program Schedule

As previously described, the SAILS experiment consists of two GAS canisters linked by a fiber optic delivery system. Development and fabrication of this experiment requires several integrated tasks to be accomplished by each of the three program participants. Figure 1 shows each of the major tasks required for the program.

Tasks Accomplished

Two technical milestones were reached this year in the development of the SAILS program. The ground based laboratory was completed and is now fully operational. The materials and processes to be tested in the SAILS experiment were also identified. This section will describe the features of the CSTAR laser lab and the rationale for selecting the materials to be used in the SAILS flight experiment.

CSTAR Laser Processing Lab

The Laser Materials Processing Lab at CSTAR is based on a JK701 Nd:YAG laser, operating at 1.06 μ wavelength, which was supplied by the SAILS industrial sponsor, Lumonics Industrial Products Division. This is a versatile industrial laser, capable of 400 W average power, 5 kW peak power, and pulse lengths from 0.5 to 20 ms. The laser beam is delivered to the processing enclosure by a 5 m long optical fiber. The lab has obtained two delivery fibers, of 1000 and 600 μ m diameter, for high power and precision processing respectively.

The laser beam delivery fiber enters the enclosure and terminates at the laser machining head, where the beam is expanded, collimated, redirected downward and focussed onto the workpiece. The machining head is mounted on a coarse vertical slide and also contains a micrometer fine focus adjustment. The turning mirror is dichroic, reflecting the laser light and transmitting visible, to allow a video camera mounted at the top of the head to see the workpiece and permits the operator to precisely locate the area to be processed. The enclosure has been fitted with an X-Y linear translation system, capable of moving a 12x12 inch sample over a 12x12 inch area. A rotary stage can be mounted on the X-Y base, with the axis either horizontal or vertical, to enable processing cylindrical parts. The stages are driven by stepper motors and 10 microstep/full step driver

modules, giving a maximum linear resolution of 1 μm .

The sample translation system is driven by an intelligent motion control board (Oregon Microsystems PC38-4), located in an IBM AT computer. The board is capable of controlling 4 axis of linear or linearly interpolated motion or circular interpolated motion on any pair of axis. This board, with its own MC68000 microprocessor, treats the host computer as an ASCII terminal. Command sequences sent from the host, either as directly typed commands or downloaded files, are queued and executed by the motion controller, thereby freeing the host computer to perform other tasks. The motion controller is also responsible for monitoring travel limit and panic kill switches, executing an orderly shutdown in the event that one of these safety interlocks is tripped.

Digital output lines of the motion controller are used to toggle several laser functions, such as laser on, shutter open/close, and single shot output, once the laser has been placed under remote control by the operator. A serial interface between the host computer and the laser is also used to download pre-programmed pulse characteristics, and to enquire laser status information.

SAILS Material and Process Selection

As the SAILS experiment is designed to demonstrate the viability and practicality of laser materials processing in space, the processes to be tested and the materials chosen all have application in space systems. Initial trials were conducted to show that the materials could be processed with the laser power anticipated for the flight system. The materials and processes selected are shown in Table 1.

The processes all have obvious practical applications, in space or on earth. Structural joining operations (welding and brazing) will be needed in the assembly and repair of man-rated habitats. Cutting will be required for removing damaged components for repair and in the recycling of space debris. Soldering of electrical and electronic components could be accomplished remotely using a dexterous manipulator and a fiber delivered laser beam, with much less heat input to nearby components than with a conventional solder iron.

Table 2 identifies each material and a specific space application. The scientific purpose of performing each process is also described. The non-

penetrated welds are most useful for comparing with similarly prepared terrestrial samples and computational models of the welding process, such as the WELDER code ^{1,2}. Full penetration welding samples, drills, cuts, brazes and solders produce engineering test pieces for later structural analysis. Comparison of these samples with those performed on earth will highlight the differences of performing these processes on orbit. The kapton diagnostic drills are used to record the beam size and focus height. The lead/tin weld sample simulates the condition of a deep penetration keyhole, and will be useful in predicting the performance of higher power lasers. Note that 15 material/process combinations are listed for the 16 sample positions. Two diagnostic runs on Kapton are scheduled to confirm proper operation of the system.

Tasks Underway

The tasks completed have laid the groundwork for developing programs to scientifically define and characterize the processes to be performed on orbit, and design and specify the components of the hardware to be used in flight.

Ground Studies

Preliminary studies were designed to show that the materials and processes under consideration could be processed with a relatively low power laser (see Table 3). A firm idea of the processing conditions for each sample is needed before detailed design of the flight hardware can begin. Therefore, a study to determine the precise processing parameters to be used for each sample, and to characterize the results of each process, is now well underway. As well as finding workable combinations of processing parameters, this study will eventually try to determine scaling relationships (depth and width of weld vs power, metal structure) between the flight power level and presently available ground-based laser power levels. This will permit prediction of the performance of higher power lasers operating under space conditions.

Table 4 shows the results to date of the study to determine the optimum processing parameters for each process. All parameters fall within the limitations of the flight laser system.

All materials and processes have been tested, but the parameters for those processes not completed on the chart have not been finalized.

Figure 2 shows photographs of spot and seam welds in 316L stainless steel under the conditions described in Table 4. Figures 2a and 2b show top and cross section views of spot welds performed in the 3.2 mm thick material. Figures 2c and 2d show top and bottom views of a full penetration seam weld performed in the 0.73 mm thick material. While the non-penetrated welds do show some porosity, all welds are strong and crack-free.

Figure 3 shows overview and detailed photos of a full penetration seam weld in 2219 aluminum, using 0.25 7mm of 4047 aluminum filler metal, under the conditions described in Table 4. The weld is smooth, uniform, and crack-free.

Initial process characterization and process parameter selection is nearing completion. Detailed analysis and testing of joints and the scaling study will begin in the next year.

Flight Hardware Design

The detailed definition of the laser characteristics and the results from the initial process characterization tests allowed a more detailed design of the flight hardware. Figures 4 and 5 show the current state of design for the laser and processing cans, respectively.

The laser can design is still in an early stage, as exact dimensions of the laser modules are not yet available. Initial estimates of size and weight indicate that a GAS can could be a very tight fit for a LUXSTAR laser without substantially redesigning the laser. As an alternative, other carrier geometries are being investigated. It remains to be determined whether repackaging the laser into a cylinder, or designing a rectangular GAS can type housing will be more feasible.

The materials processing can design is much further advanced. The sample matrix has been changed from a square array to a single circular pattern. The internal laser beam delivery has also been changed from a fiber to a free-space beam with moving optics. This configuration mimics current industrial laser practice of using a moving optics end effector to achieve more motion flexibility. Decoupling the motion axis also produces a more stable structure. Candidate hardware systems for many of the components in this can have been identified and many of the subsystems shown are drawn to scale. The design to this point is within the volume and weight restrictions of a GAS canister.

Objectives for 1993

As shown on the SAILS Program Schedule (Figure 1), the objectives for 1993 will consist mainly of flight hardware design and development activities. Specifically, the following technical tasks will be accomplished:

- Completion of flight hardware design for both the laser and materials processing canisters and interconnecting fiberoptic system.
- Procurement and development of the computer and control system.
- Procurement and development of the visual data system.
- Procurement and fabrication of the sample carrier.
- Fabrication of the materials processing canister.
- Begin integration and testing of flight hardware.

Conclusion and Acknowledgements

A program is well underway to develop the first laser materials processing workstation for use in space. As well as providing fundamental information on several laser-material interactions, this program will demonstrate the ability of laser processing to perform useful repair and fabrication operations in space.

This work is supported by CSTAR, under NASA grant NAGW-1195; The University of Tennessee Space Institute Center for Laser Applications, and Lumonics Industrial Products Division. Weld filler metals and brazes were provided by Lucas-Milhaupt Inc. The authors gratefully acknowledge their colleagues supporting this effort: Harald Bransch of Lumonics, Walt Duley and Grant Kinsman of the University of Waterloo and Carole Thomas of CSTAR.

References

1. Eraslan, A.H., Zacharia, T., and Aidun, D.K. 1986. WELDER: A computational code for simulation of fast-transient, three-phase, flow, temperature and material composition conditions during welding. Department of Mechanical Engineering, Clarkson University, Potsdam, New York, Report No. MIE-142-1986.
2. Eraslan, A.H., McCay, M.H., and McCay, T.D., Final Report: Welder-LWP, Welder Computational Model Development, Center for Space Transportation and Applied Research, Tullahoma, Tennessee (1992).

Space Applications of Industrial Laser Systems

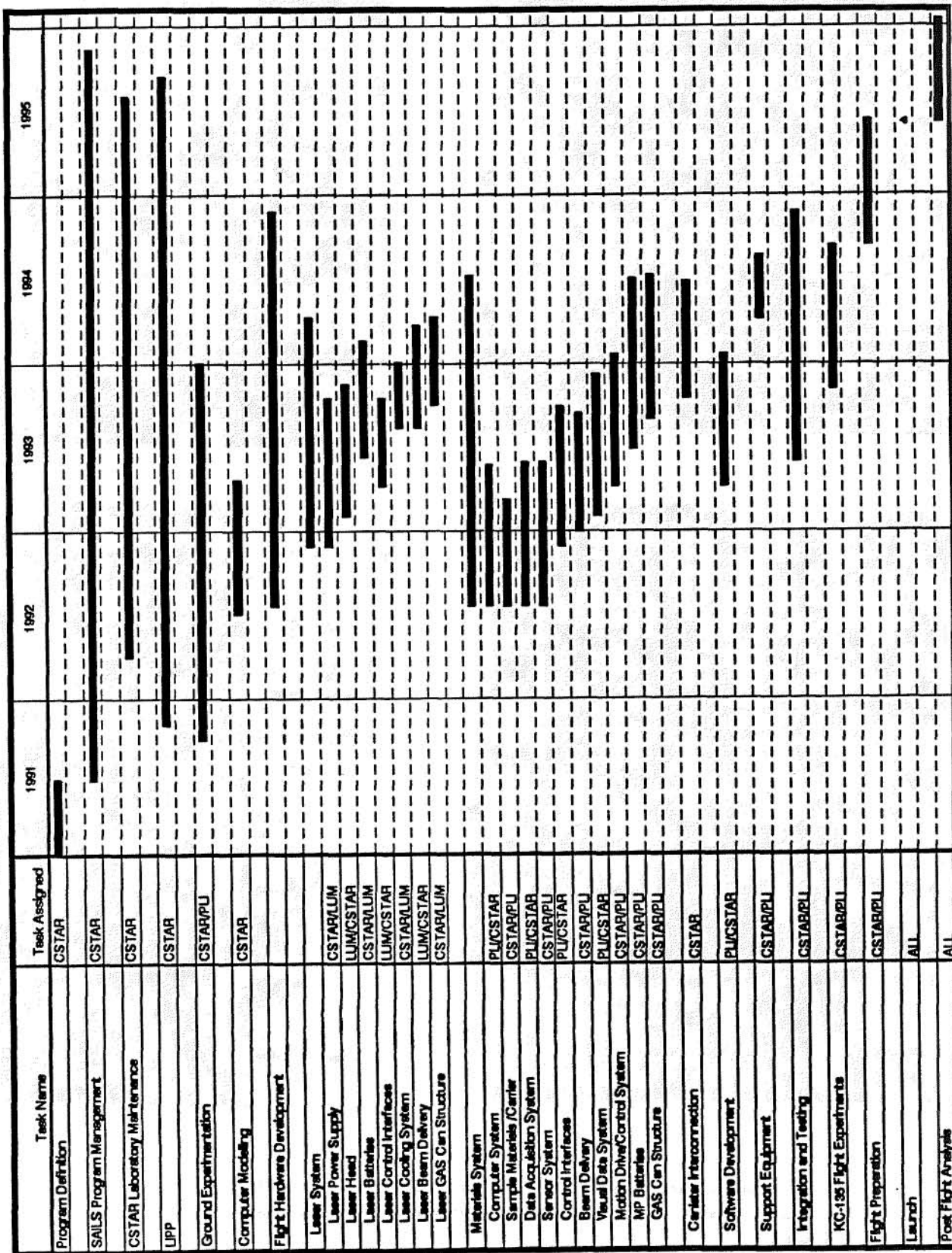


Figure 1 Task Schedule

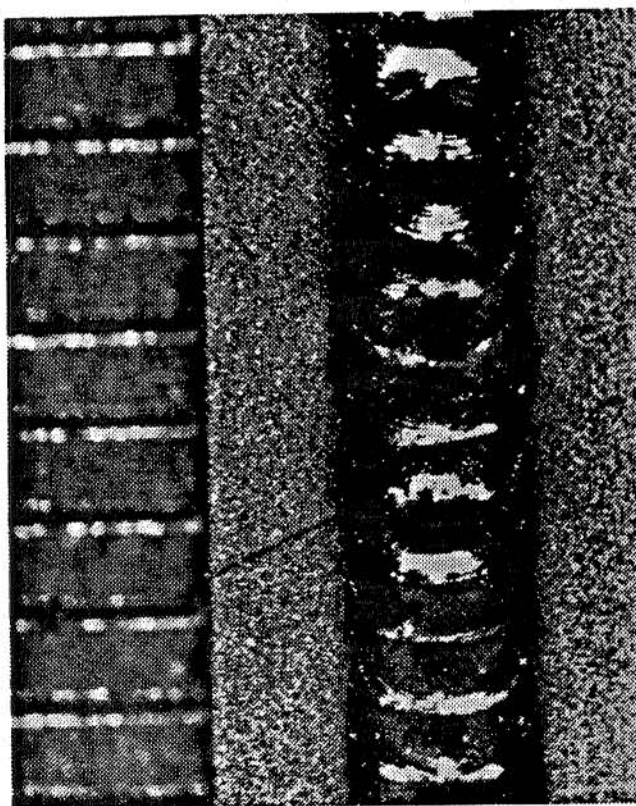
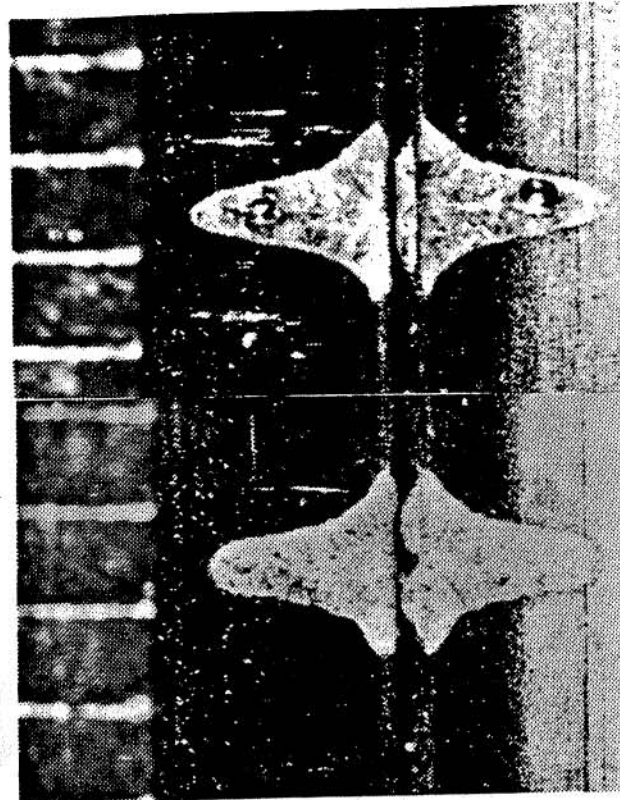
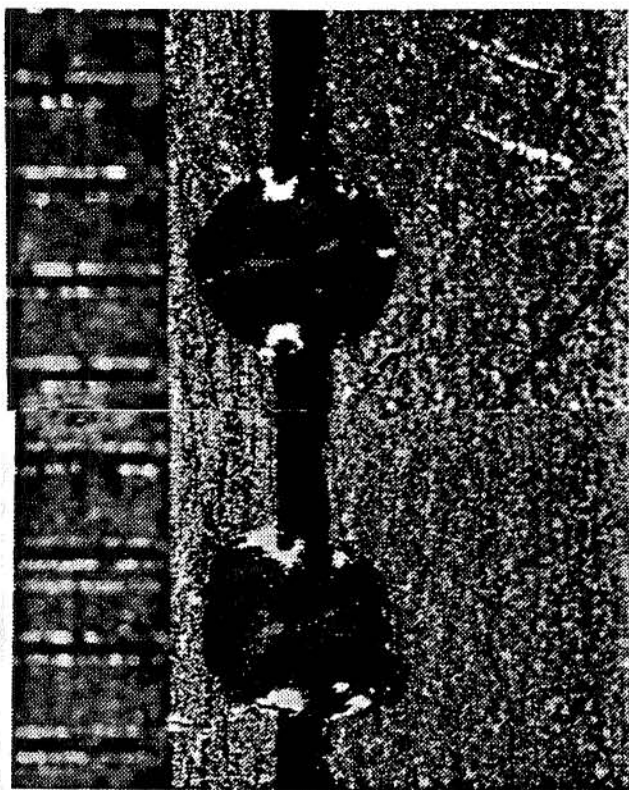


Figure 2 Laser welds of 316L stainless steel. See Table 4 for conditions. a), b) Top and side views of spot welds in 3.2 mm thick material. c), d) Top and bottom views of a full penetration seam weld in 0.73 mm thick material. Scale: 0.5 mm/div.

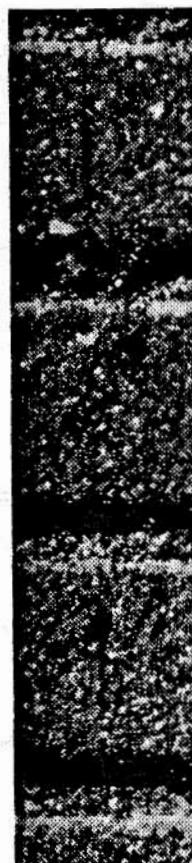
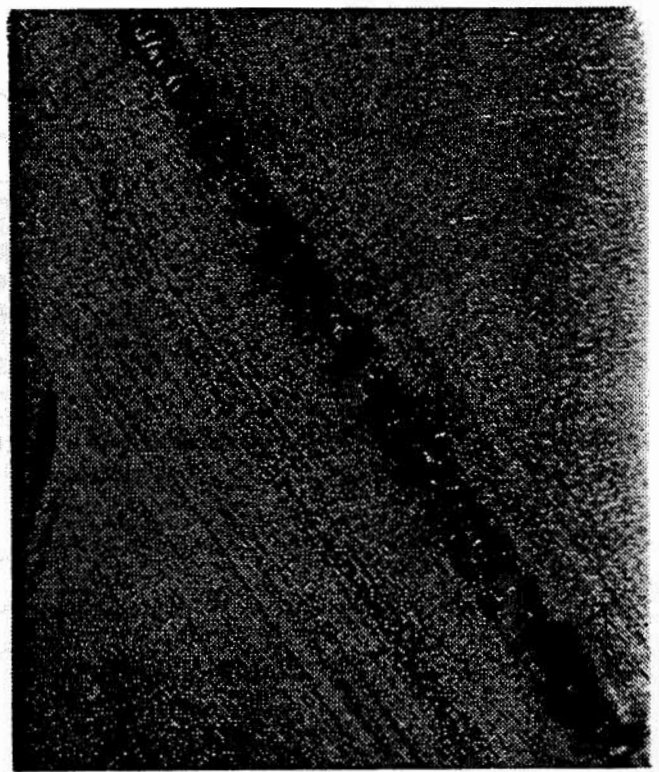


Figure 3 A full penetration laser seam weld in 2219 aluminum using 4047 aluminum filler. See Table 4 for conditions. a), b) overview. c), d) closeup. Scale: 0.5 mm/div.

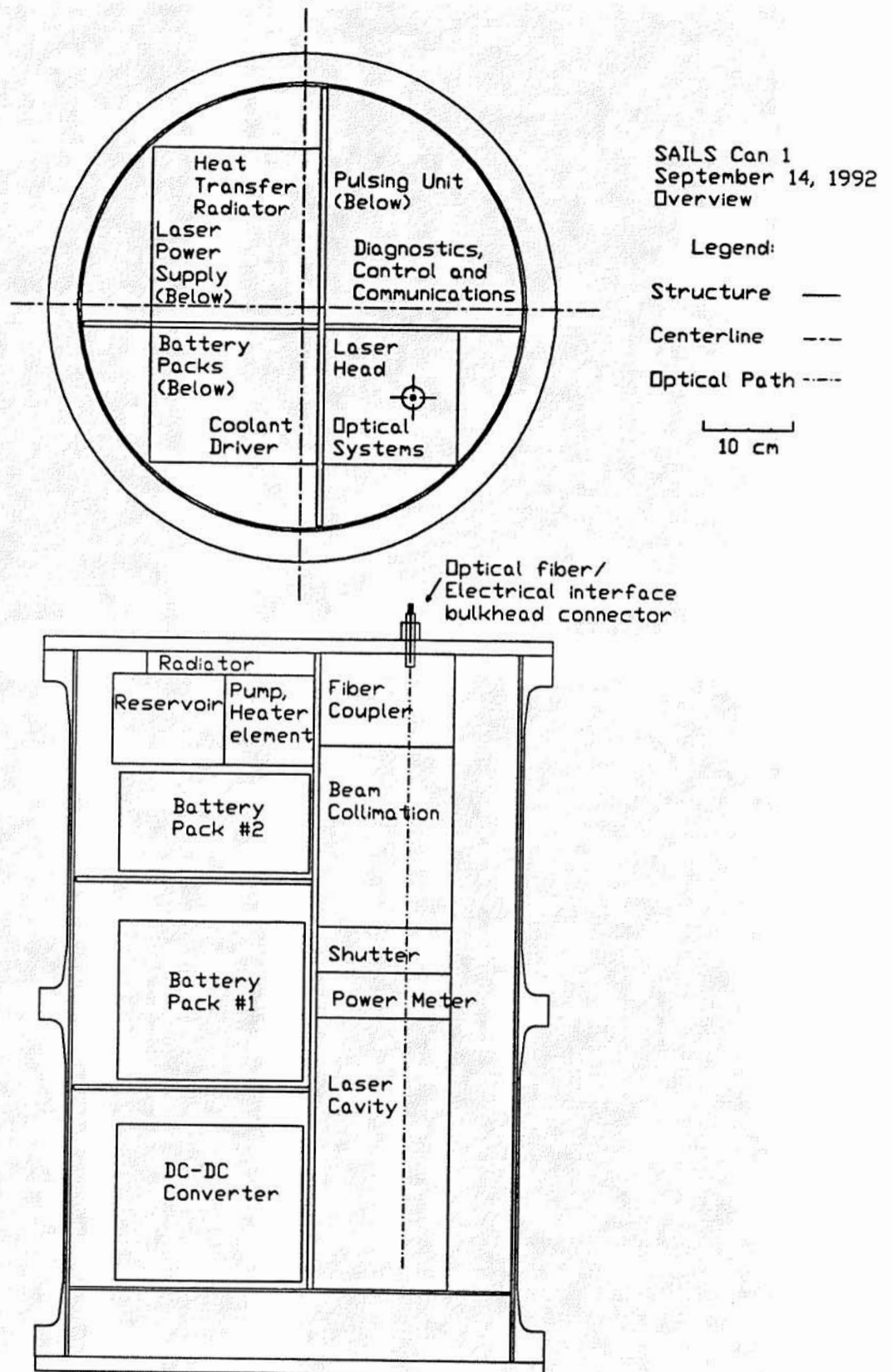


Figure 4 A preliminary design for the SAILS laser GAS can, housing a modified Lumonics LUXSTAR Nd:YAG laser.

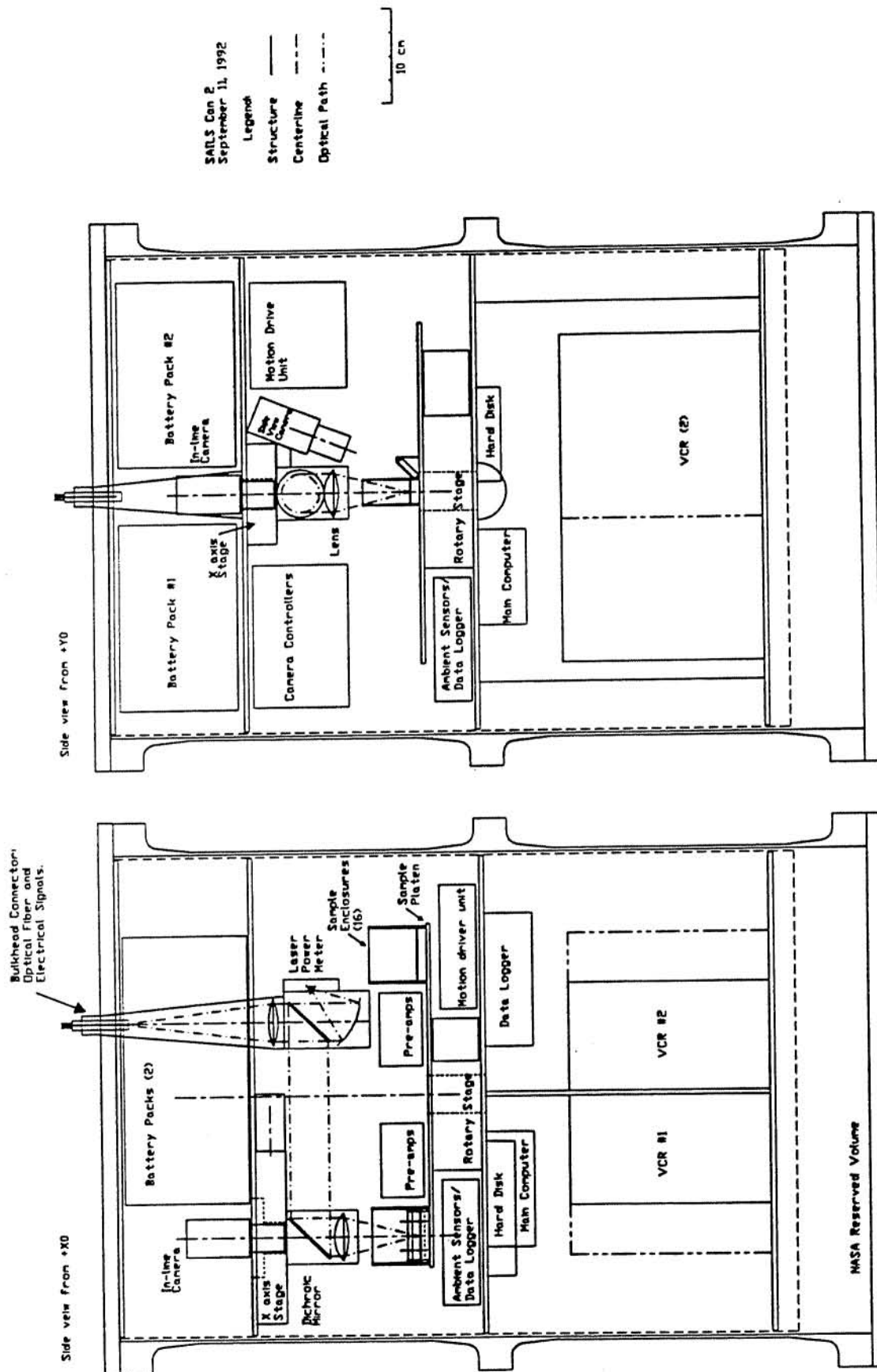


Figure 5 A preliminary design for the SAILS materials processing GAS can. This can will be linked to the laser can by an electrical and fiber-optic cable.

[REDACTED]

10/10/1944

10/10/1944

10/10/1944

10/10/1944

10/10/1944

Table 2. A detailed list of the materials and processes to be tested in the SAILS experiment and the purpose of each test.

Material	Thickness	Process	Purpose
316L Stainless Steel: Space Station fluid lines	3.2 mm	Spot/Seam Weld	Non-penetrated bead on plate weld- porosity, root effects, model comparison
		Spot/Seam Braz	Non-penetrated braze- demonstration
	0.73 mm	Spot/Seam Weld	Full penetration bead on plate weld- demonstration, model comparison
		Drill/Cut	Full penetration drill and cut- demonstration, recast layer study
2219 Aluminum: Space Station pressur- ized modules inner skin	3.2 mm	Spot/Seam Weld	Non-penetrating weld with 4047 filler- porosity, root effects, model comparison
	0.51 mm	Spot/Seam Weld	Full penetration weld with 4047 filler- demonstration, model comparison
		Drill/Cut	Full penetration drill and cut- demonstration, recast layer study
6061 Aluminum: Space Station pressur- ized modules debris shield	3.2 mm	Spot/Seam Weld	Non-penetrating weld with 4047 filler- porosity, root effects, model comparison
	0.51 mm	Spot/Seam Weld	Full penetration weld with 4047 filler- demonstration, model comparison
		Drill/Cut	Full penetration drill and cut- demonstration, recast layer study
Inconel 718: Space Station cryogenic lines	0.73 mm	Spot/Seam Weld	Full penetration bead on plate weld- demonstration, model comparison
		Drill/Cut	Full penetration drill and cut- demonstration, recast layer study
Copper: Electrical contacts	PC board	Solder	Single or multi-pulse spot solders- demonstration
Kapton: Diagnostic	0.05 mm	Drill/Cut	Laser spot size and energy diagnostic
Lead/Tin: Deep penetration model	3.2 mm	Spot/Seam Weld	Full penetration weld- example of a deep liquid pool, indication of effects of scaling to higher power

Table 4. SAILS experiment detailed parameter matrix.

Material and Thickness	Process	Defocus (mm)	Power (W)	Energy/Pulse (J)	Pulse Rate (Hz)	Pulse Length (ms)	Peak Power (W)	Speed (mm/s)
316L Stainless 3.2 mm	Spot/Seam Weld	1.05	50	9	5.5	4.3	2100	2
	Spot/Seam Braze							
316L Stainless 0.73 mm	Spot/Seam Weld	1.05	50	9	5.5	4.3	2100	2
	Drill/Cut	0	50	3.3	15	1.1	3000	1
2219 Aluminum 3.2 mm	Spot/Seam Weld w. filler	0.5	50	5.0	10	1.7	2950	2
2219 Aluminum 0.51 mm	Spot/Seam Weld w. filler	0.5	50	5.0	10	1.7	2950	2
	Drill/Cut	0.2	50	2.4	21	0.8	3000	
6061 Aluminum 3.2 mm	Spot/Seam Weld w. filler							
6061 Aluminum 0.51 mm	Spot/Seam Weld w. filler							
	Drill/Cut	0.2	50	2.4	21	0.8	3000	
Inconel 718 0.73 mm	Spot/Seam Weld							
	Drill/Cut							
Copper PC board	Solder							
Kapton 0.05 mm	Drill							
Lead/Tin 3.2 mm	Spot/Seam Weld	0.9	18	3.5	5.5	5.0	700	2

Laser Industrial Partnership Program

Michael Sharp¹, Rob Mueller², Dwayne McCay³, Mary Helen McCay⁴ and Brice Bible⁵
Center for Space Transportation and Applied Research
Tullahoma, Tennessee, USA 37388

Abstract

In conjunction with the Space Application Industrial Laser System (SAILS) program, CSTAR has developed a terrestrial program for transfer of laser materials processing technology to U.S. industry. This program, called the Laser Industrial Partnership Program (LIPP), combines state-of-the-art laser laboratory facilities, a multi-disciplinary group of scientist/engineers, and the technology acquired through the SAILS program to assist in application of lasers to manufacturing.

This program is a joint effort between CSTAR and the Center for Laser Applications at The University of Tennessee Space Institute.

The purpose of this report is to describe the strategy used in developing the program and to detail the main industry projects accomplished during FY 1992.

Introduction

One of the objectives of the NASA Centers for Commercial Development of Space is to develop commercial space products/processes which are also beneficial for ground applications. In the current economic environment, most U.S. industries are hard pressed to commit to long term commercial space development without some short term market benefits. The SAILS program provides a viable long term space application through development of a multi-purpose laser repair and fabrication workstation for Space Station Freedom and other permanent space platforms.

The LIPP program provides immediate commercial benefit through implementation of the laser materials processing technology developed through the SAILS program to U.S. industry for application to current products/processes. This is accomplished by providing a uniquely unbiased resource to industry.

Traditionally, an industry interested in lasers for manufacturing has two resources available for

technical assistance: 1) laser companies, and 2) laser job shops. 1) The laser companies often bias their recommendations toward their specific product line when an alternative process may be more appropriate for the application. In addition, these companies usually cannot devote adequate time for a thorough evaluation of the process. 2) The laser job shops are usually neither equipped nor staffed to provide technical development of a new laser product/process.

CSTAR/UTSI applies a multi-disciplinary approach to each industry requirement in an effort to identify the appropriate manufacturing technique for that particular product. This unbiased approach provides a service not currently available to industry.

1992 LIPP Objectives and Marketing Plan

This program, initiated in November 1991, has the objective of assisting industry in the application of laser materials processing technology to improve their manufacturing processes. The use of lasers by U.S. industry has been slow in developing when compared to Europe and Japan. This has contributed to the

¹Applications Engineer

²Research Engineer

³Professor

⁴Associate Professor

⁵Program Manager

decline in the global U.S. manufacturing market segment. By implementing laser technology, U.S. industry can improve the quality and production efficiency of their products, thus enhancing the global U.S. competitive position.

To implement these program objectives the following phases were identified for 1992:

- Phase 1: Develop marketing materials describing the CSTAR/UTSI laser materials processing capabilities.
- Phase 2: Identify the segment of industries to approach and develop a list of prospective companies.
- Phase 3: Contact these industries through mailings, conferences, and personal references.
- Phase 4: Schedule visits to individual companies for survey of the manufacturing floor. Arrange laboratory demonstrations at CSTAR.
- Phase 5: Develop and perform laser processing projects with industries.
- Phase 6: Evaluate progress and revise each phase as required.

1992 Progress

Progress for the first year of this program will be reported in two sections: Marketing Program (Phases 1, 2, and 3), and Industry Projects (Phases 4 and 5).

Marketing Program

- Phase 1: A marketing brochure was developed in-house in early 1992. This four color brochure displays the laser materials processing facilities at CSTAR/UTSI along with the services offered through the program to industry.

In addition, a marketing booth was purchased in April and display materials were developed for both laser materials processing and other CSTAR focus areas for use at the May TABES exhibition in Huntsville.

Phase 2: A list of approximately 150 potential industries was compiled from the following sources:

- Tennessee and Alabama industrial directories
- TVAR regional industry list
- CSTAR/UTSI industrial contacts
- Laser industry contacts

These industries were separated into high and medium prospect categories based on project probability.

- Phase 3: The high prospect industries (approximately 25 companies) were contacted initially by mail with phone followup. The remaining industries have been cataloged and will be contacted in early 1993. The strategy for targeting the high prospects has proven beneficial as described in the next section.

Industry Projects (Phases 4 and 5)

The following describes each of the industry projects accomplished during 1992 through the LIPP program:

YAG Laser Generator Repair System Siemens Nuclear Power Services

Siemens Nuclear is developing a YAG laser repair system for welding of Inconel tube sleeves into damaged steam generator piping. This system requires state-of-the-art optics and fiber beam delivery systems. During the period from March to the present, CSTAR has provided assistance in

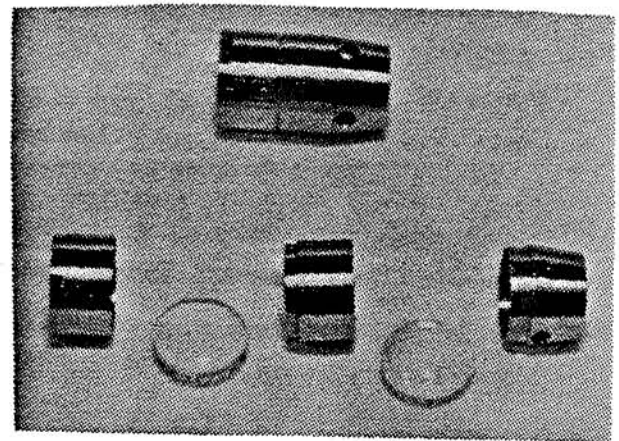


Figure 1 Lens assembly for Siemens laser welding system.

development and fabrication of the optical end effector (see Figure 1) and fiber housing systems. In addition to the laser system, CSTAR developed a technique for laser joining of thermocouples to the Inconel piping for thermal analysis of the joining process (see Figure 2). Siemens has used this

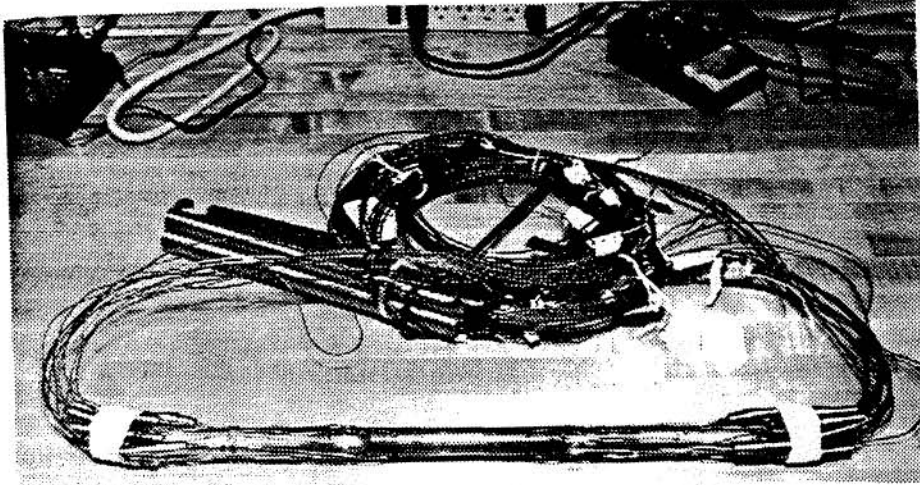


Figure 2 Test section of 3/4" Inconel piping with 24 laser-welded thermocouples.

process to validate the structural integrity of the sleeving procedure. As of this date, the laser sleeving system is nearing completion at Siemens and will become only the second of its kind in the world.

Inconel Clip Assembly Spot Welding Siemens Nuclear Power Services

After receiving the LIPP marketing information, Siemens requested that CSTAR submit a proposal for development of the process to laser weld Inconel springs onto nuclear refueling clip assemblies. These assemblies are used in nuclear facility maintenance where weld reliability is critical. In the past this work has been provided by laser job shops, resulting in varying weld reliability.

CSTAR submitted an interest and feasibility statement outlining the general requirements for this type of laser system, which would consist of a YAG laser, two axis workstation, and vision positioning system. Following analysis by Siemens, CSTAR was informed that the information was very beneficial for planning by their manufacturing division and that further development would be budgeted for 1993.

Laser Manufacturing of Thermos Components Aladdin Industries

At the recommendation of the SAILS industrial partner, Lumonics, CSTAR contacted Aladdin about determining the feasibility of using lasers for hermetic welding of stainless steel thermos containers. Conventionally, this process is performed by TIG and resistance welding techniques which result in a scrap rate of 10% due to non-hermeticity at the joint. A survey of the manufacturing facility was conducted by CSTAR and revealed that commercial laser suppliers had pressured Aladdin toward the use of CO₂ lasers without considering other possible options.

CSTAR conducted preliminary welding experiments using the Lumonics JK701 YAG laser and produced high quality hermetic welds at the critical joint areas. (See Figure 3). These welded samples along with an economic appraisal of the required system was submitted to Aladdin. Based on this information, Aladdin has selected YAG for the production laser system and is currently soliciting suppliers for the complete system.

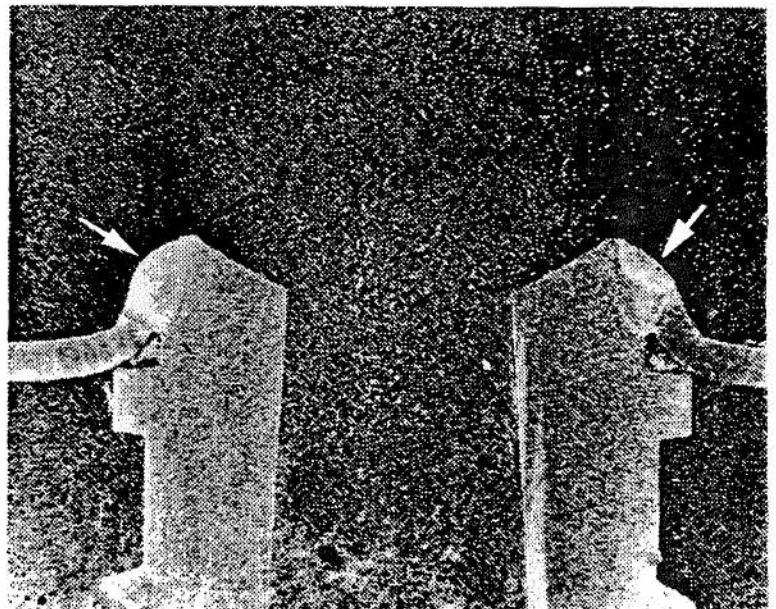


Figure 3 Cut section of laser welded thermos assembly.

Development of Transmission Bellows Assembly
Robert Shaw (Johnson Technologies)

Production of an automotive transmission altitude-correction bellows assembly by Robert Shaw is typically performed by a manual brazing process. This process is time consuming and does not always produce the required hermetic seal. CSTAR was contacted by Johnson Technologies to design and fabricate a prototype assembly using laser technology to replace this brazing process. Working with Johnson and Robert Shaw, several design and materials concepts were developed and welded using the CSTAR Lumonics YAG laser. Some of the bellows components used during the evaluation are shown in Figure 4. The main objective was to

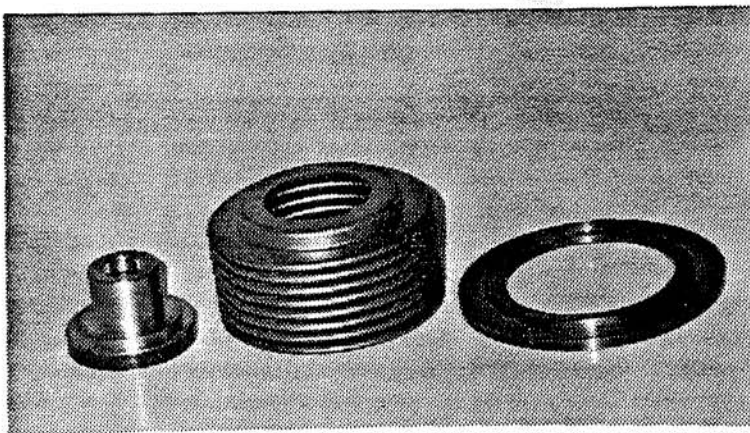


Figure 4 Automotive transmission bellows components.

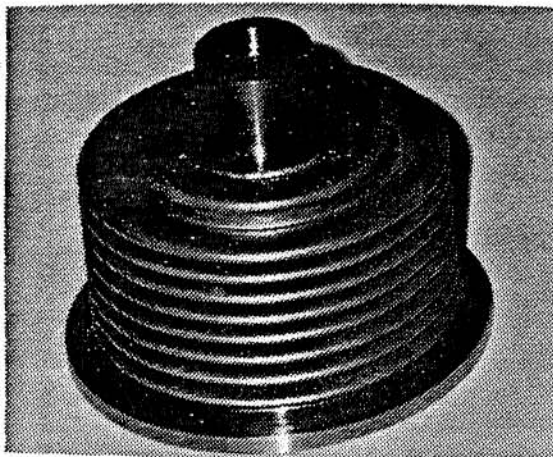


Figure 5 Laser welded bellows assembly.

produce a hermetic seal at the joints shown in Figure 5. After several prototype designs were attempted, hermeticity was achieved and a complete assembly was submitted to Robert Shaw for analysis. Based on the results of this project, Robert Shaw is considering implementing a production laser system next year.

Laser Drilling of Wire Blanks
Lukens Medical Corporation

Drilling of blind holes in 304 stainless steel blanks is required in the process of fabricating surgical products. These holes have aspect ratios (length/diameter) ranging from 6.5 to 26.0. Currently this drilling process is performed outside the United States using laser technology and returned to Lukens for finishing. This arrangement has proven uncontrollable for Lukens resulting in shipment delays, poor quality control, and high production costs. Relocation of this process to the Lukens facility could alleviate many of these problems and provide a higher quality, lower cost product. CSTAR has been approached to provide technical assistance in developing this laser process for Lukens.

Following an initial meeting at CSTAR, several sample blanks were drilled using the YAG laser and submitted to Lukens as proof of concept. Further technical discussions identified two steps for implementation of a laser drilling system at Lukens:

Step 1: Establish the feasibility for production of laser drilled wire blanks through the following tasks:

- Optimize the laser parameters for the required hole specifications through laboratory experimentation.
- Determine hole quality through structural and metallurgical analysis.
- Identify equipment requirements and cost.
- Evaluate utilization of the CSTAR laser facilities for prototype batch production.

Step 1 would provide a comprehensive analysis of lasers for this application at a minimum investment by Lukens.

Step 2: Development of the production laser system and installation at the Lukens manufacturing facility.

A draft proposal detailing these steps was submitted to Lukens in August. Response has been positive with funding budgeted by Lukens for the project to begin in late 1992.

Laser Texturing of Prosthetic Implants XYZ Medical Company

At the suggestion of Lumonics, CSTAR contacted XYZ concerning the use of laser technology for the manufacture of prosthetic implants. These titanium components require complex machining and finishing operations to accurately reproduce damaged knee and hip joints.

The surface finish of the components can greatly effect the stability of the implant due to the interaction with the surrounding bone. A finish which would allow the bone to grow into the component could greatly enhance stabilization of the implant. Currently, a contractor is employed to manually place 0.005" diameter beads onto the component and then perform a sintering process to complete the finish. XYZ has reported that this process does not provide the stability nor spacing necessary to produce the desired finish.

CSTAR and XYZ have jointly conceived the concept for laser drilling holes into the component which would allow the desired bone growth to occur. A proposal is currently being developed at CSTAR for determining the feasibility of this concept through experimental, metallurgical, structural, and economic analysis. XYZ has agreed to this concept in principle and anticipates funding the project in early 1993.

Laser Cutting of Semi-Conductor Ceramics Physitron, Inc.

From a TVAR referral, CSTAR contacted Physitron to offer assistance with a ceramic cutting application. This manufacturer of semi-conductors was interested in conducting radiation testing of electrical components. Due to the design of the chip, it would be necessary to remove a 0.32" x 0.34" section of alumina ceramic material covering the electrical materials. In addition, the cut was required to maintain a tolerance of ± 0.010 " due to the location of sensitive semi-conductor components. These constraints make it difficult for most machining operations to remove the material without affecting the surrounding components. CSTAR identified the YAG laser as the appropriate tool and, through drill

trials, determined the correct parameters for this machining operation. The final product was machined by CSTAR and returned to Physitron within the specified tolerances.

Industrial Laser Teaming Program Micro Craft Incorporated

Previous discussions between CSTAR and MICRO CRAFT had revealed the following compatible interests in laser materials processing:

CSTAR:

- Transfer the laser materials processing technology available at CSTAR/UTSI to U.S. manufacturing industries.
- Develop teaming relationships with industry to increase CSTAR equipment and manpower capabilities.
- Acquire additional industrial sponsorship for the SAILS flight program.

MICRO CRAFT:

- Expand the MICRO CRAFT equipment and capabilities portfolio to include laser materials processing.
- Develop the expertise and determine the extent and nature of the laser materials processing market before investing in a complete laser facility.

The concept of combining the resources and expertise of CSTAR with some additional equipment and an applications engineer by MICRO CRAFT was developed from these discussions. CSTAR has submitted a proposal to MICRO CRAFT detailing options for the laboratory modifications and personnel requirements for this teaming relationship.

Laser Welding of Dissimilar Alloys Rocketdyne

Rocketdyne is interested in developing the technologies for laser welding of dissimilar, reflective alloys. Candidate designs for new rocket combustion chambers involve fabrication of laser welded joints for liners, closeouts and manifold rings. These involve a combination of alloys for which very limited weldability data is available. The ability to join these alloys will present opportunities to reduce

fabrication costs on aluminum structures found on SSF and other lightweight hardware.

Rocketdyne has committed to cost sharing with CSTAR in the investigation of techniques required to join these dissimilar materials. The project is scheduled to begin in November 1993.

Future Work (Program Phase 6)

Marketing

As described in Program Phase 6, the marketing effort is to be evaluated at the end of the year to refocus toward the most successful methods and revise the marketing materials as necessary. Based on the 1992 results, the most successful industry relationships were established from recommendations by CSTAR affiliates and will be one of the main methods for marketing during 1993. In addition, it was observed that the nuclear and medical industries have applications which are particularly suited to laser technology. These industrial areas will also be targeted during 1993.

Industry Projects

It is anticipated that the open industry projects described in the 1992 Accomplishments section of this report will be continued during the coming year.

Conclusion

This laser materials processing technology transfer program has been successful in both identifying and implementing a marketing strategy. The work accomplished in 1992 and projects anticipated for 1993 demonstrate the concept as a viable commercialization program. As a result of LIPP, several manufacturing industries are currently involved in implementing laser processing technology in their facilities.

Acknowledgements

This work is supported by CSTAR IR&D funds, the University of Tennessee Space Institute Center for Laser Applications, and Lumonics Industrial Products Division.

WELDER-LMP: A FAST-TRANSIENT, THREE DIMENSIONAL
COMPUTATIONAL MODEL FOR CONTINUOUS AND
PULSED HIGH-ENERGY-DENSITY WELDING PROCESSES

Dr. Arsev Eraslan*
ERAS, Inc.

Dr. T. Dwayne McCay**

ABSTRACT

A discrete element computational model containing the pertinent physics associated with the three phase processes inherent in deep penetration (keyhole) welding of metals and alloys has been developed and used to conduct preliminary computational experiments on pulsed laser welding. The results will be compared to physical results obtained on Inconel 718 using a high power CO₂ (10.6 μm wavelength) laser at The University of Tennessee Space Institute. This paper highlights the computer model and its basic attributes relative to prediction of real time occurrences within the weld pool and surroundings for laser keyhole welding.

The following provides a brief outline of the capabilities of the WELDER-LWP Code and describes the conditions for which it is applicable.

Simulation Capabilities:

- o Considers the time-accurate, fast-transient, three-dimensional (or axisymmetric) convection, which can predict the development of the "weld-cavity", throughout the continuous or pulsed high-energy-density laser-beam or e-beam welding process.

Constitution of the three (3)-Phase [solid-liquid-gas (vapor)] Metal:

- o Considers the metal as an "alloy-metal", in general, (a) consisting of different "constituent-metals", for studying meso/macro-scale segregation problems, based on "Constituent-fractions", or (b) consisting of a single-constituent metal;

- o Considers two (2) "states", as "solid-state and phase)" and "fluid-state (multi-phase)", associated with (a) each constituent-metal, and the alloy-metal, for studying meso/macro-scale segregation problems, based on "state-fractions", or (b) the alloy-metal as a single-constituent metal;

- o Considers two (2) "phases", as (a) "liquid-fluid-phase" and (b) "gas (vapor)-fluid-phase" of the

fluid-state (multi-phase), associated with (a) each constituent-metal, and the alloy metal, for studying meso/macro-scale segregation problems, based on "phase-fractions", or (b) the alloy-metal as a single-constituent metal.

Phase-transformation Conditions:

- o Considers "non-equilibria (kinetic)", as required for high-temperature-elevation-rate conditions, or "pseudo-equilibria (static)" "solidification-liquification phase-transformation", (a) for each constituent-metal, and the alloy-metal, metal, for studying meso/macro-scale segregation problems, based on state-fractions and constituent-fractions, or (b) for the alloy-metal as a single-constituent metal;

- o Considers "non-equilibria (kinetic)", as required for high-temperature-elevation-rate conditions, or "pseudo-equilibria (static)" "condensation-evaporation phase-transformation", (a) for each constituent-metal, and the alloy-metal, metal, for studying meso/macro-scale segregation problems, based on phase-fractions and constituent-fractions, or (b) for the alloy-metal as a single-constituent metal.

Thermophysical and transport properties of the metal:

- o Considers temperature-dependent "thermophysical and transport properties" for the solid-state (and phase) and the two (2) phases, as the

* Consultant to CSTAR and President of ERAS, Inc.

**UTSI Professor, CSTAR Principal Investigator

liquid-fluid-phase and the gas (vapor)-fluid-phase, of the fluid-state (multi-phase), associated with (a) each constituent metal, and the alloy-metal, for studying meso/macro-scale segregation problems, based on constituent-fractions, state-fractions and phase-fractions, or (b) the alloy-metal as a single-constituent metal.

Surface conditions on the weld-cavity:

- Considers physically realistic, "flex-surface" (deformable, elasto-plastic) conditions, for the surface of the weld-cavity, which incorporate, individually, and explicitly, (a) the surface-tension pressure, and (b) surface-tension-shear (Marangoni) stress;
- Considers physically realistic, temperature-dependent "surface-tension-coefficient" and surface-tension-rate-coefficient", which control the surface-tension-pressure and surface-tension-shear (Marangoni) stress effects, (a) for the liquid-fluid-phase of each constituent metal, and the alloy-metal, or (b) for the alloy-metal as a single-metal;
- Considers physically realistic, "vapor-venting" conditions from the surface of the weld-cavity, (a) for each constituent-metal, as segregated evaporation, associated with more volatile constituent-metals, for studying meso/macro-scale segregation problems, based on phase-fractions and constituent-fractions, or (b) for the alloy-metal as a single-constituent metal.

High-energy-density, laser-beam or e-beam heating conditions:

- Considers, accurately, the specified geometrical details of the "footprint", as (a) mode-00 (Gaussian), (b) mode-10 (two-peak) and (3) square (top-hat), for determining the "energy-deposition flux" on the surface of the weld-cavity;
- Considers, realistically specified, "absorbtivity factors", based on the solid-state, liquid-fluid-phase or gas (vapor)-phase of the alloy-metal, for determining the energy-absorption flux" through the surface of the weld-cavity;
- Considers optically transparent characteristics of the gas (vapor)-phase of the alloy-metal, which allows (a) for the penetration,

(completely or partially) of the high-energy-density, laser-beam or e-beam, through the surface, and through the vapor-core, and consequently, (b) for the controlling heating conditions to occur at the liquid-gas (vapor) interface, enclosing the vapor-core in the weld-cavity, within the footprint;

- Considers, accurately, the specified fast-transient energy-deposition conditions, associated with tailored-pulse or pseudo-continuous (with high-frequency variations) operational conditions of the high-energy-density laser-beam or e-beam.

Environmental conditions on the workpiece:

- Considers, explicitly, specified environmental-pressure conditions on the weld-cavity, which allows for simulations of the welding process, under the space conditions and with special-atmosphere conditions over the workpiece;
- Considers modeled, approximately but realistically, free-convection-cooling conditions, from the surface of the weld-cavity and from the surface of the workpiece, throughout the welding process, including the cooling period;
- Considers, approximately but realistically, the effects of the shielding-gas-flow conditions, including (a) the stagnation-pressure variation on the surface of the weld-cavity, (b) shear-stress, induced by the flow on the surface of the weld-cavity, and (b) forced-convection-cooling conditions, from the surface of the weld-cavity and the surface of the workpiece;
- Considers, approximately, surface-plasma-formation effects, over the surface of the weld-cavity, which can alter the footprint of the high-energy-density laser-beam or e-beam.

A detailed report on the WELDER-LMP Code is in preparation and should be available early in 1993.

omit

CSTAR FOCUS AREA:

CHEMICAL PROPULSION

·Advanced Nozzle Concepts

Dr. Frank Collins
Mr. Mark Jechura
Dr. Robert H. Nichol
Dr. Robert Tramel

·Space Shuttle Main Engine Propellant Path Leak Detection Using Sequential Image Processing

Dr. L. Montgomery Smith
Ms. J. A. Malone
Dr. B.W. Bomar
Dr. Roger Crawford

·Oxygen-Rich Combustion Devices

Mr. William H. Knuth
Dr. Roger Crawford
Mr. Paul Gloyer

·Liquid Rocket Spray Combustion Stability Analysis

Dr. Ron Litchford
Dr. San-Mou Jeng, University of Cincinnati

·A Numerical Simulation of Axisymmetric, Steady-State Plasma Flow Through MPD-Type Thrusters with Applied Magnetic Fields

Dr. Herbert Thomas
Dr. Randall Chapman
Dr. George Garrison

·Computation of Two-Phase Flow In Solid Rocket Motors

Dr. San-Mou Jeng, University of Cincinnati

ADVANCED NOZZLE CONCEPTS*

5740
P-36
Frank G. Collins**
Mark Jechura***
Robert H. Nichol†
Robert Tramel††Kyle Cooper‡
Finite Sims
Manchester, TN 37355CSTAR – Center for Space
Transportation and Applied Research
UTSI Research Park
Tullahoma, TN 37388-8897
(615) 454-9294 or 455-5884Robert Abel‡‡
Rocketdyne Division
Rockwell International Corporation
Canoga Park, CA 91303**Abstract**

Computations have been performed on the 1030:1 nozzle of NASA LeRC at three chamber pressures, 360, 260, and 100 psia. The equilibrium version of the PARC2D code, PARCEQ, had to be modified for these computations by adding surface fits to the thermodynamic and transport properties of a combusting gas. Critical comparison was made between the computations at 360 psia chamber pressure and the experimental measurements. Comparison was also made with TDK performance predictions. The flow changed very significant at 100 psia. This latter case would be a good test of the TDK methodology. A low Reynolds number nozzle was also computed to provide a second test of the TDK methodology.

Computations were performed of the Calspan film cooling experiments using the Molvik Navier – Stokes code. Since the film cooling nozzle flow is three-dimensional but only a two-dimensional computation was performed, the computations and measurements did not agree in the region immediately downstream of the injection nozzle exit plane. Computations were initiated on the flow field within the subscale STME nozzle.

An altitude compensating nozzle concept was examined.

A. NASA LeRC 1030:1 Nozzle Computations

NASA LeRC 1030:1 hydrogen/oxygen nozzle experiments offered the opportunity to compare measurements, full Navier–Stokes computations, and TDK predictions under conditions where it had previously been suspected that TDK calculations

failed to reproduce the measurements [1]. One of the tests (Reading 112) was chosen for initial computations since it had previously been identified as having a laminar boundary layer throughout the nozzle [2].

The nozzle flowfield was computed using a modified version of PARCEQ which included surface fits for the thermodynamic and transport properties of the combusting hydrogen/oxygen mixture. Reading 112 was performed at an oxidant to fuel mixture ratio of 3.84 and chamber pressure of 360 psia. Saladino [3] developed an option in PARCEQ to compute the thermodynamic and transport properties of the combusting gas using statistical mechanics and kinetic theory. This program, as modified by Klomfass [4], was used to compute tables of the mixture properties $T(p,e)$, $p/p(p,e)$, $k(p,e)$, $\mu(p,e)$ and $c_p(p,e)$. The symbols

*This work was supported by Rocketdyne Division, Rockwell International and NASA Headquarters Grant NAGW-1195, NASA Headquarters, Washington, D.C. 20546

**Principal Investigator, Professor of Aerospace Engineering, The University of Tennessee Space Institute.

***UTSI GRA, presently Calspan Corporation/AEDC Operations.

†Calspan Corporation/AEDC Operations.

††Calspan Corporation/AEDC Operations.

‡Consultant.

‡‡Rocketdyne Technical Monitor.

have the following meaning: T is temperature, ρ is density, e is specific internal energy, p is pressure, k is thermal conductivity, μ is coefficient of viscosity, and c_p is the specific heat. Accurate surface fits to these properties can be obtained by introducing the transformations

$$x = \frac{e}{10^6}$$

$$y = \log_{10} \rho$$

The specific internal energy was referenced to 1 MJ/kg at 100 K and 1.25 kg/m³ to make sure that β , the ratio of the enthalpy to the internal energy, is always positive.

The resulting surface fits are shown in Figure A1 to A5. All of the surface fits agreed well with the calculated properties except for k and c_p in the low energy range, as shown in Figures A6 and A8. Since both k and c_p were independent of ρ in the low energy range, they were fitted as a function of temperature from 100 K to 1000 K, Figures A7 and A9. These fits were then incorporated into the code and were called when the temperature fell below 1000 K. It should be noted that TDK has a lower limit of 250 K, whereas PARCEQ is valid to 100 K.

GRIDGEN was used to construct a 195 by 80 grid for the prediction of the nozzle performance parameters. The grid was constructed to simulate both the nozzle and the test cell, Figure A10. The nozzle coordinates came from shop measurements and were supplied by Albert J. Pavli [5]. By including the test cell as part of the grid, specification of the subsonic outflow pressure boundary condition was avoided. This gives a more realistic calculation, improves exit plane accuracy and eliminates the need for a nozzle extension as was previously used by Orr [6].

The first points of the grid starting at the area ratio were $M \approx 0.3$, as determined using one-dimensional isentropic theory. The grid extended above the nozzle wall and downstream of the exit plane of the nozzle by the length of the exit plane nozzle radius. The grid was constructed this way to capture any expansion or compression shocks that may occur at the nozzle lip.

Because fine resolution of the boundary layer is not necessary for performance prediction, the grid packing toward the nozzle wall was only tight enough to maintain at least three points inside the subsonic portion of the boundary layer. To maintain accuracy for the axisymmetric calculation, the grid was mildly packed to the axis. A second grid concentrated near the wall was used for wall heat transfer computations.

The wall temperature profile used as the wall temperature boundary condition input was determined from a curve fit of estimated wall temperature in the region where wall temperature was not measured and experimentally determined inner wall temperature in the region where the nozzle outer wall temperature was measured [7]. During the test firing, the outer wall temperature of the nozzle was measured at 12 area ratio locations.

Examinations of the experimentally determined inner wall temperatures revealed a slight scatter of the data. The temperatures followed a zig-zag pattern alternating from 6 – 8 K increase in wall temperature to a 6 – 10 K decrease in wall temperature from point to point along the last 80 cm of the nozzle. Although some data scatter is expected, the fluctuations in temperature along the nozzle wall seem to indicate the outer wall was not

adiabatic as assumed and quite possibly the measurements were in error as well.

Since the first thermocouple for wall temperature measurement was located 2.193 cm downstream of the throat, nozzle wall temperatures upstream of this point had to be estimated. The inputs for TDK from [7] were initially used to estimate the wall temperatures in this region. However, using these temperatures, flow heating by the nozzle wall in the throat region was observed. The inputs to TDK were then thoroughly examined to determine if they were a reasonable estimation. Examination determined that the temperatures used were high, particularly in the water cooled throat region where a wall temperature of 2250 K was estimated. The TDK wall temperature estimation was then abandoned for a more reasonable temperature estimation in the throat region. Since there was a copper insert in the throat during the test firing [8], a temperature of 1100 K was used at the throat

(information was later obtained that the throat was actually made of nickel as previously mentioned, however, the temperature estimation was still not a bad approximation). This temperature, which is 258 K lower than the melting point of copper [9], seemed to be a reasonable estimation because the temperature in the throat region should have been high but not high enough to melt the copper insert. A nozzle wall temperature of 800 K was estimated upstream of the throat near the first point of the computational grid. This temperature was estimated because upstream of the throat the wall temperature must remain high since it is not far downstream from the combustion chamber, but it still must remain low enough to allow the wall temperature to peak at the throat. Both estimations of wall temperature were further justified after computations were performed and observation of the flow field showed that the flow heating by the wall was eliminated.

Having established a temperature distribution along the wall using the experimentally determined wall temperatures and the estimated wall temperatures, the data points were curve fit. Lagrange second and third order polynomials [10] were used to approximate the first six points and a cubic polynomial was used to approximate the remaining eight points, Figure A11. The cubic polynomial for the last eight points was fitted through the data to remove the scatter occurring over the last 80 cm of the nozzle. Using these polynomials and the computational grid, the wall temperature at each grid point was calculated for input as the wall temperature boundary condition.

To start the computations, one-dimensional theory was used upstream of the throat and a low velocity, low temperature, low pressure condition was specified downstream of the throat and in the test cell.

Two computations were run to predict the performance of the 1030:1 nozzle. One computation was performed with the adiabatic flame temperature assuming 100% combustion. The other computation was performed assuming incomplete combustion. The combustion chamber temperature for the incomplete combustion calculation was determined to be 2790 K using a characteristic exhaust velocity efficiency, η_c of 95.5%. The two computations were

labeled Case I and Case II for the complete combustion calculation and the incomplete combustion calculation, respectively.

A small region of separation was observed at the nozzle lip of each flow field, caused by some inflow into the nozzle from the test cell at the nozzle lip. This was eliminated by reducing the test cell ambient pressure 10% below the last data point taken on the nozzle wall and then gradually increasing the pressure back up to the measured test cell ambient pressure. This technique eliminated the inflow into the nozzle. Final convergence was determined by examining plots of mass flow rate through the nozzle, nozzle wall pressure, nozzle wall heat flux and the performance parameters for change with an increasing number of iterations. All changes in these plots were minimal and a converged steady – state solution inside the nozzle was achieved after 10,000 total iterations for Case I and after 9000 total iterations for Case II for laminar flow.

The laminar performance parameters calculated for Case I and Case II are compared in Table A1 with the test measurements and the calculated results with TDK. Case I and II bracket the test measurements. This seems to indicate that there probably is incomplete combustion occurring in the combustion chamber.

The Mach number contours for Cases I and II are shown in Figures A12 and A13, respectively. The contours show that a weak shock emanates from the throat region and a compression shock emanates from the nozzle lip. The internal shock is caused by the second derivative discontinuity near the throat. The external shock occurs because the flow leaving the nozzle is at a lower pressure than the flow in the test cell. The observance of the external shock was very satisfying because this shock was expected.

Boundary layer profiles for velocity and temperature near the exit plane for both cases are shown in Figure A14, Figure A15 and Figure A16. The viscous boundary layer profiles were as expected for two dimensional nozzle flow. The thermal boundary layer profiles show that the temperature of the flow increases away from the wall, reaches a peak and then decreases from the peak to the axis of the nozzle. This profile is as expected for cold wall nozzle flow.

Plots of calculated wall pressure compared to measured wall pressure are shown for both cases in Fig A17. The calculations are slightly lower than test data which seems to indicate that γ_e or T did not quite match the test conditions.

A new grid was used to compute the wall heat flux. Although previous performance computations revealed that most probably incomplete combustion occurred in the combustion chamber (see Table A1), computations were only performed assuming 100% combustion.

To obtain higher resolution of the boundary layer, a new grid with the packing ten times closer to the wall was constructed. For simplicity, the test cell cavity was removed from the grid and replaced with a 19 cm nozzle extension. The nozzle extension was simulated with a 16 by 60 mesh. The resulting computational grid simulating both the nozzle and the nozzle extension was a 180 by 60 mesh, Figure A18.

Heat flux calculations were made with artificial dissipation inside the boundary layer, with artificial dissipation removed inside the boundary layer and using Reynold's Analogy. The results of these calculations were then compared to the experimentally determined heat flux.

The experimentally determined heat flux for Reading 112 was obtained from the outer wall temperature measurements through a solution of the radial energy equation. Constant wall properties, no axial or circumferential conduction, adiabatic outer wall and a linear rate of temperature rise were assumed [7].

The heat flux was calculated by discretizing the heat equation

$$q_w = -k \left(\frac{\partial T}{\partial n} \right)_w$$

Artificial viscosity was removed completely for the first four points off the wall and scaled to its normal value over the next eleven points using a hyperbolic tangent scaling factor [11].

Finally, the wall heat flux was calculated by applying Reynold's Analogy to the flow field that had artificial dissipation removed inside the

boundary layer. The analogy states that for fully turbulent boundary layer flows over a flat plate with $Pr = 1$ and constant ρ , μ and k that $C_f \approx 2C_h$ [12]. Combining the forced convection equation for wall heat flux

$$q_w = h (T_{aw} - T_w)$$

the equation for the adiabatic wall temperature

$$T_{aw} = T_\infty + \frac{r U_\infty^2}{2 C_p}$$

and Reynold's Analogy

$$C_f = \frac{2 \tau_w}{\rho U_\infty^2} \approx C_h = \frac{h}{C_p \rho U_\infty}$$

an equation for wall heat flux can be developed

$$q_w = \frac{\tau_w C_p}{U_\infty} (T_\infty - T_w) + \frac{1}{2} r \tau_w U_\infty$$

For laminar flows with $0.1 \leq Pr \leq 3.0$, the recovery factor, r , can be approximated by $Pr^{1/2}$ [12]. Thus, using the above developed equation for the calculation of heat flux and the assumption for recovery factor, the wall heat flux was calculated at three locations along the nozzle wall.

The results of the three methods for the prediction of wall heat flux are compared with the experimentally determined wall heat flux in Figure A19. Note that the computational predictions of wall heat flux are significantly lower than the experimentally determined wall heat flux, whereas, the predictions by Reynold's Analogy are higher than the experimentally determined heat flux.

After completing the laminar flow calculations on the NASA LeRC 1030:1 nozzle, a new grid was constructed and turbulent calculations were performed using the Baldwin-Lomax Algebraic Turbulence Model [13]. The new grid was identical to that used for the laminar wall heat flux computations except that the grid cell packing was two times closer to the nozzle wall. The adiabatic flame temperature ($T_c = 3059$ K) used in the laminar calculations was used to simulate conditions inside

the combustion chamber. The same combustion chamber conditions were chosen in order to maintain consistency with the laminar calculations previously performed. The initial conditions for the nozzle flow field consisted of a combination of one dimensional isentropic theory from the nozzle inlet to the nozzle throat region and a low pressure, low temperature, low velocity condition from the nozzle throat region to the nozzle exit.

After initializing the flow field, 3000 iterations were run assuming laminar flow to progress the solution past the non-physical stages of the convergence process. Once a flow field resembling the steady state solution was established, the turbulence model was turned on. Additional iterations were then run to allow the turbulent boundary layer to fully converge. The boundary layer was examined every 5,000 iterations for changes in thickness and pressure. Approximately three points were observed inside the subsonic boundary layer along the entire nozzle wall. After running 27,000 additional iterations, no changes in the performance parameters or growth of the boundary layer were observed. Using this information as a basis, the turbulent boundary layer was assumed to be fully developed.

Next, additional iterations were run to remove the artificial dissipation inside the boundary layer. For the turbulent calculations, the artificial dissipation was removed between the eighth and fourth grid points off the wall. During these additional iterations, the performance parameters, the boundary layer and the nozzle wall heat flux were all monitored for changes. After an additional 25,000 iterations, no changes in the performance parameters, boundary layer or the wall heat flux were observed. The solution was therefore assumed to be fully converged after 55,000 total iterations.

The results of the calculations are shown in Table A2 and Figure A20. In Table A2, the turbulent performance results are compared to the previously calculated laminar results test data [14] and TDK (Two Dimensional Kinetics Code) [1]. In Figure A20, the predicted turbulent nozzle wall heat flux is compared to the predicted laminar wall heat flux and the experimentally determined wall heat flux [14]. The results, which show that the flow was most likely transitional, contradict findings published by Smith [15] which state that the flow in the nozzle was laminar.

A second reason for examining the 1030:1 nozzle, other than careful comparison with experiment, was to find a flow field where the TDK methodology could be expected to fail. This nozzle, operating under different conditions, was examined as a candidate for this comparison.

As a first step, the assumed wall temperature profile was modified to make it correspond more closely to that observed in the SSME nozzle. The new assumed wall temperature distribution is shown in Figure A21.

Laminar and turbulent computations, using the same procedures described above, were obtained at assumed chamber pressures of 260 and 100 psia. Only modest changes in the flow field and performance were observed at 260 psia, compared to 360 psia (see Figure A22 and Table A2). However, major changes were observed at a chamber pressure of 100 psia. Comparison of the Mach number contours of Figures A23 and A13 indicate thickening of both the shock wave and of the boundary layer. Compared to the 360 psia case (Figure A14), the exit Mach number profile is no longer relatively uniform outside of the shock wave (Figure A24) and the boundary layer is thicker (compare Figures A22 and A25). This results in a wall heat flux that is closer to the turbulent prediction for $p_c = 360$ psia near the throat but is more like the laminar prediction at the nozzle exit (Figure A26). This case will be examined using the TDK methodology in the future.

B. Low Reynolds Number Nozzle

One of the tasks was to find nozzle flows where the TDK methodology might be expected to fail and to make comparison between TDK predictions and full Navier-Stokes computations. In 1984 some unpublished measurements were performed at NASA MSFC on a small 40:1 nozzle using CO_2 as the gas. The chamber pressure and temperature were 7.4 psia and 588.9 K, respectively. The geometry of the nozzle is shown in Figure B1. Navier-Stokes computations for this flow are described in this section. The computations were completed too late to perform the TDK comparison and that will be completed later.

Carbon dioxide is an interesting molecule because it has three low-lying vibrational states with characteristic temperatures of 960.3 K, 1997.5 K, and 3380.5 K. This means that γ varies from 1.215 to approximately 1.34 through the nozzle while the composition does not change. Computing this flow field required modifying the surface fit form of PARCEQ, which was described in the previous section. Specifically, statistical mechanics provides simple expressions for C_p and γ . In addition $\gamma = \beta = h/e$. In other respects the gas behaves as a perfect gas of fixed composition. Therefore, all surface fits were replaced with the statistical mechanics expressions and a perfect gas representation was used. The Sutherland law was used for both μ and k .

An appropriate computational grid was generated using GRIDGEN. A short extension was added to the nozzle to obtain an accurate representation of the nozzle exit plane properties. The entire plenum chamber was retained in the computation. The adiabatic flame temperature computation provision of PARCEQ was used to start the computation. This essentially places stagnation conditions throughout the nozzle and has the effect of bursting a diaphragm at the nozzle exit upon initiation of the computations. The exit pressure had to be increased an order of magnitude for the first 1000 iterations and then lowered to a value of 0.0077 psia. Because of the low Reynolds number only laminar computations were performed and the wall was assumed to be adiabatic. Artificial dissipation was removed from the boundary layer as the computations neared convergence. In addition, the PARC parameter DIS4 was reduced to 0.25 and DIS2 to 0.00 and artificial dissipation was removed within the boundary layer. The overall nozzle performance is given in Table B1. Mach number contours in the nozzle are shown in Figure B2. The thickness of the boundary layer is apparent from the contours. The exit Mach number profile, Figure B3, shows that the profile is relatively flat until the edge of the boundary layer is reached. The boundary layer thickness is roughly one-fourth of the nozzle radius (Figure B4). Thus, very strong viscous-inviscid interaction is occurring within this nozzle which cannot be treated by standard boundary layer techniques.

The only property measured for this nozzle was the wall pressure. The computed pressure distribution

throughout the entire nozzle is shown in Figure B5. Comparison is made between the measured and computed wall pressure near the nozzle exit in Figure B6. The difference between the measured and computed values is presently under investigation.

This nozzle flow appears to be an ideal candidate for comparison with the TDK methodology. That comparison will be made later.

C. Film Cooled Nozzles

Computation of the Rocketdyne NASP film cooling experiments was described in the previous CSTAR Annual Technical Symposium [16]. During the present year computations of the Calspan (Holden) film cooling experiments were completed and computation of the flow field in the subscale STME nozzle was initiated. These computations will be described in this section.

The Calspan experiments [15] were performed on a sharp-edge flat plate that was placed in the CUBRC (Calspan / University of Buffalo Research Center) 48" Hypersonic Shock Tunnel (48" HST). The model configuration is given in Figure C1 and the test conditions are given in Table C1.

The sharp-edge flat plate was 32.28 in. from the leading edge to the rearward facing step. The model continued for about 20 in. downstream from the step. Forty two-dimensional supersonic nozzles exited through the flat face of the step. The model was instrumented with 45 heat flux gages and 25 pressure gages. The freestream consisted of air at a nominal Mach number of 6.4 and total temperature of 2180 R. The boundary layer naturally transitioned upstream of the step and had an approximate thickness of 0.44 in at the slot location. The boundary layer profile and thickness were not directly measured but instead were inferred from a boundary layer analysis and experimental flow visualization. A more precise velocity and temperature determination would have been preferred.

The film cooling nozzles were two-dimensional with a throat of 0.120 in., an exit of 0.404 in and a height of 0.120 in. The nozzles had been designed by the

method of characteristics with a displacement thickness correction. The design assumed that the nozzles were two-dimensional but their finite height makes their flowfield very three-dimensional. Thus, while they were designed to deliver a uniform film of helium at a Mach number of 3, computations by members of the Combustion Devices Technology Team [17] indicated that the flow is very three-dimensional and a more realistic average exit Mach number is 2.71.

The wall heat flux measurements had an estimated uncertainty of 5%. Uniform flow occurred for approximately 8 msec and all data were averaged over 2 msec. Initially measurements were made on the flat plate alone. The measured wall heat flux on the flat plate was fit with the following formula

$$\dot{Q}_w = (9.14 - 0.119x + 0.0034x^2) \text{ BTU/}$$

where x is measured in feet downstream from the slot location. The measured wall pressure distribution was approximately flat downstream of the slot location.

The measurements continued with the addition of the film cooling nozzles. First, pressure and heat flux measurements were made with zero coolant flow (Test 43), in a configuration representative of a back-ward facing step. Locally the wall heat flux increased at the reattachment shock (about 0.5 in. downstream), followed by a reduced heating region and a return to the flat plate value at about 8 in. downstream from the step. This test was followed by tests with three different coolant flow rates representing overexpanded, matched and underexpanded flows (Tests 44, 45, and 46).

The flow was computed using the Molvik Navier-Stokes code [18]. The code uses upwinding, TVD techniques and uses a finite-volume approach. Interface fluxes are computed with a temporal Riemann solver. The schemes are fully implicit with a strong coupling between the fluid dynamic and chemical equations. It can be run in a perfect gas, equilibrium or nonequilibrium mode. This code was modified by R. Nichols to include the two-equation $k - \epsilon$ turbulence model [19]. The code was run assuming a mixture of two non-reacting gases.

The computations began with the upstream flat plate section, using a 31×61 grid. The purpose of this computation was to verify the correct upstream boundary layer development. The grid was clustered next to the wall and at the downstream boundary where the flow meets the step. The region downstream of the step was computed as a separate zone with a 81×121 grid. The grid was clustered near the wall, in the region of the mixing layer and on the upstream boundary.

The computed wall heat flux for the non-flow case (Test 43) is given in Figure C2 and the pressure in Figure C3. This no-flow case is representative of a classical rearward facing step, with recirculating flow just downstream of the step. There is a sudden pressure drop downstream of the step followed by rapid increase of pressure in the reattachment region. The heat flux has a low value in the recirculating region but rapidly increases as the turbulent flow attaches to the plate. The computed heat flux is in good agreement on the flat plate, upstream of the step, and in the separated region downstream. The computed values are somewhat higher than the measurements downstream of reattachment but exhibit a trend similar to the measurements. Notice that there is large scatter in the experimental data, even though the advertised experimental accuracy was 5%. The computed pressure distribution also is in good agreement with the measurements. However, notice the very great amount of experimental scatter.

The present turbulence model uses a low Reynolds number formulation of the two-equation $k - \epsilon$ closure, corrected for compressibility effects. In this model integration is carried right down to the wall.

The computations for the film cooling Tests 44, 45, and 46 with helium as the cooling media were performed as follows. Although it is known that the flow through the nozzles is three-dimensional, two-dimensional exit properties were assumed. The assumed velocity and temperature profiles are shown in Figures C4 and C5, respectively.

A comparison between the computational and experimental heat flux measurements for flows with increasing helium cooling flow rate, Tests 44, 45, and 46, are shown in Figures C6, C7, and C8. Experimentally the cooling effectiveness increases as the helium flow increases (Figure C9). However,

the computations show only a moderate improvement with increasing helium mass flow (Figure C10). The region immediately downstream of the nozzles is incorrectly computed for all cases because two-dimensional flow was assumed. CSTAR does not have the computer facilities required to perform a full three-dimensional computation of these tests. The computed results compare favorably with the measurements for the lowest helium mass flow but deviate at the higher mass flows, underpredicting the effectiveness of the film cooling.

Pratt and Whitney has been given the task of developing a film cooled STME engine. Initial tests will be made on a subscale nozzle. Members of the Combustion Devices Technology Team have been asked by NASA MSFC to validate their codes using the Calspan (Holden) data set and then use the validated code to compute the flowfield in the subscale STME nozzle. The nozzle coordinates and operating characteristics have been supplied by Pratt and Whitney to the Team. Some nozzle characteristics are given in Table C2.

The subscale nozzle configuration is shown in Figure C11. The nozzle will be attached to an existing calorimeter chamber. Subsonic cooling, as shown in Figure C12, will be applied to protect this chamber. In addition, there will be a supersonic film injected in the usual fashion parallel to the nozzle wall.

The computations were initiated using the Molvik Navier-Stokes Code, assuming a mixture of reacting gases. Two-dimensional flow was assumed to exit each of the cooling slots. The computations used the initial composition and exit conditions shown in Figure C13. The computation grid is shown in Figures C14 and C15. It consisted of three portions of size 59 x 99, 60 x 129 and 110 x 159. The computations proceeded as follows. The flowfield inside the nozzle was initialized based on one-dimensional flow. The area ratio at each x station of the grid was used with the ratio of specific heats (γ) to determine the local Mach number. The local Mach number, density, and temperature were input to the gas properties subroutine in the Molvik code, NEQPAK, to determine the total energy. The normal hydrogen jet was initialized at the injector conditions. The velocity was assumed to turn downstream so that the hydrogen velocity was

parallel to the rocket velocity at the edge of the base. The tangential hydrogen wall jet was initialized at the injector conditions. These computations were being performed on CSTAR's IBM RISC 550 computer. However, this computer was determined to be too slow to converge the solution in a reasonable length of time (less than three months) and the computations were not continued.

References

1. Smith, T. A., Pavli, A. J., and Kacynski, K. J., "Comparison of Theoretical and Experimental Thrust Performance of a 1030:1 Area Ratio Rocket Nozzle at a Chamber Pressure of 2413 kN/m² (350 psia)," AIAA-87-2069, AIAA/SAE/ASME/ASEE 23rd Joint Propulsion Conference, June 29 - July 2, 1987.
2. Smith, T. A., "Boundary Layer as a Function of Chamber Pressure in the NASA Lewis 1030:1 Area Ratio Nozzle," AIAA-88-3301, AIAA/ASME/SAE/ASEE 24th Joint Propulsion Conference, July 11 - 13, 1988.
3. Saladino, A. J., "Equilibrium Real Gas Upgrade and Restructure of the Perfect Gas PARC2D Code Using the Partition Function Approach for the Thermochemical Properties and Kinetic Theory for the Transport Properties," Phd. Dissertation, The University of Tennessee, Knoxville, Tennessee, December, 1989.
4. Klomfass, A., "Incorporation of Thermodynamic and Transport Properties of General Gas Mixtures into Navier-Stokes codes," The University of Tennessee Space Institute Center for Advanced Space Transportation, April, 1991.
5. Pavli, A. J., NASA LeRC, Interview, October 2, 1991.
6. Orr, J. L., "SSME Nozzle Flow Field Calculations Using PARC CFD Code," M.S. Thesis, The University of Tennessee, Knoxville, Tennessee, December, 1989.
7. Kacynski, K. J., Pavli, A. J., and Smith, T. A., "Experimental Evaluation of Heat Transfer on a 1030:1 Area Ratio Rocket Nozzle," AIAA/SAE/ASME/ASEE 23rd Joint Propulsion Conference, June 29 - July 2, 1987.

8. Jankovsky, R., NASA LeRC, Interview, January 14, 1992.
9. Incropera, F. P., and DeWitt, D. P., Fundamentals of Heat Transfer and Mass Transfer, Second Edition, John Wiley & Sons, Inc., New York, 1985.
10. Burden, R. L., and Faires, J. D., Numerical Analysis, Fourth Edition, PWS-KENT Publishing Company, Boston, 1989.
11. Jechura, M. C., "Equilibrium Hydrogen-Oxygen Flow Field Calculations of a High Area Ratio Nozzle Using Full Navier-Stokes Code," M.S. Thesis, University of Tennessee, May, 1992.
12. White, F. M., Viscous Fluid Flow, McGraw-Hill Publishing Company, New York, 1974.
13. Baldwin, B. and Lomax, H., "Thin-Layer Approximation and Algebraic Model for Separated Turbulent Flows," AIAA Paper 78-257, Huntsville, Alabama, January, 1978.
14. Pavli, A. J., Kacynski, K. J., and Smith, T. A., "Experimental Thrust Performance of a High-Area-Ratio Rocket Nozzle," NASA Technical Paper 2720, April, 1987.
15. Olsen, G. C., Nowak, R. J., Holden, M.S., and Baker, N. R., "Experimental Results for Film Cooling in 2-D Supersonic Flow Including Coolant Delivery Pressure, Geometry, and Incident Shock Effects," AIAA 90-0605, January, 1990.
16. Collins, F. G., et al, "Advanced High Area Ratio Nozzles," Proceedings of the CSTAR Third Annual Technical Symposium, January 14 - 15, 1992.
17. Chen, Y. S. and Cheng, G. C., "CFD Modeling of Film Cooling Test Cases," presented at Combustion Devices Technology Team meeting, NASA MSFC, November 7, 1991.
18. Molvik, G. A., "A Computational Model for the Prediction of Hypersonic, Reacting Flows," PhD dissertation, Penn. State Univ., December, 1989.
19. Nichols, R. H., "A Two-Equation Model for Compressible Flows," AIAA-90-0494, January, 1990.
20. Steinbrenner, J. P., Chawner, J. P., and Fouts, C. L., "The GRIDGEN 3D Multiple Block Grid Generation System," Volume II, WRDC-TR-90-3022, Flight Dynamics Directorate, Wright Laboratory, Dayton, Ohio, 1990.

TABLE A1: 1030:1 Nozzle Performance Computations Reading 112 Conditions

Case	Mass Flow Rate (kg/s)	Vacuum Thrust (N)	Vacuum Specific Impulse (s)
PARCEQ with $T_c = 3059$ K	0.5026	2427	492.9
PARCEQ with $T_c = 2790$ K	0.5312	2389	459.1
TDK	0.5034	2383	482.7
Test Data	0.5266	2422	468.9

TABLE A2: 1030:1 Nozzle Performance Computations Comparison

Chamber Pressure	Flow Condition	Adiabatic Flame Temp. (K)	Mass Flow Rate (kg/s)	Vacuum Thrust (N)	Vacuum Isp (s)
2482 kPa	Laminar	3059	0.5026	2427	492.9
	Turbulent		0.4976	2326	477.1
1579 kPa	Laminar	3019	0.2761	1339	494.9
	Turbulent		0.2777	1298	477.0
689.48 kPa	Laminar	2970.88	0.1392	531.56	389.6
	Turbulent		0.1373	510.2	379.2

TABLE B1: Low Reynolds Number Nozzle Performance Computations

Mass Flow Rate (lbm/s)	Thrust (lbf)	Specific Impulse (s)
2.135×10^{-3}	0.1822	85.31

TABLE C1: Test Conditions For Calspan Film Cooling Tests

Freestream Mach Number	6.43
Slot Height	0.120 inches
Tip Thickness	0.020
Coolant Stagnation Temperature	530 R
Wall Temperature	540 R

TEST	Stagnation Pressure Psia	Stagnation Temperature R	Static Pressure Psia	Coolant Mass Flow/Nozzle Slug/Sec	Exit Plane Pressure Psia
43	2671	2181	1.0879	0.0	
44	2623	2188	1.0697	4.640×10^{-5}	0.8191
45	2486	2157	1.0138	6.644×10^{-5}	1.042
46	2640	2198	1.0739	1.077×10^{-4}	1.498

TABLE C2: Subscale STME Nozzle Conditions

Chamber Pressure	2250 psia
Chamber Temperature	6708 R
O/F	7.2
Gamma	1.1358
Supersonic Hydrogen Exit Mach Number	1.454
Supersonic Hydrogen Static Pressure	48 psia
Supersonic Hydrogen Film Mass Flux	1.51 lbm/sec

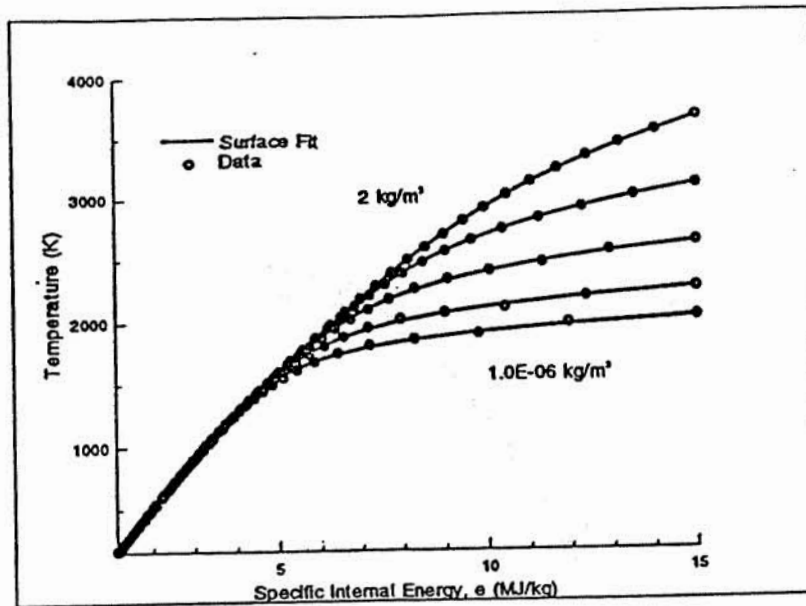


Figure A1 - Surface fit for temperature, $T(\rho, e)$, $O/F = 3.84$.

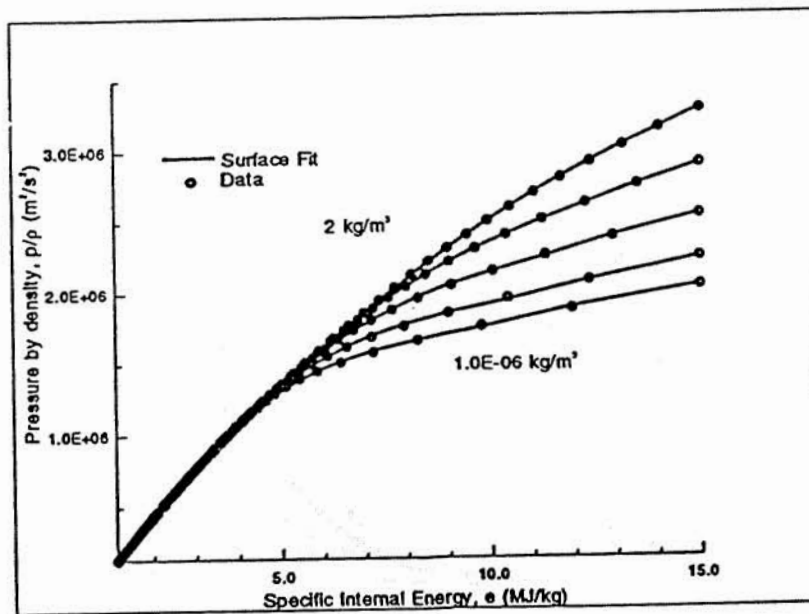


Figure A2 - Surface fit for pressure by density, $p/\rho(\rho, e)$, $O/F = 3.84$.

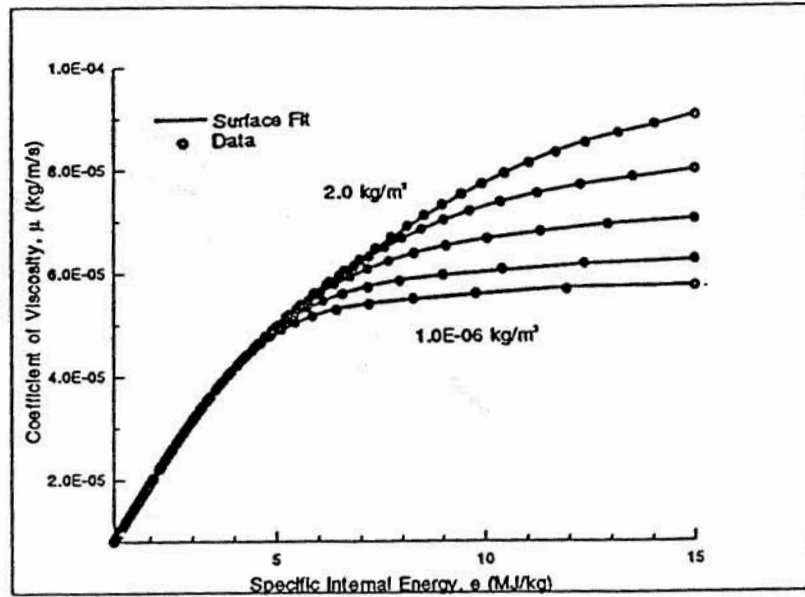


Figure A3 - Surface fit for coefficient of viscosity, $\mu(\rho, e)$, $O/F = 3.84$.

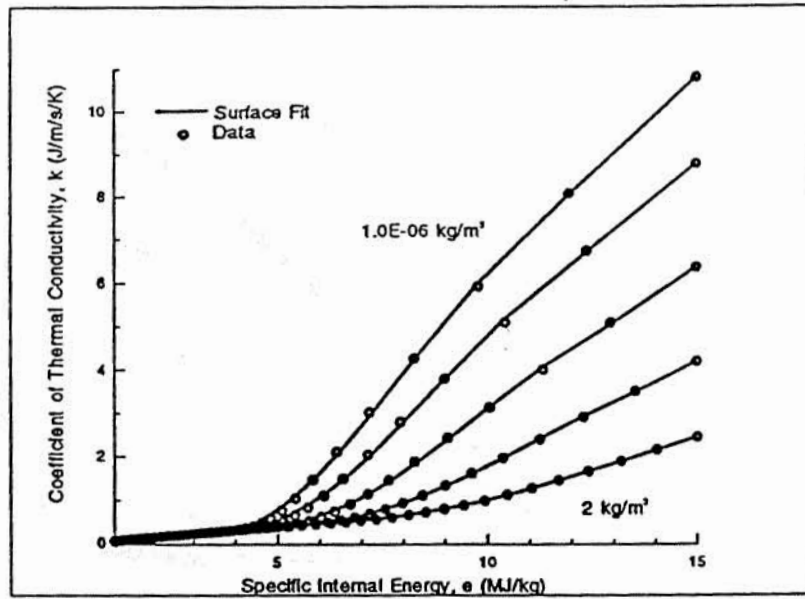


Figure A4 - Surface fit for coefficient of thermal conductivity, $k(\rho, e)$, $O/F = 3.84$.

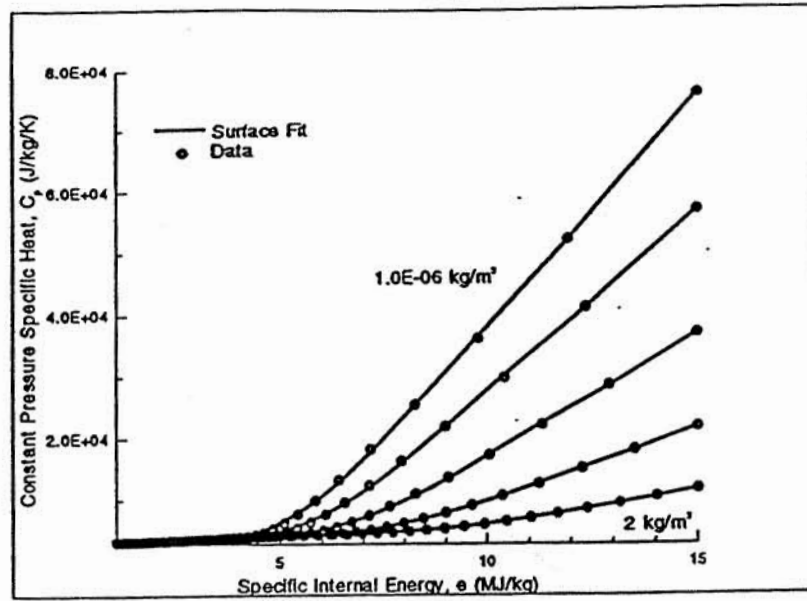


Figure A5 - Surface fit for constant pressure specific heat, $C_p(\rho, e)$, $O/F = 3.84$.

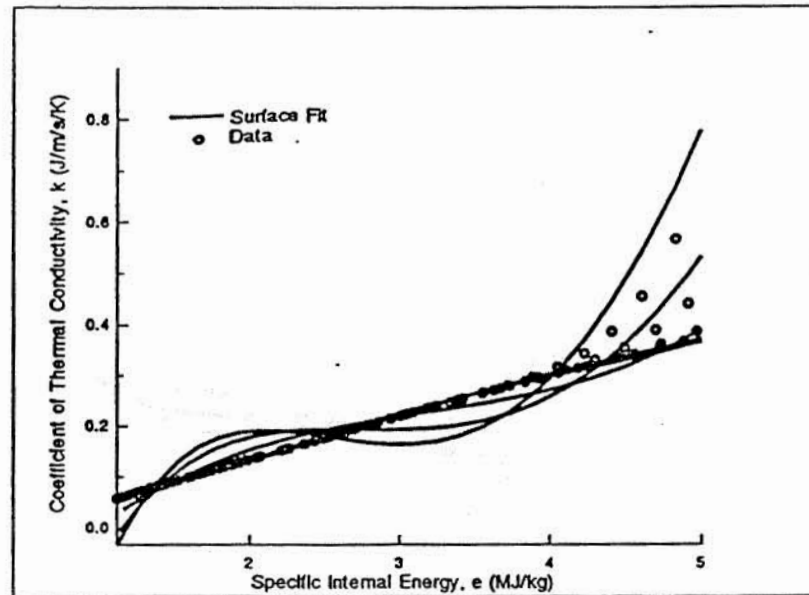


Figure A6 - Surface fit for $k(\rho, e)$ in the low e range, $O/F = 3.84$.

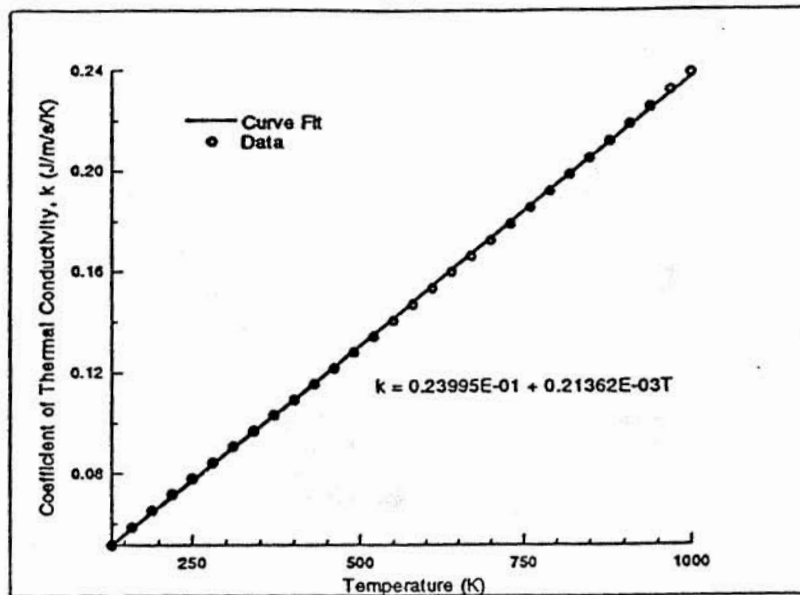


Figure A7 - Curve fit of $k(T)$ for $100 \text{ K} < T < 1000 \text{ K}$, $O/F = 3.84$.

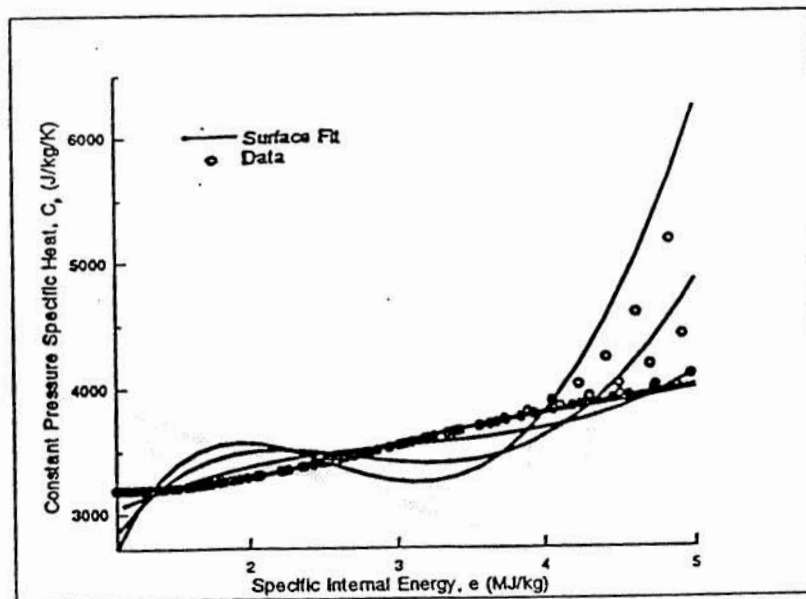


Figure A8 - Surface fit for $C_p(\rho, e)$ in the low e range, $O/F = 3.84$.

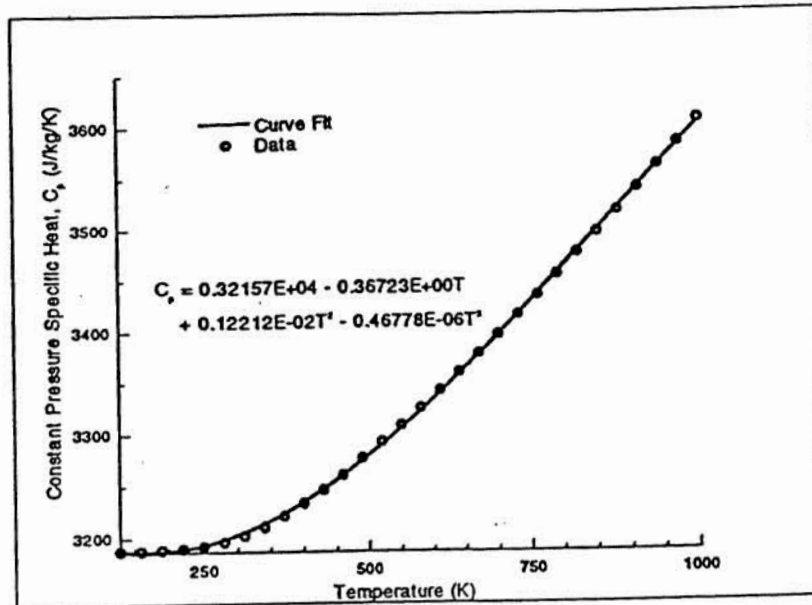


Figure A9 - Curve fit of $C_p(T)$ for $100 \text{ K} < T < 1000 \text{ K}$, $O/F = 3.84$.

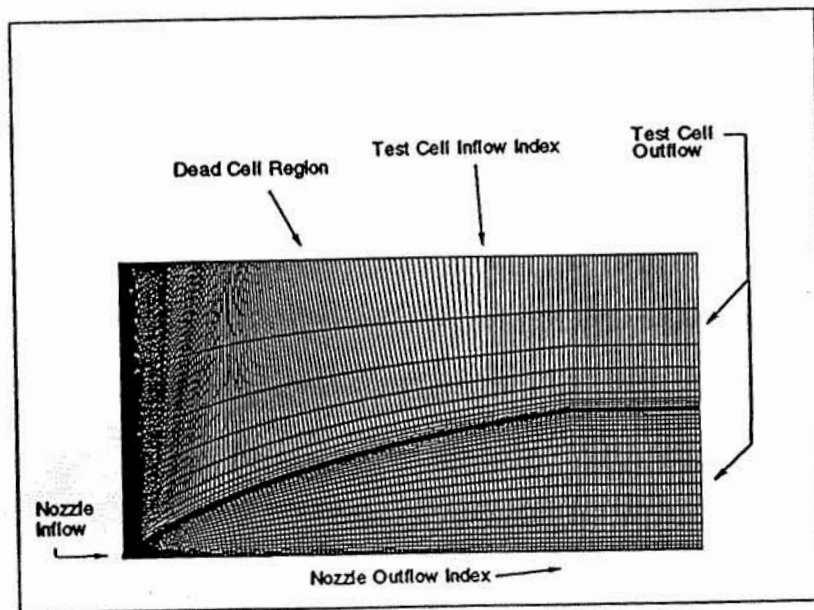


Figure A10 - Computational grid used for the performance calculations, 1030:1 NASA LeRC nozzle (every other point plotted in the radial direction).

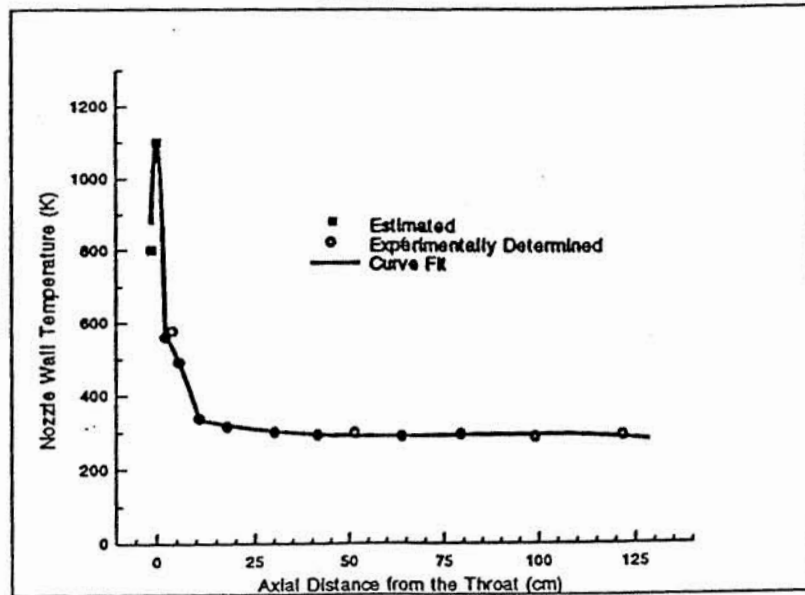


Figure A11- Plot comparing the estimated and experimentally determined temperatures with those input for the constant wall temperature boundary condition, Reading 112, 1030:1 NASA LeRC nozzle.

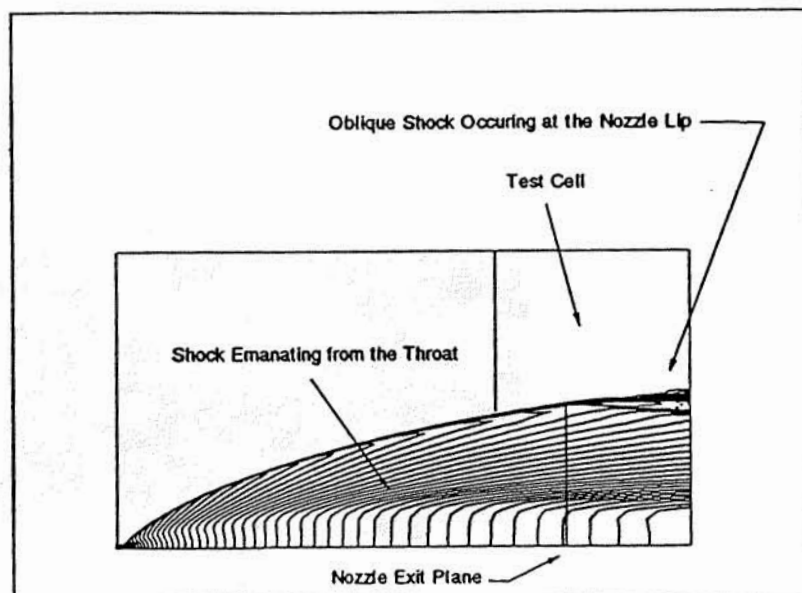


Figure A12 - Mach number contours for Case I, Reading 112 1030:1 NASA LeRC nozzle.

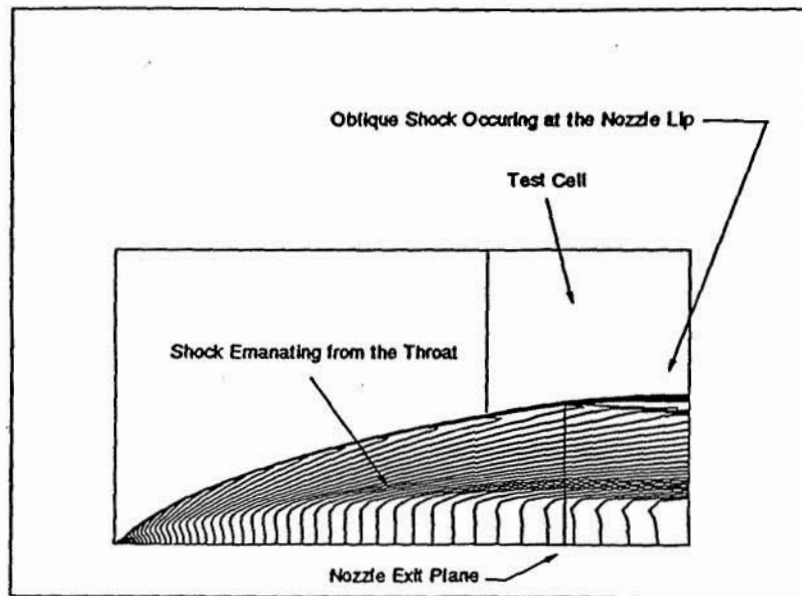


Figure A13 - Mach number contours for Case II, Reading 112 1030:1 NASA LeRC nozzle.

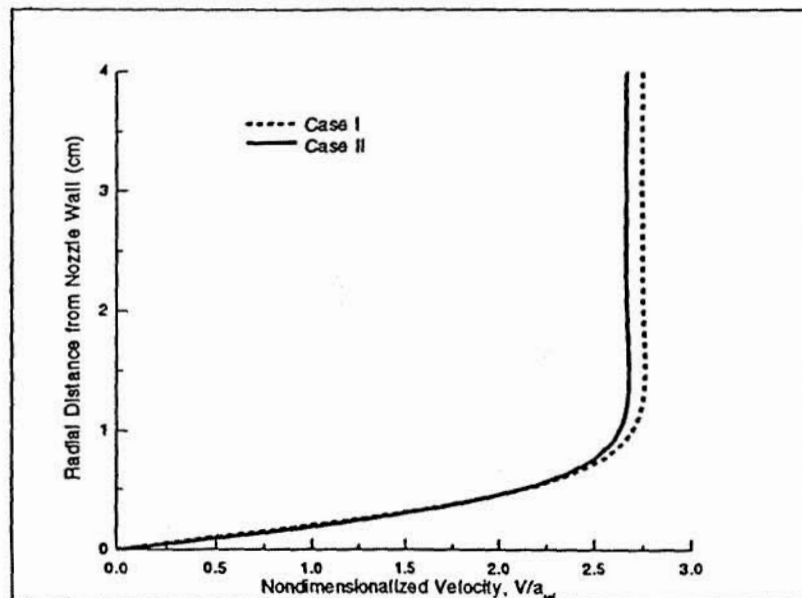


Figure A14 - Viscous boundary layer profile for Case I and Case II, 6.6525 cm upstream from the nozzle exit plane, Reading 112 1030:1 NASA LeRC nozzle.

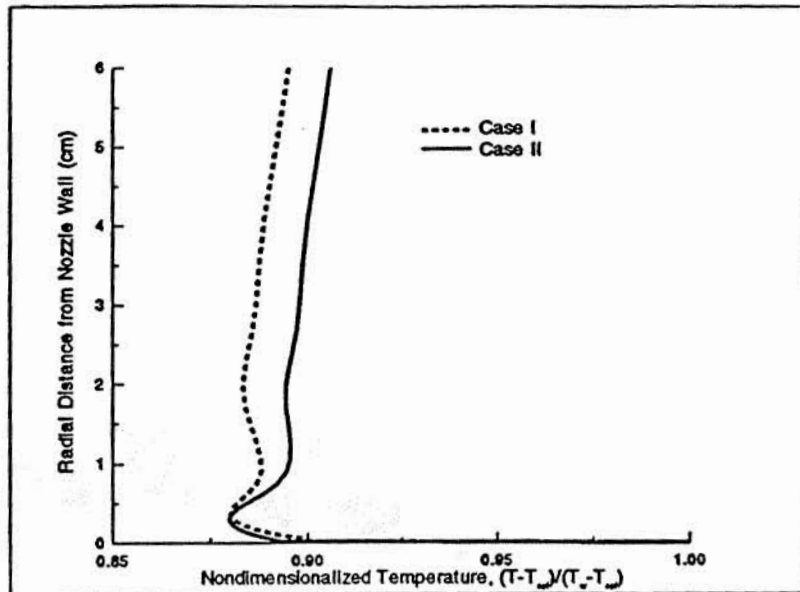


Figure A15 - Thermal boundary layer profile for Case I and Case II, 6.6525 cm upstream from the nozzle exit plane, Reading 112 1030:1 NASA LeRC nozzle.

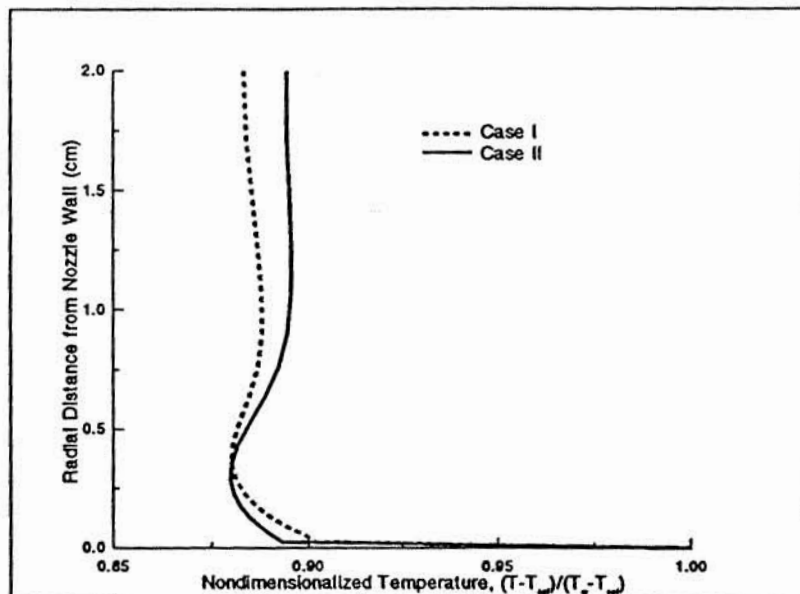


Figure A16 - Close up of thermal boundary layer profile for Case I and Case II, 6.6525 cm upstream from the nozzle exit plane, Reading 112 1030:1 NASA LeRC nozzle.

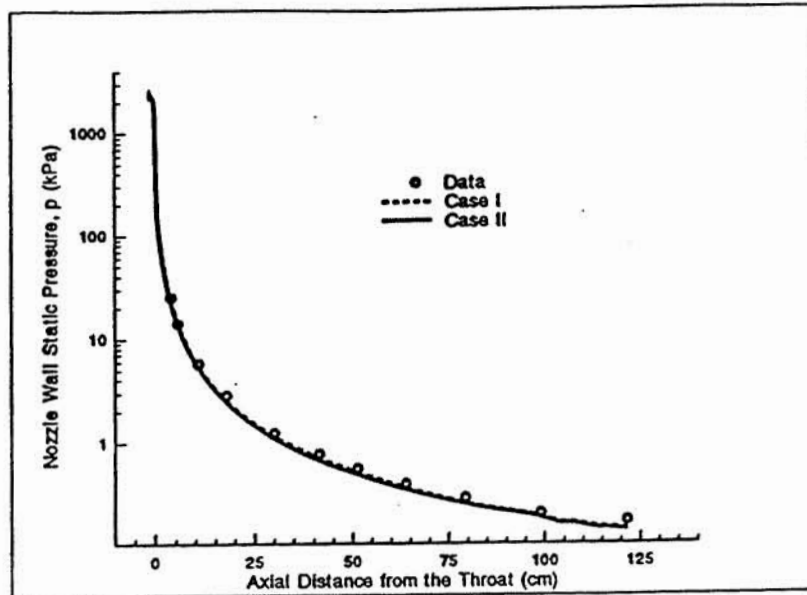


Figure A17 - Comparison of experimentally measured wall static pressure with calculated wall static pressure for Case I and Case II, Reading 112 1030:1 NASA LeRC nozzle.

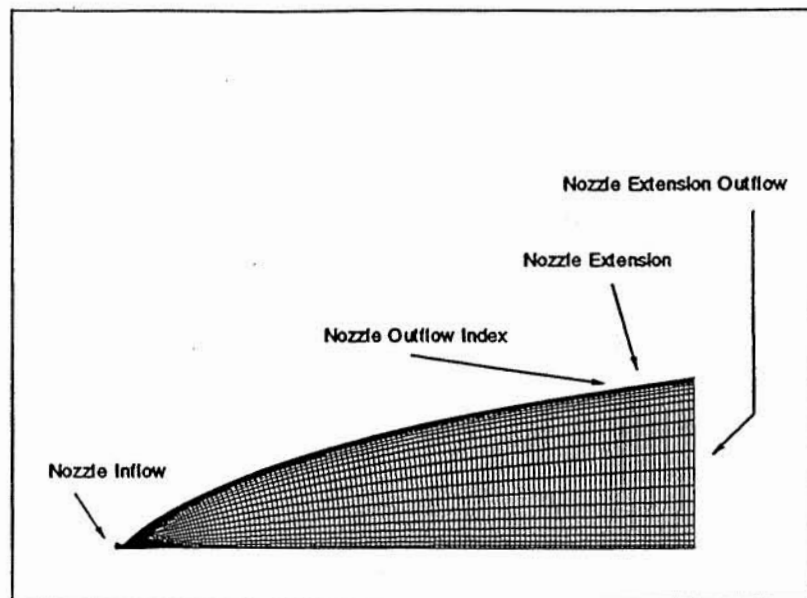


Figure A18- Computational grid used for the wall heat flux calculation, 1030:1 NASA LeRC nozzle (every other point plotted in the radial direction).

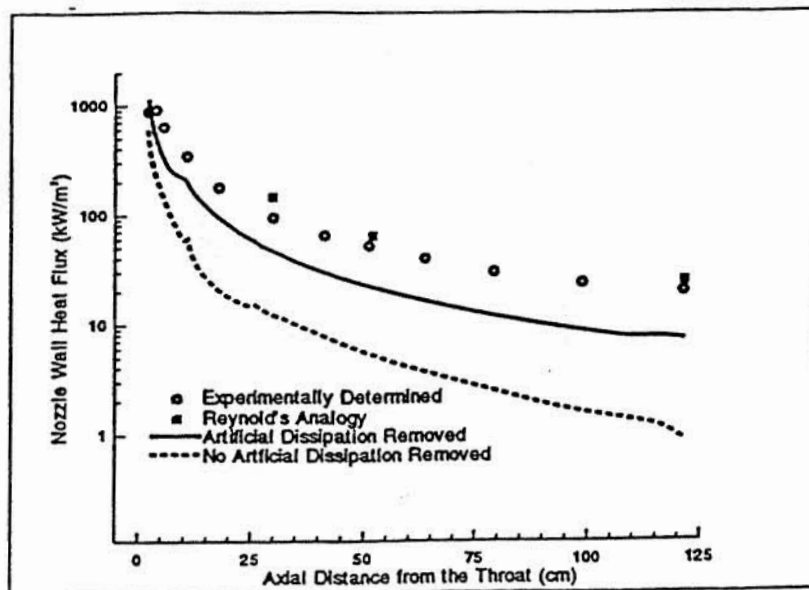


Figure A19 - Comparison of experimentally determined heat flux and calculated wall heat flux.

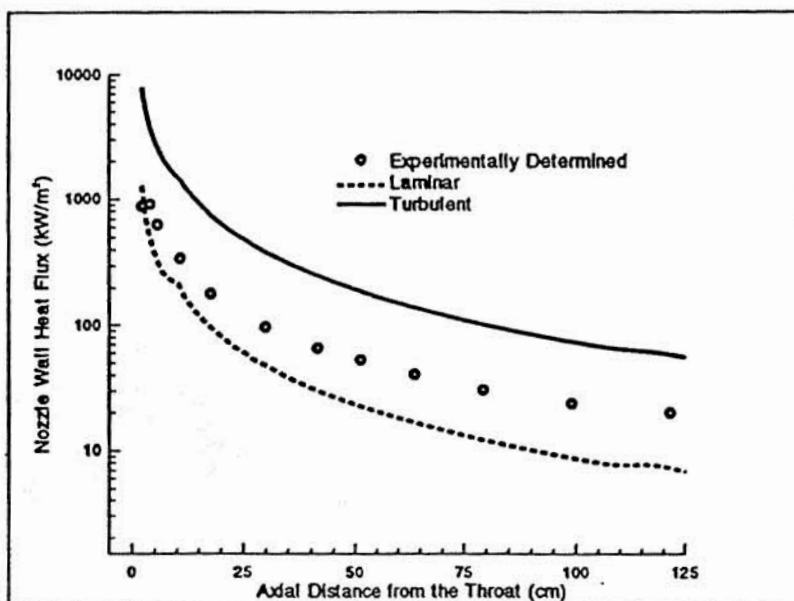


Figure A20 - Comparison of experimentally determined heat flux and calculated wall heat flux.

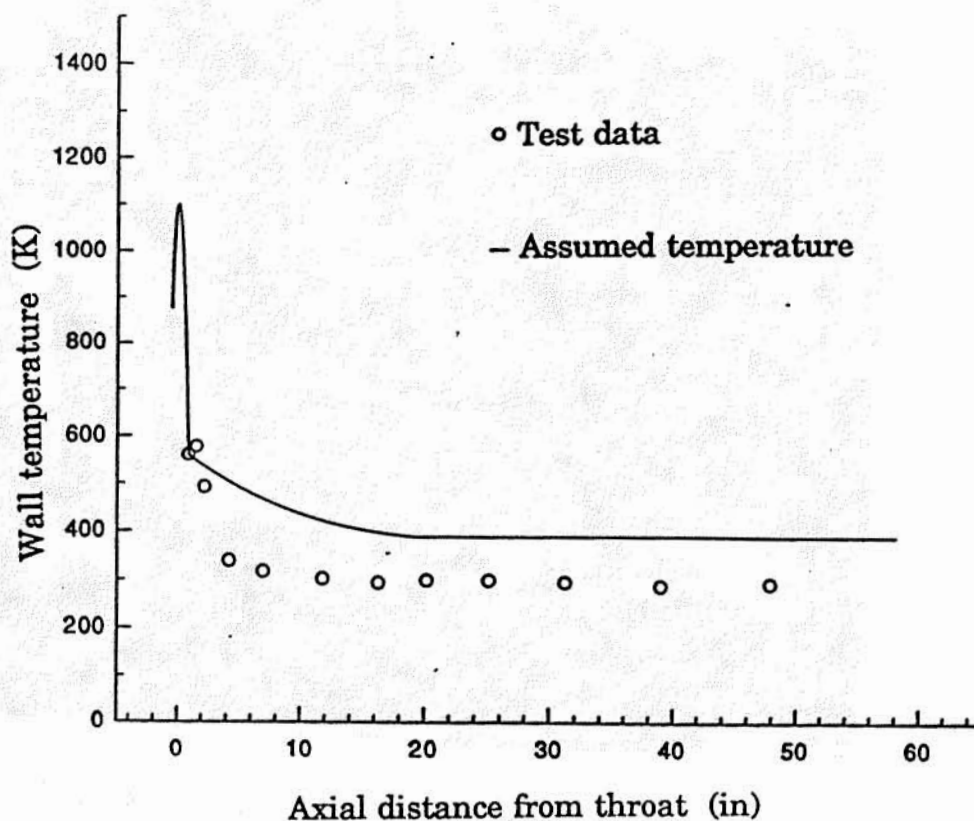


Figure A21 Comparison of measured 1030:1 nozzle wall temperature and the distribution assumed for the lower chamber pressure computations.

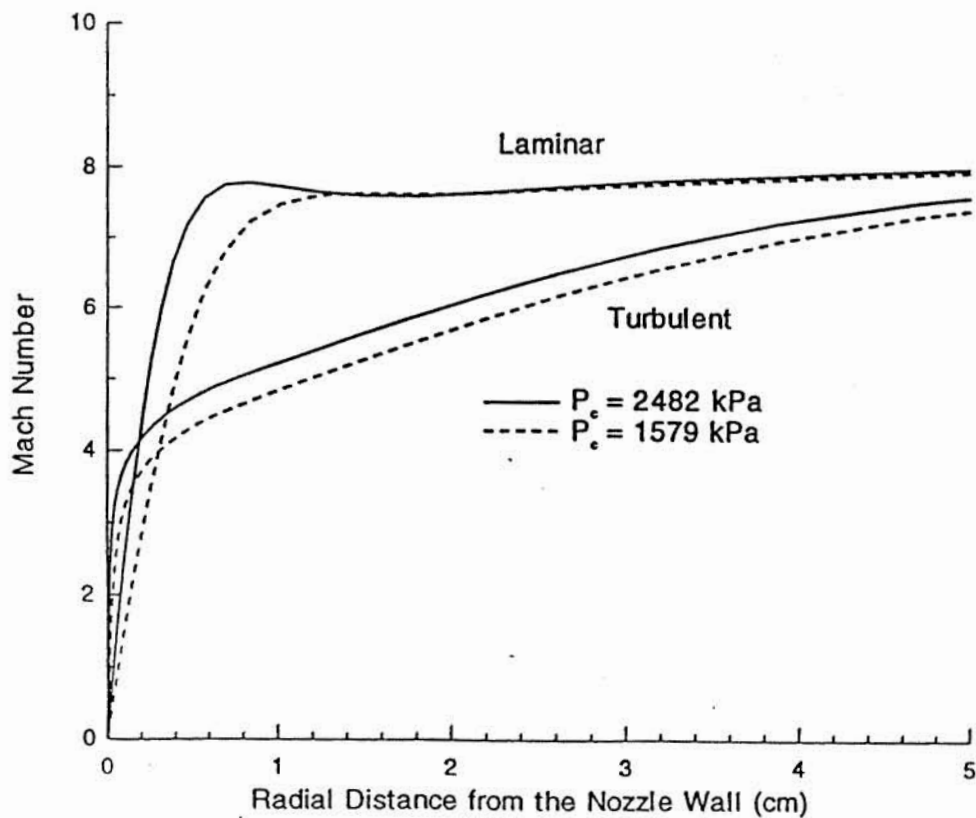


Figure A22 Computed Mach number distributions in the wall region of the 1030:1 nozzle.

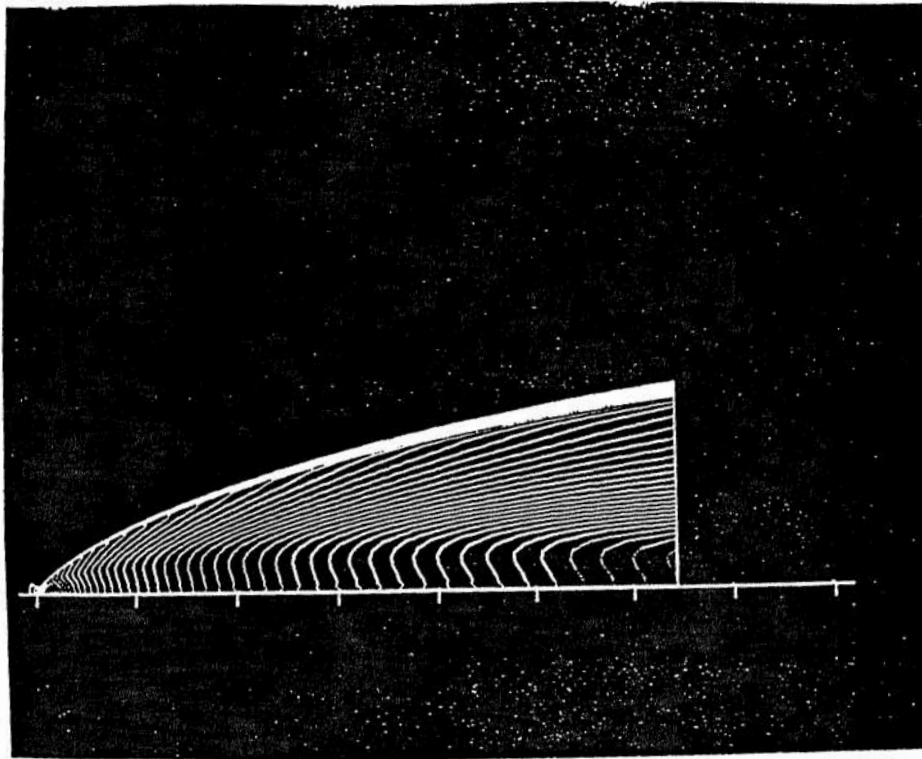


Figure A23 - Mach number contours for 1030:1 NASA LeRC nozzle,
 $p_c = 100$ psia.

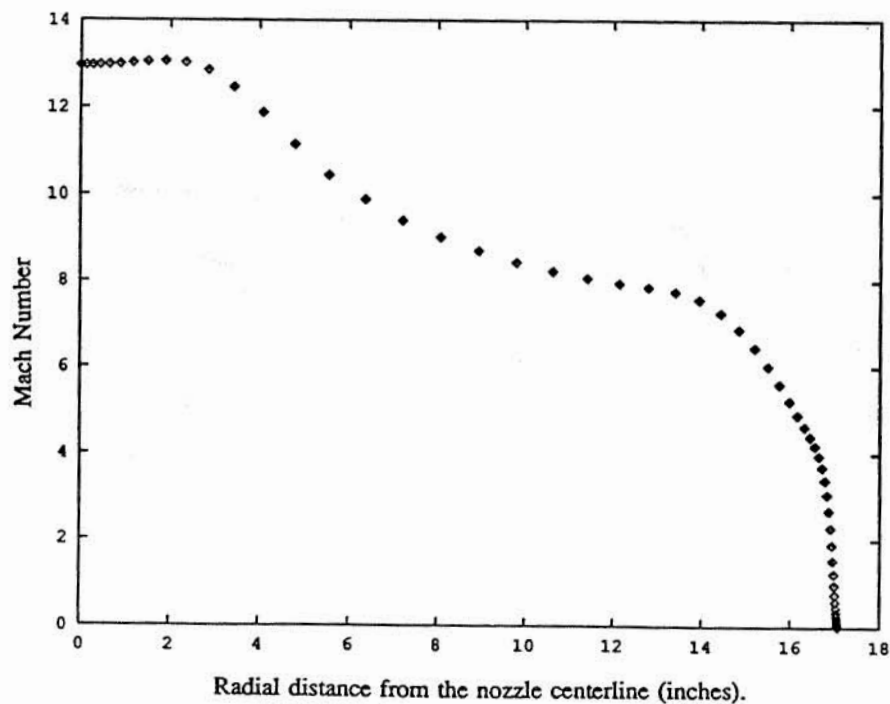


Figure A24 - Mach number distribution across the exit plane for 1030:1 NASA
 LeRC nozzle, $p_c = 100$ psia.

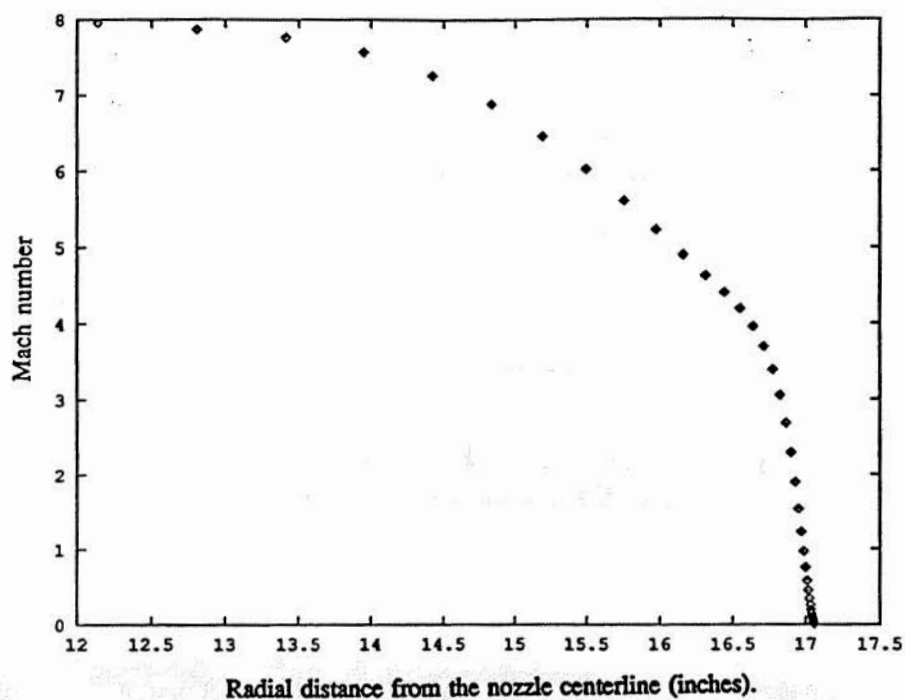


Figure A25 - Exit plane boundary layer Mach number distribution for 1030:1 NASA LeRC nozzle, $p_c = 100$ psia.

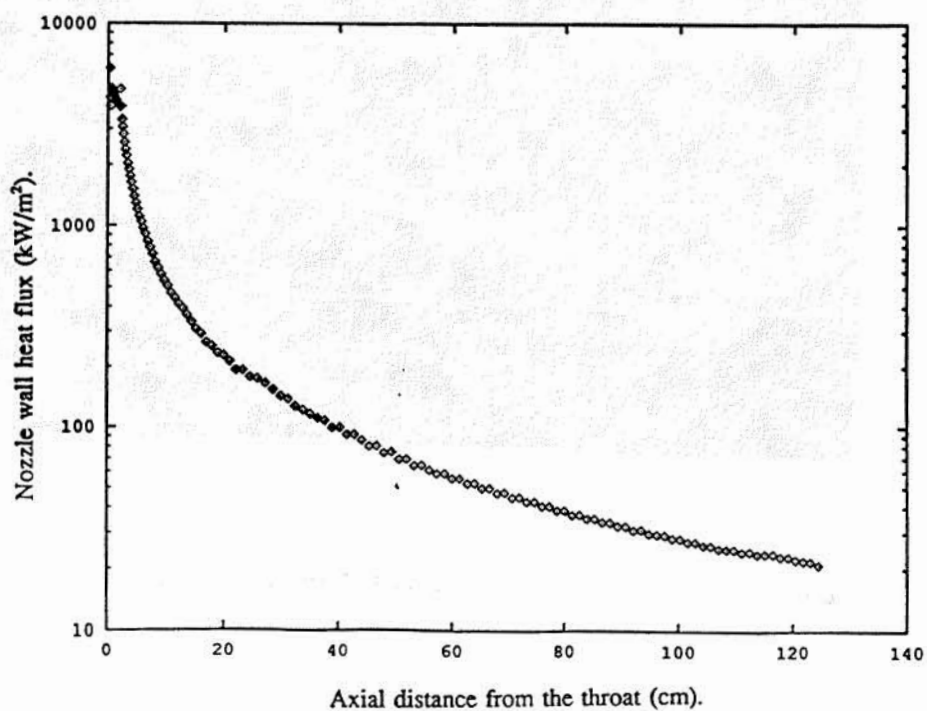


Figure A26 - Calculated wall heat flux for 1030:1 NASA LeRC nozzle, $p_c = 100$ psia.

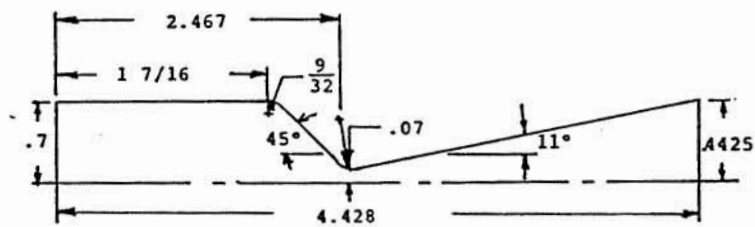


Figure B1 - Geometry of low Reynolds number 40:1 nozzle and plenum chamber.
All dimensions are in inches.

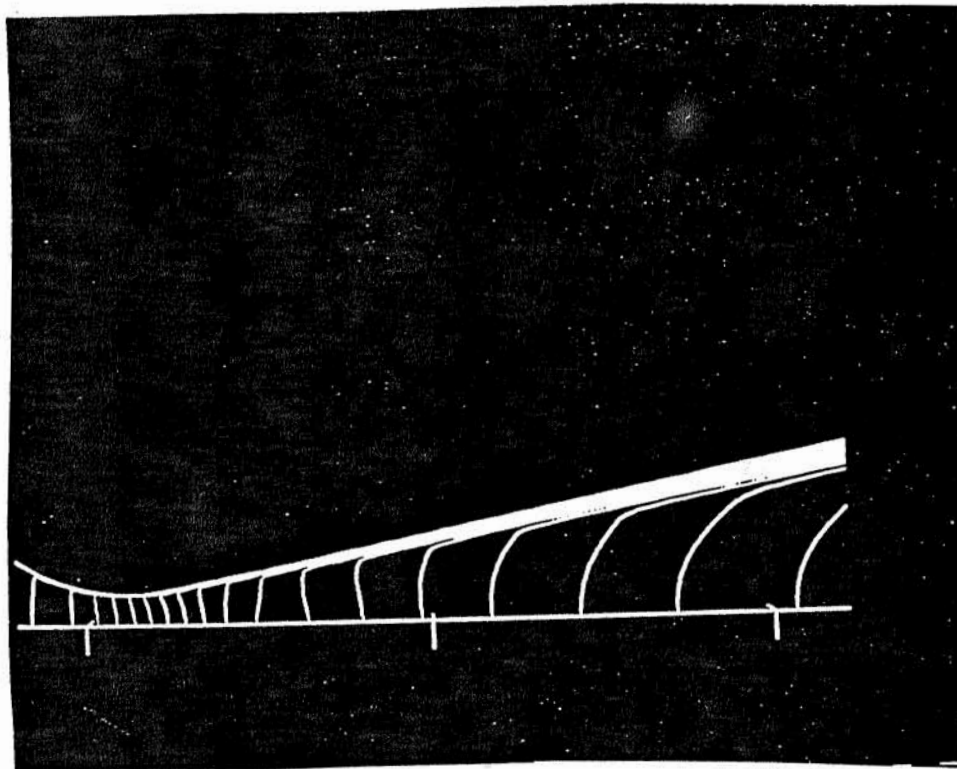


Figure B2 - Mach number contours for low Reynolds number 40:1 nozzle,
 $p_c = 7.4$ psia.

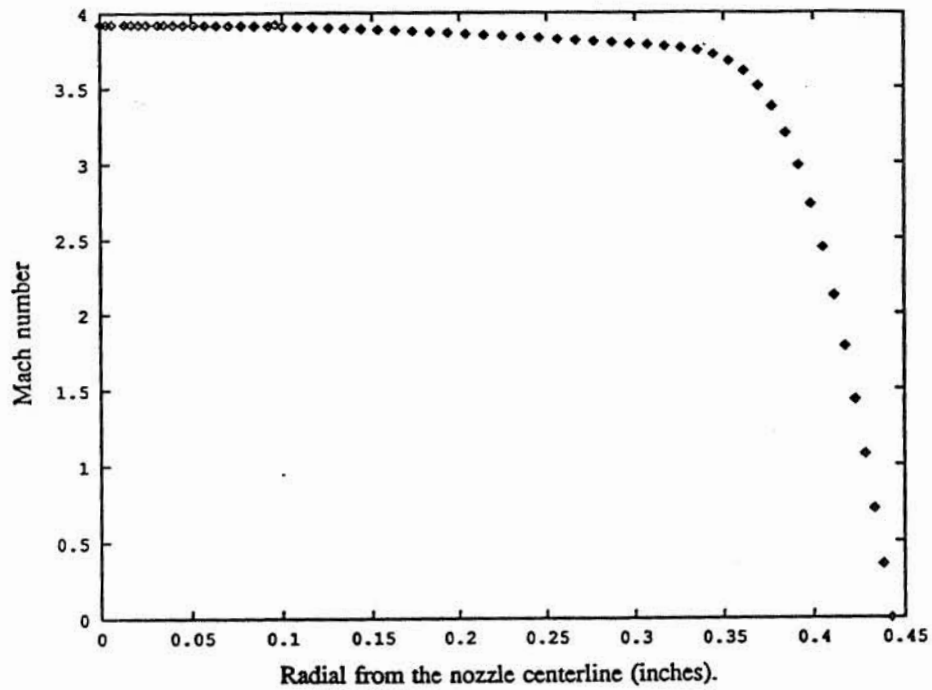


Figure B3 - Exit plane Mach number distribution for low Reynolds number 40:1 nozzle, $p_c = 7.4$ psia.

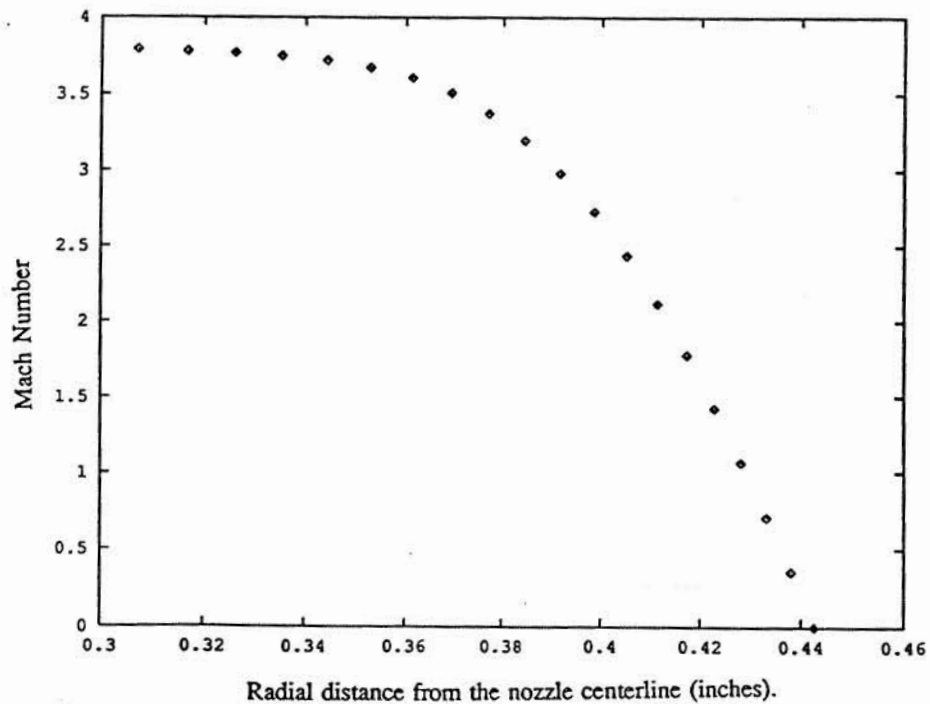


Figure B4 - Exit plane boundary layer Mach number distribution for low Reynolds number 40:1 nozzle, $p_c = 7.4$ psia.

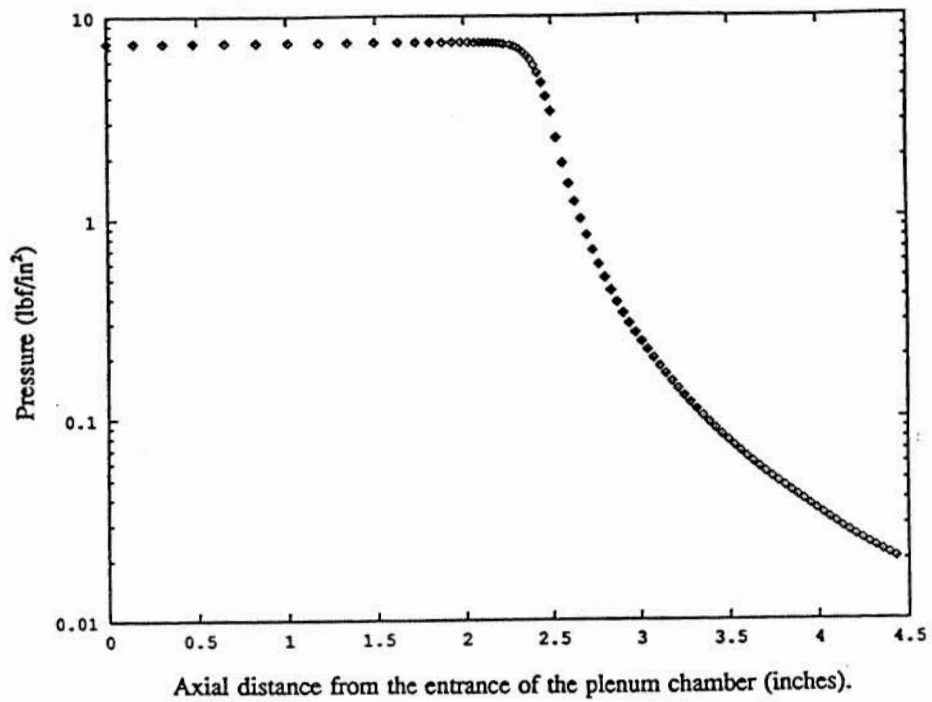


Figure B5 - Wall pressure distribution in low Reynolds number 40:1 nozzle, $p_c = 7.4$ psia.

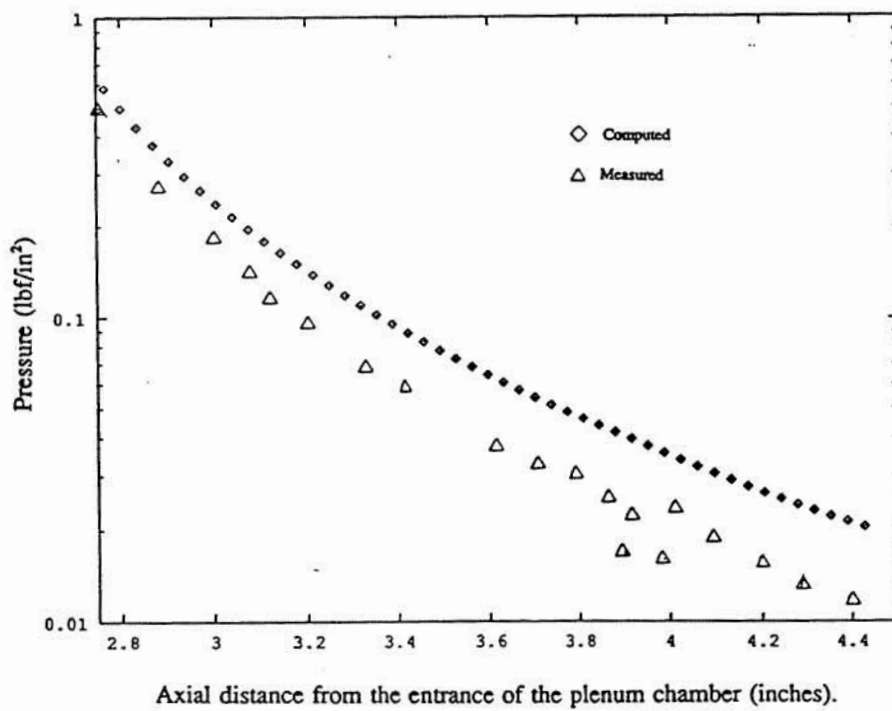


Figure B6 - Comparison of measured and computed wall pressure distribution in low Reynolds number 40:1 nozzle, $p_c = 7.4$ psia.

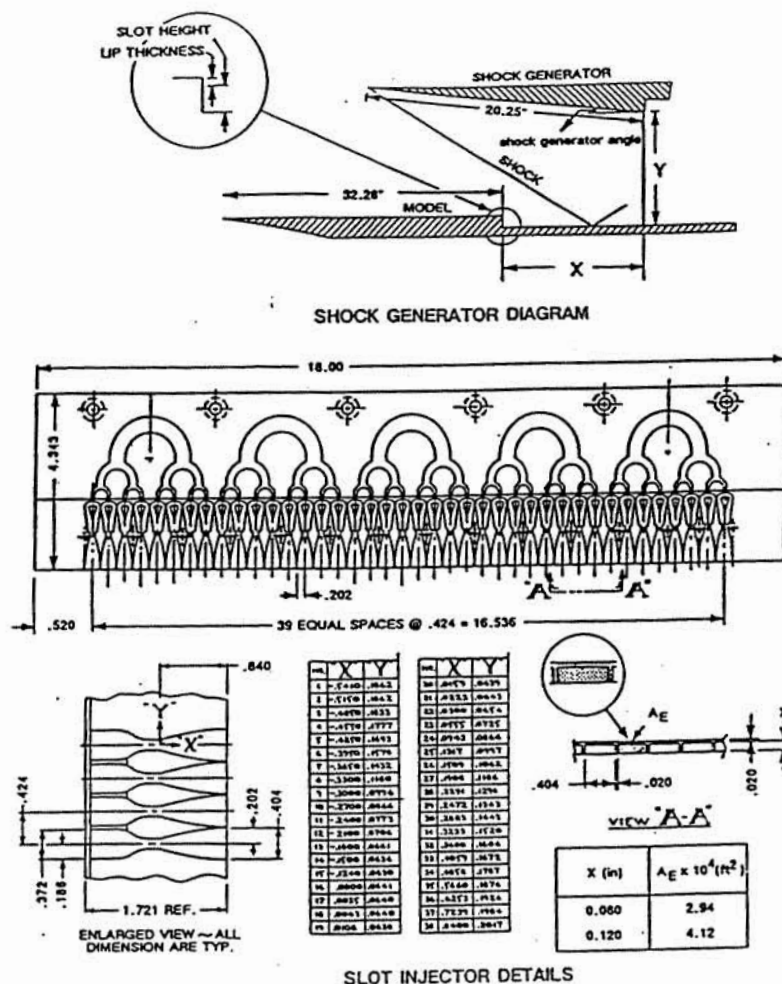


Figure C1 Configuration for Calspan (Holden) film cooling experiments.

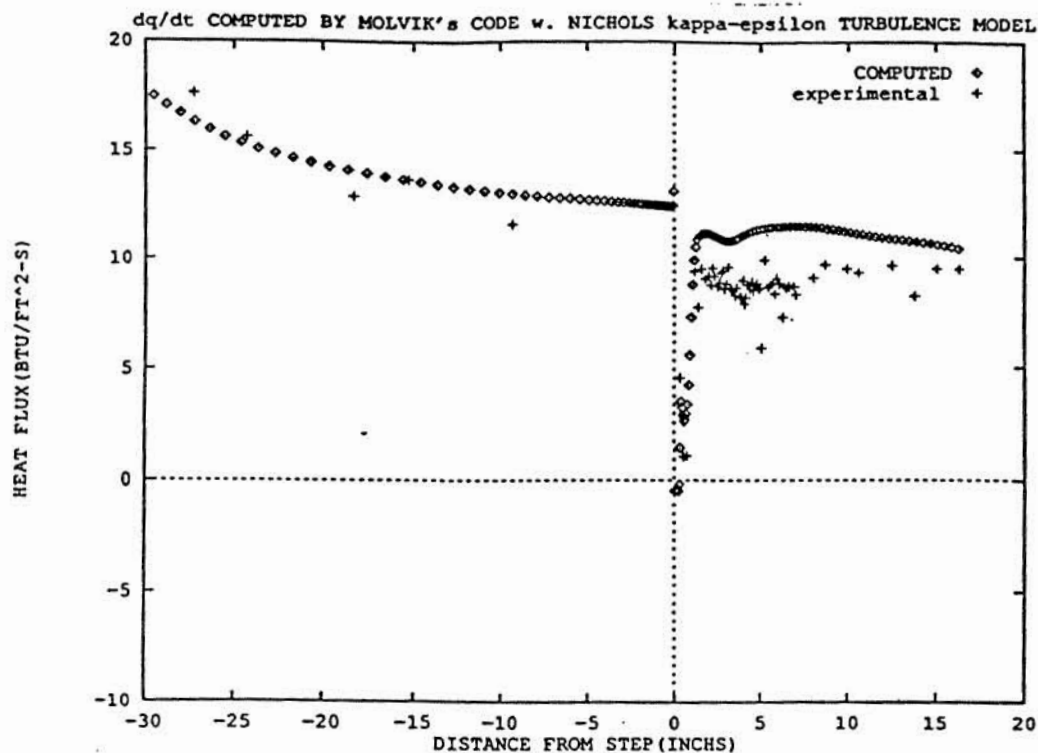


Figure C2 Experimental and calculated wall heat flux for no-flow case for Calspan test. (Test 43)

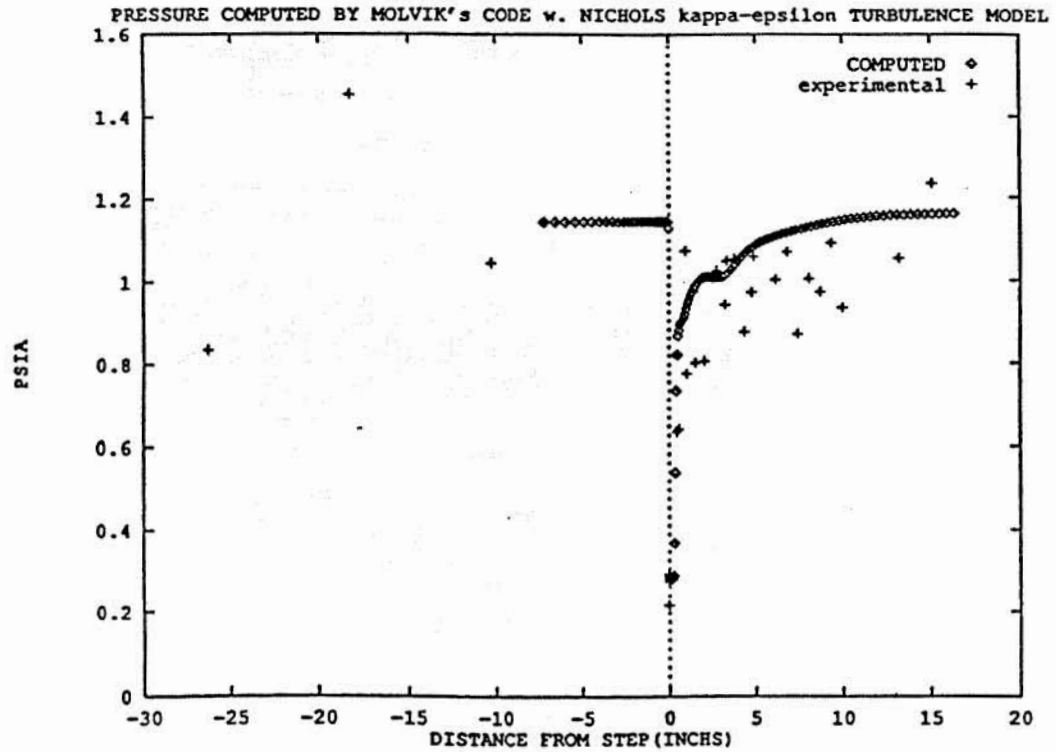


Figure C3. Experimental and calculated wall pressure distribution for no-flow case for Calspan test. (Test 43)

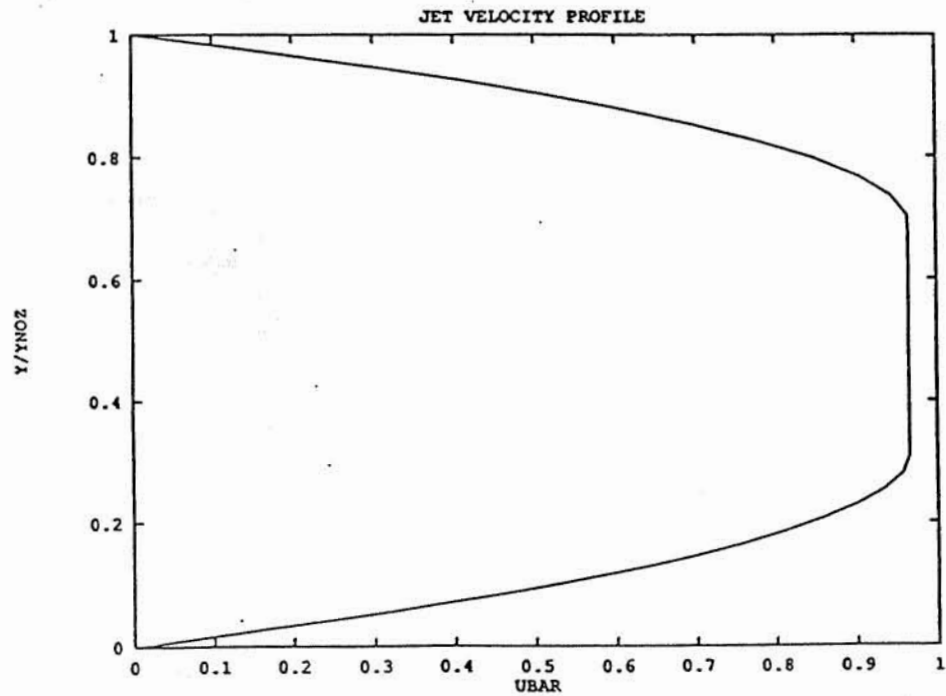


Figure C4 Assumed helium film nozzle exit plane velocity profile used for run 44 of the Calspan tests

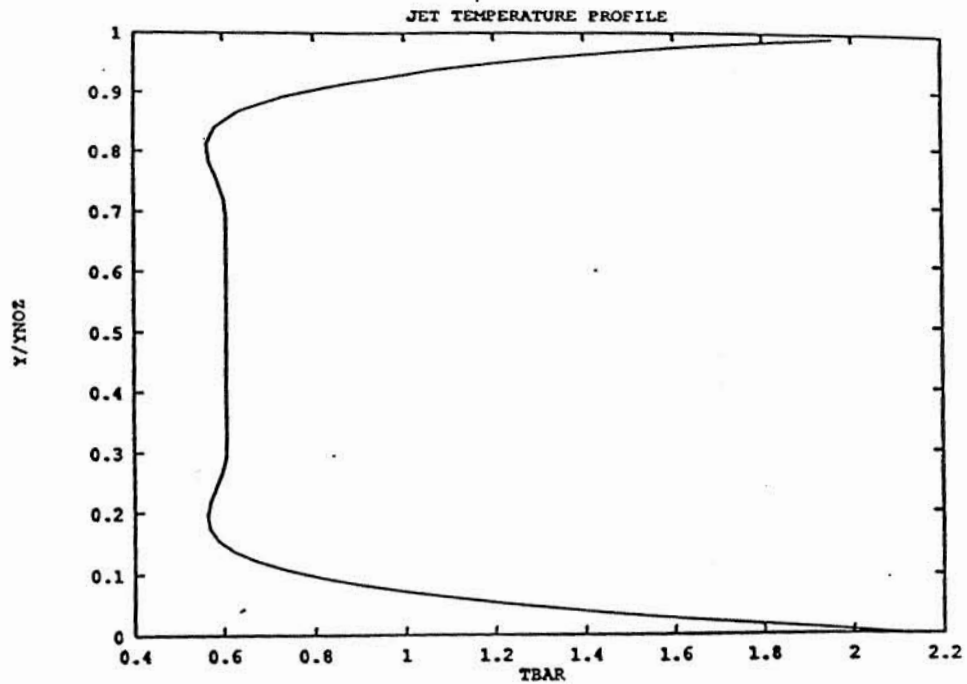


Figure C5 Assumed helium film nozzle exit plane velocity profile used for run 44 of the Calspan tests

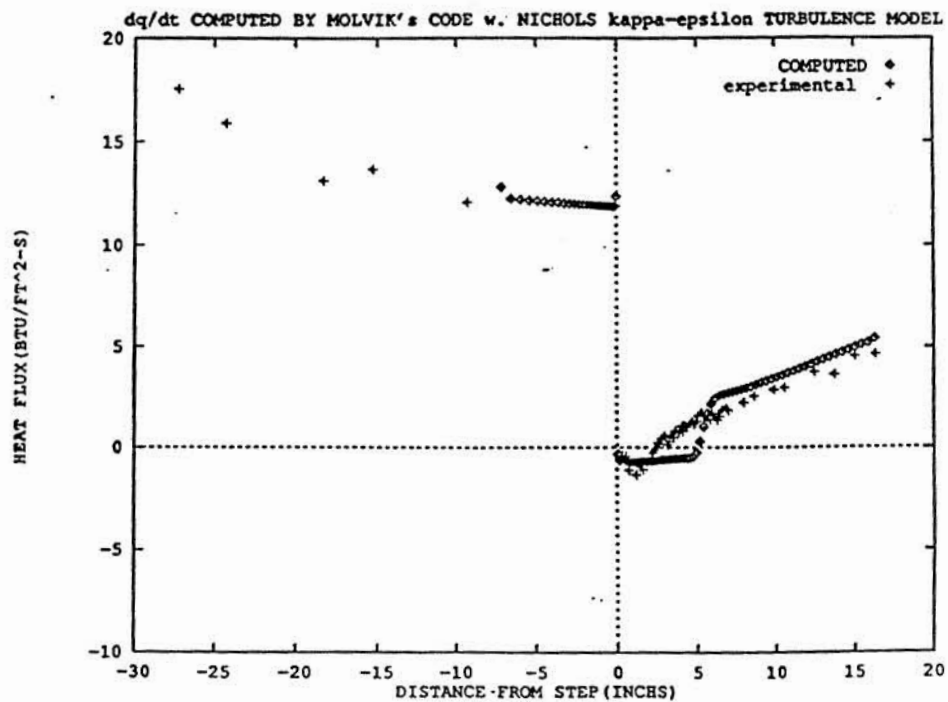


Figure C6 Comparison of computed and measured wall heat flux for run 44 of the Calspan tests

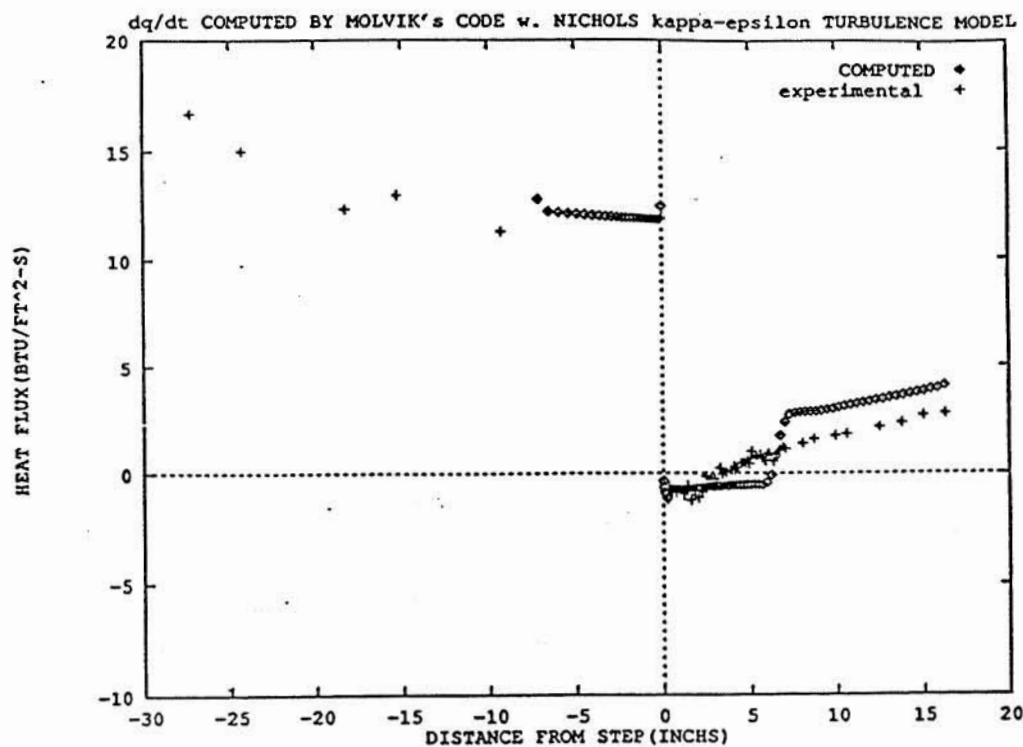


Figure C7 Comparison of computed and measured wall heat flux for Run 45 of the Calspan film cooling tests.

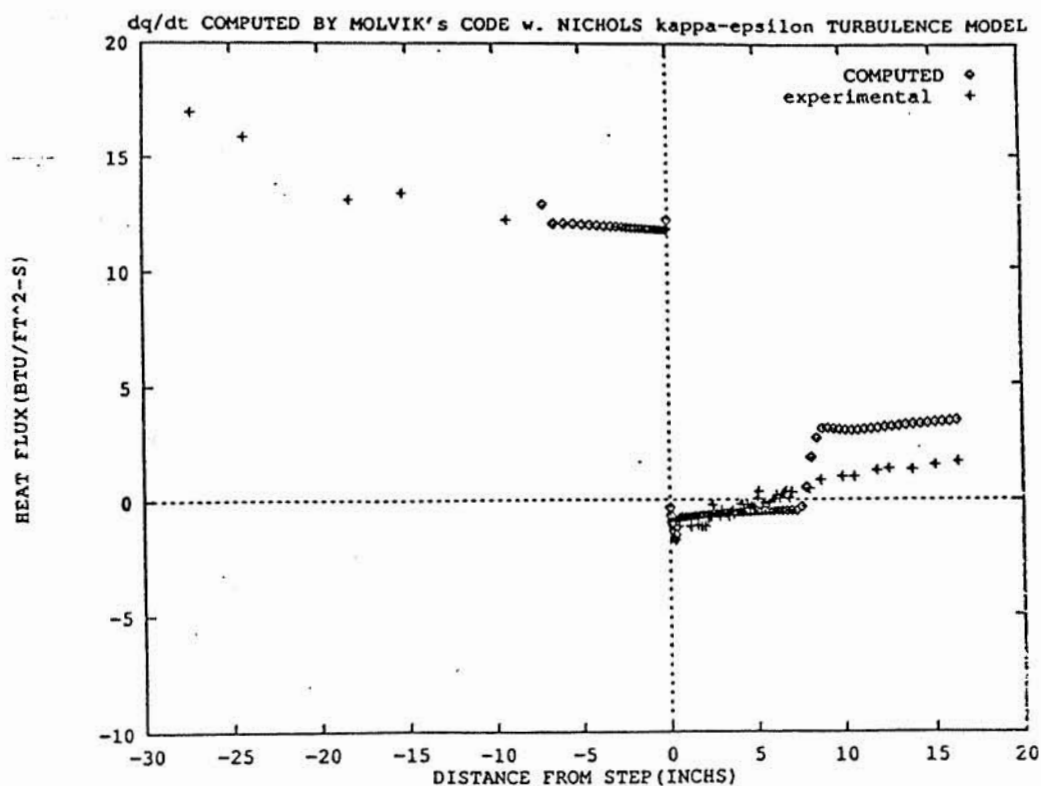


Figure C8 Comparison of computed and measured wall heat flux for Run 46 of the Calspan film cooling tests.

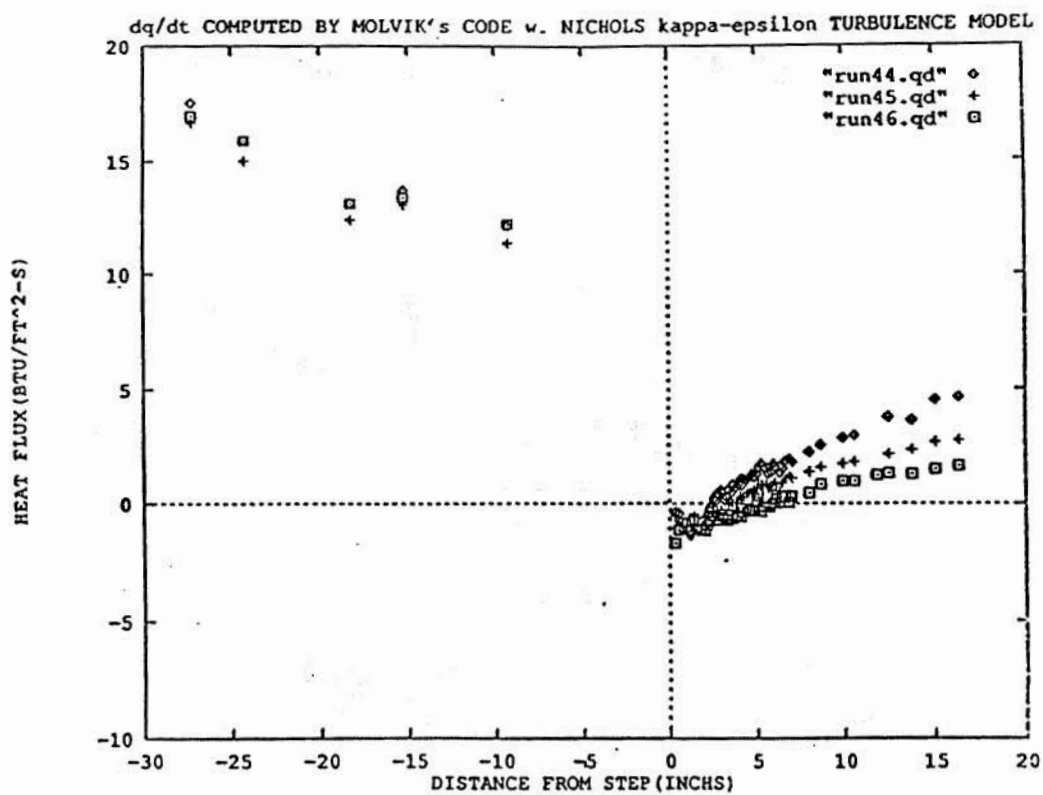


Figure C9 Measured wall heat flux for Runs 44, 45, and 46 of the Calspan film cooling tests.

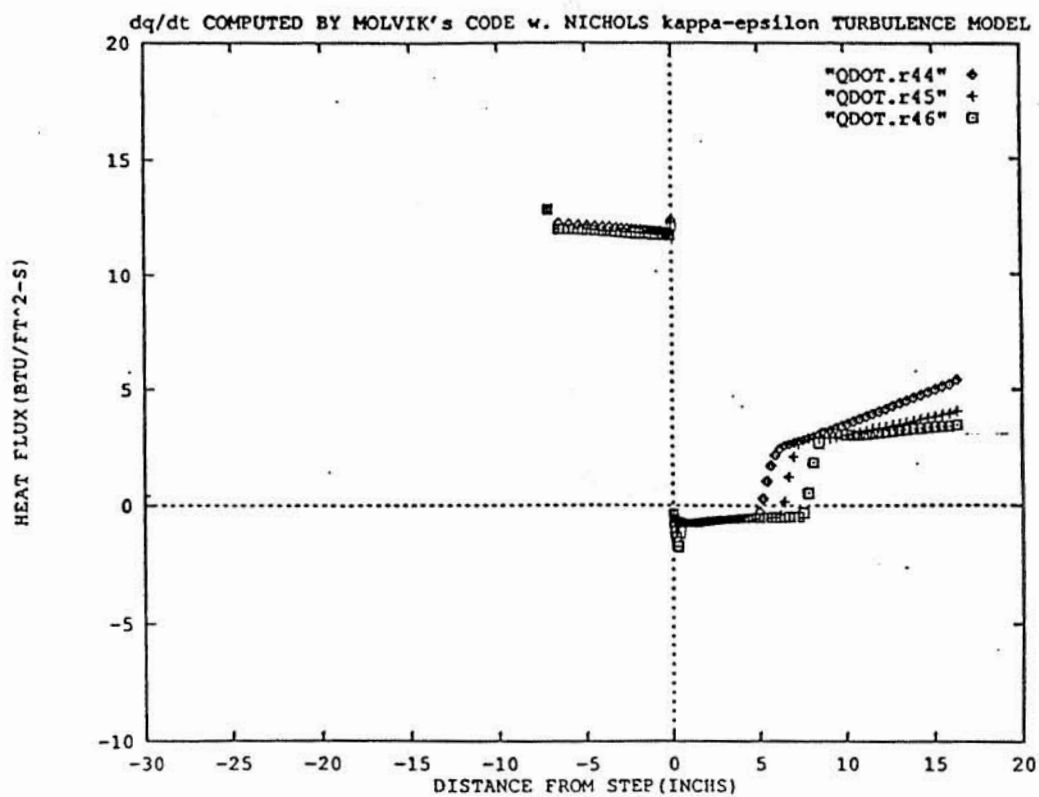


Figure C10 Computed wall heat flux for Runs 44, 45, and 46 of the Calspan film cooling tests.

SUBSCALE NOZZLE ASSEMBLY

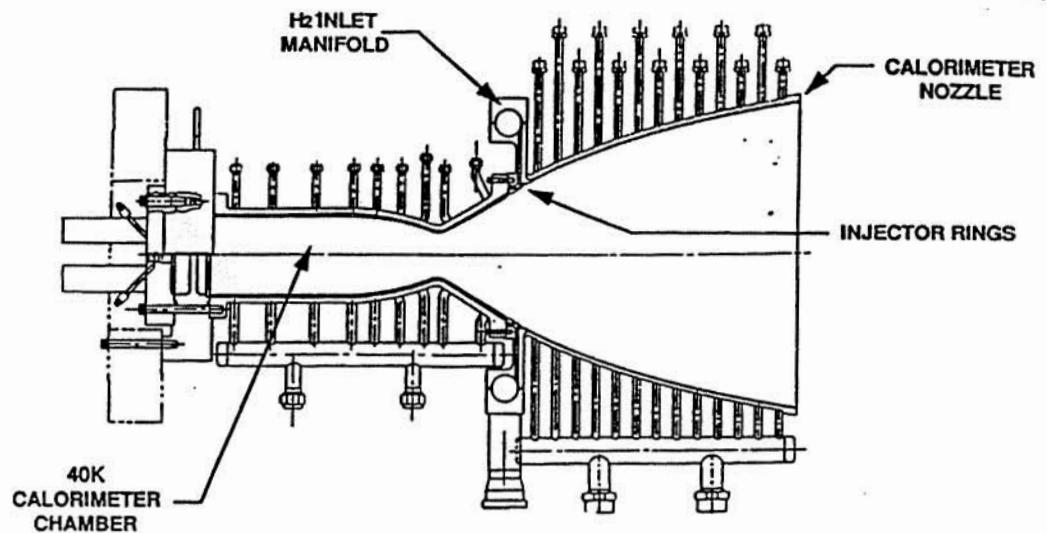


Figure C11 Subscale STME nozzle configuration [13].

ANALYSIS OF SECONDARY COOLANT CAVITY

Design Solution: Porous Stainless Steel Filter

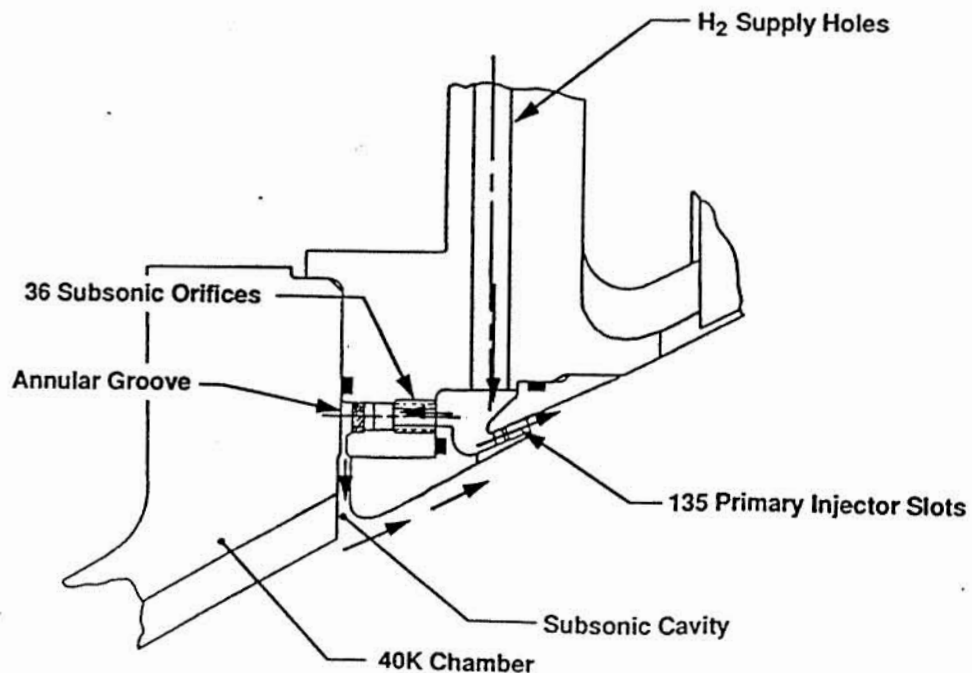
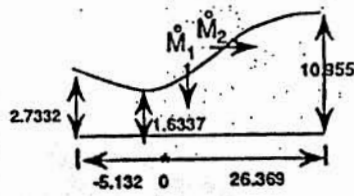


Figure C12 Details of film injection for subscale STME nozzle

STME NOZZLE GEOMETRY AND FLOW CONDITION



CHAMBER PRESSURE	2250 PSI
CHAMBER TEMPERATURE	6708°R
CHAMBER EXIT FLOW RATE (MACH = 0.213)	82.4 lbm/sec
SUBSONIC COOLANT FLOW RATE \dot{M}_1 (MACH = 0.205)	0.254 lbm/sec
SUPERSONICS (COOLANT FLOW RATE \dot{M}_2 (MACH = 1.454)	1.51 lbm/sec

CHAMBER GAS COMPOSITION	MOLE FRACTIONS
H	0.02977
H ₂	0.15003
H ₂ O	0.71975
O	0.00867
OH	0.07520
O ₂	0.01642
HO ₂	0.00010
H ₂ O ₂	0.00005

RJ-91-RS066D#14

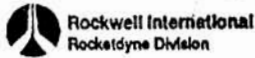


Figure C13 - STME flow conditions.

59x99 GRID 1
60x129 GRID 2
110x159 GRID 3

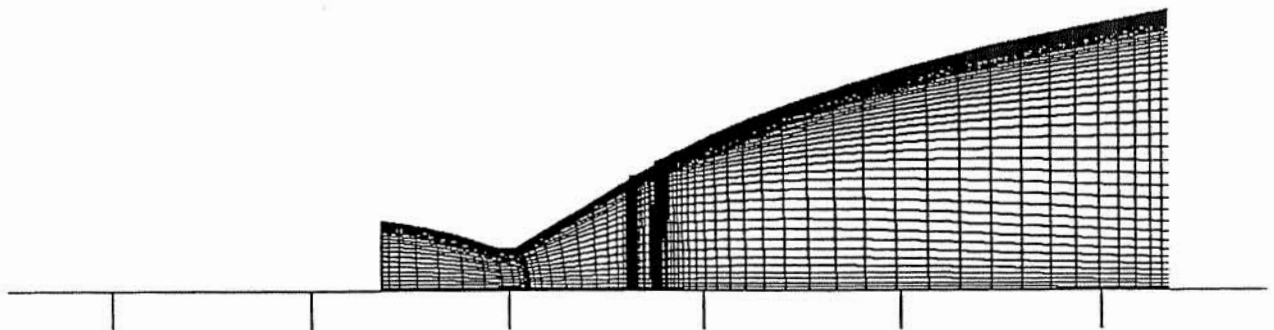


Figure C14 - Computational grid for subscale STME nozzle.

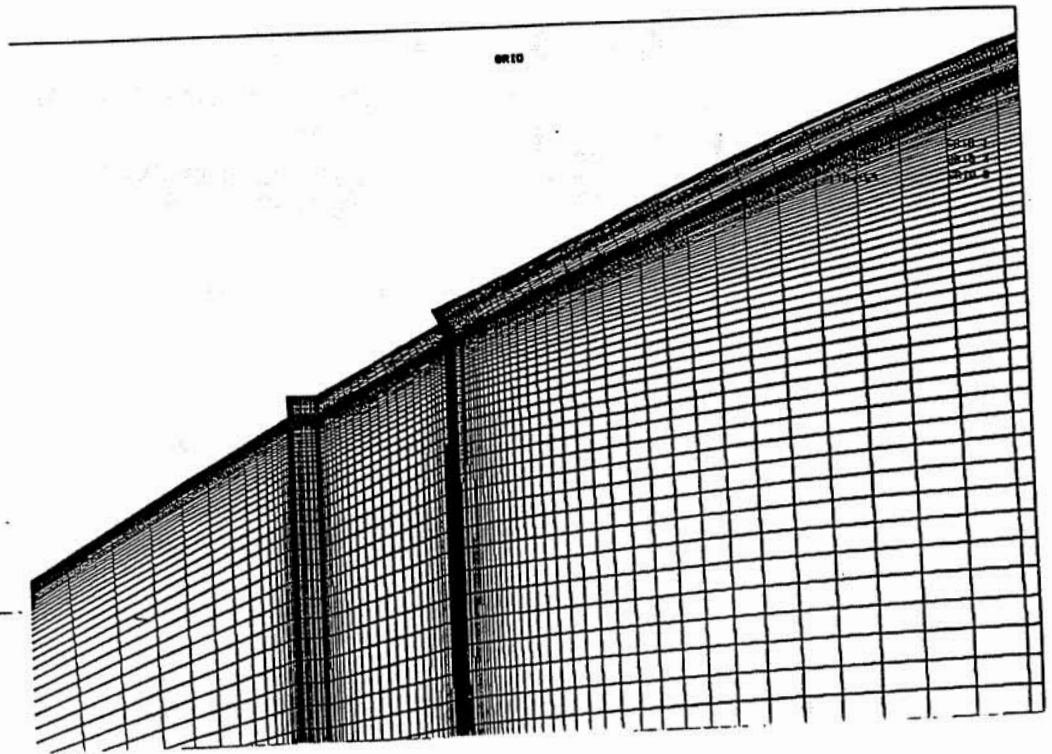


Figure C15 - Close-up of computational grid for subscale STME nozzle in the region of the injection ports.

SPACE SHUTTLE MAIN ENGINE PROPELLANT PATH LEAK DETECTION USING SEQUENTIAL IMAGE PROCESSING

L. Montgomery Smith*, J. A. Malone**, B. W. Bomar†, and R. A. Crawford‡

University of Tennessee – Calspan
Center for Space Transportation and Applied Research
University of Tennessee Space Institute
Tullahoma, Tennessee 37388-8897

ABSTRACT

Initial research using theoretical radiation transport models established that the occurrence of a leak in the powerhead of the SSME is accompanied by a sudden but sustained change in intensity in a given region of an image. During this work period, temporal processing of video images on a frame-by-frame basis has been used to detect leaks within a given field of view. The leak detection algorithm developed in this study consists of a digital highpass filter cascaded with a moving average filter. The absolute value of the output image is then averaged over the full frame to produce a single time-varying mean value estimate that is indicative of the intensity and extent of a leak. Four video sequences from an actual SSME test firing were analyzed using this technique. A hydrogen gas leak was detected approximately four seconds before existing sensors initiated shutdown during the test. The resulting plots of the full frame mean value versus time verify the effectiveness of the system. A detailed specification of the hardware and software required to implement the algorithm in real time was performed. The proposed system consists of a personal-computer-based system with commercially available add-in cards capable of digitizing and processing standard RS-170 format video signals at 30 frames per second.

I. INTRODUCTION

The rapid detection of propellant leaks from the Space Shuttle Main Engine (SSME) during test firing is crucial to the prevention of catastrophic failures. Ruptures of high-pressure

lines and internal components due to thermal shock, mechanical stress, erosion, and material fatigue often result in failure modes with sufficiently long time constants to allow detection and safe shut down. Recent advances in imaging and image processing technology provide the hardware necessary for visual and infrared observation of these phenomena and the computing capability required for processing the signals and detecting the occurrence of a leak within the field of view. Thus, a system capable of detecting leaks from images acquired sequentially during test firing in real time is of value to the development of the SSME and is realizable with current technology. This study investigated this approach and established its feasibility and applicability to the program.

*UTSI/CLA/CSTAR, Assistant Professor of ECE

**ERC/CSTAR, Research Engineer

†UTSI/CSTAR, Associate Professor of ECE

‡UTSI/CLA/CSTAR, Professor of AE/ME

This work was sponsored jointly by the Center for Space Transportation and Applied Research and the National Aeronautics and Space Administration under Grant NAG8-140, through the Center for Laser Applications (CLA) at the University of Tennessee Space Institute (UTSI).

Previous work in this area by Shohadaee and Crawford [1], [2] concentrated on establishing the feasibility of observing hot or cold leaks using infrared imaging. The theoretical models developed were used to predict radiation transport in absorbing, emitting and scattering media. These models predicted the intensity of both background and plume radiation reaching a sensor location, and they were used for designing validation experiments. The feasibility of infrared detection of leak plumes was demonstrated on subscale simulated plumes to determine sensitivity, signal-to-noise ratio, and general suitability. Both hot and cold leaks were readily detected as measurable intensity changes by the sensor.

However, to detect the occurrence of a leak, the temporal aspects of the process must be considered. The previous analysis showed that the occurrence of a leak should result in a sudden change in intensity in a given region of an image. Furthermore, the change should be sustained for a typical persistent leak. The time variation of the intensity at a point within the area of the leak should therefore be similar to that of a step function, although other smaller intensity variations are also present due to normal operating conditions. The problem becomes that of detecting a step function in the presence of additive noise.

The leak detection system presented here was designed to quickly and automatically detect a step-like change in intensity in a sequence of images [3], [4]. Temporal processing is carried out at each point in full-frame digitized video data. The system consists of a causal, recursive high-pass filter that removes slowly-varying background intensities cascaded with a moving average filter that accumulates transmitted sustained changes. The absolute value over the full output frame is averaged to produce a time-varying mean value indicative of the level and spatial extent of any leak.

The leak detection algorithm has been implemented on a general purpose digital image processor and successfully applied to actual test-stand firing data. Four video image sequences of a SSME test-stand firing were analyzed with this technique to evaluate its performance under actual firing conditions. A hydrogen leak was detected in three of the four camera views approximately 4 sec before existing sensors initiated an early shutdown.

In order to implement the algorithm in real-time with a standard 30 frames/sec video signal, a system with memory for approximately 16 previous frames and a processing throughput of 37 million operations/sec is required. A personal-computer-based system meeting these specifications has been designed with commercially-available add-in cards utilized where possible. Verification of timing requirements has been carried out with a software simulator to establish proper system operation.

The following section describes the leak detection algorithm and discusses some of the considerations for implementing it on digital image processing equipment. Section III discusses the processing of the four video sequences from a SSME test firing. Specifications for a real-time data acquisition and processing system implementing the algorithm are presented in Section IV. A summary and conclusions are given in Section V.

II. THE LEAK DETECTION

Time-varying intensity levels in video images are an inherently discrete signal with a sampling rate of 30 Hz for standard television format. Therefore, techniques of digital signal processing are directly applicable to the analysis. A detailed derivation of the step detection algorithm used in this study was given in [4] along with a numerical analysis of its performance. For completeness, a brief

description of it is presented here.

The processing algorithm developed for this application can be broken down into four component blocks. The first three blocks involve processes that are applied in parallel at each point (pixel location) in the image, while the fourth incorporates the spatial information over the entire field of view. In concept, the four steps can be described as follows:

1. A highpass filter is applied to remove the constant or slowly-varying background intensity while passing sudden changes.
2. A moving average filter accumulates any sustained changes transmitted through the highpass filter.
3. The absolute value of the output from the moving average is taken to allow for detection of positive or negative intensity changes.
4. The pixel values of the output image are summed or averaged over the field of view to produce a single time-varying quantity indicative of the extent and intensity of a leak.

For speed of response and simplicity of computation, the highpass filter has been chosen as a single-pole recursive filter with a z-domain transfer function given by

$$F(z) = \frac{1 + \beta}{2} \frac{1 - z^{-1}}{1 - \beta z^{-1}} \quad (1)$$

The cutoff frequency of the filter is determined by choice of the pole value β .

The moving average filter has a transfer function

$$G(z) = \frac{1}{n} \sum_{k=0}^{N-1} z^{-k} \quad (2)$$

$$= \frac{1}{n} \frac{1 - z^{-N}}{1 - z^{-1}}$$

These two filtering operations can be combined into a single cascade connection with an effective transfer function given by

$$H(z) = F(z) G(z) \quad (3)$$

$$= \frac{1 + \beta}{2N} \frac{1 - z^{-N}}{1 - \beta z^{-1}}$$

which corresponds to the difference equation

$$y(n) = \beta y(n-1) + \frac{1 + \beta}{2N} [x(n) - x(n-N)] \quad (4)$$

Equation (4) is the difference equation defining the temporal filtering that is carried out at each point in the image. Processing is completed by taking the absolute value of the resulting signals at all pixel locations and averaging them over the full field of view.

While equation (4) conceptually describes the filtering process at each pixel location, the actual implementation consists of the recursive computation given by

$$y(n) = \beta y(n-1) + x(n) - x(n-N) \quad (5)$$

Multiplication by the gain factor $(1 + \beta)/2N$ is performed on the sum of the absolute values of the output pixels in conjunction with normalization to obtain the mean value. This substantially reduces computational requirements.

It has been shown [4] that the signal-to-noise ratio of the output signal can be maximized for a given value of β by choosing the number of terms in the moving average according to

$$N = - \frac{1.2564}{\ln \beta} \quad (6)$$

This condition sets the memory requirements of the system in terms of previous input images that must be stored.

III. APPLICATION TO TEST STAND DATA

The system has been applied to visible wavelength image data acquired during an actual SSME test firing in which a premature shutdown occurred. Following the ignition sequence, the engine entered mainstage mode and operated normally for roughly 3.5 sec. At that time, hydrogen gas began to leak from the low pressure fuel turbopump (LPFTP). This leaked gas ignited intermittently, causing small flames about the powerhead for approximately 4 sec until a large flash fire was detected by an external sensor and the shutdown sequence was initiated.

Four image sequences of this test transcribed from film onto magnetic videotape were supplied by the National Aeronautics and Space Administration (NASA). These sequences correspond to four different views of the engine powerhead taken during the same test firing from data acquisition cameras which were denoted numbers 1, 6, 7, and 8 by NASA. Figure 1 shows the fields of view for each of these four camera positions. These images were acquired prior to ignition and therefore are clearer than those processed during the firing. The most prominent features in these photographs are the low pressure fuel turbopump (LPFTP) discharge duct (Fig. 1(a,d)) and the low pressure oxidizer turbopump (LPOTP) discharge duct (Fig. 1(b,c)). The LPFTP from which the leak occurred is barely visible in the upper right hand corner of Fig. 1(d) (camera position 8). (Because of the wide-angle lenses used on the cameras, features are

somewhat distorted.) Figure 1(a) (camera position 1) shows the typical vapor clouds that are present during an engine test.

This image data was transferred to an optical disc recorder/player and processed frame-by-frame with the leak detection algorithm. Because of the large amount of noise in this data, it was found that values for β and N of 0.91 and 13, respectively, were required for processing. (Use of higher values was limited by the number of frame buffers available in the image processor.) Processing began just prior to ignition following a pre-test synchronization flash and concluded with the post-test mode. For each sequence, a plot of the output mean value (average intensity of the output image) versus frame number was computed and is shown in Figs. 2(a-d).

The peaks in the plots of Figs. 2(a-d) correspond to the events occurring during the engine test. The peaks detected during ignition were caused by lights being turned on and by the plume forming at the bottom of the nozzle. Ignition also caused the nozzle to vibrate which shook loose frost that had accumulated on various cold engine components. These events caused the first large peaks in the output mean plots. As the engine entered mainstage mode, the mean value output reduced to that caused by the noise.

The leak near the LPFTP resulted in a large peak in the output mean value at approximately 6.1 sec in Fig. 2(d) (camera position 8), and smaller, but still noticeable peaks at the same time in Figs. 2(a) and 2(b) (camera positions 1 and 6). While the leak was detected in three of the four sequences, it was most obvious from camera position 8. The leak caused a flow that purged the vapor clouds normally surrounding the powerhead and cleared the field of view. Flames are visible from 6.1 to 10.1 sec in camera position 6 data and resulted

in substantial output mean values during that time as shown in Fig. 2(b).

The flash fire at 10.1 sec is evident in all the plots of Fig. 2. It was detected by the monitoring systems presently in use and the shutdown sequence was initiated. The engine vibration and water spray associated with shutdown and post-test procedures also result in large peaks in the output mean value in all four plots of Fig. 2.

As the plots in Fig. 2 show, if this system had been implemented for this engine test, the leak/no leak decision would have probably been positive at approximately 6.1 sec. Thus, the engine would have begun shutdown 4.1 sec before the systems presently implemented indicated. This analysis of these four data sets thus demonstrates the potential value of this technique for monitoring SSME test firings.

IV. SYSTEM SPECIFICATIONS

The conceptual structure of the system required to implement the leak detection algorithm is shown in Fig. 3 along with a summary of the nominal system specifications. An A/D converter (or frame grabber) digitizes the input video voltage signal. This data is then transferred via an internal data bus to one or more high-speed digital signal processors where the bulk of the numerical computations is carried out. The resulting output sequence of mean values is then transferred to the host computer for display and archival storage.

The proposed system is intended for standard RS-170 format input video signals with a framing rate of 30 Hz and 480 lines/frame. Adequate resolution is achieved by digitizing each line into 512 samples. The dynamic range of the intensity values can be covered with 8 bits (1 byte) per pixel. If this A/D conversion

operation is carried out in a dedicated frame grabber and data transferred to other processing hardware, the continuous transfer rate of the internal data bus is nominally 7.4 Mbytes/sec.

Examination of equation (5) shows that at each pixel, 3 arithmetic operations -- 1 multiply and 2 adds -- are required for the filtering process. Also, the absolute value constitutes one operation/pixel, and the sum over the field of view requires one operation/pixel. For a 480×512 image pixel array and a 30 Hz framing rate, the necessary effective processing speed is thus roughly 37 million operations/sec.

Memory requirements for the processors are governed by the number of terms in the moving average N , which is determined by the criterion given in equation (6). Practical experience with SSME test stand data has shown that up to 15 previous input frames in addition to the present can be required for proper performance. One additional frame is needed for the previous output frame. While input frames can be stored in 1 byte/pixel integer format, the output frame must be in 4 byte/pixel floating-point format. The total memory required is thus 5 Mbyte of access memory.

This system design is intended to compute the sum of the absolute values of the outputs defined by (5), normalize by the appropriate scale factor $((1 + \beta)/(2N \times 480 \times 512))$, and transfer those values to the host computer via its internal bus at the framing rate of 30 Hz. This produces the final mean value at discrete time intervals. This value will be written to disk for archival storage. In addition, the value can be compared with a threshold value during processing to determine whether the "red line" condition has been exceeded indicating a leak has occurred. Another feature is that a manual override from the keyboard must be

provided to prevent false alarms from occurring during the ignition sequence and other planned anomalous events.

Figure 4 is a block diagram of the recommended system. An overlay frame grabber (OFG) from Imaging Technology, Inc. was selected for the video digitizing function because of its ability to continuously output all frames of digitized video data over a standard synchronous digital data bus -- the VISIONbus. The VISIONbus data is split into four separate streams, each of which is routed to a separate Texas Instruments TMS320C40 32-bit floating-point digital signal processor using a custom-built interface board which sends either every fourth pixel or every fourth row of pixels to the same processor. This interface is the only custom-built component in the system and can be fabricated on a single PC-plug-in card with four synchronous first-in first-out memories (FIFOs) and five state machines. The four C40 processors are located on two Spirit-40 AT/ISA dual-C40 PC-plug-in boards from Sonitech International, Inc.

A C40 assembly language program was written to verify that the C40 processors can perform the processing of (5) in the time available. This program carries out the calculations of (5), takes the absolute value of the pixels computed from (5), and sums these absolute values. The program was run on a C40 simulator and was optimized to minimize the processing time required per pixel. With appropriate local and global bus memory, and 40 MHz C40 processors, the program requires 9 instruction cycles of 50 nsec each to process one pixel giving a total processing time of 450 nsec/pixel. Although pixels become available on the VISIONbus at an average rate of one every 136 nsec, each of the four C40 processors only receives a new pixel every 544 nsec. Thus, the 450 nsec/pixel processing time is sufficient to guarantee that incoming video data can be

continuously processed. Sufficient memory is available in this system for storing the image currently being processed and 15 past images. Therefore, a value as large as $N = 15$ can be used in (5).

V. CONCLUSIONS

A method for detecting abrupt, step-like changes in a time sequence of images has been developed, implemented on general-purpose equipment, and tested. The detection algorithm functions by filtering the input data with a cascade connection of a highpass filter and a moving average. The absolute value of the resulting image is then averaged over the field of view to determine a mean value estimate. This time-varying value can then be compared to a pre-set threshold to determine a "red-line" condition for shutdown.

This method has been applied to actual video data acquired during a SSME test firing. The analysis of the test-stand data indicates the applicability of this technique to actual SSME test firings and its ability to identify anomalous events.

A system has been identified and specified for real-time on-line implementation of this method for SSME leak detection. This system uses an IBM compatible personal computer as a host platform and an Imaging Technology Overlay Frame Grabber with the VISIONbus for data acquisition and transfer. Processing is carried out by four TMS320C40 processors located on two Sonitech Spirit-40 add-in cards and requires that a custom interface be fabricated to transfer data from the frame grabber to the processors. The processing algorithm has been programmed and proper timing to achieve the required effective throughput rate has been verified.

Future work in this effort includes examining the effectiveness of the algorithm in infrared imaging applications and other test stand data sequences. Work is also planned to extend this technique to color image processing to detect sudden changes in plume color that otherwise may not result in detectable intensity variations. Finally, application to actual launch-pad data is also a possibility.

ACKNOWLEDGEMENTS

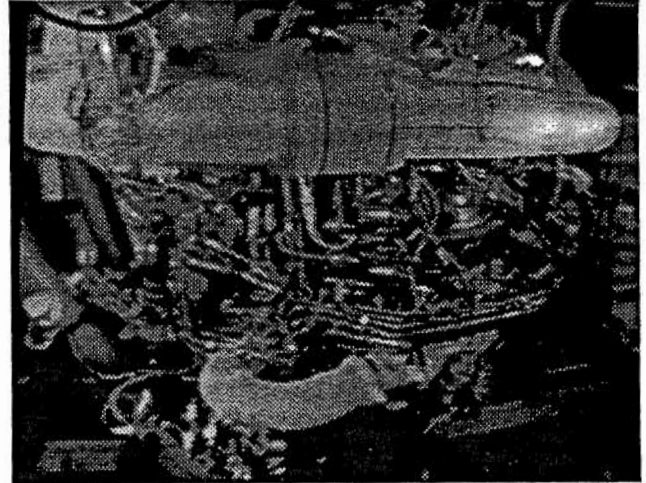
The authors would like to express their sincere appreciation to Prof. T. Dwayne McCay for several useful discussions regarding the SSME.

REFERENCES

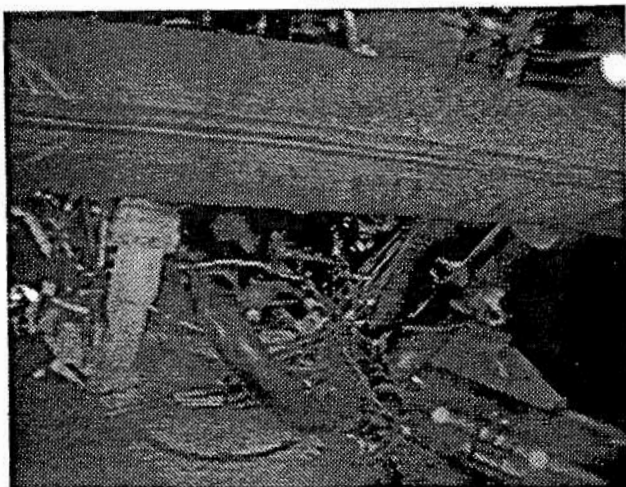
- [1] A. A. Shohadaee, "Leak detection feasibility investigation using infrared radiation transfer in absorbing, emitting and scattering media," Doctoral dissertation, Dept. of Mech. Engr., Univ. of Tennessee, Knoxville, TN, 1990.
- [2] A. A. Shohadaee and R. A. Crawford, "SSME leak detection feasibility investigation by utilization of infrared sensor technology," Center for Advanced Space Propulsion Second Annual Technical Symposium Proceedings, Tullahoma, TN, Nov. 1990.
- [3] J. A. Malone, "A system for leak detection using sequential image processing," Master's thesis, Dept. of Elec. Engr., Univ. of Tennessee, Knoxville, TN, 1991.
- [4] J. A. Malone and L. M. Smith, "A system for sequential step detection with application to video image processing," IEEE Trans. on Industrial Electronics, vol. IE-39, pp. 277-284, Aug. 1992.



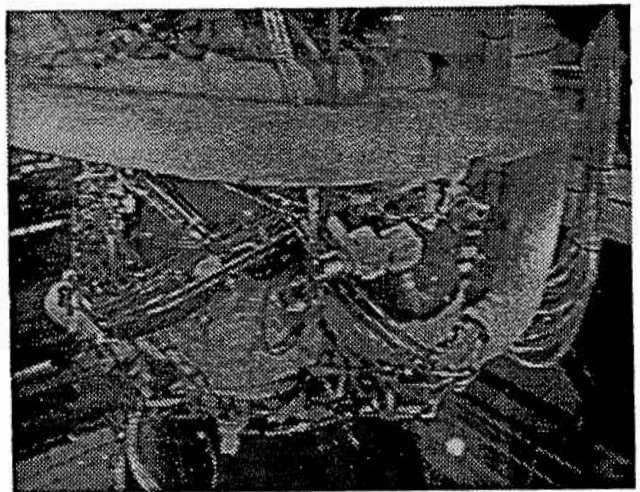
(a)



(b)

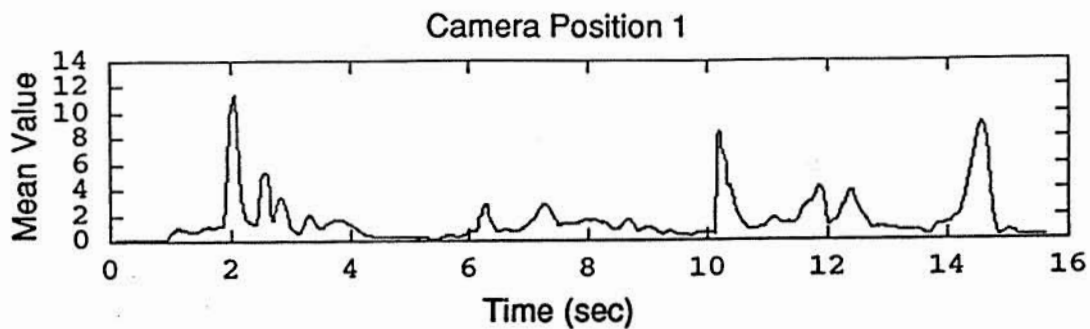


(c)

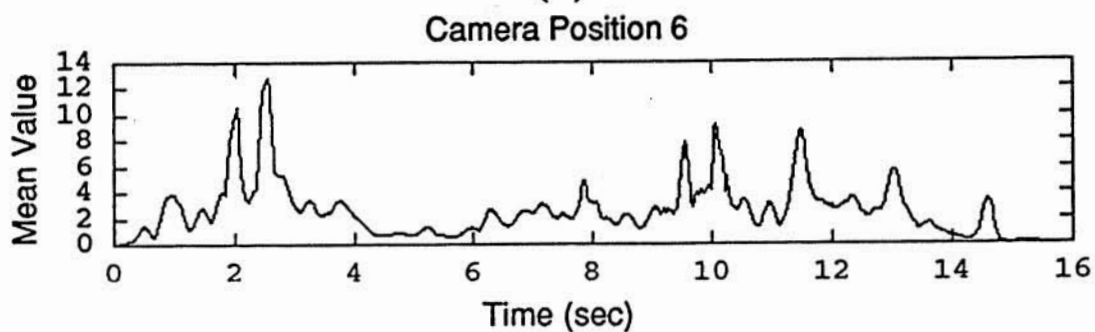


(d)

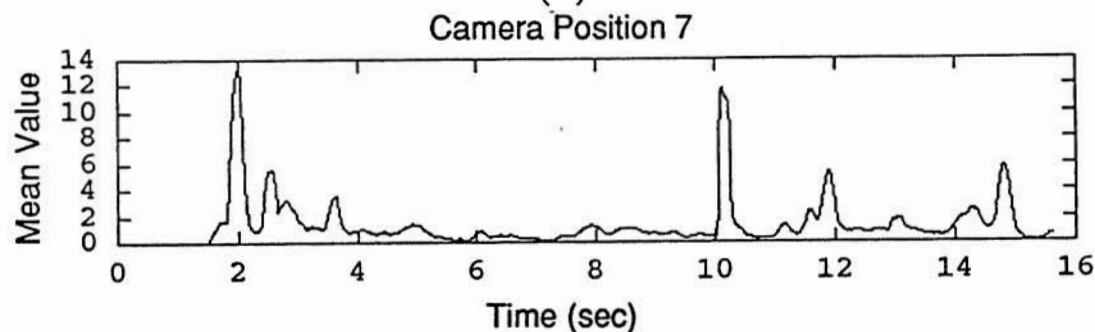
Figure 1. Fields of view for each of the four cameras: (a) position 1, (b) position 6, (c) position 7, (d) position 8.



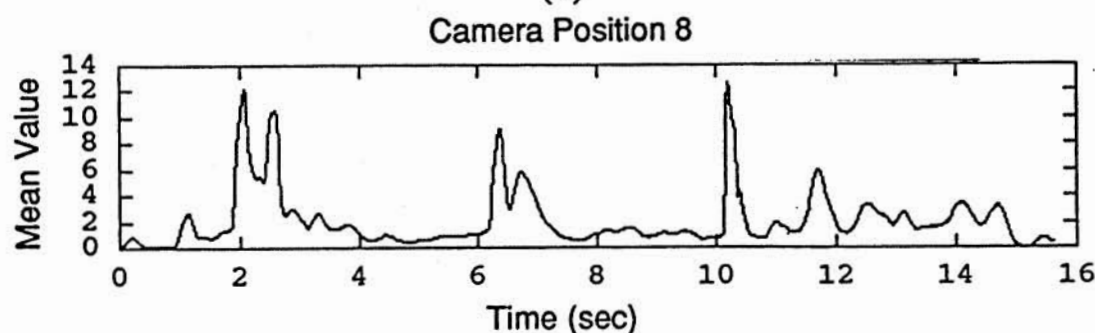
(a)



(b)

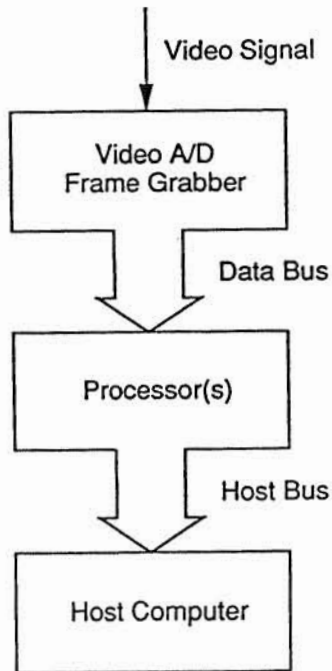


(c)



(d)

Figure 2. Mean value of output images versus time for test-stand video data. Note the detection of the leak near 6.1 sec. (Some initial data from camera position 7 (c) was missing, so output was set to zero in that range.)



Input: 30 frames/seconds

Format: 480 x 512 x 1 byte pixels/frame

Transfer Rate: 7.4 Mbytes/second

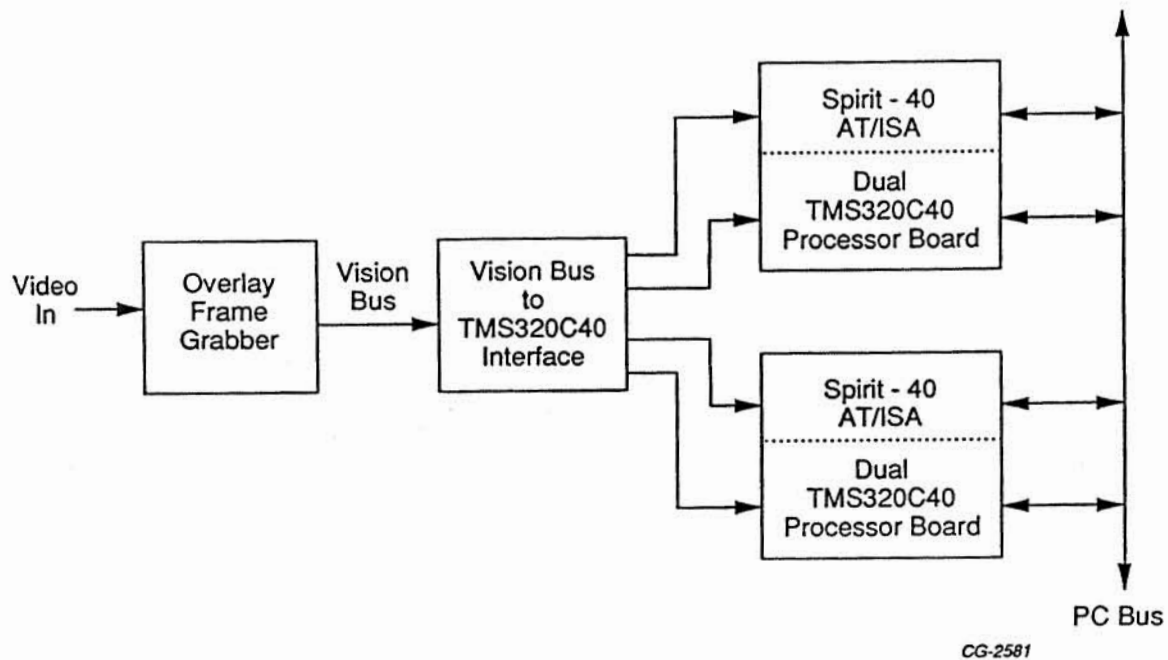
Memory: 16 previous frame buffers

Algorithm: 5 operations/pixels

Processing Rate: 37 MOps/second

CG-2497

Figure 3. Basic system configuration and nominal specifications.



CG-2581

Figure 4. Block diagram of recommended system using TMS320C40 processors.

GL-3120

OXYGEN-RICH COMBUSTION DEVICES

5950
P-20
Mr. William H. Knuth*
Dr. Roger Crawford+
Mr. Paul Gloyer++University of Tennessee - Calspan
Center for Space Transportation and Applied Research
The University of Tennessee Space Institute
Tullahoma, Tennessee 37388-8897**ABSTRACT**

Work has continued on the oxygen-rich combustion technology program, to develop the configurations and design parameters suited to operation in the highly oxygen rich combustion regime. The work has been performed in three areas: analytical modeling, empirical test planning and technology application studies.

Analytical modeling of the process has been initiated. The more complex aspects of the modeling are those which must predict the propellant mixing process in the combustion zone. Initial assessments of the model results indicate that a working combustor can be analyzed in sufficient detail to support the design process.

Work has also proceeded on the planning and preparation for testing of an existing Rocketdyne combustor, modified to operate with an oxygen-rich injector design. The combustor has windows which will allow observation and analysis of the combustion process. Testing will be accomplished in the new combustion test facility at UTISI. The combustor refurbishment has been completed by Rocketdyne, and the configuration for the test installation specified.

Application investigations were continued, and extended to include ground test facilities such as the large subscale solid rocket combustion simulator (LSSRCS), being installed at MSFC, as well as Hybrids and advanced modular booster rockets.

COMBUSTION MODELING

Modeling of LOX/LH2 combustion processes at mixture ratios far from stoichiometric is not a precise analytical task. It is difficult to model reacting flow fields with large temperature gradients and the temperature at nor near the ignition temperature. When the temperature is above the ignition temperature, the propellants will react and heat is released. When the temperatures remain below ignition temperature, the propellants merely wash downstream as mixed gases.

Since the un-ignited propellants do not contribute heat of combustion, the temperatures are even lower

than might be anticipated on the basis of mixture ratio alone, further reducing the likelihood of complete combustion of the fuel species.

In our modeling, we have assumed, as a starting point, that all of the hydrogen has been brought to ignition temperature and burned, in order to avoid the temperature profile uncertainty noted above. To make this assumption valid, we have designed a combustor which enforces the conditions necessary to make the assumption valid.

Specifically, the combustor uses a LOX film-cooled central combustion can which operates at a mixture ratio close to stoichiometric. This produces temperatures well above that needed for ignition, and assures that any hydrogen present will react with the abundant oxygen atmosphere. It is the intent that all combustion occurs within the can envelope.

* CSTAR Assistant Director, Chemical Propulsion
+ UTISI Professor, CSTAR Principal Investigator
++ UTISI/CSTAR Graduate Research Assistant

The combustion products exiting the can are bathed in cold fresh oxygen, which mixes and blends with the hot gases. With appropriate mixing, the constituents reach a well-stirred state which provides a uniform temperature, highly oxygen-rich, gas as the output product of the combustor.

This configuration approach assures the full combustion of the hydrogen and allows the analysis to focus on the time-averaged mixing processes and the heat and mass transfer of the device, as opposed to attempting to model highly non-linear, and time-varying processes.

Another fortunate aspect of this approach is that the physical device is durable, in that it is of no benefit to design close to thermal limits. The mixture design ratios are in the range of 80-120:1. Temperature of the well-mixed products will be on the order of 200 to 500 degrees F. These benign temperatures mean we can design and build the combustor with confidence, and obtain empirical data to refine and extend the analytical model.

ANALYTICAL MODELING

[This section is presented in the format of the original paper prepared by P.W. Gloyer]

OXYGEN RICH COMBUSTION GAS GENERATOR TECHNOLOGY

P.W. Gloyer, W.H. Knuth, R.A. Crawford

University of Tennessee - Calspan
Center for Space Transportation and
Applied Research

The University of Tennessee Space Institute
Tullahoma, Tennessee 37388-8897

ABSTRACT

This paper describes oxygen rich combustion research which is being carried out at The University of Tennessee Space Institute with the support of the Center for Space Transportation and Applied Research. The focus of the research is the investigation of oxygen gas generator concepts for use with liquid rocket engines. The theoretical and modeling aspects of a selected concept are

presented, together with a refined concept resulting from the findings of the study.

1. INTRODUCTION

Oxygen rich combustion has the potential to open up new rocket engine cycles for use. One aspect of this technology, is the vaporization of liquid oxygen by an oxygen gas generator.

In conjunction with the development of the oxygen gas generator, several other areas need to be investigated. The compatibility of materials with oxygen at various temperatures, pressures and states needs to be affirmed to the extent necessary for the conditions which will be encountered within the gas generator.

In some gas generator designs, the two phase flow properties and heat transfer of oxygen, (transport properties) will effect the configuration as well as the technology requirements. This becomes a significant factor in selection of the design and in planning the necessary research. To the extent practical, a design which avoids unproven technical issues is sought.

Oxygen-rich combustion research was conducted in the mid 1960's. This research stopped for various reasons, including the preception of potential operational difficulties. Other cycles were selected for study and application, and research on oxygen gas convertors waned.

In the early '80's research on oxygen began to appear again. One focus was on the use of oxygen as a coolant,(Ref. 3, 4 and 5), in rocket engines. Other interest developed at Acurex, Aerojet, Rocketdyne and others, (Ref. 1, 2, 8, 11 and 18) in the use of oxygen, as a working fluid in oxygen driven turbopumps.

Since earlier research, technology in materials, combustion and computation has been developed which makes the use of oxygen as a working fluid much safer. The use of oxygen as a coolant and as a turbine drive gas in rocket engine cycles has the potential to improve performance and reduce cost. These advantages are the result of the large reduction in turbine operating temperatures, as well as design simplifications throughout the entire propulsion system.

The research summarized within this document involves the early stages of the development on an oxygen-rich gas generator concept. The author's work was performed at The University of Tennessee Space Institute with funding and assistance from the Center for Space Transportation and Applied Research. This work is part of a research program to develop technology and gather information leading to the development of an operational oxygen-rich preburner for use in a new rocket engine family.

The work focuses on the computer modeling, and design development of a conceptual regeneratively heated oxygen gas generator. As the work progressed, it became evident that several areas of analysis and design complexity could be avoided by a design approach which substitutes direct contact heating for regenerative heating originally envisioned. These findings are noted at appropriate points in the report, and the alternative design concept is described.

2. APPLICATIONS

An operational oxygen-rich gas generator has several potential applications in rocket propulsion systems. These applications have the potential to reduce cost and increase performance. Performance improvements result from the ability to use oxygen as the turbine working fluid, which opens the way to use cost-effective topping and expander cycles, which do not waste propellant overboard. It is also practical to operate at higher chamber pressures, with lower gas turbine inlet temperatures, than with bleed cycle engines, See References 1 and 2.

Several engine cycles benefit from the use of an oxygen gas generator in this manner. These cycles include the augmented expander, the full flow staged combustion and the LH₂ staged combustion/expander hybrid.

The Fuel-only topping cycle, such as SSME, uses hydrogen-rich gas to drive the LOX turbopump. One problem with this cycle is that hydrogen rich gas is on the turbine side of the turbopump, while liquid oxygen is on the pump side. This requires the use of a positive dynamic shaft seal between the turbine and the pump. The dynamic shaft seal adds

significant cost, lower reliability and greater complexity.

An oxygen-rich gas generator, in a full flow topping cycle, provides oxygen-rich gas to drive the LOX turbopump turbine so the dynamic shaft seal can be eliminated. The reduced complexity results in a safer and more reliable turbopump.

Additional benefits arise from the use of this oxygen gas generator cycle, by designing the turbopump to take advantage of the properties of an oxygen rich flow. A typical LOX/LH₂ rocket engine runs at a mixture ratio of about 6.0. This means there is roughly six times as much oxygen mass flow as there is hydrogen mass flow. The oxygen rich gas is less energetic on a per lb basis, but still has ample energy to drive the LOX turbopump, even at cool temperatures. The turbine power equation:

$$P = mc_p (T_{o \text{ in}} - T_{o \text{ out}})$$

can be used to illustrate the comparison between oxygen drive gas and hydrogen drive gas. If we ratio this expression for the two gases we get:

$$\frac{P_O}{P_H} = \frac{M_O}{M_H} \frac{C_{PO}}{C_{PH}} \frac{\Delta T_{OO}}{\Delta T_{OH}}$$

This shows that the high mass flow of oxygen available makes up for the higher energy content of the hydrogen. Also, since all of the hydrogen (about 30% more), can now be used to drive the LH₂ turbopump, a significant temperature reduction is available there as well.

The cool oxygen gas has significantly higher molecular weight than the hydrogen rich gas. From the expression for the turbine nozzle ideal exit velocity, C_o , it is shown that the high molecular weight will result in a low C_o for Oxygen at a given temperature.

$$C_o \approx \sqrt{\gamma R T_o}$$

Since Turbine performance is related to the ratio U_t/Co , it is observed that a low turbine tip speed (U_t) is desired for oxygen rich drive gas, which has a low Co . This results in low centrifugal stresses in the blades and disks. (see Reference 1 and 2.) The lower temperature and speed eliminates the need for exotic turbine materials. This reduces the turbopump cost and allows designs which result in greater safety and reliability.

Another possible use of the oxygen gas generator is as the pressurant source for LOX tanks. For such applications, the liquid oxygen would be vaporized and fed into the LOX tank tank pressure. This would eliminate the need for nitrogen or helium tanks for pressurization of the LOX tank.

3. CHARACTERISTICS

The concentric counter flow generator concept, see Figures 1 and 2, that was the initial focus of this research, has the following features and characteristics:

- * The annular LOX flow is regeneratively heated by the high temperature oxygen-rich combustion products within the inner tube.
- * The LOX is to be completely vaporized in the annulus prior to reaching the injector.
- * The prototype generator will operate at mass flow rates of approximately 1.0 lbm/sec.
- * The generator will operate at overall mass mixture ratios of approximately 100 - 200.
- * The combustion region will use an annular oxygen sheath around the flame for cooling.

The gas generator, see Figures 1 and 2, operates by admitting liquid oxygen into the base of the annular region between the outer tube and the inner tube, (chamber liner). The liquid oxygen flows up the annulus, while being heated from the inner tube. In the original concept, the liquid oxygen will boil as it moves upward through the annulus, until it is completely vaporized.

The chamber liner is perforated to allow small amounts of oxygen vapor to pass into the inner tube

to serve as film coolant. At the upper end of the annulus, the remaining oxygen vapor enters the injector. The injector meters the oxygen flow and provides the injection pattern for mixing with the fuel.

Hydrogen gas is injected into the flow in a coaxial pattern which has proven effective in other oxygen-hydrogen burners. The flame zone will be located between the hydrogen stream and the oxygen stream. References 13, 14, 15, 16, 19 and 20 discuss the flame mechanics. The injector pattern provides for all of the hydrogen to be injected in a local region at the center of the injector. Local mixture ratio will be on the order of 30 to 40. This will produce a high enough temperature to assure complete combustion of the hydrogen.

The oxygen rich stream outside of the core combustion zone will serve as a heat sink and insulator to help keep the combustion products from reaching the liner and to keep the liner well below ignition temperature, see Figure 3.

The oxygen that flows through the perforations in the liner is added to the oxygen rich region, as the flow moves downward through the inner tube, to cool the combustion products in the mixing flows.

The reacted flow is mixed completely to give a uniform flow temperature. The final temperature will be the result of the overall mixture ratio chosen for the design. The flow is then directed out of the device.

It is recognized that this type of gas generator has several features which would be desirable to avoid. In particular, vaporizing the oxygen before injection presents analytical and design complexity and operational risk.

4. ANALYTICAL MODEL

An understanding of the physics and operation of the oxygen gas generator is a necessary part of the technology program. This section discusses a computer program developed to model the fluid mechanics and heat transfer of the oxygen gas generator. It also describes areas of potential problems and means identified to circumvent such areas.

4.1 Assumptions

The modeling of the gas generator focuses on the bulk fluid properties. The model assumes one-dimensional axisymmetric flow in the calculations. The boundary layer and radial flow influence has been neglected.

Since the phase change of the LOX in the annulus is a dominant factor in the model, the energy equation plays a major role in the code development. An accurate accounting of the flow energies is necessary to ensure LOX vaporization without generator failure. Generator failure was assumed to occur when wall material reaches ignition temperature.

The conservation of mass equation is used to account for the mass flow of the oxygen and hydrogen through the generator. It was decided that the momentum equation could be ignored at this early stage for several reasons. The first is that the velocities everywhere are relatively low so the momentum terms are negligibly small. Since the main part of the operation of the generator involves the energy transfer and generation, the energy equation is of more importance to the design. Also, the pressure drop through the generator can be calculated with sufficient accuracy for design, and will be calibrated and accounted for in the supply pressure settings once the generator is built.

So, the model deals only with the mass and energy equations shown below:

Mass:

$$M_{\text{mix}} = M_{\text{LOX}} + M_{\text{H}_2}$$

Energy:

$$M_1 * C_{p_1} * T_1 + M_H * C_{p_H} * T_H + Q_{\text{gen}} - M_1 * L - M_m * C_{p_m} * T_m = 0$$

where:

M_{mix} = Mass Flow of the Mixture of Hydrogen and Oxygen

M_{LOX} = Mass Flow of the Liquid Oxygen

M_{H_2} = Mass Flow of the Hydrogen

M_1 = Mass Flow of the Liquid Oxygen

C_{p_1} = Specific Heat of LOX at Injection

T_1 = Temperature of LOX at Injection

M_H = Mass Flow of the Hydrogen

C_{p_H} = Specific Heat of Hydrogen at Injection

T_H = Temperature of Hydrogen at Injection

Q_{gen} = Heat Released from Hydrogen Oxygen Combustion

L = Heat of Vaporization of LOX

M_m = Mass Flow of the Mixture of Hydrogen and Oxygen

C_{p_m} = Specific Heat of the Mixture at the Exit

T_m = Temperature of the Mixture at the Exit

4.2 Computation

The model makes use of known input and exit conditions of the generator and incrementally computes conditions along the generator length. The model computes the characteristics of the annular flow and the inner flow simultaneously using control volumes and determines the heat transfer between the control volumes. This information is then used to determine the flow characteristics at the next location, see Figure 4. The model increments toward the injector and adjusts the generator length to achieve complete vaporization of the LOX. At the same time the program establishes matching flow properties for the inner and annular flows based upon continuity.

The approach is made complex by the need to account for the heat transfer and phase change processes. A design which does not require such a phase change, and therefore does not require heat transfer considerations along the liner length would be less complex analytically, as well as in design and experiment. A design which maintains liquid upflow in the annulus achieves the simplification desired.

4.3 Combustion

Control of combustion and combustion stability in the inner tube, see Figure 3, is necessary. Control of the combustion, in effect, means control of local mixture ratios and mixing. If the combustion occurs too fast, i.e. too close to the injector face, local temperatures may become too high (over 3600 degrees K for stoichiometric) and the injector will suffer typical face burnout caused by incorrect injector pattern. This problem is seldom experienced with coaxial injectors which tend to spread the combustion zone out due to the protracted mixing length of the coaxial streams.

As noted, the combustion temperature is controlled by the mixture of the gases. The temperature of this combustion is chosen to be above the ignition temperature of oxygen-hydrogen mixtures in order to assure that all the hydrogen is reacted. Around the central combustion zone, a sheath of pure oxygen is injected to shield the liner from contact with the combustion products. The sheath of pure oxygen acts upon any stray hydrogen to prevent combustion from occurring near the tube wall. Additional cold oxygen is added to the sheath from the annulus by mass transfer through the holes in the liner tube.

After a distance determined by the character of the flow, the flame in the inner tube may become unstable. This should not be a problem in the combustor of the mixture ratio and geometry being considered here. However, if it should happen,

turbulent mixing of the combustion products and the protective pure oxygen sheath could occur. This could lead to excessive wall temperatures

A simplified laminar diffusion flame is assumed as a first estimate in the combustion model. This simplification is acceptable at this level of research since the combustion region is a small part of the entire length. The heat generated by the flame is assumed to be distributed evenly along the length of the flame in the model. These model assumptions will be refined when test data becomes available.

4.4 LOX Vaporization

The liquid oxygen vaporization at high pressure in the gas generator is one of the most complex and important parts of this technology. Several factors make analytical prediction of the vaporization difficult. The vaporizing flow is moving in an annular region between two tubes. Since the outer tube wall must be thick to structurally contain the high pressure flow, an insulated outer wall can be assumed.

A second factor is that the flow in the annular outer tube is coupled to the flow in the inner tube due to the regenerative nature of the generator. The boiling rate of the LOX is dependent upon the heat flux

across the inner tube (liner) wall. The heat flux depends on the temperature difference, the liner thickness and the flow properties of both flows. The difficulty is that the inner tube flow is downstream of the annular flow and is therefore dependent upon the boiling upstream. The model overcomes this coupling by calculating simultaneously the inner and annular flow properties starting from the LOX input and oxygen output and working towards the hydrogen injector.

4.5 Heat Transfer

The heat transfer through the liner from the inner flow to the outer annular flow is the primary factor in the operation of the gas generator. Without heat transfer, the liquid oxygen would not vaporize until it arrived at the combustion zone. The heat transfer across the liner at each location is a combination of two convective layers and one conduction layer. The conduction layer is determined by both the liner thermal conductivity and thickness and the temperature difference across the liner.

$$q_r = -k (2 \pi r L) dT/dr$$

The convective layer on the inner surface of the liner is easily determined since the fluid is all gas in the inner tube.

$$q_r = h (2 \pi r L) \Delta T$$

with the convective coefficient, h , being determined from the appropriate Nusselt number.

The convective layer on the outer surface of the liner is more difficult to model. This layer has three regions which can be treated separately. The first is when all of the fluid is liquid and the boiling is negligible. This convective layer is also determined from the convective equation above but using the liquid properties. The third region is when all of the fluid is gas and the droplets are negligible. This convective layer also uses the convective equation above with the gas properties.

The second region is more complex. This region is where there are two phases of fluid present due to boiling. This region has many subregions and is difficult to model without extensive experimentation. As a first estimate, a model developed by Chen

(1963) was taken from Reference 12, where it is discussed in detail.

These equations were combined in the model and are used to compute the heat transfer across the liner.

The following are the equations that pertain to the heat transfer calculations:

$$Q = \frac{A * (T_i - T_a)}{\frac{1}{h_i} + \frac{R}{k} * \ln\left(\frac{R+t}{R}\right) + \frac{\left(\frac{R}{R+t}\right)}{h_a}}$$

where

A = Inner Surface Area of Liner Segment
 T_i = Temperature of the Inner Tube Flow
 T_a = Temperature of the Annular Tube Flow
 h_i = Convective Coefficient on the Liner Inner Surface
 h_a = Convective Coefficient on the Liner Outer Surface
R = Inner Radius of Liner
t = Thickness of Liner
k = Liner Thermal Conductivity

For the LOX and the oxygen gas segments in the annular tube:

$$h_a = Nu * K / D_H$$

where

h_a = Convective Coefficient on the Liner Outer Surface
Nu = Annular Flow Nusselt Number
K = Annular Flow Thermal Conductivity
 D_H = Hydraulic Diameter of Annular Flow
For the inner flow segments:

$$h_i = Nu * K / 2 * R$$

where

h_i = Convective Coefficient on the Liner Inner Surface
Nu = Inner Flow Nusselt Number
K = Inner Flow Thermal Conductivity

R = Inner Radius of Liner Tube

For the two phase annular flow, from Reference 12:

$$XP = \left(\left(\frac{1 - X_i}{X_i} \right)^{.9} \left(\frac{\rho_v}{\rho_l} \right)^{.5} \right) \left(\left(\frac{u_l}{u_v} \right)^{.1} \right)$$

$$F = 1 / XP$$

$$Nu = .023 Re^8 Pr^4$$

$$h_i = Nu_i * K_l / D_H$$

$$H_{FC} = h_i * F$$

$$H_{NB} = 8 * (T_{liner} - T_{boil})^2$$

$$H_{2ph} = H_{NB} + H_{FC}$$

where:

XP = Model Variable
 X_i = Flow Quality
 ρ_v = Vapor Density
 ρ_l = Liquid Density
 u_l = Liquid Viscosity
 u_v = Vapor Viscosity
F = Model Variable
Nu = Liquid Nusselt Number
 K_l = Liquid Thermal Conductivity
 D_H = Hydraulic Diameter of Annular Flow
 H_{FC} = Forced Convective Coefficient
 H_{NB} = Nucleate Boiling Convective Coefficient
 T_{liner} = Temperature of Liner
 T_{boil} = Boiling Temperature of Oxygen
 H_{2ph} = Two Phase Flow Convective Coefficient

5. MODEL RESULTS

Figure 5 shows the trends of the model for various mass flows. As can be seen, the desired exit temperature has a significant affect on the generator

length that is required to vaporize all of the LOX before injection.

Figure 6 compares the gas temperature obtained from the model for various oxygen/hydrogen mass ratios with the predicted temperatures from NASA SP 273, Reference 21, runs for various oxygen/hydrogen mass ratios, see Figure 8. Figure 6 shows good agreement between the model and NASA SP 273 predictions.

Figure 7 shows the temperature profile of the inner tube for a mass flow of 1.0 lbm/s and a desired exit temperature of 1500°R. According to Figure 7 the flow does not reach the stainless steel ignition temperature of 1650 deg K.

6. CONCERNS

One failure mode that has a strong influence on the generator design is the compatibility of the generator materials with the high pressure warm oxygen gas. Care must be taken in the selection of the generator material. Some materials are more resistant to oxidation than others and should be used in the generator where possible. References 7, 9, 10, 11 and 17 discuss the oxygen materials compatibility.

Two materials with good oxygen resistance are stainless steel and copper. One of these materials could be used in the liner. The stainless steel has good strength allowing a thin wall, while the copper has a high thermal conductivity allowing a thicker wall to be used for the liner. The final selection of the materials will be made in the final design. But even with oxygen resistant materials, care must be taken to keep the generator operation within the materials compatibility limit.

A transition through the stoichiometric combustion mixture ratio on start up may cause materials failure due to the elevated flame temperature, as shown in Reference 6. This can be avoided by starting the oxygen flow prior to the introduction of the hydrogen.

7. NEW CONCEPT

The operation of the generator with two phase flow, as in the original concept, is undesirable from an engineering view point. The presence of a two

phase flow with a variable gas/liquid ratio hinders the predictability of the generator. The fluid properties of two phase oxygen are not well known because they are continually changing in the generator due to boiling. The convective heat transfer due to the two phase flow is difficult to predict, as discussed in Reference 12.

To overcome these problems, new concepts are being investigated. One version operates above critical pressure, (720 psia), (5 MN/m^2), to avoid the "steam dome" for oxygen, see Figure 9, when heated. Operating the generator above the critical pressure of oxygen avoids the phase change problems. In this region, the density change from liquid to gas is smaller and predictable.

In the new concept, the high pressure LOX will be heated to a temperature above 160 degree K while flowing in the annular region, see Figure 2. When the oxygen is sufficiently heated, the flow will be turned from the annular tube to the inner tube. A pressure drop across an injector plate will transition the LOX to gas. The gaseous oxygen will form a sheath around the hydrogen, as in the original concept.

The problem of having to operate the unit as a heated wall still exists, as does the potential for liner overheating. A gas generator that does not require such a heat transfer device is called a direct contact heater, wherein the heat to vaporize the LOX is delivered by mixing the combustion products directly with the oxygen to be heated and allowing the heat to be transferred by mixing the two.

This approach seems to offer a high degree of margin, since no materials exceed the temperature of the final mixed gases, and most of the unit operates at LOX temperature. Analysis and design are greatly simplified and precision of analytical results is not necessary because all surfaces can be grossly over-cooled by the abundant surplus oxygen.

More investigation is necessary for these new concepts before any conclusions can be reached. But, these concepts appear to have the characteristics that make further investigation worthwhile.

This work has been performed at The University of Tennessee Space Institute, with funding and

assistance from the Center for Space Transportation and Applied Research.

8. REFERENCES

1. Knuth, W.H., and Crawford, R.A., Oxygen-Rich Combustion Process Applications and Benefits, AIAA-91-2042, June 1991.
2. Knuth, W.H., Full-Flow Staged Combustion Cycle Application to Advanced Transportation, Acurex Corp., Huntsville, AL, October 1989.
3. Price, H.G., Cooling of High-Pressure Rocket Thrust Chambers with Liquid Oxygen, J. Spacecraft and Rockets, Vol. 18, No. 4, 1980, pp. 338 - 343.
4. Armstrong, E.S., Liquid Oxygen Cooling of Hydrocarbon Fueled Rocket Thrust Chambers, AIAA-89-2739, July 1989.
5. Armstrong, E.S. and Schlumberger, J.A., Cooling of Rocket Thrust Chambers with Liquid Oxygen, AIAA-90-2120, July 1990.
6. Bailey, C.R., A Preliminary Investigation of Oxidizer-Rich Oxygen-Hydrogen Combustion Characteristics, NASA TM-X-53371, MSFC, AL, December 1965.
7. Bransford, J.W., Ignition of Metals in High Pressure Oxygen, NASA-CP-2372, June 1984, pp. 134-148.
8. Kramer, R. and Martin, J., Underdeveloped Rocket Cycle Applications to Advanced Earth to Orbit Transportation, AIAA-90-2438, July 1990.
9. Stoltzfus, J.M. and Benz, F.J., "Determination of the Relative Resistance to Ignition of Selected Turbopump Materials in High Pressure Oxygen," NASA JSC-WSTF-TR-324001.
10. Aerojet Tech Systems Co., Final Report Oxygen Materials Compatibility Testing, NASA CR-182195, January 1989.
11. Acurex Corp., Final Report "Materials Compatibility with Oxidizer Rich Gases at Elevated Temperatures and Pressure, NASA Contract NAS 8-36713, June 10, 1987.
12. Whalley, P.B., Boiling Condensation and Gas-Liquid Flow., Oxford University Press, New York, NY, 1987.
13. Beer, J.M., and Chigier, N.A., Combustion Aerodynamics, Halsted Press Division, John Wiley & Sons Inc., New York, NY, 1972.
14. Shchelkin, K.I., Gasdynamics of Combustion, Mono Book Corp., Baltimore, Maryland, 1965.
15. Bradley, John N., Flame and Combustion Phenomena, Methuen and Company LTD, London, England, 1969.
16. Gaydon, A.G., Flames Their Structure, Radiation and Temperature, Halsted Press, John Wiley & Sons Inc., New York, NY, 1953.
17. Hust, J.G. and Clark, A.F., A Survey of Compatibility of Materials with High Pressure Oxygen Service, Cryogenics June 1973, pg 325 - 336.
18. Peroulis, C. et al., Boiling Oxygen Experimental Studies in an Electrically Heated Tube, AIAA-88-2842, 24th Joint Propulsion Conf., 1988.
19. Hersch, Martin, Hydrogen-Oxygen Chemical Reaction Kinetics in Rocket Engine Combustion, NASA-TN D-4250, Dec. 1967.
20. Clarke, J.F. and Moss, J.B., On the Structure of a Spherical H_2-O_2 Diffusion Flame, Combustion Science and Technology, Vol 2, 1970, pg 115-129.
21. Gordon and McBride, Computer Program for Calculation of Complex Equilibrium Compositions, NASA SP-273, NASA Lewis Research Center, 1971.

TEST PLANNING

FACILITY

The UTSI combustion devices test laboratory is a newly completed facility, which offers convenient capabilities for hot firing model and full scale combustors, gas generators and small rocket engines. Five individual test cells in a modern facility setting are available. Propellants can be brought in by

tanker truck, and/or tube trailer and delivered to the test either in liquid or gas form. Plans include provision for on-site propellant storage and supply, as budget permits and the rate of testing requires.

TEST HARDWARE

For this phase of the program, Rocketdyne has a need to test an existing combustor that had been used for combustion diagnostics tests.

Although it does not embody all the features described in the section on analytical models, it does allow a significant degree of combustion process observation and instrumenting. It is of a size that fits the UTSI test facility capability, and is available at only the cost of window refurbishment. Rocketdyne is proceeding with the refurbishment effort.

An alternate test combustor design has also been identified. It is designed and sized to serve as a LOX tank pressurization device. This combustor is configured more like the analytical model, and may be more directly compared to the theoretical results. It would also have the advantage of serving as a pre-prototype for a flight-type gas generator for LOX tanks. Once testing of the Rocketdyne combustor is done, consideration will be given to the fabrication and testing of a flight-type design.

There is still another set of Oxygen-rich combustion hardware in existence. This is a 4000 lbf thrust, LOX/RP-1 staged combustion liquid rocket motor. It was originally designed to demonstrate the freedom from combustion instability at low chamber pressure, and with low injector pressure drop. It has been fired extensively in the staged combustion mode, but limited results are available from the oxygen-rich first stage chamber. We will seek an approach by which to obtain this combustor for further testing.

APPLICATIONS ASSESSMENTS

Most applied technology programs undertaken by a CCDS involve a significant level of application feasibility investigation.

CSTAR is actively pursuing studies of propulsion systems and combustion devices which would use the technology of oxygen-rich combustion, and/or combustion devices. Much of the work has been

focused on rocket applications. In particular, we have extended previous studies to encompass applications to large liquid propulsion systems and to HYBRID rockets of all sizes.

One feature being stressed in the application studies is modularization. In full topping cycle propulsion, the propellant turbopumps are quite independent and self-contained. They need only a small amount of the opposite propellant for their operation. It is therefore practical to cluster turbopumps into pump galleries (or modules) wherefrom all turbopumps feed all chambers. This approach is particularly attractive when the output of the pump module is high pressure, cool gaseous propellant, which can be safely piped and regulated to thrust chamber modules. Modular systems allow propulsion components to be developed as separate, self-contained systems, capable of being combined and integrated, building block style, into several vehicle types and sizes. This approach avoids the need to make a commitment to a specific new vehicle program before the details of the components are known. It allows proven components to be integrated into new applications without the need to await an advanced technology. It provides an avenue for incorporating evolutionary technologies into existing vehicles. It also avoids the risk that some critical technology will not mature in time for vehicle needs, and cause a major program setback.

HYBRIDS

Hybrids also present an application opportunity for the oxygen-rich combustion technology. In particular, the pump-fed hybrids may derive design benefits.

Rocket turbopump designs in which the turbopump function is to convert low pressure liquid oxygen from the tank to high pressure gaseous oxygen for delivery to the fuel grain can be readily developed. Such turbopumps have been studied at CSTAR, and shown to be simple, low cost, safe and reliable. They compare favorably with pressure-fed systems in terms of cost, weight, safety, performance and reliability.

The hybrid rocket designer can design the rocket for a gas-fed fuel grain, a gas-type injector, and gas injection into the secondary chamber, if used. Avoiding the need to pipe high pressure cryogenic

liquids around the rocket reduces cost, improves safety and reduces operating complexity.

ACKNOWLEDGEMENT

Support for this project is provided partially by Rocketdyne Division, Rockwell International Corporation, Canoga Park, CA and partially by UT-Calspan Center for Space Transportation and Applied Research, Tullahoma, TN, under NASA Grant No. NAGW-1195.

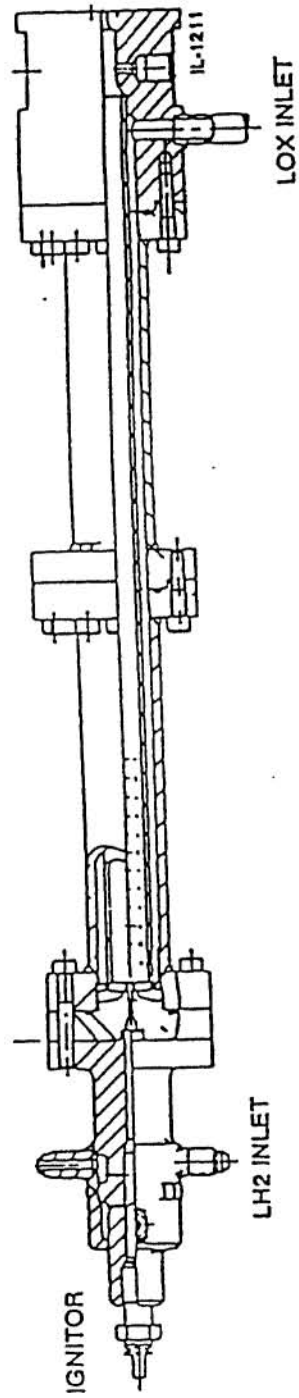


Figure 1 Oxygen Gas Generator

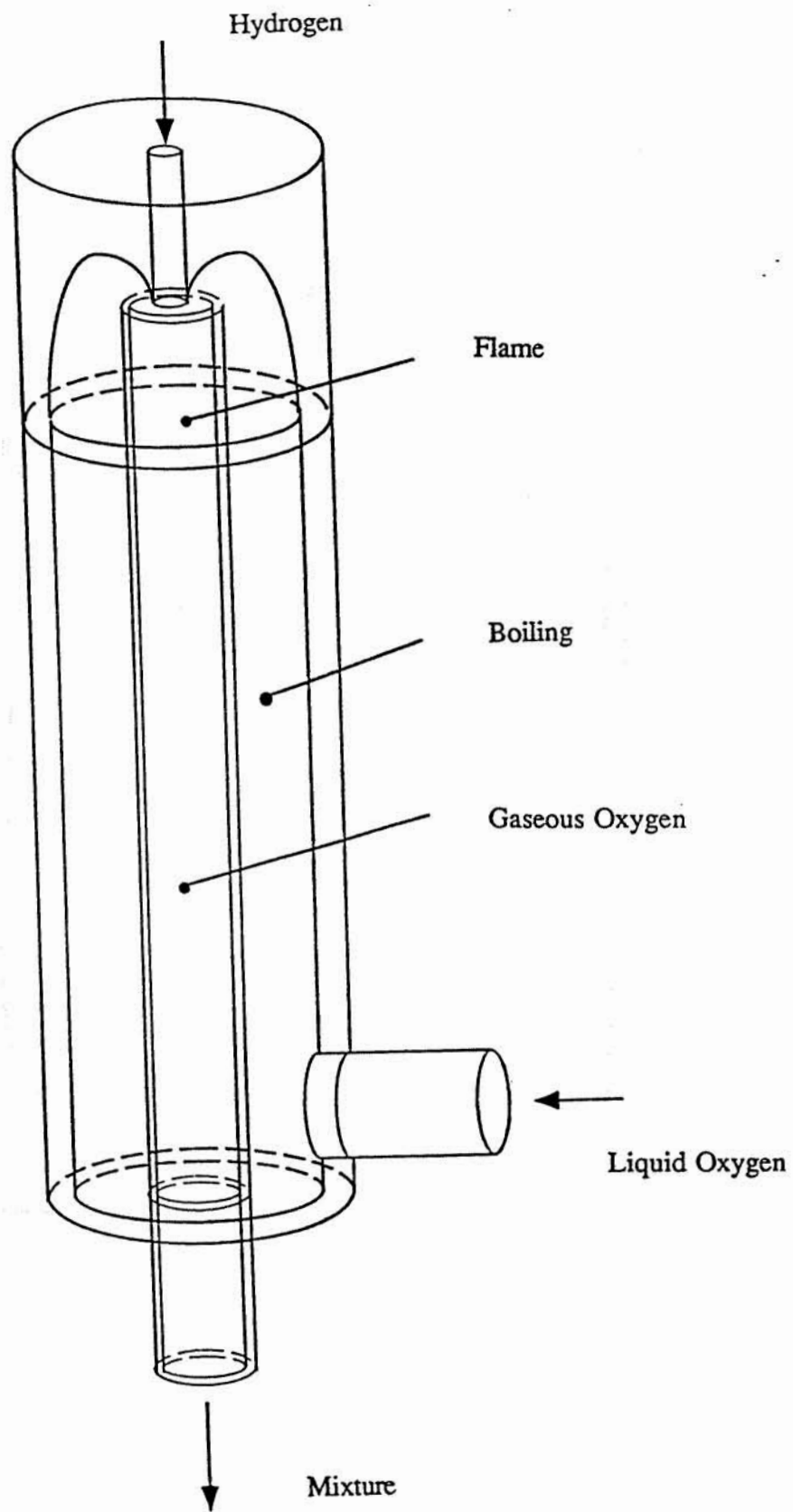


Figure 2 - Oxygen Gas Generator Schematic

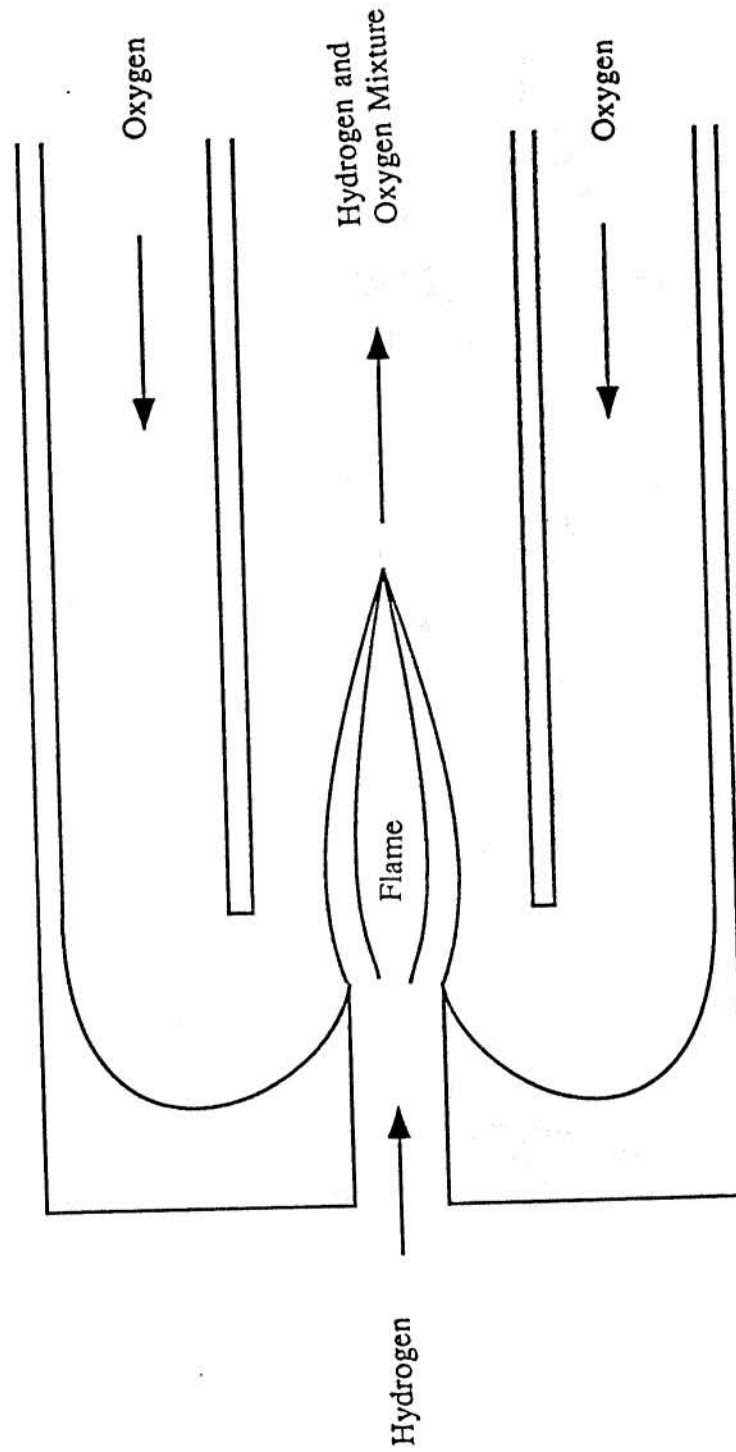


Figure 3 - Combustion Region

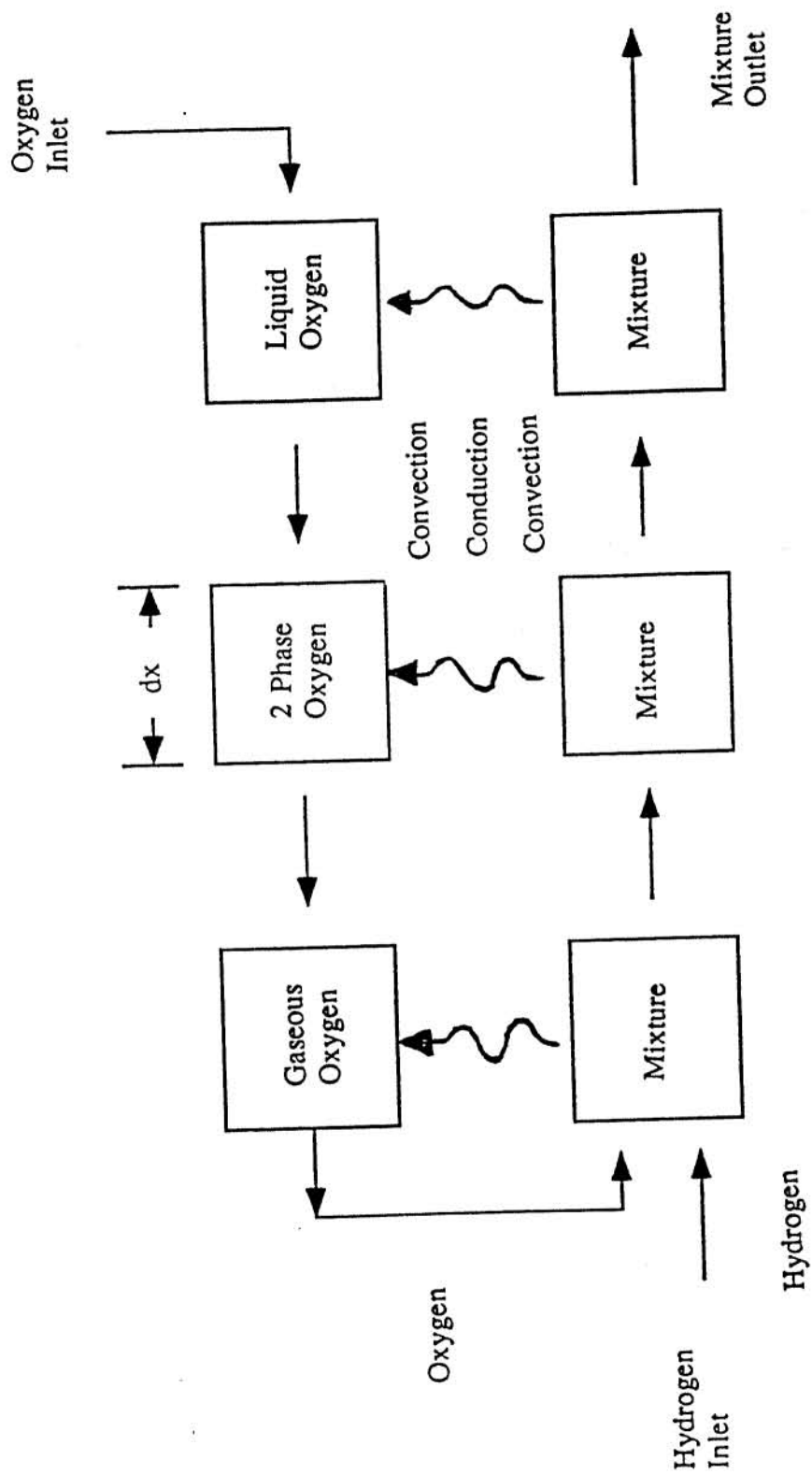


Figure 4 - Model Computation

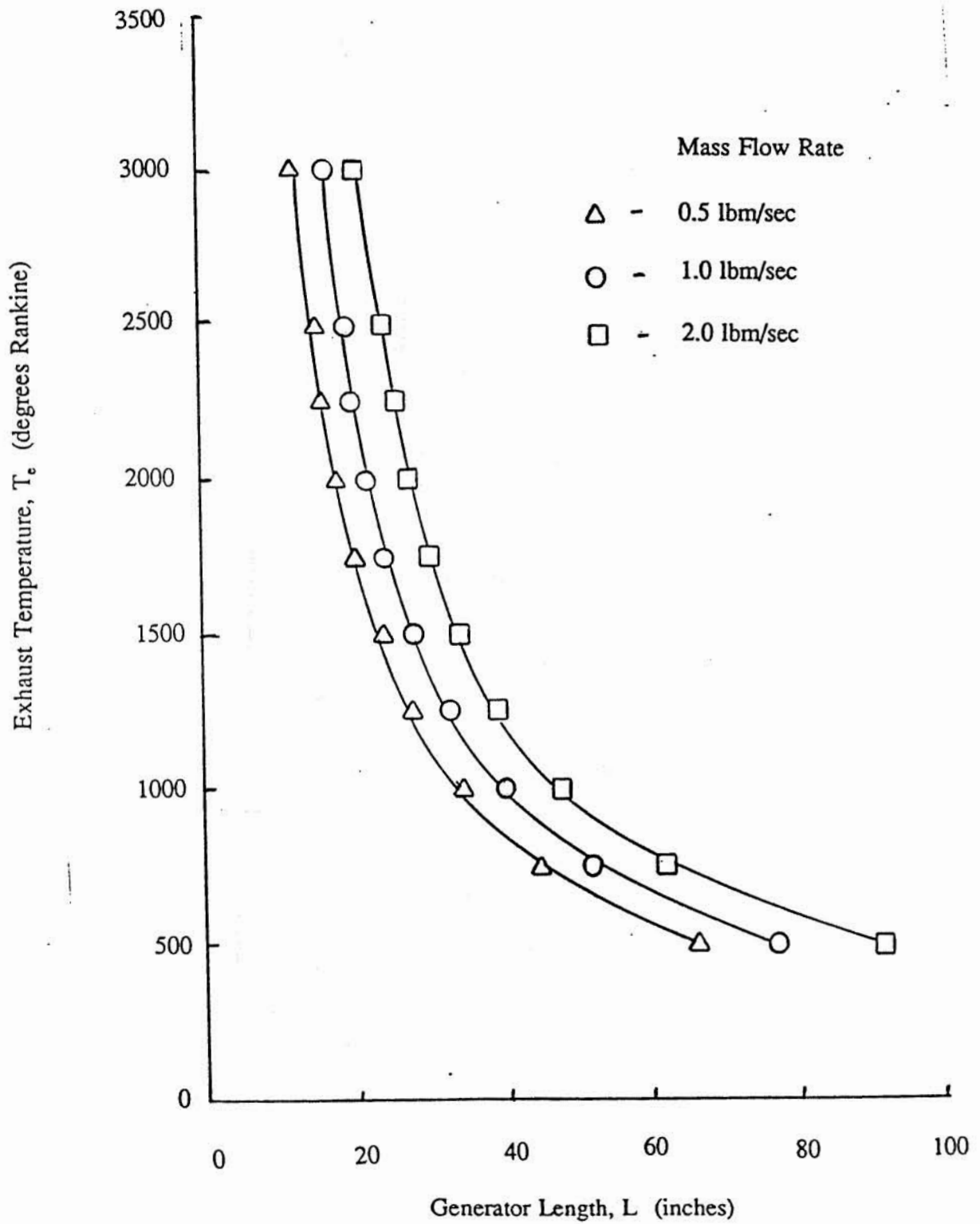


Figure 5 - Generator Length Necessary to Vaporize LOX for Desired Exhaust Temperatures.

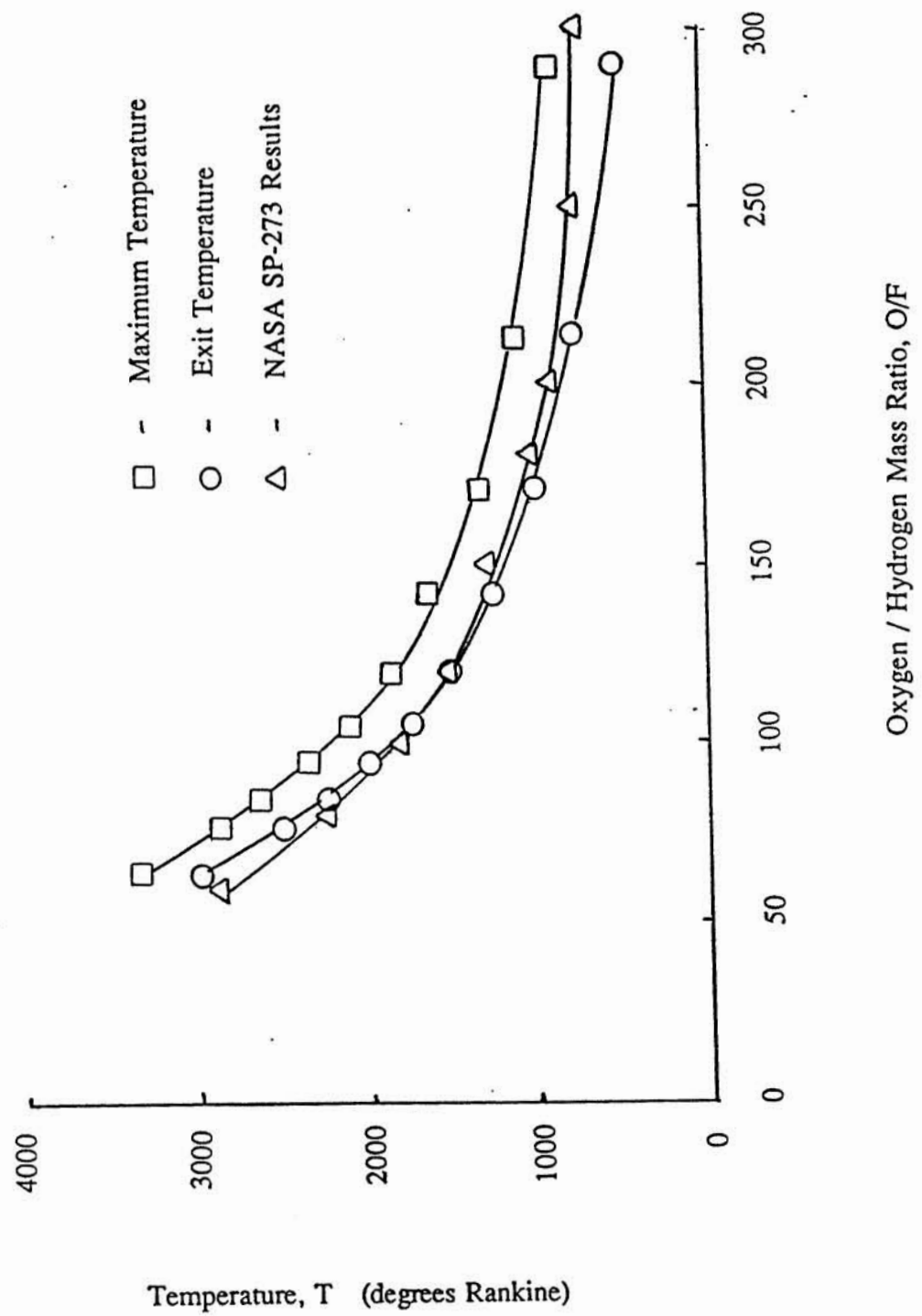


Figure 6 - Comparison of Temperatures and Oxygen/
Hydrogen Mass Ratios.

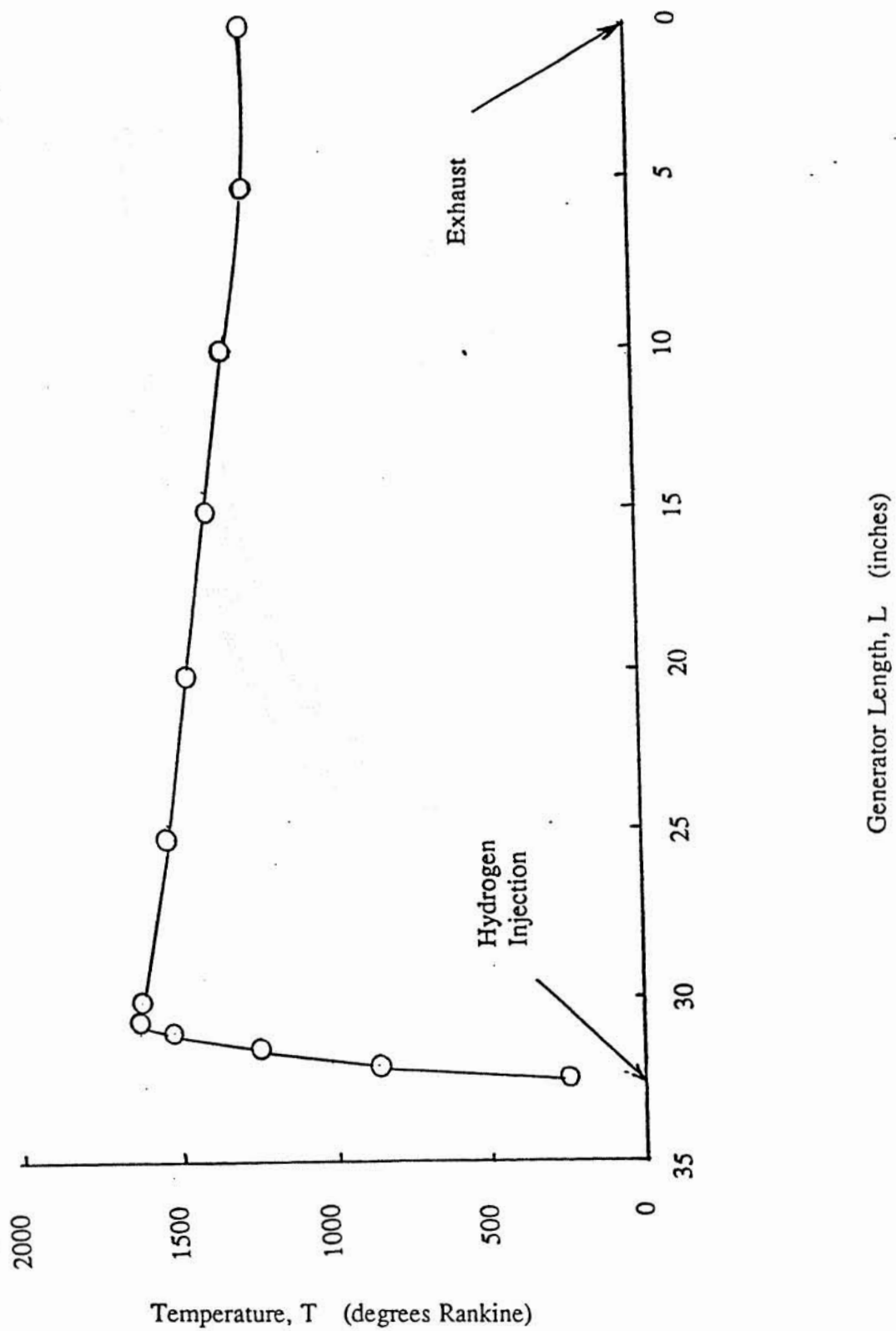


Figure 7 - Temperature Profile of Inner Tube Flow

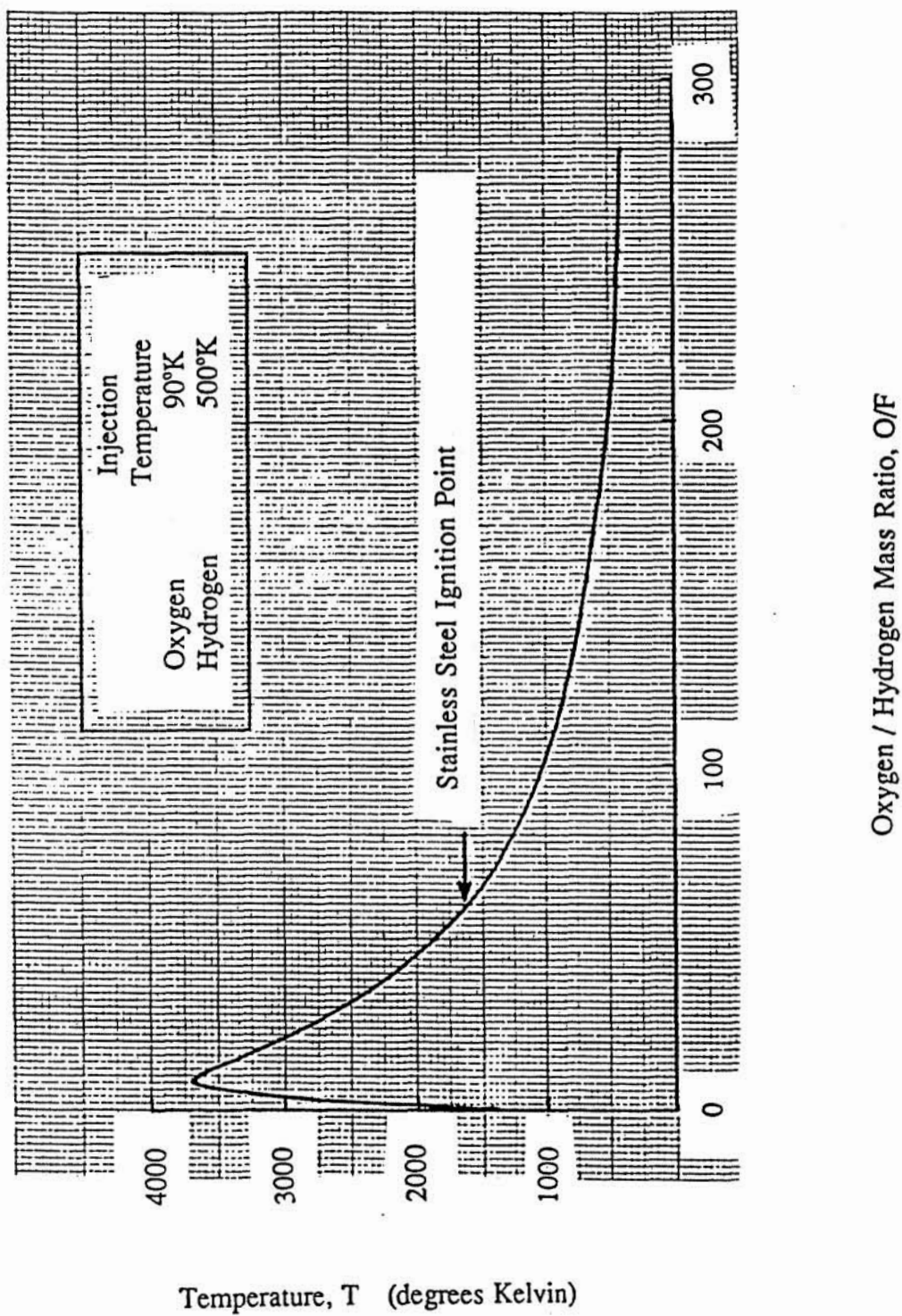


Figure 8 - Hydrogen / Liquid Oxygen Combustion
Temperatures for Various O/F Ratios

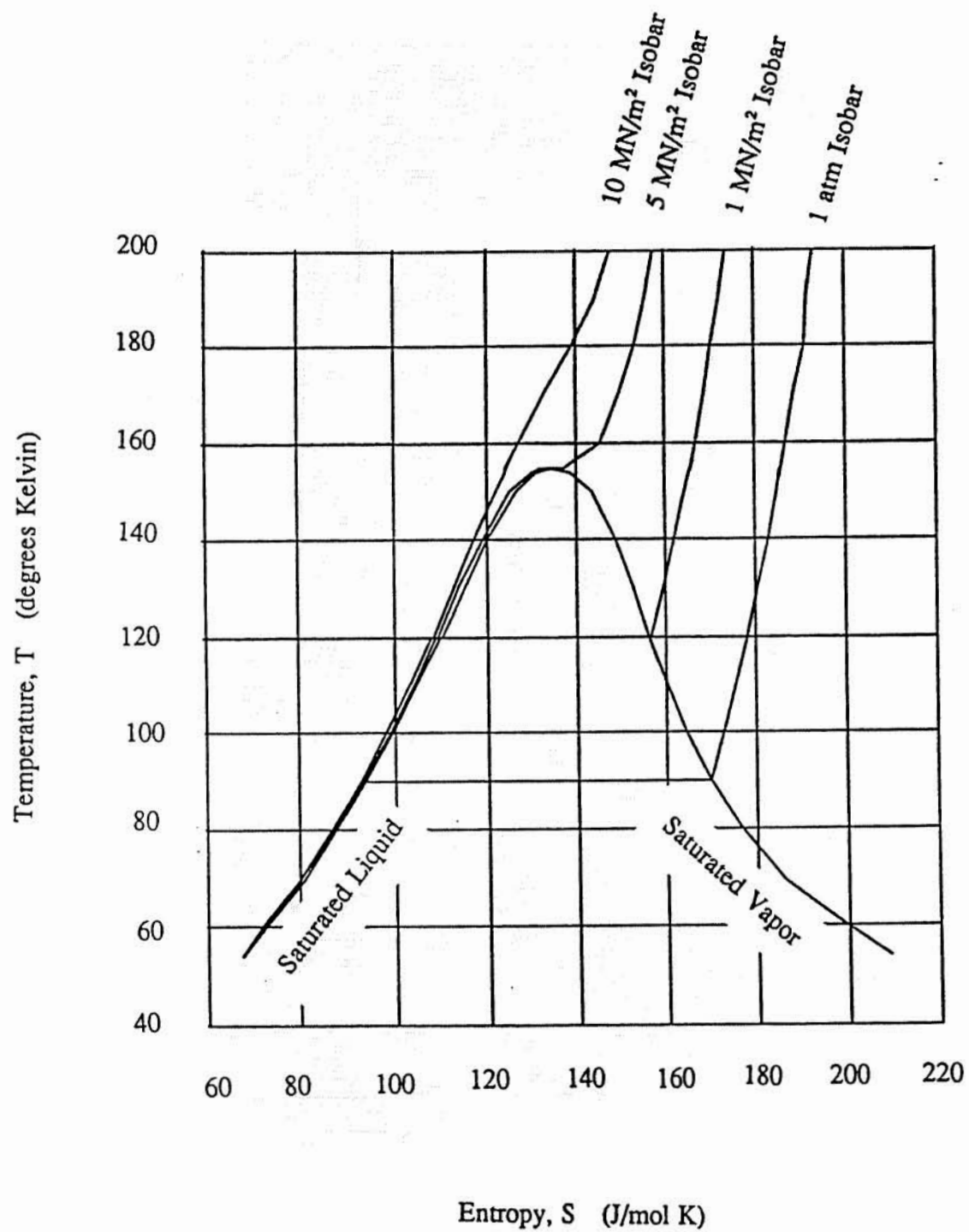


Figure 9 - Phase Diagram for Oxygen

LIQUID ROCKET SPRAY COMBUSTION STABILITY ANALYSIS

Ron J. Litchford[†]
University of Tennessee Space Institute
Tullahoma, Tennessee 37388

92A 48828

San-Mou Jeng[‡]
University of Cincinnati
Cincinnati, Ohio 45221

Abstract

A computational methodology for the analysis of spray combustion stability in liquid rocket combustors has been constructed. The analysis is based on the unsteady, quasi-two-dimensional Euler equations with interphase source terms derived from a Lagrangian treatment of the combusting spray. An axisymmetric combustor geometry is analyzed in terms of an equivalent annular computational domain with periodicity conditions which may further be specialized for a rectangular combustor geometry or reduced to a quasi-one-dimensional description for pure longitudinal-mode analyses. The propellant spray is represented by Lagrangian tracking of computational parcels each having a droplet spatial distribution described by a probability density function. The propellant burning rate is described by the d^2 vaporization law with the Ranz-Marshall convection correlation and a one-parameter phenomenological pressure-sensitive response index. The longitudinal- and tangential-mode instability characteristics of a generic combustor were investigated using the developed methodology. Intrinsic longitudinal-mode instability was observed at relatively high pressure-sensitive combustion response levels. The resulting limit cycle oscillation consisted of a single steep-fronted pressure wave undergoing repeated injector and nozzle reflections at the fundamental acoustical frequency. Intrinsic tangential-mode instability was observed even with vanishing pressure-sensitive combustion response. The observed instability exhibited mode switching from a single steep-fronted traveling pressure wave to two steep-fronted waves traveling in opposing directions. These extremely high-amplitude pressure waves were localized very near the injector face in a manner consistent with the shocklike waves observed in some experiments.

Introduction

This paper reports on some recent efforts to apply modern computational techniques to the analysis of spray combustion stability in liquid-fueled rocket engines. Such efforts seem justified on the basis that numerical methods allow for a more comprehensive analysis of combustion instability than can be achieved using classical analytical treatments. By accounting for nonlinear behavior and allowing for more comprehensive physical submodeling, a computational approach becomes very alluring with the promise of shedding valuable insight on the mysterious connections between unsteady combustion and organized flow oscillations. From a practical standpoint, an efficient computational tool can also serve as a valuable design aid. In this paper, we outline our attempt to construct the basic framework for such an engineering analysis tool with emphasis on robustness and efficiency while capturing the essential features of the physical phenomena.

When attempting such a development, it is necessary to recognize that numerical solution techniques are beset with their own special vexations in application and that physical theories for unsteady combustion phenomena retain a certain degree of uncertainty. Meaningful analysis of the problem is not yet a simple matter of mere implementation. For example, both the dissipative and dispersive characteristics of a particular scheme can have an important influence on numerical accuracy in unsteady flow problems as demonstrated by Hsieh.¹ Also, because combustion instability is basically a wave phenomenon, implementation of appropriate boundary conditions is not trivial. Stability is greatly determined by the transmission and reflection of flow disturbances incident on the boundaries. Furthermore, instability oscillation modes typically involve multidimensional effects and time accurate solutions are required imposing additional computational burden. The foremost difficulty, however, is the absence of definitive physical submodeling for unsteady combustion.

The complex physics of unsteady spray combustion in liquid rocket engines can still only be grossly modeled using our best contemporary descriptions. Even with these available descriptions, there is difficulty in implementing the modeling within a CFD framework without introducing excessive computational penalties or nonphysical numerical noise. For

[†] Research Engineer, UT-Calspan Center for Space Transportation and Applied Research, Member AIAA.

[‡] Associate Professor, Aerospace Engineering and Engineering Mechanics, Member AIAA.

Copyright © American Institute of Aeronautics and Astronautics, Inc., 1992. All rights reserved.

instability problems, such nonphysical noise is of central importance. Strong numerical noise can falsely trigger nonlinear instabilities and yield misleading results.

The problems described above make the prediction and description of spray combustion instabilities especially difficult. Currently, stability analysis methods can serve only as guides leading to qualitative understanding rather than a priori quantitative predictions from first principles. By adapting contemporary computational techniques and refined physical submodeling, however, this situation may hopefully be improved. In fact, considerable progress is being made toward achieving this goal by several researchers.²⁻⁸

In this paper, our intent is to contribute to such an effort by developing a computational framework suitable for spray combustion stability analyses. Our desire is that the resulting development serve initially as a useful research code and ultimately as a design aide following the introduction of more complete physical submodeling. Emphasis is placed on computational efficiency and robustness. At this early stage of code development, a simple spray combustion physical submodel is considered with a one-parameter phenomenological pressure-sensitive combustion response index. It seems wise to first obtain results using a simplified instability model in lieu of more complicated physical submodeling with inherently more convoluted effects. With this controlled approach, we hope to develop a computational framework more efficiently and still gain insight into the basic physical phenomena. Once established, the retrogressive nature of this developmental approach may be relaxed by substituting more refined physical submodeling.

Theory

Physical Model

Recognizing that the physical model must ultimately describe transverse-mode instabilities but that computational efficiency is also essential, we have adapted the equivalent annular combustor representation for an actual axisymmetric combustor geometry as formulated by French researchers.^{2,3} Although this approach neglects radial-mode instabilities, it allows for a description of the more important tangential-modes with the computational savings derived from using a two-dimensional grid. The resulting formulation may also be specialized for rectangular combustors or reduced to a quasi-one-dimensional description for pure longitudinal-mode analyses. The resulting computational framework is therefore quite versatile.

The geometry of an axisymmetric combustor and an equivalent annular computational domain is shown

in Fig. 1. Here, the axial coordinate of the computational domain corresponds directly to that of the actual engine. The transverse length l , however, is chosen to match the desired n^{th} tangential mode of the real combustor. Periodicity of the transverse coordinate is also required. With these two lengths, the annular width b is fixed such that the cross-sectional areas match. Clearly, b is a function of axial position only. If analysis of a rectangular combustor is desired, l is taken as the height, b becomes a variable width, and the transverse periodicity condition is replaced by solid wall boundary conditions. For a quasi-one-dimensional analysis, l is taken as unity and b becomes a variable cross-sectional area.

We consider a bi-propellant system with injection of a gaseous oxidizer and a fuel spray at the injector face. Treatment of the gas phase was simplified by neglecting viscous/turbulence effects except for interphase momentum exchange. Physical modeling of the combustion process was simplified by invoking the following assumptions:

- (1) Fuel is injected as a monodispersed spray of droplets - atomization is neglected.
- (2) The local mean vaporization rate is determined by applying the quasi-steady d^2 vaporization law with corrections for convection and pressure sensitivity.
- (3) Combustion is assumed to occur infinitely fast following vaporization of the fuel droplets.
- (4) Analysis is restricted to fuel-lean operating conditions only so that all fuel is completely consumed.
- (5) The gas-phase combustion products are assumed to be calorically as well as thermally perfect.

Gas-Phase Formulation

In our development, the gas phase is treated using an Eulerian description with appropriate source terms for interphase transport coupling with the spray. The problem thus reduces to solving the unsteady, quasi-two-dimensional Euler equations which may be written in conservative form using matrix notation as

$$\frac{\partial Q}{\partial t} + \frac{\partial E}{\partial x} + \frac{\partial F}{\partial y} = H \quad (1)$$

where the conserved variable vector Q is defined by

$$Q = \begin{bmatrix} \rho b \\ \rho u b \\ \rho v b \\ \rho e b \end{bmatrix} \quad (2)$$

and the convective flux vectors E and F are defined

by

$$E = \begin{bmatrix} \rho ub \\ (\rho u^2 + p)b \\ \rho uvb \\ (\rho e + p)ub \end{bmatrix} \quad F = \begin{bmatrix} \rho vb \\ \rho uvb \\ (\rho v^2 + p)b \\ (\rho e + p)vb \end{bmatrix} \quad (3)$$

The vector H contains contributions due to the variable annular width and interphase transport source terms. We denote this vector as the sum of two components

$$H = H_1 + H_2 \quad (4)$$

For single-phase flow, only H_1 need be considered to account for the variable annular width effect on the axial momentum equation. It consists of a single component

$$H_1 = \begin{bmatrix} 0 \\ p \frac{\partial b}{\partial x} \\ 0 \\ 0 \end{bmatrix} \quad (5)$$

For two-phase flow, the source vector H_2 must be included to account for interphase transport effects on the continuous-phase conservation equations. The source vector H_2 has the form

$$H_2 = \begin{bmatrix} b \Sigma \dot{w}_i \\ b \Sigma [\dot{w}_i u_{pi} + D_{xi}] \\ b \Sigma [\dot{w}_i v_{pi} + D_{yi}] \\ b \Sigma \dot{w}_i [\Delta q_i + \frac{e_i^2}{2}] + b \Sigma [u D_{xi} + v D_{yi}] \end{bmatrix} \quad (6)$$

The perfect gas equation of state $p = \rho RT = (\gamma - 1)[e - \rho \frac{e^2}{2}]$ completes the governing system where $e = C_v T + \frac{e^2}{2}$ represents the total internal energy.

This inhomogeneous form of the Euler equations retains a hyperbolic character. Thus, the Jacobian coefficient matrix $A = \partial E / \partial Q$ has real eigenvalues u , $u + c$, u , and $u - c$ with the speed of sound defined by $c = \sqrt{\gamma p / \rho}$. Similarly, the eigenvalues of the Jacobian coefficient matrix $B = \partial F / \partial Q$ are v , v , $v + c$, and $v - c$. Following conventional practice, A and B may be diagonalized such that

$$\begin{aligned} T_x^{-1} M^{-1} A M T_x &= \Lambda_x \\ T_y^{-1} M^{-1} B M T_y &= \Lambda_y \end{aligned} \quad (7)$$

where $M = \frac{\partial Q}{\partial V}$ is a transformation matrix from the conservative variables Q to the primitive variables V , T_x and T_y are similarity transformation matrices formed from the eigenvectors of the primitive variable Jacobian coefficient matrices $M^{-1} A M$ and $M^{-1} B M$, and Λ_x and Λ_y are the diagonal eigenvalue matrices.

For convenience, we may define positive and negative eigenvalue matrices as Λ_x^+ and Λ_y^+ where '+' indicates the occurrence of positive eigenvalues only and '-' indicates only negative eigenvalues. It follows, therefore, that

$$\begin{aligned} A &= M T_x (\Lambda_x^+ + \Lambda_x^-) T_x^{-1} M^{-1} = A^+ + A^- \\ B &= M T_y (\Lambda_y^+ + \Lambda_y^-) T_y^{-1} M^{-1} = B^+ + B^- \end{aligned} \quad (8)$$

and

$$\begin{aligned} |A| &= M T_x (\Lambda_x^+ - \Lambda_x^-) T_x^{-1} M^{-1} = A^+ - A^- \\ |B| &= M T_y (\Lambda_y^+ - \Lambda_y^-) T_y^{-1} M^{-1} = B^+ - B^- \end{aligned} \quad (9)$$

Numerical Scheme

Numerical solution of the Euler equations is accomplished through optional spatial finite-difference discretizations and a separate time-integration method. In selecting discretization methods, we desired a conservative formulation capable of yielding meaningful spatial resolution without spurious numerical oscillations. In selecting a time-integration method, we desired meaningful time-accuracy and good numerical stability. These properties are central to the description of unsteady flows typically encountered in a combustion stability analysis. Therefore, both the dissipative and dispersive characteristics of a numerical scheme are important to the problem. Of course, efficiency is always of utmost concern.

An assessment of numerical techniques for such unsteady flow calculations has been carried out by Hsieh.¹ Based on his results, explicit Runge-Kutta multi-stage time-integration with 6th order central differencing of the convective fluxes and 4th order artificial dissipation yield very good all around performance. He also found that 2nd order, upwind flux-differencing with Roe averaging of the Jacobian coefficient matrices and nonlinear flux limiters to achieve TVD conditions performed very well with regard to shock capturing but entailed higher dissipative errors in multidimensional problems. Our construction of a computational method for spray combustion stability is based on adopting the best performing techniques from this study.

The development of the numerical scheme begins from the spatially discretized Euler equations yielding a system of ODEs of the form

$$\frac{dQ_{j,k}}{dt} = -R(Q_{j,k}) \quad (10)$$

where $R(Q_{j,k})$ represents an explicit spatial operator. Applying the 4-stage Runge-Kutta method yields the

operational sequence

$$\begin{aligned}
 Q_{j,k}^{(0)} &= Q_{j,k}^n \\
 Q_{j,k}^{(1)} &= Q_{j,k}^n - \frac{1}{4} \Delta t R(Q_{j,k}^{(0)}) \\
 Q_{j,k}^{(2)} &= Q_{j,k}^n - \frac{1}{3} \Delta t R(Q_{j,k}^{(1)}) \\
 Q_{j,k}^{(3)} &= Q_{j,k}^n - \frac{1}{2} \Delta t R(Q_{j,k}^{(2)}) \\
 Q_{j,k}^{n+1} &= Q_{j,k}^n - \Delta t R(Q_{j,k}^{(3)})
 \end{aligned} \quad (11)$$

With 6th order central differencing of the convective fluxes and the addition of 4th order artificial dissipation, the explicit spatial operator takes the form

$$\begin{aligned}
 R(Q_{j,k}) &= \frac{1}{60\Delta x} \left(E_{j+3,k} - 9E_{j+2,k} + 45E_{j+1,k} \right. \\
 &\quad \left. - 45E_{j-1,k} + 9E_{j-2,k} - E_{j-3,k} \right) \\
 &\quad + \frac{1}{60\Delta y} \left(F_{j,k+3} - 9F_{j,k+2} + 45F_{j,k+1} \right. \\
 &\quad \left. - 45F_{j,k-1} + 9F_{j,k-2} - F_{j,k-3} \right) \\
 &\quad + D_{j,k}^{(x)} + D_{j,k}^{(y)} - H_{j,k} \quad (12)
 \end{aligned}$$

The dissipation vector for the streamwise coordinate is⁹

$$D_{j,k}^{(x)} = \frac{\epsilon}{8\Delta t} \left(Q_{j+2,k} - 4Q_{j+1,k} + 6Q_{j,k} \right. \\
 \left. - 4Q_{j-1,k} + Q_{j-2,k} \right) \quad (13)$$

with a similar definition for the transverse coordinate. This central difference scheme is very efficient and the method of choice in most cases.

For a more computationally intensive approach, a characteristic-based spatial discretization using upwind flux-differencing is included as an alternative where the explicit spatial operator may be written in terms of numerical flux vectors treated on a locally one-dimensional basis.

$$\begin{aligned}
 R(Q_{j,k}) &= \frac{1}{\Delta x} \left[\tilde{E}_{j+\frac{1}{2},k} - \tilde{E}_{j-\frac{1}{2},k} \right] \\
 &\quad + \frac{1}{\Delta y} \left[\tilde{F}_{j,k+\frac{1}{2}} - \tilde{F}_{j,k-\frac{1}{2}} \right] - H_{j,k} \quad (14)
 \end{aligned}$$

Here, the 1st order accurate numerical flux vector is defined for the streamwise coordinate by

$$\begin{aligned}
 \tilde{E}_{j+\frac{1}{2},k}^{(1)} &= \frac{1}{2} \left[E_{j,k} + E_{j+1,k} \right. \\
 &\quad \left. - |\tilde{A}|_{j+\frac{1}{2},k} (Q_{j+1,k} - Q_{j,k}) \right] \quad (15)
 \end{aligned}$$

where the Jacobian coefficient matrix \tilde{A} is evaluated using the Roe averaged quantities^{10,11}

$$\begin{aligned}
 \rho_{j+\frac{1}{2},k} &= \sqrt{\rho_{j+1,k} \rho_{j,k}} \\
 u_{j+\frac{1}{2},k} &= \frac{u_{j,k} \sqrt{\rho_{j,k}} + u_{j+1,k} \sqrt{\rho_{j+1,k}}}{\sqrt{\rho_{j,k}} + \sqrt{\rho_{j+1,k}}} \\
 v_{j+\frac{1}{2},k} &= \frac{v_{j,k} \sqrt{\rho_{j,k}} + v_{j+1,k} \sqrt{\rho_{j+1,k}}}{\sqrt{\rho_{j,k}} + \sqrt{\rho_{j+1,k}}} \\
 h_{j+\frac{1}{2},k} &= \frac{h_{j,k} \sqrt{\rho_{j,k}} + h_{j+1,k} \sqrt{\rho_{j+1,k}}}{\sqrt{\rho_{j,k}} + \sqrt{\rho_{j+1,k}}} \\
 c_{j+\frac{1}{2},k}^2 &= (\gamma - 1) \left[h_{j+\frac{1}{2},k} - \frac{q_{j+\frac{1}{2},k}^2}{2} \right]
 \end{aligned} \quad (16)$$

Similar relations hold for the transverse fluxes in terms of the Jacobian coefficient matrix \tilde{B} .

As developed, the above 1st order accurate scheme exhibits robust nonoscillatory behavior, but spatial resolution is poor. Direct substitution of 2nd order difference formulas does not improve matters either since this leads to the generation of spurious oscillations. To circumvent this difficulty, Harten¹² has introduced the total-variation-diminishing (TVD) property and derived sufficient conditions for constructing schemes which satisfy this property. Such constructions have been carried out for both explicit and implicit time integration schemes.^{13,14} The mechanisms currently in use for satisfying TVD conditions are based on some kind of gradient limiting procedure. We adapt such a procedure based on a nonlinear flux limiter. The second-order convective flux vector is obtained by adding corrective terms to the first-order flux vector. A generalized form which may be specialized for second-order central, second-order upwind, or third-order biased upwind schemes is given by Hsieh¹ as

$$\begin{aligned}
 \tilde{E}_{j+\frac{1}{2},k}^{(2)} &= \tilde{E}_{j+\frac{1}{2},k}^{(1)} + \frac{1-\kappa}{4} \left[\Delta \hat{E}_{j-\frac{1}{2},k}^+ - \Delta \hat{E}_{j+\frac{1}{2},k}^- \right] \\
 &\quad + \frac{1+\kappa}{4} \left[\Delta \hat{E}_{j+\frac{1}{2},k}^+ - \Delta \hat{E}_{j+\frac{1}{2},k}^- \right] \quad (17)
 \end{aligned}$$

where

$$\begin{aligned}
 \Delta \hat{E}_{j+\frac{1}{2},k}^- &= (MT)_{j+\frac{1}{2},k} \Delta \hat{\sigma}_{j+\frac{1}{2},k}^- \\
 \Delta \hat{E}_{j+\frac{1}{2},k}^+ &= (MT)_{j+\frac{1}{2},k} \Delta \hat{\sigma}_{j+\frac{1}{2},k}^+ \quad (18)
 \end{aligned}$$

$$\begin{aligned}
 \Delta \hat{\sigma}_{j+\frac{1}{2},k}^- &= \min \text{mod} [\Delta \sigma_{j+\frac{1}{2},k}^-, \beta \Delta \sigma_{j-\frac{1}{2},k}^-] \\
 \Delta \hat{\sigma}_{j+\frac{1}{2},k}^+ &= \min \text{mod} [\Delta \sigma_{j+\frac{1}{2},k}^+, \beta \Delta \sigma_{j+\frac{3}{2},k}^+] \quad (19)
 \end{aligned}$$

$$\begin{aligned}
 \Delta \sigma_{j+\frac{1}{2},k}^- &= \frac{1}{2} (\Lambda - |\Lambda|)_{j+\frac{1}{2},k} \\
 &\quad (T^{-1} M^{-1})_{j+\frac{1}{2},k} (Q_{j+1,k} - Q_{j,k}) \\
 \Delta \sigma_{j+\frac{1}{2},k}^+ &= \frac{1}{2} (\Lambda + |\Lambda|)_{j+\frac{1}{2},k} \\
 &\quad (T^{-1} M^{-1})_{j+\frac{1}{2},k} (Q_{j+1,k} - Q_{j,k}) \quad (20)
 \end{aligned}$$

and the minmod operator is defined by

$$\begin{aligned} \text{minmod}[x, y] &= \text{sgn}(x) \\ &\quad \max[0, \min\{|x|, y \text{sgn}(x)\}] \end{aligned} \quad (21)$$

Similar forms hold for the transverse flux vector. The values of κ corresponding to the type of scheme are presented in Table 1. The constant β is a compression parameter which is restricted to the range $1 \leq \beta \leq (3 - \kappa)/(1 - \kappa)$ with $\beta = 6$ when $\kappa = 1$.

Boundary Conditions

Boundary conditions for the computational analysis are implemented according to the propagation of information along the flow characteristics. On a locally one-dimensional basis, for instance, each eigenvalue may be associated with a particular characteristic. If the eigenvalue is positive, its corresponding characteristic is right/up running. Conversely, if the eigenvalue is negative, its characteristic is left/down running. When a characteristic runs out of the computational domain, the boundary condition depends on the internal flow field, and a numerical boundary condition must be formulated which depends on the computed solution. The number of unknown flow parameters minus the number of numerical boundary conditions gives the number of physical boundary conditions which must be imposed.

For the subsonic inflow boundary, there are three in-running characteristics requiring three imposed physical conditions. In this analysis, we demand that the incoming gas-phase mass flux, flow angle (swirl), and entropy remain constant. The fixed gas-phase mass flux inflow implies the injection rate is insensitive to fluctuations at the injector face. Pressure-sensitive injection may be considered by including an appropriate injector admittance condition.

For the outflow boundary, the flow is supersonic in the diverging section of the nozzle and all characteristics are out-running so that no physical conditions need be specified. However, it suffices for developmental purposes to consider a subsonic outflow boundary condition at the nozzle entrance by making the short-nozzle approximation.¹⁵ Here, the flow is assumed to accelerate to sonic velocity in zero length. The physical condition imposed for the single in-running characteristic in this case is a fixed Mach number. Although this approximation is strictly valid for pure longitudinal-mode oscillations only, we utilize the approximation for the sake of simplicity even when transverse velocity components appear. At worse, this approach underestimates the nozzle damping effect. For the purpose of obtaining a mean flow prior to making a stability calculation, we also have the option of specifying the static pressure at the nozzle entrance.

Boundary conditions for the transverse direction are irrelevant for the annular combustor geometry in that it is only necessary to insure periodicity. When specializing for rectangular combustor geometries, solid wall boundary conditions are invoked by forcing the normal velocity component to zero.

Spray Combustion Formulation

Treatment of the propellant spray is simplified by neglecting the atomization process and assuming the injection of groups of discrete droplets at specified time intervals. Each droplet group is then represented by a probability density function (pdf) in space. The behavior of the droplets within each group is determined from the history of a single discrete computational parcel whose instantaneous position corresponds to the mean of the pdf. Conversely to the gas phase, these parcels are treated in a Lagrangian fashion. Knowing the pdf's mean location and size at a given instant, we may calculate the probable number of physical droplets in each cell to evaluate interphase transport.

The purpose of the pdf representation is to minimize the numerical shot noise which normally results when each parcel is described by a delta function point source and the droplet spray is undersampled. The numerical noise problem arising from the point source representation may be minimized by using a large number of parcels but with great sacrifice in computational efficiency. This fundamental difficulty can be so troubling that an Eulerian description of the spray is generally preferred. By introducing a distributed parcel representation, we hope to alleviate the generation of nonphysical numerical noise normally associated with a Lagrangian approach without suffering severe computational penalty.

In this development, we employ a rectangular uniform pdf shape as depicted schematically in Fig. 2. The streamwise width of this pdf corresponds to the product of the propellant injection velocity and a specified injection time interval. We currently impose an injection time interval such that this width is about 1.5 times the streamwise cell length. The width of the pdf in the transverse direction is currently equated to the transverse cell length. In addition, we require that these characteristic dimensions of the pdf shape remain fixed throughout a parcel's lifetime. A general theory has been developed to incorporate the time evolving width of the pdf due to turbulent dispersion,¹⁶ but we are neglecting turbulence effects in the present development.

The mean position of each pdf is determined from Lagrangian tracking of a single computational parcel characterizing the behavior of the physical droplets in the group. The equations governing particle motion

are

$$\frac{d\vec{u}_p}{dt} = \frac{3\rho_g C_D}{4\rho_p d_p} |\vec{u}_g - \vec{u}_p| (\vec{u}_g - \vec{u}_p) \quad (22)$$

$$\frac{d\vec{x}_p}{dt} = \vec{u}_p \quad (23)$$

For the sake of efficiency, we linearize Eq. (22) by holding $(\rho_g/\rho_p)(C_D/d_p)|\vec{u}_g - \vec{u}_p|$ constant over the computational time step and integrate analytically. This gives the updated parcel velocity as

$$\vec{u}_p \approx \vec{u}_{p0} \exp\left[\frac{-\Delta t}{\tau}\right] + \vec{u}_g \left\{1 - \exp\left[\frac{-\Delta t}{\tau}\right]\right\} \quad (24)$$

The parcel position is obtained through an even simpler treatment by using explicit Euler integration

$$\vec{x}_p \approx \vec{x}_{p0} + \vec{u}_p \Delta t \quad (25)$$

These approximate equations yield minimal error for small computational time steps and are sufficient for engineering calculations. Evaluation of parcel motion is simplified even further in the current analysis by neglecting parcel motion in the transverse direction. This simplification may be relaxed as desired but at increased computational expense.

Physical modeling of the unsteady spray combustion process is an essential element of the stability analysis. A comprehensive description should be able to account for the effect of local flow fluctuations, in the form of organized flow oscillations as well as turbulence, on interphase transport and the propellant combustion rate. Frankly, such a complete description does not exist. Even the best current modeling techniques retain a measure of uncertainty and are generally quite complicated and encumbering. Because we wish to avoid such unnecessary complication during the developmental process, we have adapted the relatively simple d^2 -law for droplet vaporization and have included simple multiplicative corrections for convective effects and pressure sensitivity. The instantaneous combustion rate of a parcel thus has the form

$$\dot{m} = \frac{\pi}{4} \rho_p d_p \beta K_v K_p \quad (26)$$

where the correction factor for convective effects is given by the Ranz-Marshall correlation as¹⁷

$$K_v = 1 + 0.3 Re^{1/2} Pr^{1/3} \quad (27)$$

The factor representing pressure sensitive combustion response is derived from the classical two-parameter $n - \tau$ formulation proposed by Crocco.¹⁸

In the $n - \tau$ instability model, the propellant is assumed to undergo combustion after some time lag τ following injection. The mass burning rate during combustion is also assumed to be proportional to pressure raised to the power n . Recognizing that our Lagrangian description of the spray yields a time lag effect somewhat analogous to that of the τ parameter, we concern ourselves only with the pressure-sensitive combustion response strength as represented by the n parameter. We then note that for small pressure changes about the mean the power law pressure dependence is approximately represented by a proportional relationship between burning rate and instantaneous pressure. Thus, expressing the burning rate as the sum of a mean and fluctuating quantity $\dot{m} = \bar{\dot{m}} + \dot{m}'$, we introduce a pressure-sensitive combustion response index α , analogous to n , such that

$$\frac{\dot{m}'}{\bar{\dot{m}}} = \alpha \frac{p'}{\bar{p}} \quad (28)$$

If we further assume that the d^2 -law corrected for convective effects only represents the mean burning rate, we may write the pressure-sensitive correction factor as

$$K_p = 1 + \alpha \frac{p'(t; x_p)}{\bar{p}(x_p)} \quad (29)$$

The notation expressing the functional dependency of the pressure fluctuation implies that $p'(t; x_p)$ be evaluated at time t at the instantaneous location of the parcel x_p . This approach is somewhat artificial but serves as a useful construct for developmental purposes and is not devoid of merit as a phenomenological description.

Computational Methodology

Application of the above modeling scheme requires a two-part approach. First, a mean flow must be computed by specifying the mean combustor pressure at the nozzle entrance and setting $\alpha = 0$. Because of the unsteadiness induced by the convection correction, it is generally not possible to get a fully converged steady-state flow field in this way. We avoid this difficulty by freezing the source terms once it becomes obvious that additional convergence is impossible and then continue the calculation. With the source terms frozen the calculation converges very rapidly. For a multidimensional analysis, we also find it expedient to import a 1D mean flow solution. Once a mean flow field is obtained for reference by whatever method, stability calculations are performed by restarting the code using the short-nozzle boundary condition and a specified combustion response index.

Results and Discussion

There are two important combustor characteristics which influence stability. One is the localized combustion response to flow field fluctuations. Another is the mean combustion distribution. It is these characteristics which greatly determine the tendency for a pressure wave to be amplified or attenuated. In our combustion model, the combustion response index and, to a certain extent, the Ranz-Marshall convection correlation describe the combustion response. On the other hand, the mean spray combustion distribution is controlled by the mean burning rate constant in conjunction with the Lagrangian tracking formulation.

Based on this spray combustion model, we have used the constructed computational methodology to investigate the stability characteristics of a representative generic combustor. The propellant properties considered are given in Table 2. The combustor physical conditions are given in Table 3. Because we wished to examine the effect of combustion distribution on stability, particularly longitudinal-mode, a mean flow field was computed for three different burning rate constants to obtain a range of mean spray lengths. The burning rate constants and their resulting mean spray lengths are summarized in Table 4. The mass flow rate, Mach number, and temperature distributions for the computed mean flow fields are shown in Fig. 3.

Our approach was two prong in that we first performed a longitudinal-mode stability analysis using a pure 1D description and then examined tangential-mode instability using the equivalent annular combustor formulation. In both cases, we varied the pressure sensitive combustion response index to determine the levels needed for the combustor to become intrinsically unstable. The results of this evaluation are described in the following sections.

Longitudinal-Mode Stability Characteristics

The longitudinal-mode calculations were performed using characteristic-based upwind flux differencing for spatial discretization. The 1D grid contained 101 evenly spaced nodes. To determine intrinsic combustor stability, we examined the pressure history at the nozzle entrance as it evolved following restart from the mean flow with nonzero combustion response. Triggered instability was also briefly examined by pulse combusting a specified fraction of the spray following restart.

In Fig. 4, stable combustion behavior is demonstrated for a spray length to combustor length ratio of 0.6 and a combustion response index of 0.9. Clearly there is a pressure oscillation in the combustor, but its amplitude is too small to be of significance. In

contrast, Fig. 5 shows intrinsic instability when the combustion response index is increased to 1.0. Here we see classical exponential growth of the pressure wave in the linear regime followed by attainment of a nonlinear limit cycle oscillation where amplification is balanced by damping and nozzle losses. The limit cycle oscillation manifests a well defined steep-fronted pressure wave which is truly periodic. The absence of numerical noise is noteworthy.

Indeed, the spectral composition of the waveforms in Figs. 4 and 5 reveal that they are virtually noiseless. The low amplitude pressure wave observed during stable combustion is seen to be almost sinusoidal. However, the nonlinear limit cycle pressure wave observed during unstable combustion has a substantial contribution from higher harmonics. In both cases the fundamental frequency is found to correspond with the classical acoustical frequency. This behavior was characteristic of all calculations.

For additional insight, the fluctuations in velocity, temperature, and entropy are shown in relation to fluctuations in pressure during unstable combustion in Fig. 7. These waveforms are clearly periodic, but they are far from sinusoidal. The nonlinear character of the wave phenomena during unstable combustion is evident. The pressure profile within the unstable combustor is also shown in Fig. 8 at various time intervals where we see a single pressure wave impinging the injector head and being reflected toward the nozzle.

As a summary of the longitudinal-mode stability calculations, a stability map has been constructed and presented in Fig. 9. In this map, the intrinsic stability limit is plotted against a normalized combustion response strength and a normalized mean spray length. The combustion response strength is defined as the product of the response index and the mean burning rate since it is this product which determines the magnitude of the fluctuating burn rate as the spray length is expanded or contracted. This is evident from an inspection of Eqs. (26) and (29). What we find is that as the spray combustion region is expanded to encompass a larger portion of the combustor, damping effects increase. While some energy is always added in phase with the wave, with an increasingly larger combustion region there is an increase in energy added out of phase with the wave. The net effect is greater stability. In contrast, as the spray combustion region is contracted and concentrated near the injector face, there is a simultaneous reduction in the out-of-phase contributions and increase in the in-phase contributions. The net effect is greater instability.

To make an important point concerning our instability model, the pressure history for a combustion pulsed (3% of total spray) stability calculation is pre-

sented in Fig. 10. Here, we find the same stability behavior as for the non-pulsed case except that the development of the limit cycle occurs much faster. The resulting waveforms are identical to that obtained for non-pulsed stability. This is further demonstrated by the spectral composition of the waveform in Fig. 11. The reason for this behavior is that the combustion response is linearly related to pressure as seen in Eq. (28). For a nonlinear model, pulsed stability could differ greatly from non-pulsed stability.

Tangential-Mode Stability Characteristics

All tangential-mode calculations were performed using 6th order central differencing for spatial discretization. The 2D grid for the annular combustor geometry contained 51 nodes in the axial coordinate and 30 nodes in the tangential coordinate. The transverse length was chosen to match the first tangential mode, and the annular width was adjusted to obtain the correct cross-sectional area. The inflow was constrained to have zero swirl. Again, intrinsic stability behavior was examined by restarting from a mean flow field imported from the 1D analysis.

Pressure histories for a spray length to combustor length ratio of 0.6 and a combustion response index of 0.1 are given in Fig. 12 demonstrating the development of an intrinsic tangential-mode instability. These pressures were recorded at 1/10 of the combustor length from the injector and at 3 tangential locations differing by a phase angle of $\pi/2$. We observe the evolution of an extremely high-amplitude pressure wave traveling around the combustor although combustion response is extremely small. In fact, instability was observed for this combustor even with zero pressure sensitive combustion response. Evidently, the Ranz-Marshall convective correlation offers enough sensitivity to velocity fluctuations to support a pressure wave. The reason for this behavior is attributed to minimal damping from drag, streamwise convective losses, and out-of-phase energy contributions. Obviously, the combustor is much more susceptible to tangential-mode instabilities than longitudinal-modes in accord with practical experience.

Also observable is mode switching which occurs during the 10 to 25 msec time interval following restart. The short term instability up to 10 msec consists of a single unidirectional traveling high-amplitude pressure wave. This is evidenced by an exploded view of the short term pressure histories in Fig. 13. We clearly see that the unstable pressure waveforms at $\theta = 0$ and $\theta = \pi$ are exactly half a period out of phase. In the exploded view, we also observe that the pressure wave is almost entirely positive biased, is shocklike in nature, and has a fundamental frequency corresponding to the first spinning

tangential-mode acoustical frequency of the chamber. Furthermore, there are some superimposed high frequency components which show up spectrally in Fig. 14 consisting of low level noise and possible precursors to mode switching.

Following mode switching, the pressure waveforms at $\theta = 0$ and $\theta = \pi$ are exactly in phase and oscillate at twice the fundamental frequency. This long term instability mode is shown in Fig. 15 during the time interval 35 to 40 msec after restart. Here, we also see that the pressure at $\theta = \pi/2$ is now oscillating at the fundamental frequency with very high amplitude peaks centered between the lower amplitude ones manifested at $\theta = 0$ and $\theta = \pi$. Obviously, the instability now consists of two pressure waves traveling in opposing directions which meet at $\theta = \pi/2$ and $\theta = 3\pi/2$ to form two extremely large pressure spikes on opposite sides of the combustor.

The pressure field behavior during instability is exhibited more clearly in the flooded contour plots of Figs. 16 and 17 which show the combustor pressure history during the short term and long term modes, respectively. A revealing feature discernable from these flooded contour plots is the observation that the severity of the instability is localized near the injector face. The magnitude of the pressure wave diminishes rapidly downstream most probably as a result of increased streamwise convective losses as the Mach number increases. The wave is also curved with the nozzle end leading the injector end. One can clearly ascertain the rationale and effectiveness of baffles in controlling tangential-mode instabilities from these results.

Another noteworthy feature of this analysis is that the basic features of the instability are in accord with experimental results for a combustor with similar physical conditions.¹⁹ The research combustor used in the referenced experimental work was 11 inches in diameter while the combustor of this analysis is about 10 inches in diameter. Experimentally, a single high-amplitude shocklike pressure wave was observed sweeping about the chamber at the injector face with a period of 470 μ s corresponding to the first spinning tangential-mode acoustical frequency. The pressure wave was found to decay very rapidly in amplitude and curve in the direction of rotation as one moved away from the injector toward the nozzle entrance. For the short term instability of our calculations, the period was about 435 μ s in correspondence with the acoustical frequency, and we clearly have a strong shocklike pressure wave decaying rapidly in strength and curving in the direction of rotation downstream from the injector. That these essential features are common is encouraging and indicative that the analysis has indeed captured at least the basic physics.

Conclusion

Based on preliminary evaluation, the constructed computational methodology appears promising as a research tool and potential design/development aide for investigating the stability characteristics of liquid rocket engines. The low numerical noise properties of the method are very favorable, and Lagrangian treatment of the spray offers improved flexibility for direct modeling of spray combustion. In our judgment, the achievement of low noise while using a Lagrangian technique is noteworthy considering that the number of computational parcels was kept to a minimum through the use of probability distributions for the propellant spray. The qualitative agreement between a predicted tangential-mode instability, where a shocklike pressure wave was found to sweep about the chamber near the injector face, with existing experimental results is also encouraging.

Although the current development has been confined to a simplified linear pressure-sensitive combustion response model, more comprehensive physical submodeling may easily be implemented as desired. In fact, the most important use of the developed computational tool may well be as a research test bed for investigating the effect of various physical submodels on combustor stability characteristics. In conjunction with experimental data, much can be learned about the physical nature of combustion driven instabilities. With time, as modeling becomes more refined through an interplay between experiment and computation, it should be possible to evolve a support capability for aiding in design/development and investigating new combustor concepts.

Acknowledgments

This work was conducted as part of an ongoing spray combustion stability project supported by the University of Tennessee-Calspan Center for Space Transportation and Applied Research, UT Space Institute, Tullahoma, TN 37388 under NASA Grant NAGW-1195 and in part by Rocketdyne Div., Rockwell Int., Canoga Park, CA 91303 with Mr. Merlin Schuman as technical monitor.

Nomenclature

English Symbols

A, B	Jacobian coefficient matrices
\bar{A}, \bar{B}	Roe-averaged Jacobian coefficient matrices
b	annular combustor width (m)
C_p	constant-pressure specific heat (J/kg K)
C_v	constant-volume specific heat (J/kg K)
C_D	drag coefficient,

$$= 24(1 + Re^2/6)/Re ; Re < 1000$$

$$= 0.44 ; Re \geq 1000$$

c	speed of sound (m/s)
d	diameter (m)
\bar{D}	momentum exchange per unit volume (N/m ³), $= \bar{n} \frac{\pi}{8} d_p^2 \rho C_D \bar{u}_p - \bar{u}_g (\bar{u}_p - \bar{u}_g)$
E, F	convective flux vectors
\bar{E}, \bar{F}	numerical flux vectors
\hat{E}, \hat{F}	gradient limited flux vectors
e	total internal energy (J/kg)
g	gravitational acceleration (m/s ²)
H	source vector
h	specific stagnation enthalpy (J/kg)
K_v	Ranz-Marshall forced-convection correction
K_p	pressure-sensitive combustion rate correction
l	transverse combustor length (m)
l_c	streamwise combustor length (m)
M	conservative to primitive variable transformation matrix or mach number
\dot{m}	mass vaporization rate (kg/s)
\bar{n}	particle density (particles/m ³)
Pr	Prandtl number
p	pressure (Pa)
Q	conserved variable vector
q	modulus of velocity (m/s)
Δq	net specific energy generation (J/kg)
R	ideal gas constant (J/kg K)
Re	particle diameter based Reynolds number
s	specific entropy (J/kg K)
T	similarity transformation matrix or temperature (K)
t	time (s)
u, v	velocity components (m/s)
V	primitive variable vector, $= b[\rho, u, v, p]^T$
\dot{w}	mass vaporization rate per unit volume (kg/m ³ s)
x, y	space coordinates (m)

Greek Symbols

α	pressure-sensitive combustion response index
β	compression parameter or burning rate constant (m ² /s)
γ	specific heat ratio
ϵ	dissipation parameter
κ	spatial discretization selection parameter
Λ	eigenvalue matrix
λ	conductivity (W/mK)
μ	viscosity (kg/ms)
ρ	density (kg/m ³)
σ	flux-limiter parameter
τ	particle relaxation time (s), $= (4/3)(\rho_p/\rho_g)(d_p/C_D)(1/ \bar{u}_g - \bar{u}_p)$

Subscripts and Superscripts

g	gas-phase property
-----	--------------------

i	grid index, parcel group index
j	grid index
l	liquid spray
n	time index
o	original value
p	parcel property
x, y	coordinate components
$+$	downstream influence
$-$	upstream influence
$*$	reference condition
$\vec{()}$	vector
$\bar{()}$	mean value
$()'$	fluctuation about mean

References

1. Hsieh, K. C., "Assessment of Numerical Techniques for Unsteady Flow Calculations," AIAA Paper No. 89-1956, 1989.
2. Habiballah, M., Lourme, D., and Pit, F., "PHE-DRE - Numerical Model for Combustion Stability Studies Applied to the Ariane Viking Engine," *J. Propulsion and Power*, Vol. 7, No. 3, pp. 322-329, 1991.
3. DuBois, I. and Habiballah, M., "Numerical Simulation of High-Frequency Instability in an Oxygen/Hydrogen Rocket Engine," AIAA Paper No. 91-1860, 1991.
4. Venkateswaran, S., Grenda, J., and Merkle, C., "Computational Fluid Dynamic Analysis of Liquid Rocket Combustion Instability," AIAA Paper No. 91-1609, 1991.
5. Grenda, J., Venkateswaran, S., and Merkle, C., "Liquid Rocket Combustion Instability Analysis by CFD Methods," AIAA Paper No. 91-2085, 1991.
6. Bhatia, R. and Sirignano, W. A., "One-Dimensional Analysis of Liquid-Fueled Combustion Instability," *J. Propulsion and Power*, Vol. 7, No. 6, pp. 953-961, 1991.
7. Grenda, J., Venkateswaran, S., and Merkle, C., "Multidimensional Analysis of Combustion Instabilities in Liquid Rocket Motors," AIAA Paper No. 92-3764, 1992.
8. Kim, Y., Chen, Z., and Chen, C., "Prediction of Combustion Instability in High-Pressure Liquid Propellant Rocket Engines," AIAA Paper No. 92-3763, 1992.
9. Beam, R. M. and Warming, R. F., "An Implicit Finite-Difference Algorithm for Hyperbolic Systems in Conservation-Law Form," *Journal of Computational Physics*, Vol. 22, pp. 87-110, 1976.
10. Roe, P. L., "Approximate Riemann Solvers, Parameter Vectors, and Difference Schemes," *Journal of Computational Physics*, Vol. 43, pp. 357-372, 1981.
11. Roe, P. L., "Characteristic-Based Schemes for the Euler Equations," *Annual Review of Fluid Mechanics*, Vol. 18, pp. 337-365, 1986.
12. Harten, A., "High-Resolution Schemes for Hyperbolic Conservation Laws," *Journal of Computational Physics*, Vol. 49, pp. 357-393, 1983.
13. Yee, H. C., Warming, R. F., and Harten, A., "Implicit Total Variation Diminishing (TVD) Schemes for Steady-State Calculations," *Journal of Computational Physics*, Vol. 57, pp. 327-360, 1985.
14. Yee, H. C., "Construction of Explicit and Implicit Symmetric TVD Schemes and Their Applications," *Journal of Computational Physics*, Vol. 68, pp. 151-179, 1987.
15. Crocco, L. and Sirignano, W. A., "Effect of the Transverse Velocity Component on the Nonlinear Behavior of Short Nozzles," *AIAA J.*, Vol. 4, No. 8, pp. 1428-1430, 1966.
16. Litchford, R. J. and Jeng, S-M., "Efficient Statistical Transport Model for Turbulent Particle Dispersion in Sprays," *AIAA J.*, Vol. 29, No. 9, pp. 1443-1451, 1991.
17. Ranz, W. E. and Marshall, W. R., "Evaporation from Drops - Part I," *Chemical Engineering Progress*, Vol. 48, No. 3, pp. 141-146, 1952.
18. Crocco, L., "Aspects of Combustion Stability in Liquid Propellant Rocket Motors - Parts I and II," *ARS Journal*, Vol. 21, No. 6, pp. 163-178, Nov. 1951, and Vol. 22, No. 1, pp. 7-16, Jan. 1952.
19. Clayton, R. M., Rogero, R. S., and Sotter, J. G., "An Experimental Description of Destructive Liquid Rocket Resonant Combustion," *AIAA J.*, Vol. 6, No. 7, pp. 1252-1259, 1968.

Table 1 Scheme Switching Parameter

Scheme	κ
2 nd Order Upwind	-1
2 nd Order Central	1
3 rd Order Biased Upwind	1/3

Table 2 Propellant Properties

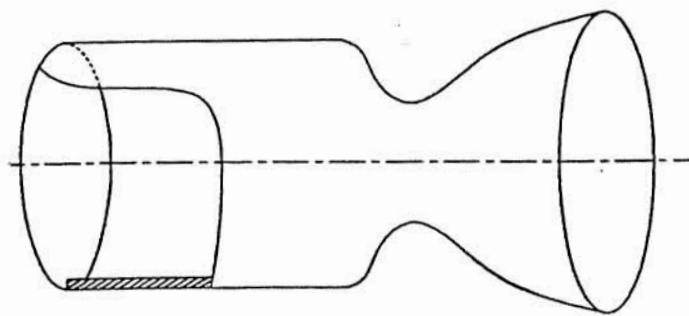
γ	1.2
C_p	1800 J/kg K
Δq	20(10) ⁶ J/kg
ρ_i	750 kg/m ³
μ	5(10) ⁻⁴ kg/m s
λ	1(10) ⁻¹ W/m K

Table 3 Combustor Physical Conditions

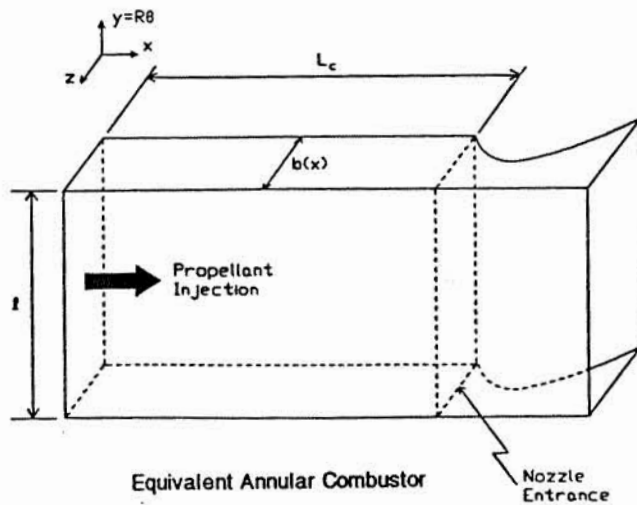
l_c	0.5 m
A_c	0.05 m ²
\bar{P}_c	34 atm
\dot{m}_c	40 kg/s
\dot{m}_i / \dot{m}_c	0.25
d_i	100 μ m
$u_{i,c}$	75 m/s

Table 4 Mean Burning Rate / Spray Length

β	l_i / l_c
1.4	0.36
1.0	0.60
0.8	0.90



Axisymmetric Combustor



Equivalent Annular Combustor

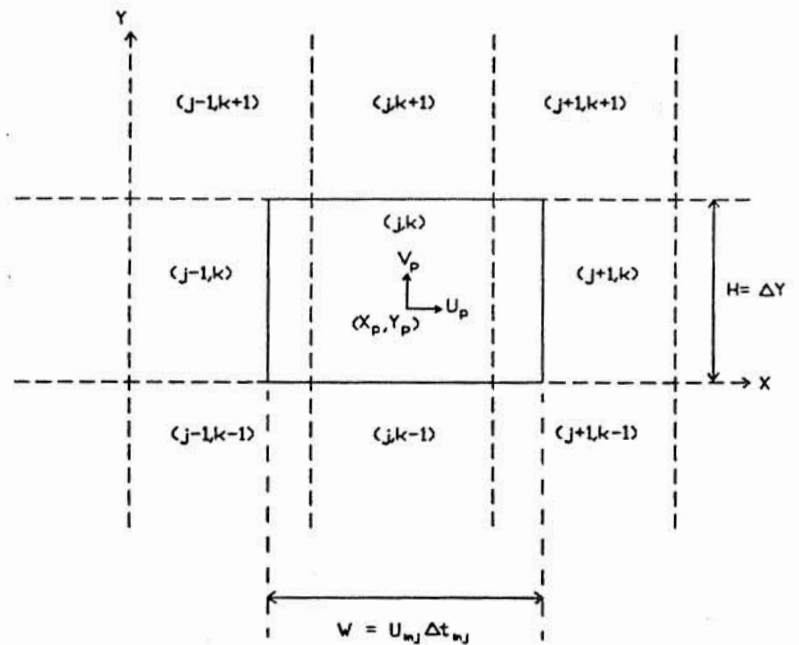
Nozzle
Entrance

Figure 2. Schematic of rectangular uniform pdf in relation to computational grid.

Figure 1. Schematic of physical combustor and equivalent annular computational geometry.

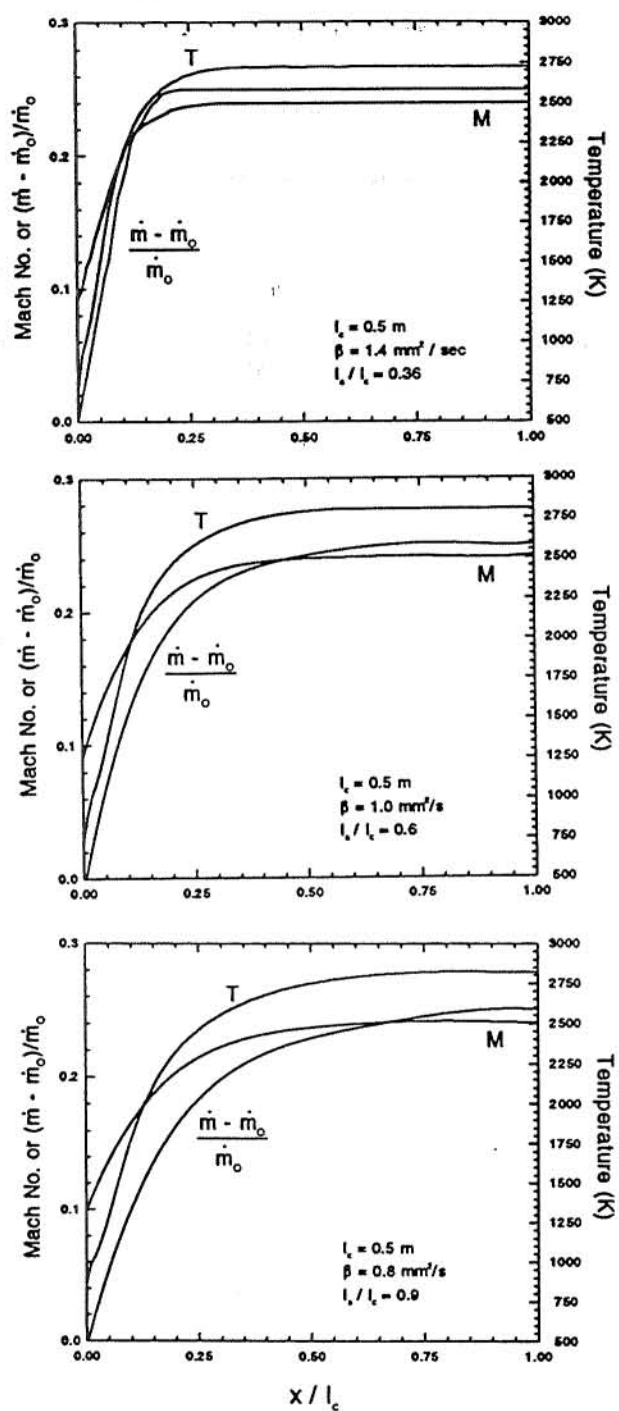


Figure 3. Computed mean flow field.

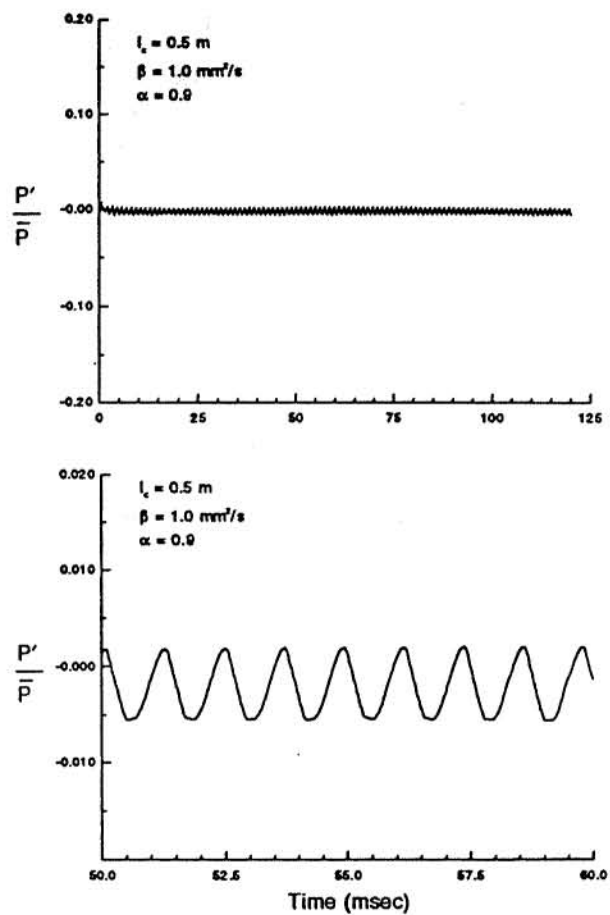


Figure 4. Longitudinal-mode, non-pulsed combustor stability calculation (stable).

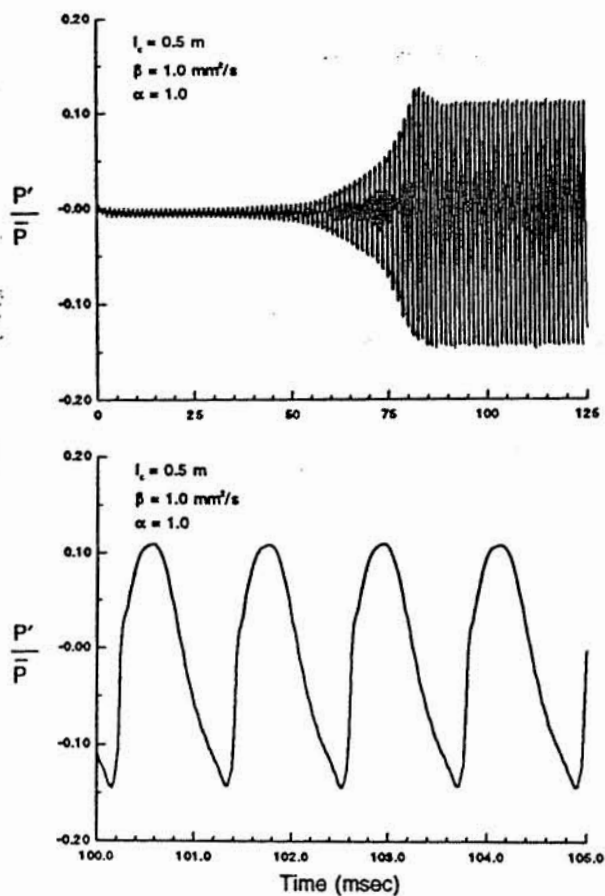


Figure 5. Longitudinal-mode, non-pulsed combustor stability calculation (unstable).

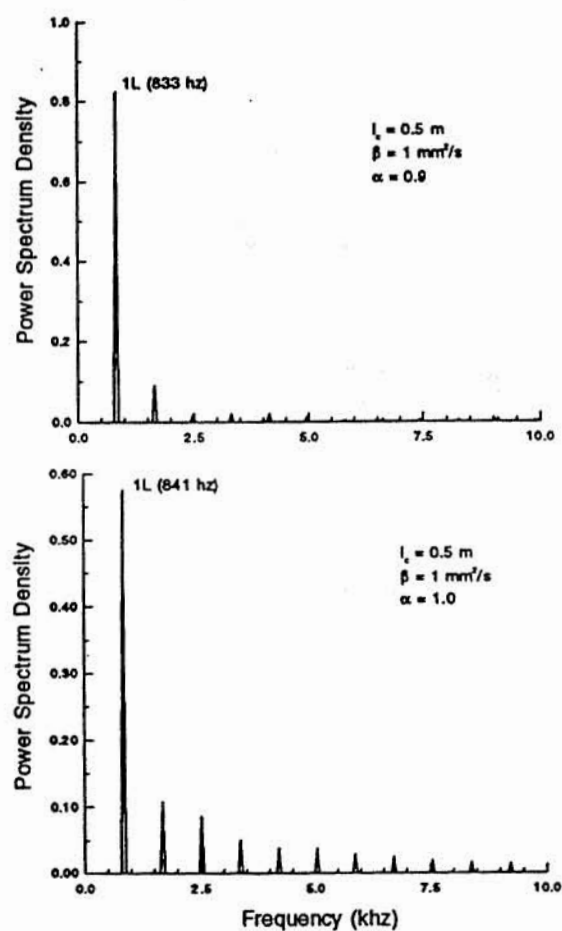


Figure 6. Spectral composition of pressure wave during stable and unstable combustion.

Figure 7. Fluctuation of flow parameters during unstable combustion.

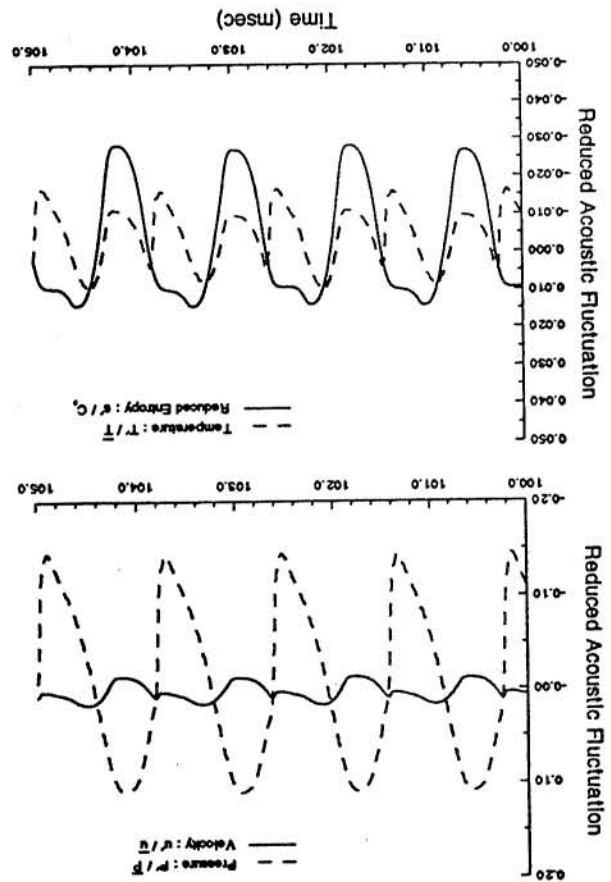


Figure 9. Longitudinal-mode combustor stability map.

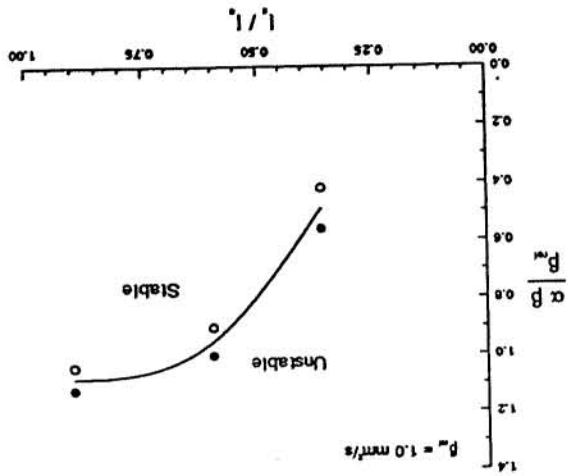
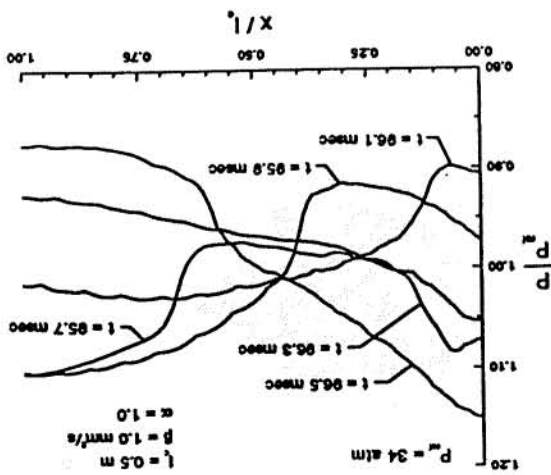


Figure 8. Pressure profiles during unstable combustion.



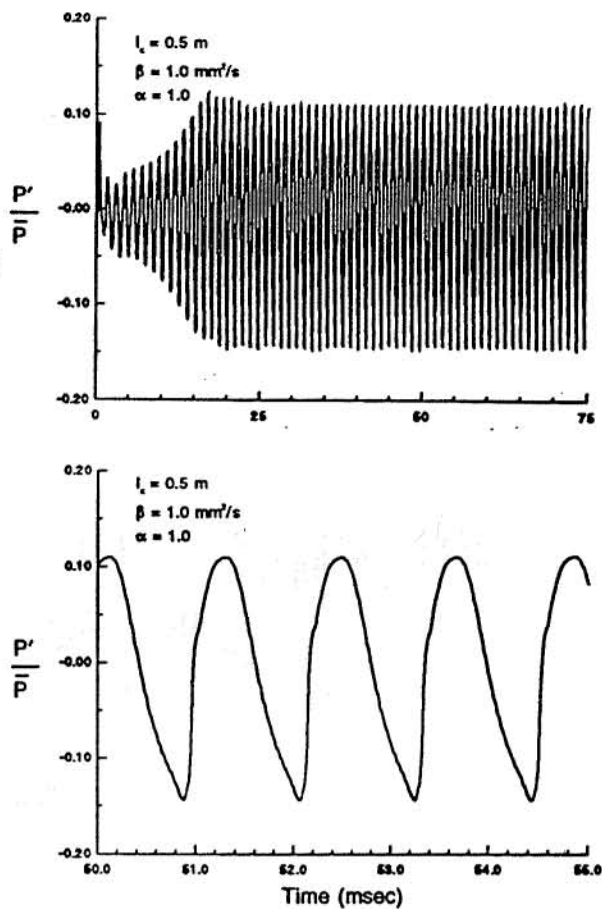


Figure 10. Longitudinal-mode, pulsed combustor stability calculation (unstable).

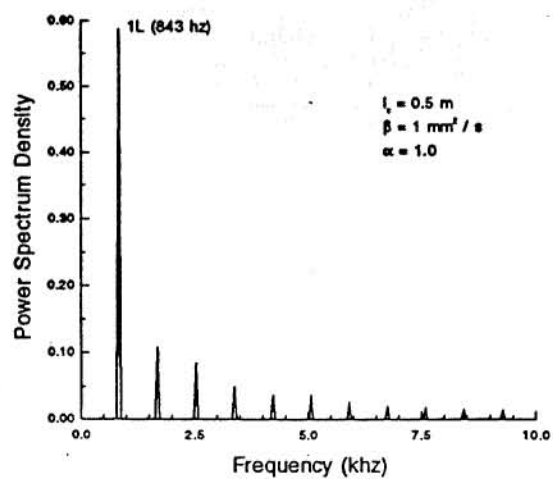


Figure 11. Spectral composition of pressure wave from pulsed stability calculation.

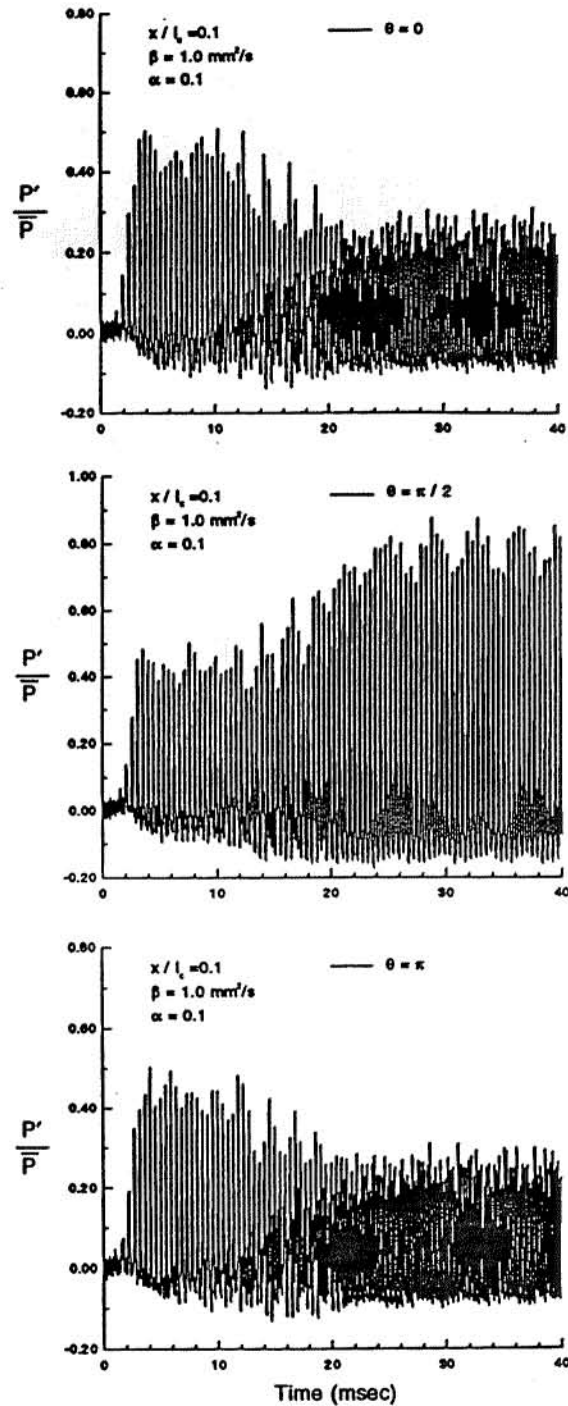


Figure 12. Tangential-mode, non-pulsed combustor stability calculation (unstable).

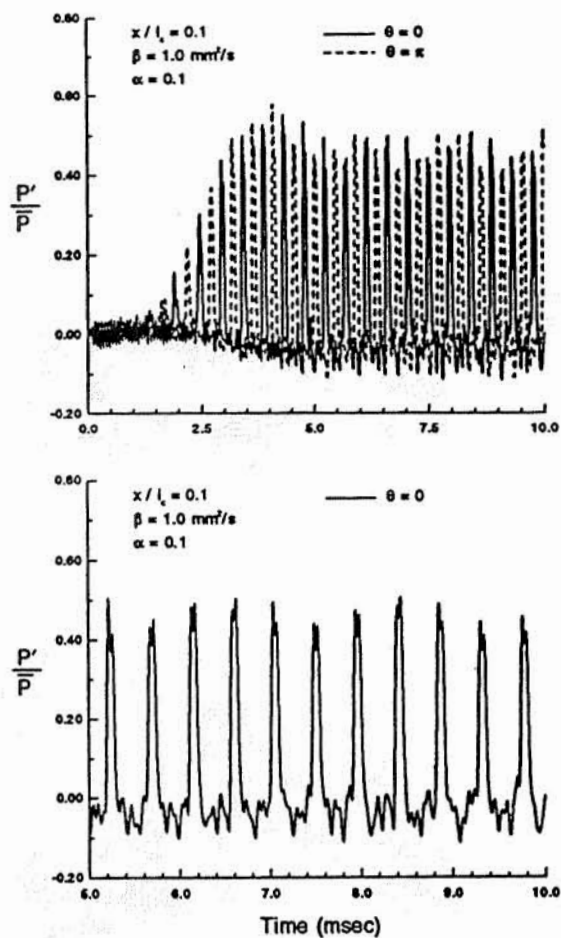


Figure 13. Short term tangential-mode instability.

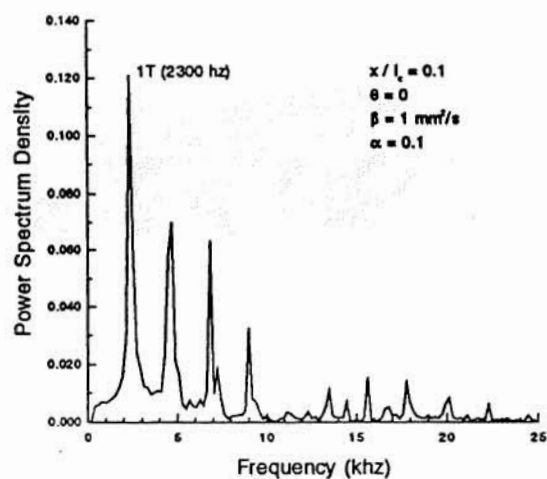


Figure 14. Spectral composition of tangential pressure wave for short term mode.

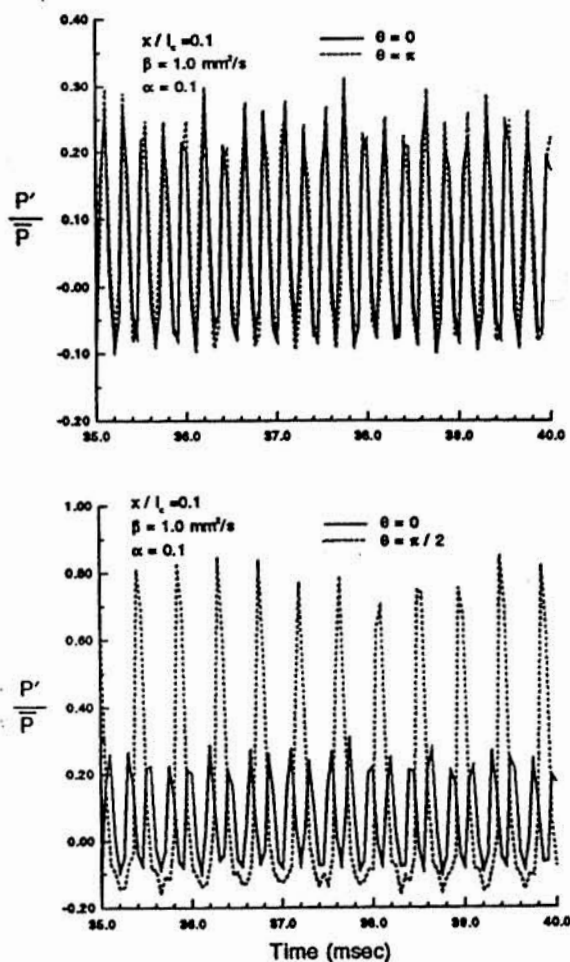


Figure 15. Long term tangential-mode instability.

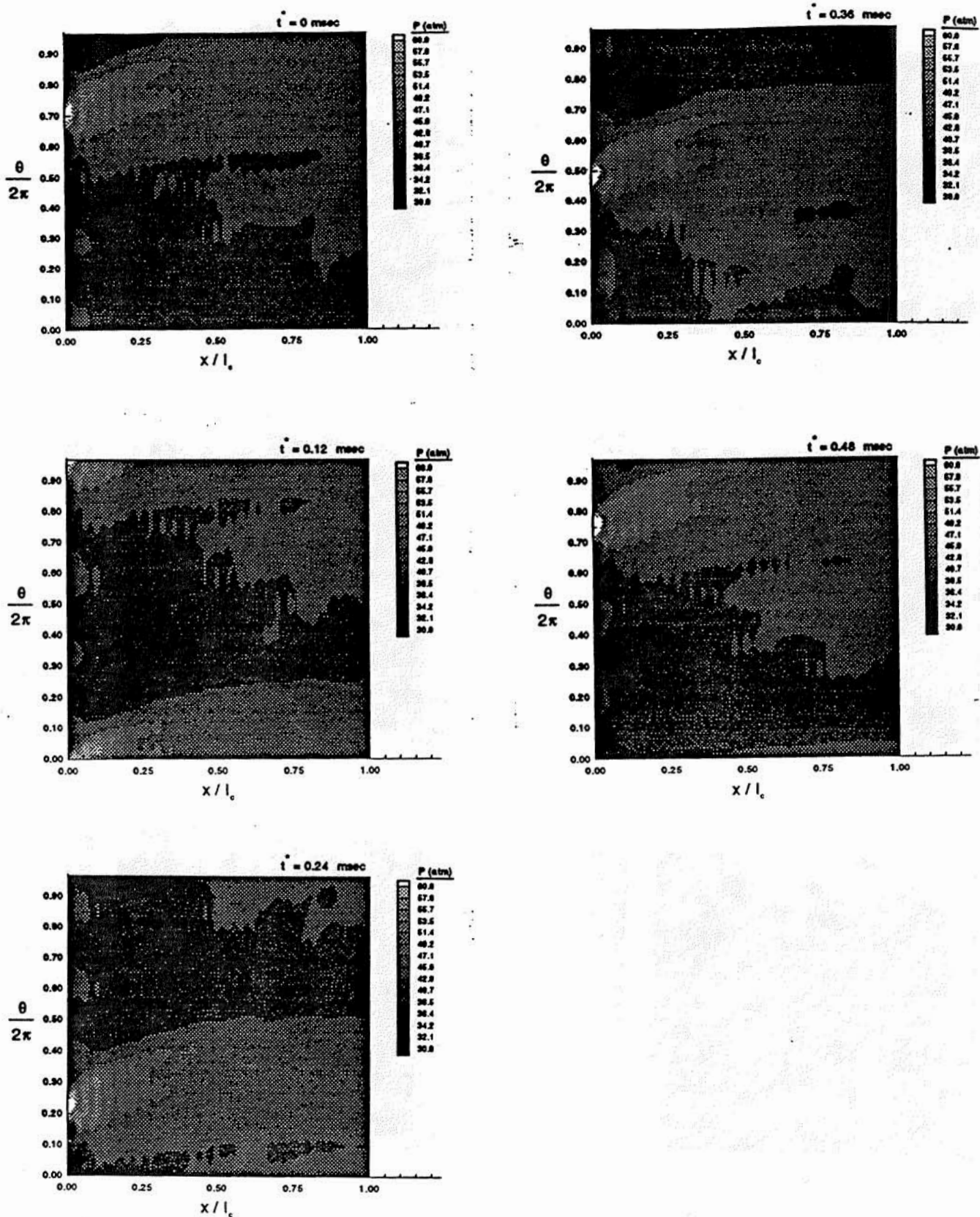


Figure 16. Combustor pressure history over one period of short term mode.

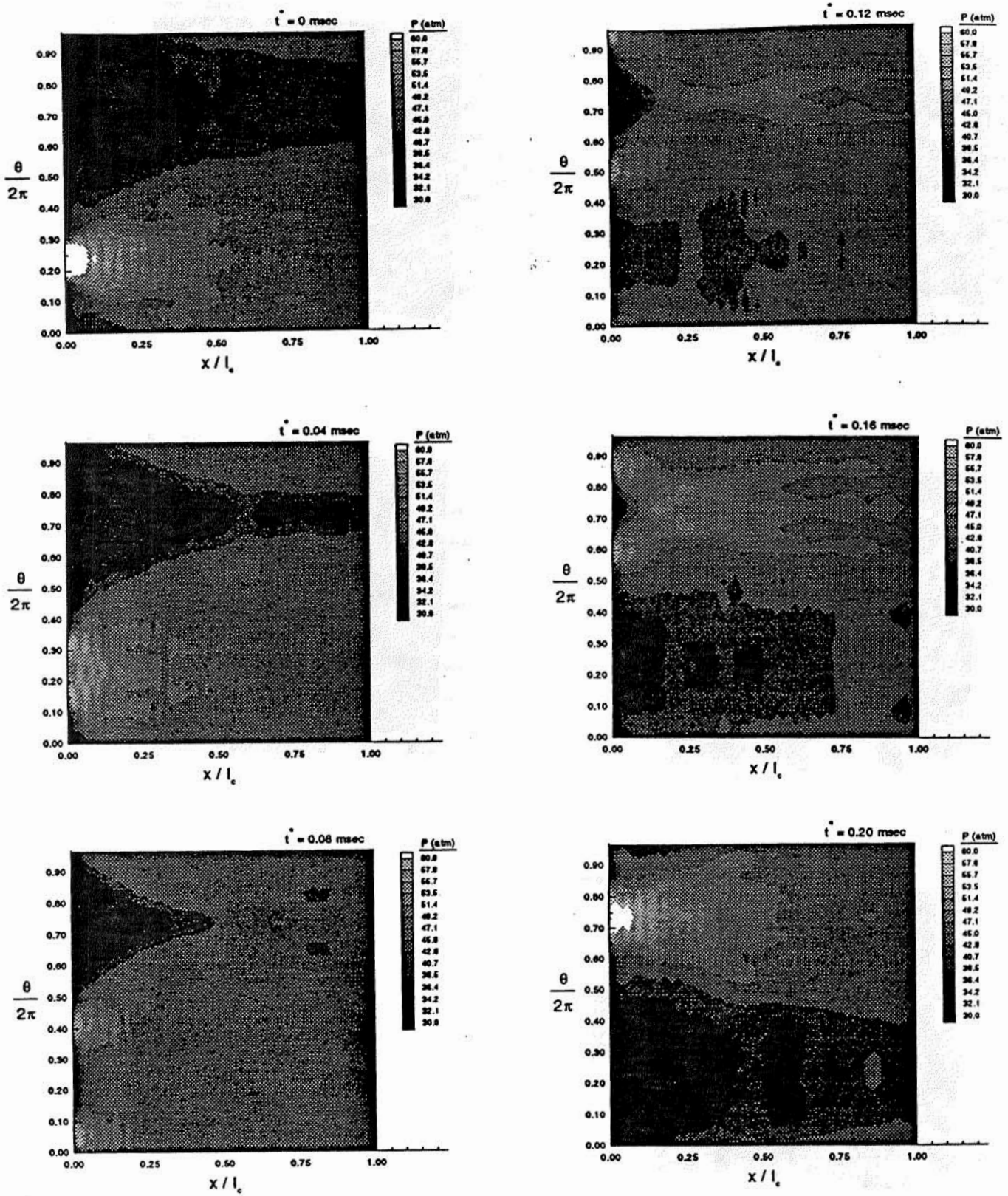


Figure 17. Combustor pressure history over one-half period of long term mode.

A NUMERICAL SIMULATION OF AXISYMMETRIC, STEADY-STATE PLASMA FLOW THROUGH MPD-TYPE THRUSTERS WITH APPLIED MAGNETIC FIELDS

Herbert Thomas*, Randall Chapman†, and George W. Garrison‡

Center for Space Transportation and Applied Research
UTSI Research Park
Tullahoma, TN 37388-8897

Abstract

An axisymmetric, implicit, finite-difference algorithm is formulated for the steady-state performance prediction of arcjet and MPD-type thrusters subject to both self-induced and applied magnetic fields. The azimuthal momentum equation is included in the algorithm to accommodate the swirl flow induced by the applied magnetic field. Thermal non-equilibrium is taken into account with the ionization level calculated using Saha's equation evaluated at the electron temperature. In addition, viscous and Hall effects are considered.

The code is applied to a geometry that allowed comparisons with numerical and experimental data. A parametric study is performed for different current and applied magnetic field levels. It is found that an applied magnetic field can significantly increase the performance of electromagnetic thrusters at high currents.

Nomenclature

a	=	speed of sound	t	=	time
B_ℓ	=	magnetic field in " ℓ " direction ($\ell = r, \phi, z$)	T_{ave}	=	average temperature
c_v	=	specific heat at constant volume	T_e	=	electron temperature
e	=	total energy of gas or electronic charge	T_s	=	heavy particle temperature
E_ℓ	=	electric field in " ℓ " direction	u	=	radial velocity component
J_ℓ	=	current density in " ℓ " direction	v	=	azimuthal velocity component
k	=	Boltzmann constant	w	=	axial velocity component
K	=	equilibrium constant	z	=	axial direction
m_s	=	mass of species " s "	Z	=	partition function
n_e	=	electron number density	α_1	=	fraction of singly ionized atoms
n_s	=	heavy species number density	α_2	=	fraction of doubly ionized atoms
p	=	pressure	γ	=	gas specific heat ratio
Pr	=	Prandtl Number	η	=	general curvilinear coordinate
r	=	radial direction	η_e	=	electron thermal conductivity coefficient
Re	=	Reynolds Number	μ	=	gas viscosity
Rm	=	Magnetic Reynolds number	μ_0	=	magnetic permeability
S	=	Magnetic Pressure Parameter			

* Graduate Research Assistant

† Principal Engineer, Member AIAA

‡ Executive Director, Member AIAA

ξ	=	general curvilinear coordinate
ξ_1	=	first ionization energy level
ξ_2	=	second ionization energy level
ρ	=	gas density
σ	=	electrical conductivity
τ_{ij}	=	stress tensor component in " ℓ_j " plane
ν_{es}	=	electron-heavy particle collision frequency
ϕ	=	azimuthal direction
ω_e	=	electron cyclotron frequency
τ_e	=	mean electron collision time
$\omega_e \tau_e$	=	Hall coefficient
∇	=	vector gradient operator

1. Introduction

Future planned space missions will require increasingly higher mission velocities and more efficient propulsion systems [1-3]. Due to the expected availability of significant electric power for space applications, electric propulsion is a candidate system for these missions.

Several electric propulsion concepts appear attractive. One promising concept is the Magneto Plasma Dynamic (MPD) Thruster. In an MPD thruster, electromagnetic fields exert a force on an electrically conducting propellant (plasma) and accelerate the propellant through the device. Exhaust velocities ten times higher than with conventional chemical propulsion systems can be realized [4], and thrust values are estimated at up to 100 N [5]. The performance of MPD thrusters may be enhanced even more, if applied magnetic fields are used.

Even though the underlying principles of MPD type thrusters have been known for many decades, the physical processes are so complex that a complete and accurate analytical model is difficult, if not impossible, to construct. The application of magnetic fields adds significantly to the complexity of the physical processes within the thruster. A model of the physical processes and a prediction of thruster performance is, however, desirable to bring MPD thrusters to an operational status.

For this reason, numerical simulations of MPD thrusters have been attempted over the past few years in the United States, Japan and Germany. The only attempt to numerically simulate the plasma flow

through an MPD thruster with induced and applied magnetic fields was performed in Japan [6,7]. However, the model used in these studies is inadequate to provide an accurate description. Especially, the assumption of a quasi one-dimensional flow field is certainly inadequate to describe the processes accurately, since a major effect of an applied magnetic field is the creation of a swirl flow. Additionally, Hall effects and variable conductivity are neglected.

The performance improvements possible with applied magnetic fields warrants increased study. It is, therefore, the goal of this effort to provide a more accurate model in an attempt to increase the understanding of applied field MPD thrusters.

2. Describing Equations

2.1 Model Assumptions

The Knudsen number in MPD type thrusters is generally small enough so that a collision dominated model for the flow field is valid. The set of equations that describes the system includes the coupled flow field and electromagnetic field equations, an equation of state, and expressions for the various transport coefficients.

The model is formulated in cylindrical coordinates with axisymmetry assumed. The azimuthal components of the magnetic field, momentum, and current density are retained. However, gradients in the azimuthal direction are neglected. An azimuthal magnetic field is induced due to the current. The azimuthal momentum and current density are required due to the presence of an applied magnetic field. Hall effects which result from the presence of induced and applied magnetic fields are important and therefore included.

The propellant is assumed to be described by an ideal gas equation of state with the electron excitation neglected. The plasma is not in thermal equilibrium and is described by separate electron and heavy particle temperatures. Equilibrium ionization is assumed and the degree of ionization is determined from Saha's equation evaluated at the electron temperature. A Reynolds number on the order of 10000 exists in these devices and thus, viscous effects become important for an accurate description and are included. The collision cross-sections and transport

properties are determined from the flow field properties. In addition, electrode sheath effects are neglected as are radiation losses from the plasma.

2.2 Fluid Equations

The Navier Stokes solver that is used for the flow field equations treats the plasma as a Reynolds averaged, single temperature fluid. The electron temperature and density are then determined by solving a separate electron energy equation and assuming equilibrium ionization. The complete set of non-dimensionalized conservation equations for mass, momentum and energy follows:

mass:

$$\frac{\partial \rho r}{\partial t} + \frac{\partial \rho r u}{\partial r} + \frac{\partial \rho r w}{\partial z} = 0$$

radial momentum:

$$\begin{aligned} \frac{\partial(\rho r u)}{\partial t} + \frac{\partial(\rho r u^2 + p r)}{\partial r} + \frac{\partial(\rho r u w)}{\partial z} = \\ \frac{1}{Re} \left[\frac{\partial \tau_{rr}}{\partial r} + \frac{\partial \tau_{rz}}{\partial z} - \tau_{\phi\phi} \right] \\ + SRm r (J_z B_r - J_r B_z) + p + \rho v^2 \end{aligned}$$

azimuthal momentum:

$$\begin{aligned} \frac{\partial(\rho r v)}{\partial t} + \frac{\partial(\rho r v u)}{\partial r} + \frac{\partial(\rho r v w)}{\partial z} = \\ \frac{1}{Re} \left[\frac{1}{r} \frac{\partial r^2 \tau_{r\phi}}{\partial r} + \frac{\partial \tau_{z\phi}}{\partial z} \right] \\ + SRm r (J_r B_z - J_z B_r) - \rho v u \end{aligned}$$

axial momentum:

$$\begin{aligned} \frac{\partial(\rho r w)}{\partial t} + \frac{\partial(\rho r w u)}{\partial r} + \frac{\partial(\rho r w^2 + p r)}{\partial z} = \\ \frac{1}{Re} \left[\frac{\partial \tau_{zz}}{\partial z} + \frac{\partial \tau_{rz}}{\partial r} \right] + SRm r (J_r B_\phi - J_\phi B_r) \end{aligned}$$

energy:

$$\begin{aligned} \frac{\partial r e}{\partial t} + \frac{\partial[r w(e+p)]}{\partial z} + \frac{\partial[r u(e+p)]}{\partial r} = SRm r (J_z E_z + J_r E_r) \\ + \frac{1}{Re} \frac{\partial}{\partial z} \left[r w \tau_{zz} + r u \tau_{rz} + r v \tau_{z\phi} + \frac{r m w}{Pr(\gamma-1)} \frac{\partial a^2}{\partial z} \right] \\ + \frac{1}{Re} \frac{\partial}{\partial r} \left[r w \tau_{rz} + r u \tau_{rr} + r v \tau_{r\phi} + \frac{r m w}{Pr(\gamma-1)} \frac{\partial a^2}{\partial r} \right] \end{aligned}$$

where e is the total energy given by:

$$e = \rho(c_v T_{ave} + \frac{(u^2 + v^2 + w^2)}{2}) + \alpha_1 C_1 + \alpha_2 C_2$$

with

$$C_1 = \frac{\xi_1 e}{\gamma(\gamma-1)k} \quad C_2 = \frac{\xi_2 e}{\gamma(\gamma-1)k}$$

As can be seen, the model allows for two degrees of ionization.

The Navier Stokes solver uses a single temperature in the calculations, whereas the model considers the plasma to have separate electron and heavy particle temperatures, with the heavy particles (neutrals and ions) assumed to be in thermal equilibrium. To accommodate the Navier Stokes solver, an average temperature for the plasma (T_{ave}) is defined and given by:

$$T_{ave} = T_s + (\alpha_1 + 2\alpha_2) T_e$$

The pressure of the plasma is the sum of the partial pressures

$$p = n_s k T_s + n_e k T_e$$

or in terms of T_{ave} :

$$p = n_s k T_{ave}$$

The Navier Stokes solver uses the assumption of a constant Prandtl number, the Sutherland viscosity law, and Stokes hypothesis to determine the thermal conductivity and viscosity coefficients. It also employs the Baldwin and Lomax, two equation algebraic turbulence model to determine turbulent flow.

2.3 Electromagnetic Equations

The magnetic induction equation can be derived by combining Maxwell's equations

$$\frac{1}{c^2} \frac{\partial \mathbf{E}}{\partial t} - \nabla \times \mathbf{B} = -\mu_0 \mathbf{J}$$

$$\frac{\partial \mathbf{B}}{\partial t} + \nabla \times \mathbf{E} = 0$$

with Ohm's law including Hall effects:

$$\mathbf{J} = \sigma(\mathbf{E} + \mathbf{u} \times \mathbf{B}) - \frac{\omega_e \tau_e}{|\mathbf{B}|} (\mathbf{J} \times \mathbf{B})$$

Taking the curl of Ohm's law, substituting the curl of the electric field in Maxwell's equation, and replacing the current density by the curl of the magnetic field, one obtains the magnetic induction equation, which expresses the electromagnetic problem only in terms of the magnetic field.

$$\begin{aligned} \frac{\partial \mathbf{B}}{\partial t} + \nabla \times \left[\frac{\nabla \times \mathbf{B}}{\sigma \mu_0} \right] - \nabla \times (\mathbf{u} \times \mathbf{B}) \\ + \nabla \times \left[\frac{\omega_e \tau_e}{\sigma \mu_0 |\mathbf{B}|} (\nabla \times \mathbf{B}) \times \mathbf{B} \right] = 0 \end{aligned}$$

Since changes in the azimuthal direction are neglected, the vector equation reduces to a single scalar equation for the induced magnetic field in the azimuthal direction.

The radial and axial current densities are determined from the induced azimuthal magnetic field:

$$\begin{aligned} J_r &= -\frac{1}{Rm r} \frac{\partial r B_\phi}{\partial z} \\ J_z &= \frac{1}{Rm r} \frac{\partial r B_\phi}{\partial r} \end{aligned}$$

The azimuthal current density is due to the applied magnetic field and is determined from the azimuthal component of Ohm's law. The azimuthal electric field vanishes due to axisymmetry, and the radial and axial electric fields are determined from rearranging Ohm's law.

$$\mathbf{E} = \frac{1}{\sigma} \left[\mathbf{J} + \frac{\omega_e \tau_e}{|\mathbf{B}|} (\mathbf{J} \times \mathbf{B}) \right] - (\mathbf{u} \times \mathbf{B})$$

The radial component of the electric field is integrated between the electrodes to determine the voltage across the plasma.

2.4 Electron Density and Energy Equations

The electrical conductivity and Hall parameter appearing in the electromagnetic equations are strong functions of the electron density and temperature. Electrons in an arc generated plasma typically have a much higher temperature than ions and neutrals. The model uses a separate electron energy equation, apart from the overall energy conservation equation utilized in the fluid equations, to calculate the electron temperature. The electron energy equation can be found in [8,9] and is rewritten in terms of the quantities determined from the fluid and electromagnetic equations. Neglecting the kinetic energy of the electrons as compared to the translational energy and neglecting viscous effects, the following electron energy equation is found.

$$\begin{aligned} \frac{\partial}{\partial t} \left[\frac{3}{2} n_e k T_e \right] - \frac{\partial}{\partial r} \left[5kT_e \left[n_e \frac{u}{2} + \frac{J_r}{e} \right] \right] \\ - \frac{\partial}{\partial z} \left[5kT_e \left[n_e \frac{w}{2} + \frac{J_z}{e} \right] \right] - \frac{\partial}{\partial r} \left[\eta_e \frac{\partial T_e}{\partial r} \right] - \frac{\partial}{\partial z} \left[\eta_e \frac{\partial T_e}{\partial z} \right] = \\ J_r E_r + J_z E_z + 3n_e m_e k \sum_s \frac{v_{es}}{m_s} (T_s - T_e) \end{aligned}$$

The collision term includes contributions from elastic electron-ion and electron-neutral collisions, with inelastic collisions are neglected. The heat conduction term includes contributions from electron thermal conduction and electron conduction currents, with thermal diffusion neglected. The electron thermal conductivity coefficient is calculated as in [9].

The electron density is determined assuming equilibrium ionization using Saha's equation. The equilibrium constants for the first and second degree of ionization are given by:

$$K_1 = \left[\frac{2\pi m_e k T_e}{h^2} \right]^{\frac{3}{2}} \frac{2Z_1^{elec}}{Z_0^{elec}} \exp \left\{ -\frac{\xi_1}{k T_e} \right\}$$

$$K_2 = \left[\frac{2\pi m_e k T_e}{h^2} \right]^{\frac{3}{2}} \frac{2Z_2^{elec}}{Z_1^{elec}} \exp \left\{ -\frac{\xi_2}{k T_e} \right\}$$

3. Algorithms and Boundary Conditions

3.1 Flow Field

The Navier Stokes solver is an implicit finite difference code based on the Beam and Warming approximate factorization algorithm [10]. The hyperbolic fluid equations (excluding the electromagnetic terms, i.e., Lorentz force and Joule heating) are written in vector, strong conservative law form and transformed into general, axisymmetric, curvilinear coordinates.

$$\frac{\partial \bar{Q}}{\partial t} + \frac{\partial \bar{E}}{\partial \xi} + \frac{\partial \bar{F}}{\partial \eta} = \frac{1}{Re} \left[\frac{\partial \bar{E}_v}{\partial \xi} + \frac{\partial \bar{F}_v}{\partial \eta} \right]$$

Where \bar{Q} is the conservation variables vector, \bar{E} and \bar{F} are the ξ - and η -components of the inviscid flux vectors, and \bar{E}_v and \bar{F}_v are the ξ - and η -components of the viscous flux vectors.

Euler backward time differencing is applied to the above equation with the viscous flux vectors time lagged to allow formation of the scalar tridiagonal algorithm.

$$\Delta \bar{Q}^n + \Delta t^n \left[\frac{\partial \bar{E}^{n+1}}{\partial \xi} + \frac{\partial \bar{F}^{n+1}}{\partial \eta} \right] = \frac{\Delta t^n}{Re} \left[\frac{\partial \bar{E}_v^n}{\partial \xi} + \frac{\partial \bar{F}_v^n}{\partial \eta} \right]$$

Where Δ is the forward time difference. The inviscid flux vectors are nonlinear functions of the conservation variables vector and are time linearized by

$$\begin{aligned} \bar{E}^{n+1} &= \bar{E}^n + A^n \Delta \bar{Q}^n \\ \bar{F}^{n+1} &= \bar{F}^n + B^n \Delta \bar{Q}^n \end{aligned}$$

where A and B are the Jacobian matrices.

$$A = \frac{\partial \bar{E}}{\partial \bar{Q}} \quad B = \frac{\partial \bar{F}}{\partial \bar{Q}}$$

Time linearizing the above equation gives

$$\begin{aligned} & \left[I + \Delta t \left[\frac{\partial A^n}{\partial \xi} + \frac{\partial B^n}{\partial \eta} \right] \right] \Delta \bar{Q}^n = \\ & - \Delta t \left[\frac{\partial \bar{E}^n}{\partial \xi} + \frac{\partial \bar{F}^n}{\partial \eta} \right] + \frac{\Delta t}{Re} \left[\frac{\partial \bar{E}_v^n}{\partial \xi} + \frac{\partial \bar{F}_v^n}{\partial \eta} \right] \end{aligned}$$

where I is the identity matrix.

Using the method of approximate factorization for the operator on $\Delta \bar{Q}^n$ results in:

$$\begin{aligned} & \left[I + \Delta t \frac{\partial A^n}{\partial \xi} \right] \left[I + \Delta t \frac{\partial B^n}{\partial \eta} \right] \Delta \bar{Q}^n = \\ & - \Delta t \left[\frac{\partial \bar{E}^n}{\partial \xi} + \frac{\partial \bar{F}^n}{\partial \eta} \right] + \frac{\Delta t}{Re} \left[\frac{\partial \bar{E}_v^n}{\partial \xi} + \frac{\partial \bar{F}_v^n}{\partial \eta} \right] \end{aligned}$$

The factorization scheme is then implemented by the alternating direction sequence:

$$\begin{cases} \left[I + \Delta t \frac{\partial A^n}{\partial \xi} \right] \Delta \bar{Q}^* = RHS \\ \left[I + \Delta t \frac{\partial B^n}{\partial \eta} \right] \Delta \bar{Q}^n = \Delta \bar{Q}^* \end{cases}$$

where:

$$RHS = -\Delta t \left[\frac{\partial E^n}{\partial \xi} + \frac{\partial F^n}{\partial \eta} \right] + \frac{\Delta t}{Re} \left[\frac{\partial E_v^n}{\partial \xi} + \frac{\partial F_v^n}{\partial \eta} \right]$$

The spatial derivatives flux vectors are replaced by the appropriate differences:

$$\begin{aligned} (I + \Delta t \delta_\xi A^n) \Delta \bar{Q}^* &= RHS \\ (I + \Delta t \delta_\eta B^n) \Delta \bar{Q}^n &= \Delta \bar{Q}^* \end{aligned}$$

$$RHS = -\Delta t (\delta_\xi E^n + \delta_\eta F^n) + \frac{\Delta t}{Re} (d_\xi E_v^n + d_\eta F_v^n)$$

where the central differences are defined:

$$\begin{aligned} \delta_\xi E &= \frac{1}{2} [E(\xi+1, \eta) - E(\xi-1, \eta)] \\ \delta_\eta F &= \frac{1}{2} [F(\xi, \eta+1) - F(\xi, \eta-1)] \\ d_\xi E_v &= E_v(\xi+\frac{1}{2}, \eta) - E_v(\xi-\frac{1}{2}, \eta) \\ d_\eta F_v &= F_v(\xi, \eta+\frac{1}{2}) - F_v(\xi, \eta-\frac{1}{2}) \end{aligned}$$

In addition, artificial viscosity is introduced to provide stability.

This set of equations requires the solution of a block-tridiagonal set of matrices. Splitting the matrices A and B into the eigenvector and eigenvalue matrices

$$A = T_1 \Lambda_1 T_1^{-1} \quad B = T_2 \Lambda_2 T_2^{-1}$$

where Λ is the diagonal matrix of eigenvalues, and T is the matrix of right eigenvectors with T^{-1} its inverse. Thus, the diagonalized form of the algorithm is then the tridiagonal set of equations

$$T_1 \left[I + \Delta t \frac{\partial \Lambda_1}{\partial \xi} \right] T_1^{-1} T_2 \left[I + \Delta t \frac{\partial \Lambda_2}{\partial \eta} \right] T_2^{-1} \Delta \bar{Q} = RHS$$

which can be solved by a variant of Gaussian elimination (an extended Thomas algorithm). However, the time-accuracy of the code is not conserved.

As mentioned previously, the viscous terms are time lagged and not included in the implicit part of the Navier Stokes solver. The model incorporates the electromagnetic terms (Lorentz force and Joule heating) into the Navier Stokes solver in the same manner.

The inlet flow is assumed to be normal to the entrance plane, with the stagnation temperature and pressure specified. A distinct advantage of the Navier Stokes solver utilized in this study is the capability of transonic flow simulations. Thus, the inlet velocity is allowed to be subsonic. The electrode and insulator surfaces are treated with the no-slip, isothermal boundary condition. The centerline is treated with the slip, adiabatic boundary condition.

3.2 Magnetic Induction and Electron Energy Equations

The magnetic induction and electron energy equations are solved separately with the same implicit finite difference algorithm. The elliptic equations are written in nondimensional form and transformed into general, axisymmetric, curvilinear coordinates. Euler backward time differencing is used and the spatial derivatives are replaced by appropriate central differences. This results in a system of tridiagonal equations for each time step, which are solved using a modified Gauss-Seidel Successive Over Relaxation (SOR) scheme [11]. The procedure is time marched until steady-state is reached.

To obtain the boundary conditions for the induced magnetic field at the electrode surfaces, Ohm's law is

expressed in terms of only the electric and magnetic fields using Maxwell's equations. The normal derivative is then eliminated resulting in one differential equation along the surface. The induced magnetic field is $B_\phi = \mu_0 J / 2\pi r$ at the upstream side of the electrodes and zero at the downstream side of the electrodes. Also, the tangential electric fields at electrode surfaces are zero. From these conditions, the differential equation can be solved to obtain the induced magnetic field along the electrode surfaces. The boundary condition for the induced magnetic field at insulator surfaces is $r \cdot B_\phi = \text{constant}$. In addition, the outer grid boundary is treated as an insulator.

The boundary values for the electron temperature equation are found by performing an energy balance between Joule heating and the energy transfer between heavy particles and electrons due to collisions. The electron temperature, therefore, is not directly specified and can vary over a boundary segment.

4. Results

The code is applied to an MPD-type thruster geometry, similar to the one used in Stuttgart [12,13]. Due to numerical stability problems at the perpendicular interfaces between electrodes and insulators, a short (~10 mm) insulator section was added to the entrance of the device. The geometry and orthogonal grid is depicted in Figure 1. The grid size is 25 radial \times 35 axial.

Results of a parametric study are presented to demonstrate the codes versatility and to demonstrate the effect of an applied magnetic field on the performance of a thruster. The propellant used for this study is argon. Four current levels are specified, 3.0, 7.5, 12.5, and 17.5 kA, in combination with three levels of applied magnetic field strengths, 0, 0.1, and 0.2 T. The applied magnetic field is assumed to be constant and axial. Omission of data points for the 17.5 kA input current and 0.2 T applied magnetic field case are due to convergence problems.

The initial heavy particle temperature is specified at 3500 °K and the initial electron temperature is determined according to the electron energy balance. The code developed numerical problems when the heavy particle and electron temperatures were set at 300 °K and 5000 °K, respectively, corresponding to the entrance conditions in [53]. The electron temperature decreased rapidly, probably due to the

insertion of the insulator sections upstream of the electrodes which prevented significant currents densities and the resultant Joule heating from occurring at the entrance.

An initial pressure is specified which results in a mass flow rate of 20-30 g/s. The computations became unstable when a pressure was set, which resulted in a mass flow rate of 6 g/s, corresponding to the entrance conditions in [53]. The flow became choked at the upstream region of the electrodes due to Joule heating. The background pressure is set at 0.5 torr.

For these initial conditions, the Mach number is ~0.5 at the entrance and the pressure is typically 50-70 torr in the interelectrode region. Each calculation required about 3000 iterations to converge and 5-6 hrs cpu time.

An example of the electric field and current density streamlines in nondimensional form are given in Figures 2 and 3, respectively. In Figure 3, the contribution from the axial Hall current ($J_z = \omega \tau J_\phi B_\phi / B$) can be readily seen. The current density streamlines exhibit an almost perpendicular attachment at the downstream portion of the electrodes, with an increasingly inclined attachment towards the upstream portion. The Hall parameter as well as the induced magnetic field increases towards the upstream section of the thruster. Therefore, the Hall effect is more pronounced at the upstream portion of the thruster, than at the downstream portion.

In Figure 4, the voltage is plotted as a function of input current for the above mentioned applied magnetic field strength. Also indicated by the dashed line are experimentally obtained voltage values from Stuttgart [14] without an applied magnetic field. The voltage predictions are approximately four to five volts lower than the experimentally determined values. This is probably due to the fact that the sheath effects and the resulting voltage drop at the electrodes are neglected in these calculations. The trend, however, is very well predicted by the code.

Visible is an increase in voltage with an increase of the applied magnetic field. If one neglects the Hall parameter and assumes that the axial velocity and the induced magnetic field are not affected by the applied magnetic field, it can be shown from Ohm's law in the radial direction that the radial electric field balances with the product of the applied axial magnetic field

and the azimuthal velocity. Since the azimuthal velocity itself increases with the applied magnetic field (due to the Lorentz force), a non-linear increase in the electric field, and thereby in the voltage, with an applied magnetic field appears reasonable.

The same functional relationship for the power is visible in Figure 5. Again, experimental data obtained by Stuttgart [14], are represented as a dashed line. The difference between calculated and experimentally obtained voltage is visible in this figure, as well. The non-linear increase in power with the input current can be verified by simple analytical solutions.

The thrust is plotted as a function of input current at the applied magnetic field strengths in Figure 6. Interesting to note is the increased impact of an applied magnetic field on the thrust at higher input currents. This, and other observations, indicates that the thruster operates more as an electrothermal device for the lower input currents and more as a electromagnetic device for the higher input currents, which most likely is due to the high mass flow rates used in these calculations. Obviously, the effect of an applied magnetic field is more beneficial for electromagnetic thrusters.

5. Summary and Conclusions

A numerical model to simulate the plasma flow through an MPD-type thruster with induced and applied magnetic fields is presented. Viscosity, thermal non-equilibrium and varying transport properties and cross-sections are included in the model.

The results obtained with the code indicate a significant effect of an applied magnetic field on the performance of MPD-type thrusters. Further investigation of applied field MPD thrusters seems, therefore, desirable.

Future efforts will focus on extending the calculations to lower mass flows rates, and including finite-rate ionization, equilibrium and kinetic chemistry for propellants other than argon, and electrode sheath effects.

References

1. Sutton, George P., *Rocket Propulsion Elements - An Introduction to the Engineering of Rockets*, Fifth

Edition, Wiley-Interscience, 1986.

2. Mead, Franklin B., "Future Possibilities for Nonconventional Propulsion Developments at the Air Force Rocket Propulsion Laboratory," CPIA Publication XXX (Proceedings), 1986.

3. Kelly, J.D., "Free Radicals, Electronic Metastables, and Other Energetic Molecules as Potential Rocket Propellants," Presented at the AIAA/ASME/SAE/ASEE 24th Joint Propulsion Conference, Boston, Massachusetts, July 1988, AIAA 88-3172.

4. King, D.Q., "Design and Operation of a 100 kW, Subscale MPD Engine," May 1987, AIAA 87-1020.

5. Burton, R.L., Clark, K.E., and Jahn, R.G., "Thrust and Efficiency of a Self-Field MPD Thruster," Presented at the AIAA/JSASS/DGLR 15th International Electric Propulsion Conference, Las Vegas, Nevada, April 1981, AIAA 81-0684.

6. Kimura, I., Toki, K., and Tanaka, M., "Current Distribution on the Electrodes of MPD Arcjets," AIAA Journal, Vol. 20, No. 7, 1982, pp. 889-892.

7. Nishida, M., Kaita, K., and Tanaka, K., "Numerical Studies of the Flow Field in a Low Power DC Arcjet Thruster," presented at the AIAA/DGLR/JSASS 20th International Electric Propulsion Conference, West Germany, 1988.

8. Candler, G. and MacCormack, R., "The Computation of Hypersonic Ionized Flows in Chemical and Thermal Nonequilibrium," Presented at the AIAA 26th Aerospace Sciences Meeting, Reno, Nevada, January 1988, AIAA 88-0511.

9. Park, C., *Nonequilibrium Hypersonic Aerothermodynamics*, Wiley, 1990.

10. Cooper, G.K., "The PARC Code: Theory and Usage," Final Report, AEDC TR-87-24, 1987.

11. Thomas, Herbert, "A Numerical Simulation of Axisymmetric, Steady-State Plasma Flow with Self-Induced and Applied Magnetic Fields", Ph.D. Dissertation, University of Tennessee, August 1991.

12. Kurtz, H.L., Auweter-Kurtz, M., Merke, W.D., and Schrade, H.O., "Experimental MPD Thruster Investigations," AIAA 87-1019, May 1987.

13. Sleziona, P.C., Auweter-Kurtz, M., and Schrade, H.O., "Numerical Codes for Cylindrical MPD Thrusters," Presented at the DGLR/AIAA/JSASS 20th International Electric Propulsion Conference, West Germany, October 1988, IEPC 88-038.

14. Private communications with the "Institut für Raumfahrtssysteme" (IRS), Universität Stuttgart, Germany, 1991.

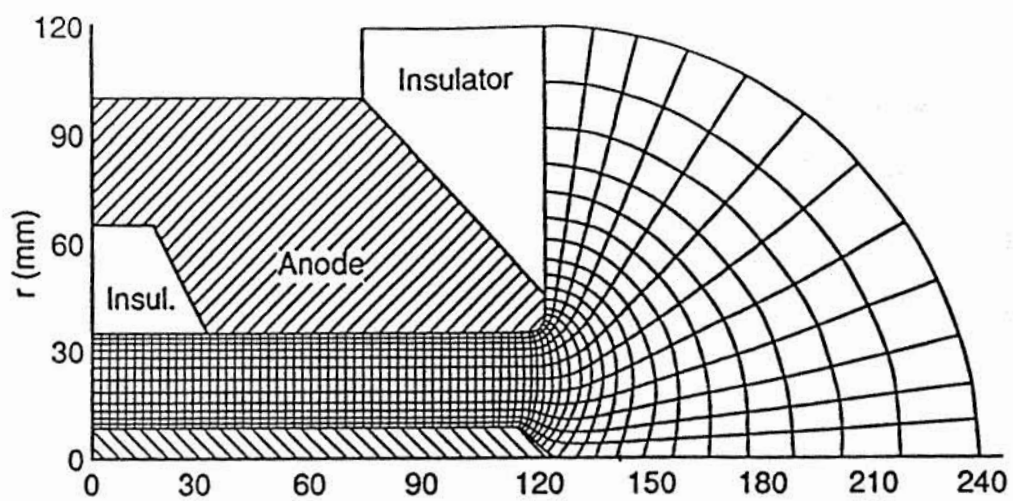


Figure 1. MPD-type thruster geometry used in calculations.

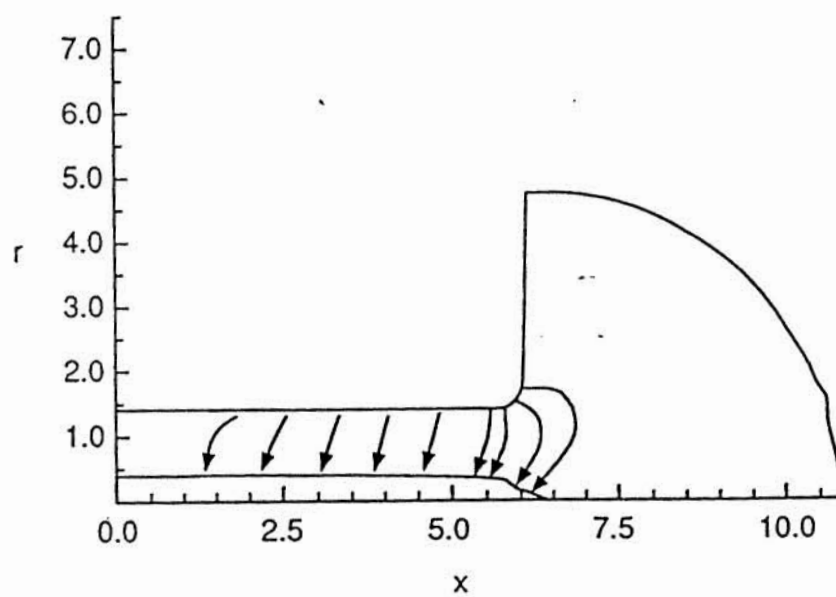


Figure 2. Electric field streamlines.

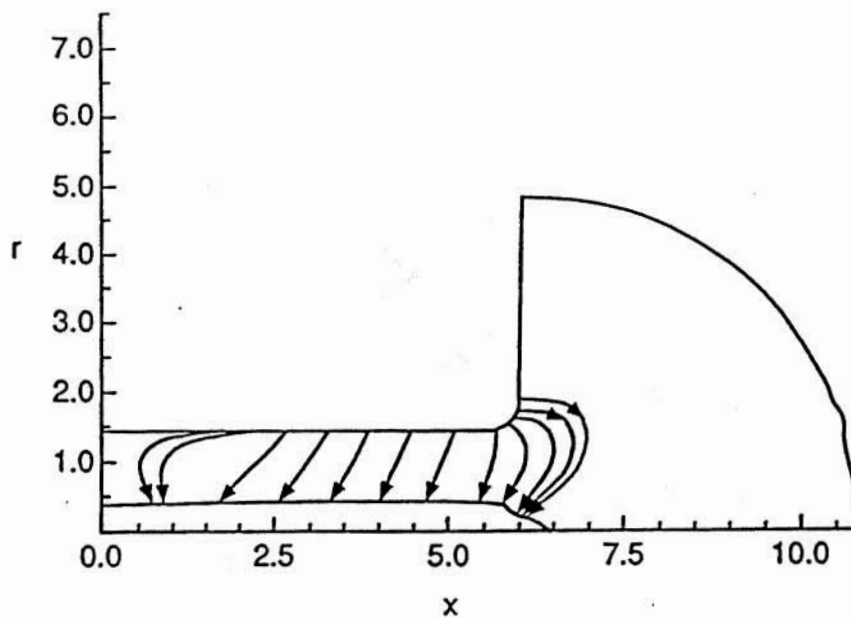


Figure 3. Current density streamlines.

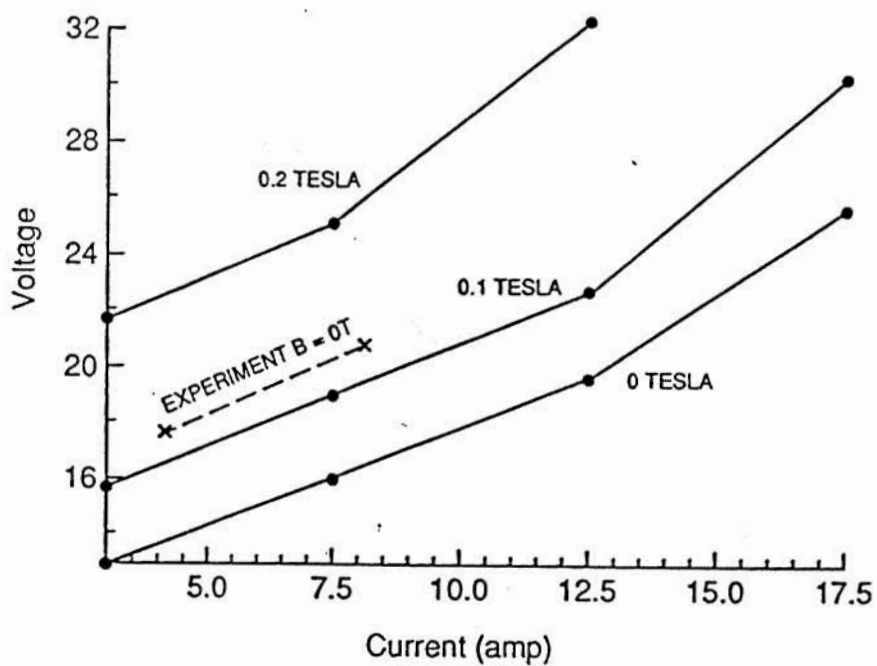


Figure 4. Voltage as a function of input current at various magnetic field strengths.

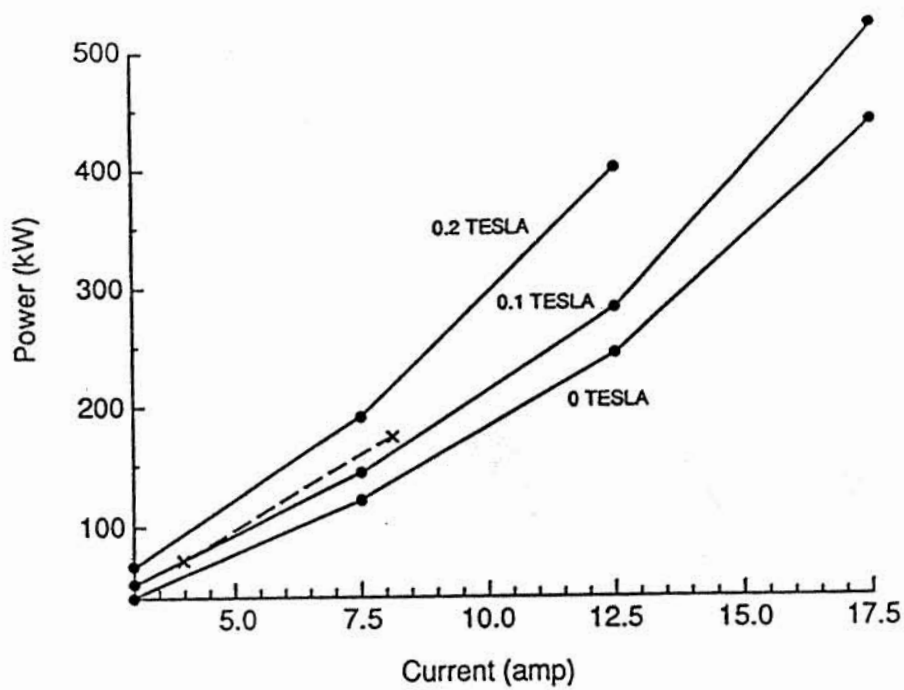


Figure 5. Power as a function of input current at various magnetic field strengths.

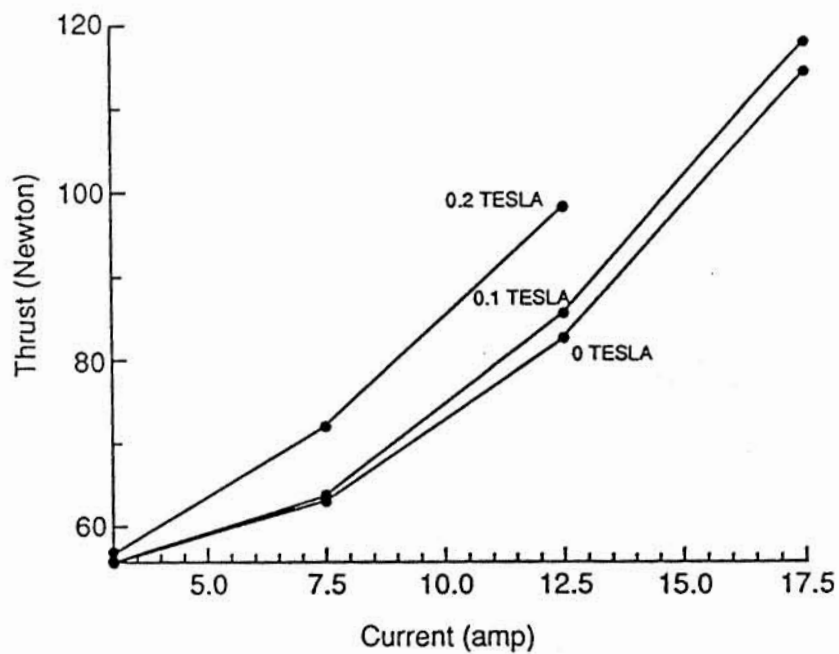


Figure 6. Thrust as a function of input current at various magnetic field strengths.

COMPUTATION OF TWO-PHASE FLOW IN SOLID ROCKET MOTORS

513-20
NAB
N96-70534

San-Mou Jeng *
University of Cincinnati
Cincinnati, OH 45221

ABSTRACT

A computer code (two-dimensional or axisymmetric) has been developed to analyze two-phase flow in solid rocket motors. The primary objective of this study has been to improve the computational efficiency and numerical accuracy of the particle-phase solver. This newly developed particle solver is based on the Lagrangian formulation. The code can be easily coupled with any existing gas-phase solver. In this paper, two gas phase solvers, RPLUS and FNS3D, have been coupled with the developed code and tested against two solid rocket nozzles. The effect of particle loading ratio and particle size on the rocket performance are then investigated.

INTRODUCTION

Metallized solid propellants are frequently used in solid rocket motors (SRM) to increase specific impulse and total thrust level. The most commonly used metal additives are aluminum particles. When this metallized solid propellant burns, two types of particles can be found in the exhaust gases: Al/Al_2O_3 composite particles and small smoke particles. For example, measurements of particle sizes for the Space Shuttle solid rocket booster (SRB) reveal that 80 % of the particle mass was comprised of 15 micrometer "smoke" particles and about 20% of the particle mass was comprised of about 115 micrometer.

The presence of these particles in the rocket may contribute to the performance loss or may interact with the motor walls causing surface damage. Therefore, it is important to study the effect of solid particles on rocket performance. In SRM configuration, numerical analysis based on single-phase formulation is not accurate particularly in high particle loading conditions since particles inside the solid rocket motors may not follow the gas streamlines.

Usually, larger or heavier particles have higher inertia and can not follow the acceleration, deceleration, and turning of the gas flows. Particles tend to follow gas streamlines more closely in larger thrusters or in SRMs operated at higher pressures. In this case, particles either have longer flow residence time or are subjected to larger drag force from gases.

Although particle's effect is important to SRM's performance, general design practice is still based on single-phase flow characteristics. This is partly due to the fact that tools for two-phase flow computations have not matured yet. The objective of this research is to establish an efficient two-phase flow computer code for solid rocket motors. A combined Eulerian-Lagrangian approach is adopted to analyze steady-state two-phase flows in SRMs. The trajectories of particles with various sizes in two solid rocket motors are then investigated. Effect of particle loading ratio on the gas flow field are also studied.

GOVERNING EQUATIONS

Gas Phase

The governing equations are taken to be the two-dimensional, compressible, Reynolds-averaged Navier-Stokes equations. Written in a strong conservative form, the governing equations can be expressed as follows:

$$\frac{\partial Q}{\partial t} + \frac{\partial}{\partial x} (E - E_v) + \frac{\partial}{\partial y} (F - F_v) = H \quad (1)$$

Here x and y are Cartesian coordinates, Q is the dependent variable, E and F are the convective flux vectors:

$$Q = \begin{pmatrix} \rho \\ \rho u \\ \rho v \\ \rho e \end{pmatrix}$$

* Associate Professor, Aerospace Engineering and Engineering Mechanics.

$$E = \begin{pmatrix} \rho u \\ \rho u^2 + p \\ \rho uv \\ u(\rho e + p) \end{pmatrix} \quad F = \begin{pmatrix} \rho v \\ \rho uv \\ \rho v^2 + p \\ v(\rho e + p) \end{pmatrix} \quad (2)$$

E_v and F_v are the viscous flux vectors:

$$E_v = \begin{pmatrix} 0 \\ \tau_{xx} \\ \tau_{xy} \\ u\tau_{xx} + v\tau_{xy} - q_x \end{pmatrix} \quad F_v = \begin{pmatrix} 0 \\ \tau_{yx} \\ \tau_{yy} \\ u\tau_{yx} + v\tau_{yy} - q_y \end{pmatrix} \quad (3)$$

and H is the source vector:

$$H = \begin{pmatrix} S^m \\ S^{mu} \\ S^{mv} \\ S^e \end{pmatrix} \quad (4)$$

The specific total energy, e , shear stress components, τ , and heat flux components, q , are given as:

$$e = C_v T + \frac{1}{2} (u^2 + v^2) \quad (5)$$

$$\tau_{xx} = 2\mu \frac{\partial u}{\partial x} - \frac{2}{3}\mu \left(\frac{\partial u}{\partial x} + \frac{\partial v}{\partial y} \right) \quad (6.a)$$

$$\tau_{yy} = 2\mu \frac{\partial v}{\partial y} - \frac{2}{3}\mu \left(\frac{\partial u}{\partial x} + \frac{\partial v}{\partial y} \right) \quad (6.b)$$

$$\tau_{xy} = \tau_{yx} = \mu \left(\frac{\partial u}{\partial y} + \frac{\partial v}{\partial x} \right) \quad (6.c)$$

$$q_x = -k \frac{\partial T}{\partial x}, \quad q_y = -k \frac{\partial T}{\partial y} \quad (7)$$

In the preceding expressions, ρ is the density, u and v are the Cartesian velocity components, p is the pressure, and e is the specific total energy. The source term H represents the interfacial exchange of mass, momentum and energy between gas and particle phase and are derived from Lagrangian particle trajectory calculations.

Particle Phase

Treatment of the solid particle can be simplified by neglecting the effect of evaporation and agglomeration. The equations governing particle motion are

$$F_p = \frac{\pi}{8} \rho d_p^2 C_D |V - V_p| (V - V_p) \quad (8)$$

where V_p is the particvelocity, and d_p is the particle diameter. The drag coefficient used in this study is

$$C_D = \frac{24}{Re_d} \left[1 + \frac{Re_d^{2/3}}{6} \right] \quad \text{for } Re_d < 10 \quad (9)$$

$$0.424 \quad \text{for } Re_d > 1000$$

$$Re_d = \frac{\rho |V - V_p| d_p}{\mu} \quad (10)$$

Where the Reynolds number is defined based on the particle diameter and relative velocity between gas and particle. The coupling between gas phase and particle phase solution is based on the particle-in-cell (PIC) concept. From the PIC method, the source term for gas flow for each gas phase computational cell (i,j) is written

as:

$$S_{i,j}^{mu} = -\sum (u_{p,out} - u_{p,in}) \dot{m}_p \quad (11)$$

$$S_{i,j}^{mv} = -\sum (v_{p,out} - v_{p,in}) \dot{m}_p \quad (12)$$

$$S_{i,j}^e = -\sum \left(\frac{1}{2} u_{p,out}^2 - \frac{1}{2} u_{p,in}^2 \right) \dot{m}_p \quad (13)$$

Where \dot{m}_p is the mass represented by a given computational particle.

NUMERICAL PROCEDURE

Gas Phase

Among many numerical schemes, the implicit schemes require the inversion of block matrices and become more computationally expensive. However, for two-phase flows with high particle loading, the explicit schemes may not be as robust as the implicit schemes due to strong source terms in momentum and energy equations. In the present study, both implicit (Van Leer's flux-vector splitting with Steger-Warming's LU algorithm, RPLUS)¹ and explicit (four-stage Runge-Kutta, FNS3D)² codes are adopted to solve the gas phase equations. For heavy particle loading cases, the implicit scheme (RPLUS code) is necessary to achieve good numerical stability.

Solid Phase

In the conventional approach for two-phase flow calculations, solid particles are tracked using Lagrangian coordinates and marched downstream by following the time step for the gas phase solver. Due to the limited CFL number in the gas phase solver, the time step is very small and thus a very long time period is needed to reach steady state. In addition, positions and velocities of numerous particles need to be recorded in the numerical simulation necessitating a large memory storage space.

In the newly developed method, a number of particle groups are tracked using Lagrangian coordinates and a march to the downstream cell by cell in the gas phase grid system. During the particles' marching, gas phase solu-

tions remain the same.

The marching procedure can be described as follows.

1. give the initial positions and velocities to the particle groups and release them at the entrance (or cell interfaces at $i=1$)
2. calculate new positions at new cell interface using old particle velocities
3. calculate times needed for particle travelling from old to new positions.
4. use the times derived from step 3 and solve the equations of motion of particles to obtain new particle velocities
5. repeat step 2, 3 and 4 several times to determine new positions at cell interface and new particle velocities.
6. update particle positions and velocities and go back to step 2.
7. repeat steps 2 to 6 until all particles move out of the computational domain.

Coupling between Gas and Solid Phase

The gas-phase solver (FNS3D or RPLUS) is coupled with the solid phase solver as follows

1. run gas phase solver to obtain a set of steady state solutions without particle loading.
2. run solid phase solver to obtain source terms in momentum and energy equations at steady state by keeping the gas phase solutions unchanged.
3. use the newly calculated source terms in step 2 and run the gas phase solver for a number of iterations
4. repeat 2 and 3 until the gas phase solutions fully converge.

RESULTS AND DISCUSSIONS:

Two different solid rocket nozzles were considered in this study: a traditional convergent-divergent nozzle (CDN) and a realistic solid rocket booster (SRB). Computational grids of gas flow are either 41 by 26 or 131 by 21. Particle trajectories and source terms in equation 4 were updated every five hundred iterations in the gas flow solver. Five thousand particles were released from the nozzle inlet and tracked through the solid rocket motors to calculate the momentum and energy exchange between the particle phase and gas phase. All computations were performed on a Cray Y-MP and achieved convergence in ten-minute of CPU time. In this study, effect of three particle sizes (diameter of 2, 20 and 100 micrometers) and three loading ratios (0, 10 and 30 percent) on the solid rocket performance are investigated.

Baseline gas phase velocity vectors and Mach number contours of a single-phase CDN flow are shown in fig.

1. The inlet conditions were specified as constant total

temperature (400K), constant total pressure (either 3 or 30 atms) and zero radial velocity. Particle trajectories within a nozzle can be affected by many factors (e.g. nozzle size, gas density, particle size et al.) Ratio of particle inertia time (depending on the particle density and diameter, and gas phase density) to particle flow residence time (depending on nozzle size) determines how close particles can follow the gas phase streamlines. In this study, we used three different particle sizes and two gas densities to illustrate the capability of the developed code. Figures 2-4 show the particle trajectories in the CDN. In order to avoid clogging up the figure, only sixteen out of five thousand particle trajectories are plotted.

Generally speaking, particle loading ratio has little effect on the particle trajectory although gas velocity may have been altered due to the momentum exchange between the gas and particle phase. In figure 2, the inlet conditions of nozzle are total temperature at 400 K and total pressure at 3 atms. The 2 micron particles follow gas streamlines well and are accelerated by the local gas velocities. In the same figure, it is noted that particles do not move to the near-wall region in the divergent section. For 20 micron particles, part of them hit the wall of the convergent section and rebound into the gas flow and get swept to the nozzle exit. For 100 micron particles, many particles rebound several times before they leave the nozzle. It is also noted that large particles in this nozzle flow gain very little momentum from the gas phase.

When the nozzle is operated at 400 K with pressure increased ten times to 30 atms, the gas density becomes ten times higher. In this case, although the 2 micron particles follow the gas phase quite well (as shown in Fig. 3(a)), the behavior of 20 and 100 micron particles are different from those in the low pressure cases. As shown in Figs. 3 (b) and (c), part of the 20 micron particles hit the wall and leave the nozzle before they cross the centerline. Compared to the low pressure case, none of 100 micron particles have multiple-bounce on the wall before leaving the nozzle. This is because the gas flow has higher momentum at higher pressure and thus carries solid particles more easily.

Effect of particle loading on the gas flowfield are shown in Figs. 4 and 5. Gas phase Mach number contours of flows loaded with 2 and 100 micron particles are compared. In all cases, particle velocities at the entrance of the nozzle are the same as gas velocity at the entrance centerline. As particles move downstream, they are accelerated and gain axial momentum from the gas phase. For particles of 2 micron, since they follow gas flow very closely, more momentum is extracted from the gas phase. Therefore, the gas flowfield is altered more significantly compared to that in the 100 micron case. In cases of 2 micron with various loading ratio (as shown in Fig. 4),

the sonic line is pushed downstream when the loading ratio increases. Since higher loading means larger particle concentration, more gas phase momentum is transferred to the particles. This results in slower gas velocities and the movement of the sonic line. In contrast to the 2 micron cases, velocities of 100 micron particles change very little from the nozzle inlet to the exit due to their large inertia. This phenomenon can be seen in Figs. 2(c) and 3(c) and very little momentum is extracted from the gas phase. Therefore, the Mach number contours in Fig. 5 are all similar and are almost the same as that of the single-phase flow (Fig. 1 (b)).

The performance loss of rockets due to the presence of particle loading are illustrated in Figs 6 and 7. Velocity and pressure distribution at nozzle exit, which are directly related to the specific impulse (not accounting the impulse generated from the particles) of the rocket, shows little change for cases of 100 micron particles with various ratios while, for 2 micron cases, both gas phase velocities and pressures monotonically decrease as loading ratio increases. Gas mass flowrate through the nozzle can be found in Table 1 and are also affected by the particle loading and particle size. As can be seen in Table 1, the mass flowrate of the gas phase decreases when the momentum loss from gas to solid phase increases. This trend is consistent with the findings discussed in the last two paragraphs.

In addition to the conventional CD nozzle geometry, particle-laden flows in SRB were also studied. The conditions at SRB inlet are 400 K of total temperature and 30 atms of total pressure. Figure 8(a) shows the gas velocity vectors with zero particle loading. Trajectories and velocity vectors of two different particle sizes (2 and 100 microns) in the 30% particle loaded SRB chamber are shown in Figs. 8(b) and (c).

Two micron particles follow the gas flow closely due to their small inertia. They can not penetrate the low speed gas flow around the burnback region. In contrast, due to the large inertia of large particles (100 micron), some of them pass through the low speed gas flow and hit the wall. In our calculations, the collisions between wall and particles are assumed to be elastic. Some particles collide with the wall several times until they gain enough inward radial momentum to escape from the burnback region. Combination of this radial momentum and axial drag force imposed by the gas flow makes these particles move downstream along the center region of the divergent section.

In this study, the particle phase has stronger impact on gas flowfield of SRB than that of CD nozzles. Figure 9(a) shows Mach number contours in a SRB with zero loading. Effect of 30 percent particle loading (2 and 100 microns) are illustrated in Figs. 8(b) and (c). It is

indicated that the average mach number at the nozzle exit are lower than that of zero-loading case (Fig. 9(a)). The distributions of Mach number near the throat have been significantly altered due to the interactions between particles and gas phases. Physical mechanisms governing this phenomenon are still under investigation.

CONCLUSION

A computer code for two-phase flows in solid rocket motors has been developed. The major advantage of this code is the achievement of better numerical accuracy with higher computational efficiency (less CPU time and storage space). The capability of this code has been demonstrated by simulating two-phase flowfields in two solid rocket motors.

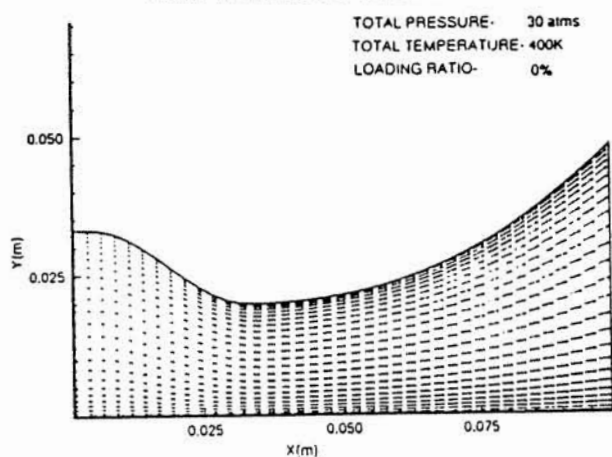
REFERENCES

1. Tsai, Y. L., and Hsieh, K.-C., "Comparative Study of Computational Efficiency of Two LU Schemes for Non-Equilibrium Reacting Flows," AIAA Paper No. 90-0396, 28th Aerospace Sciences Meeting, January, 1990.
2. Gielda, T. P., Deese, J. E. and Agarwal, R. K. "Efficient Finite-Volume Parabolized Navier-Stokes Solutions of Highly Maneuverable Reentry Vehicle Flowfields," AIAA Paper No. 90-3013, 8th AIAA Aerodynamics Conference, August, 1990.

Particle size vs. Loading Ratio	2 μm	20 μm	100 μm
10 % ($P_t = 3 \times 10^5 \text{ Pa}$)	97.7 %	99.2 %	99.5 %
30 % ($P_t = 3 \times 10^5 \text{ Pa}$)	92.7 %	98.3 %	99.4 %

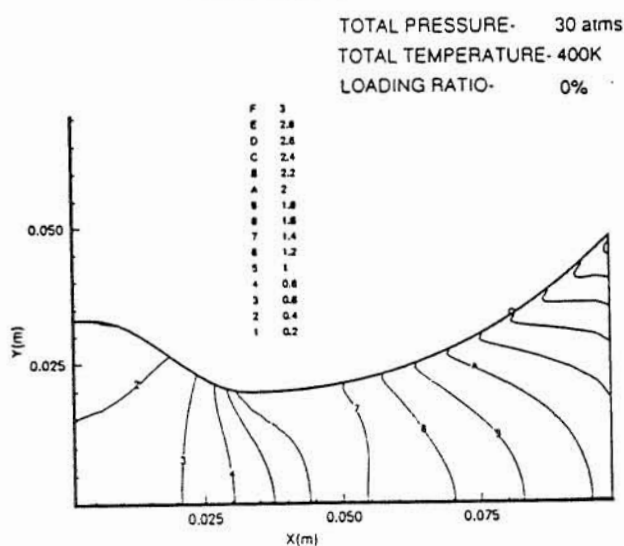
Table. 1. Ratio of Gas Mass Flow Rate
($\dot{m}_{\text{gas, two-phase}} / \dot{m}_{\text{gas, single-phase}}$)

GAS VELOCITY VECTORS



(a) Velocity Vector Field

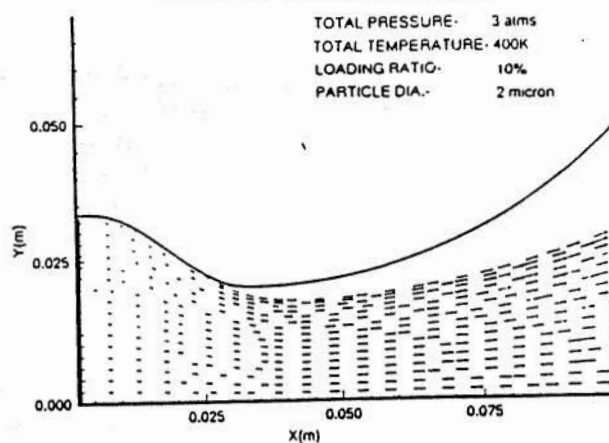
MACH NUMBER CONTOURS



(b) Contour Plot of Mach Numbers

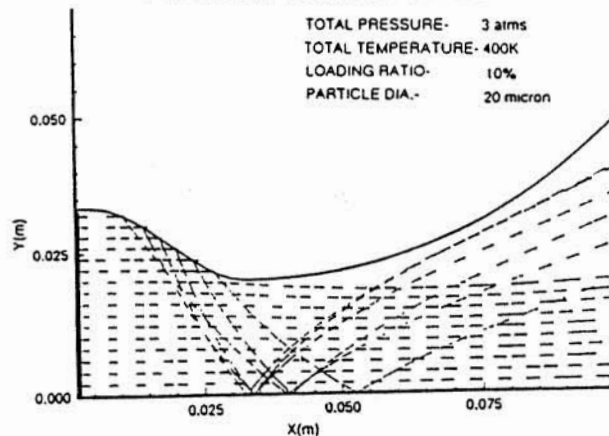
Fig. 1. Single Phase (Gas) Solution:

PARTICLE TRAJECTORIES



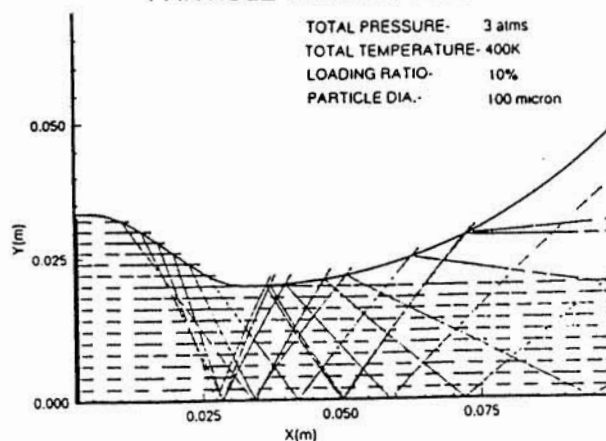
(a) 2 μm

PARTICLE TRAJECTORIES



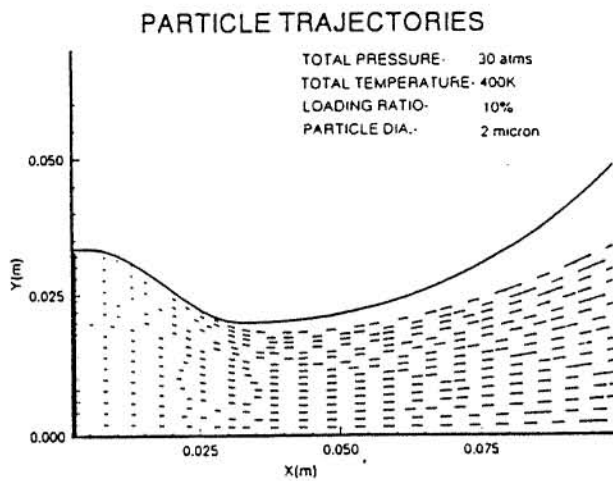
(b) 20 μm

PARTICLE TRAJECTORIES

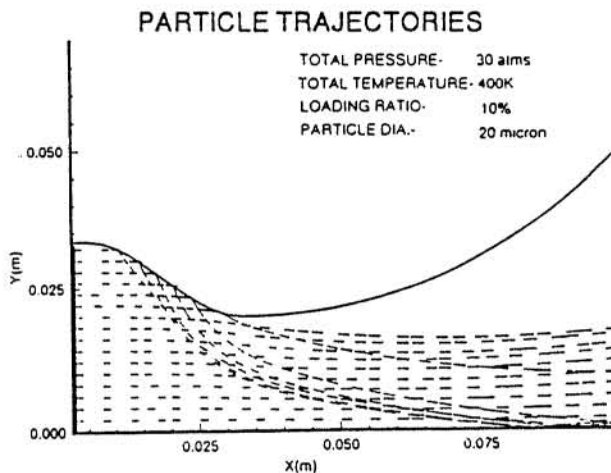


(c) 100 μm .

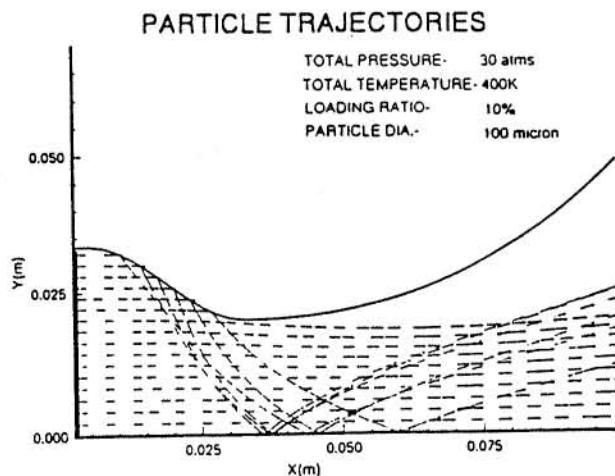
Fig. 2. Particle Trajectories of Various Particle Diameters in Low-Loading-Ratio (10 %) and Low Pressure (3 atm) Two-Phase Nozzle Flows



(a) 2 μ m



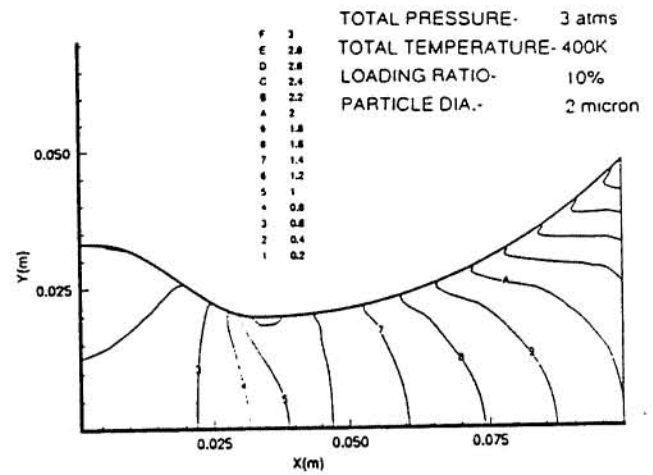
(b) 20 μ m



(c) 100 μ m.

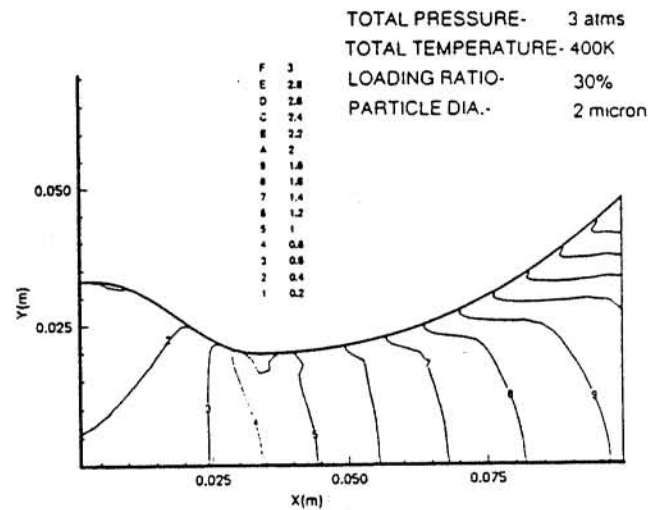
Fig. 3. Particle Trajectories of Various Particle Diameters in High-Loading-Ratio (30 %) and High Pressure (30 atm) Two-Phase Nozzle Flows.

MACH NUMBER CONTOURS



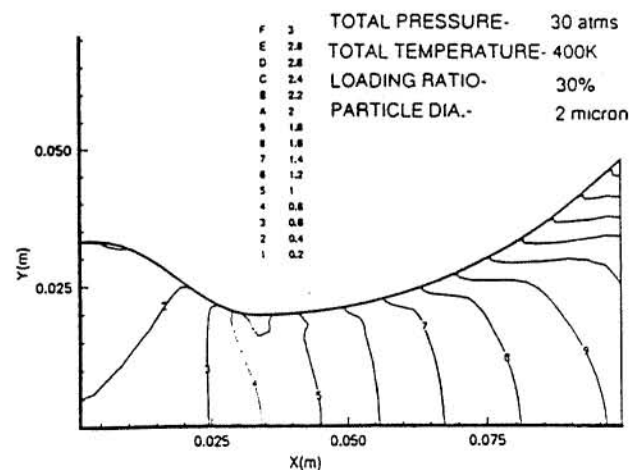
(a) 10 % Loading Ratio and 3 atm Pressure,

MACH NUMBER CONTOURS



(b) 30 % Loading Ratio and 3 atm Pressure,

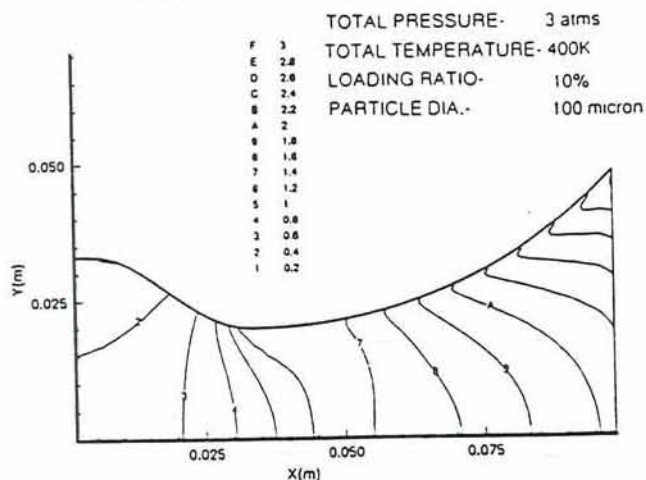
MACH NUMBER CONTOURS



(c) 30 % Loading Ratio and 30 atm Pressure.

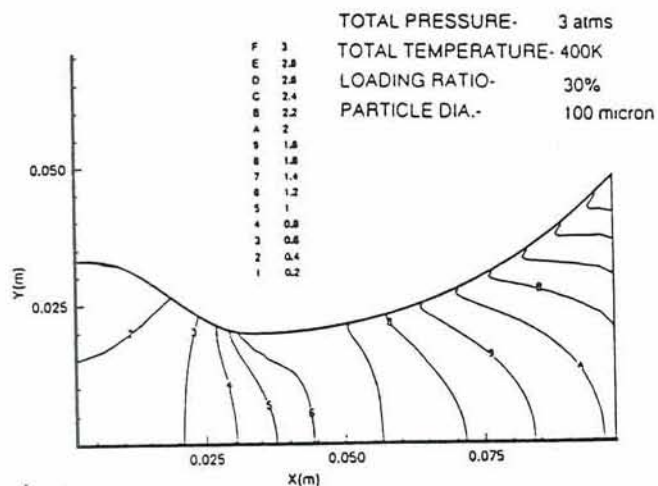
Fig. 4. Mach Number Contours of Two-Phase Nozzle Flows with 2 μ m Particles at Various Loading Ratios and Pressures.

MACH NUMBER CONTOURS



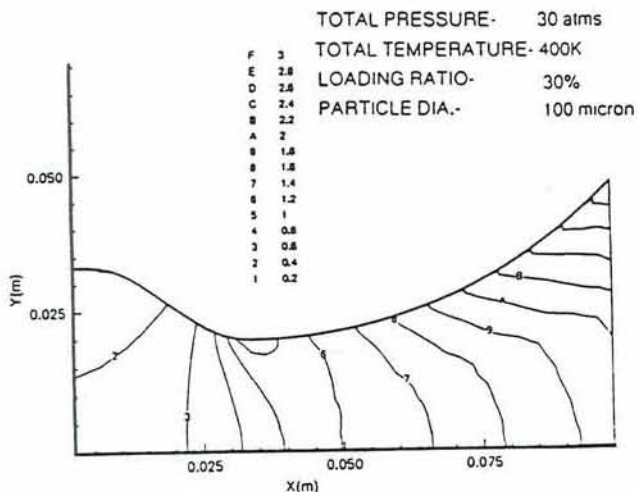
(a) 10 % Loading Ratio and 3 atm Pressure,

MACH NUMBER CONTOURS



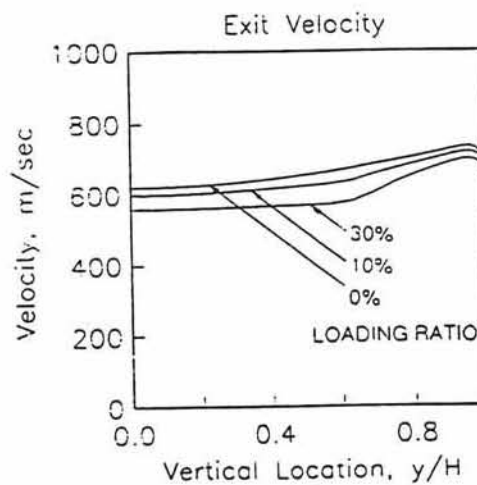
(b) 30 % Loading Ratio and 3 atm Pressure,

MACH NUMBER CONTOURS

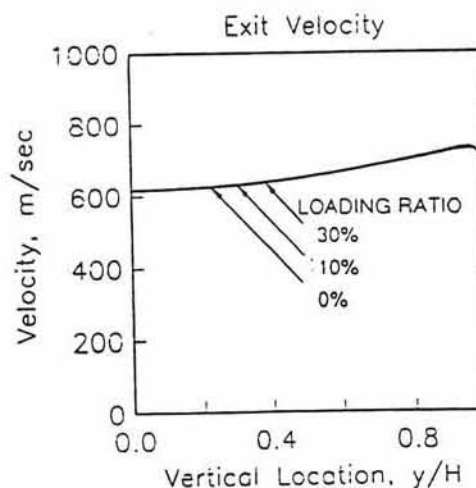


(c) 30 % Loading Ratio and 30 atm Pressure.

Fig. 5. Mach Number Contours of Two-Phase Nozzle Flows with 100 μ m Particles at Various Loading Ratio and Pressures.

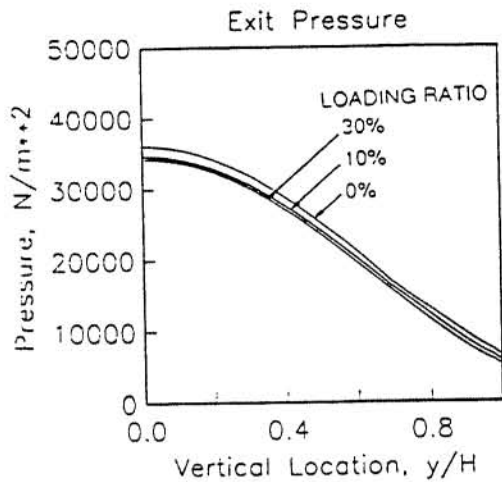


(a) 2 μ m

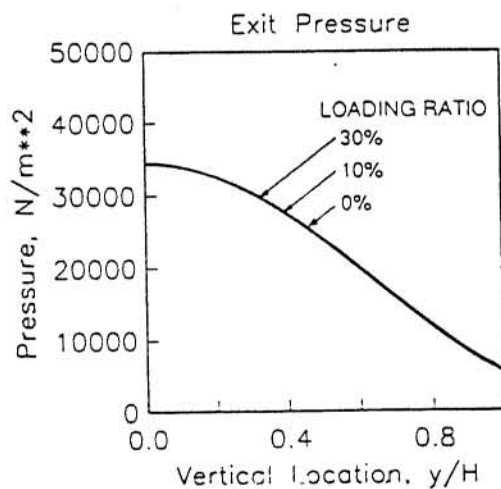


(b) 100 μ m

Fig. 6. Total Velocity Distributions along Vertical Direction at Nozzle Exit for Cases with Various Particle Sizes and Loading Ratios at Low Pressure (3 atm).



(a) 2 μm

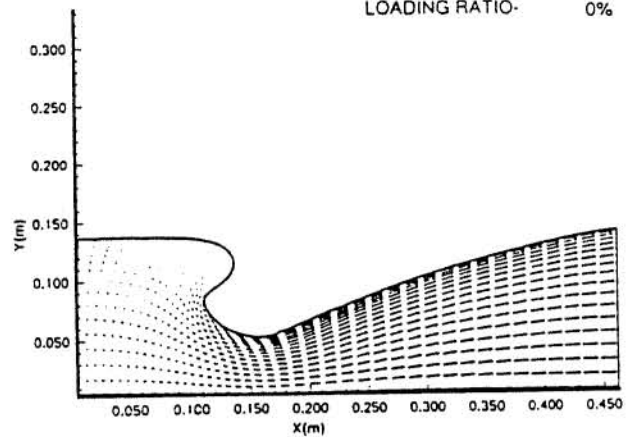


(b) 100 μm

Fig. 7. Static Pressure Distributions along Vertical Direction at Nozzle Exit for Cases with Various Particle Sizes and Loading Ratios at Low Pressure (3 atm).

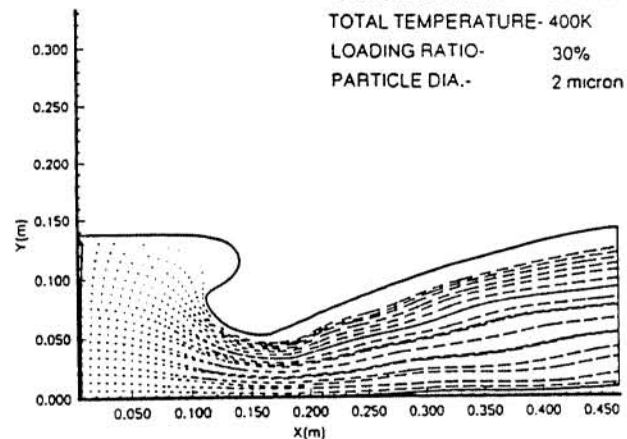
GAS VELOCITY VECTORS

TOTAL PRESSURE- 30 atm
TOTAL TEMPERATURE- 400K
LOADING RATIO- 0%



PARTICLE TRAJECTORIES

TOTAL PRESSURE- 30 atm
TOTAL TEMPERATURE- 400K
LOADING RATIO- 30%
PARTICLE DIA.- 2 micron



PARTICLE TRAJECTORIES

TOTAL PRESSURE- 30 atm
TOTAL TEMPERATURE- 400K
LOADING RATIO- 30%
PARTICLE DIA.- 100 micron

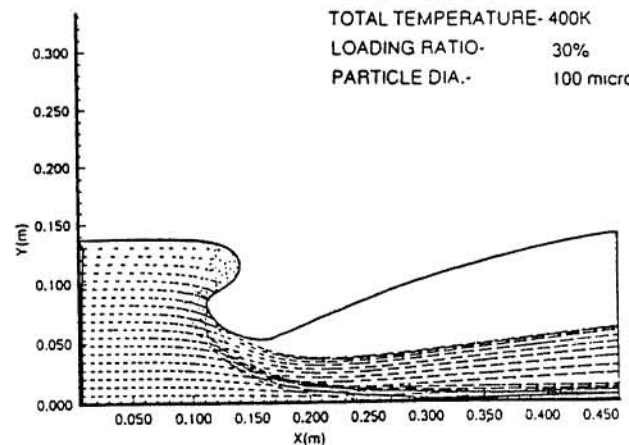
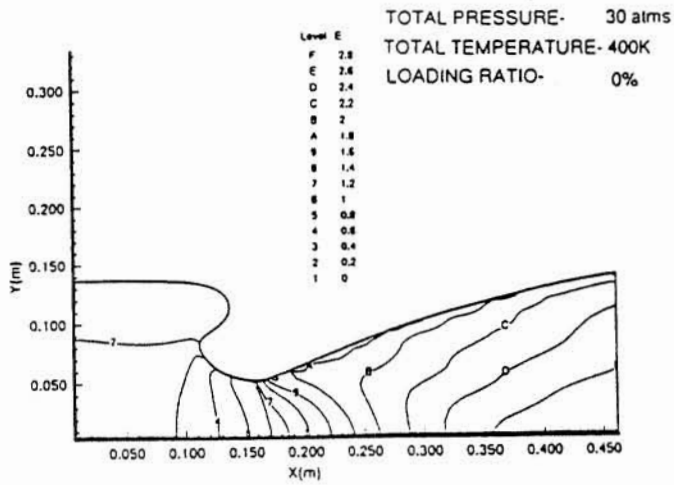


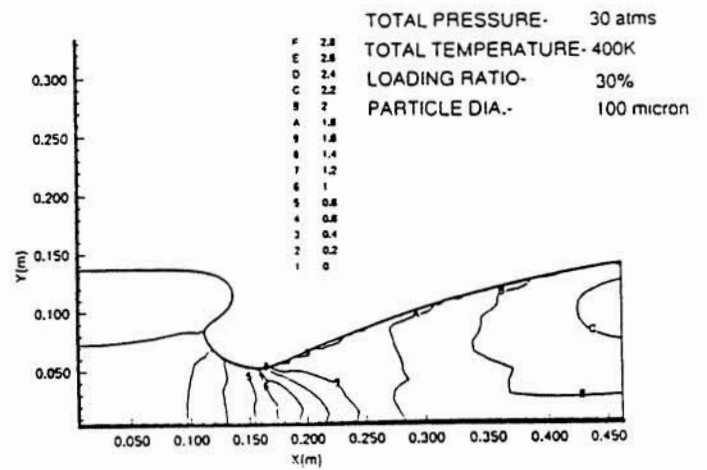
Fig. 8. Gas Velocity Vectors and Particle Trajectories in SRM.

MACH NUMBER CONTOURS



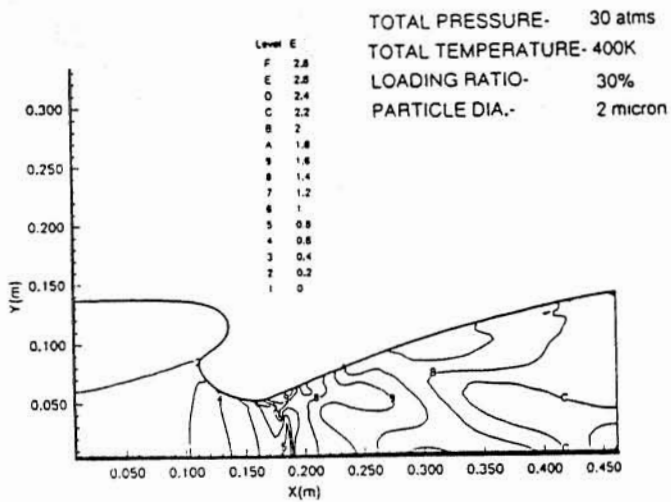
(a) No Particle Loaded.

MACH NUMBER CONTOURS



(c) 100 μ m Particles, 30 % loading ratio

MACH NUMBER CONTOURS



(b) 2 μ m Particles, 30 % loading ratio.

Fig. 9. Gas Phase Mach Number Contours of SRM.

CSTAR FOCUS AREA:

COMPUTATIONAL METHODS

·Anomaly Detection of Turbopump Vibration in Space Shuttle Main Engine Using Statistics and Neural Networks

Dr. Ching F. Lo
Ms. Kewei Wu
Dr. B.A. Whitehead

·An Integrated Knowledge System for the Space Shuttle Hazardous Gas Detection System

Dr. Ching F. Lo
Dr. George Z. Shi
Mr. Carl Bangasser
Ms. Connie Fensky

·Fluid Mechanics Computer Based Lab Simulator

Dr. Ahmad D. Vakili
Dr. Edward M. Kraft

Anomaly Detection of Turbopump Vibration in Space Shuttle Main Engine Using Statistics and Neural Networks

C. F. Lo*, K. Wu+ and B.A. Whitehead++

Abstract

The statistical and neural network methods have been applied to investigate the feasibility in detecting anomalies in turbopump vibration of SSME. The anomalies are detected based on the amplitude of peaks of fundamental and harmonic frequencies in the power spectral density. These data are reduced to the proper format from sensor data measured by strain gauges and accelerometers. Both methods are feasible to detect the vibration anomalies. The statistical method requires sufficient data points to establish a reasonable statistical distribution data bank. This method is applicable for on-line operation. The neural network method also needs to have enough data to train the neural networks. The testing procedure can be utilized at any time so long as the characteristics of components remain unchanged.

Introduction

The feasibility study for detecting anomalies in turbopump vibration data has been conducted with data from ground tests 902-473, 902-501, 902-519, and 904-097 of the Space Shuttle Main Engine (SSME). The study has been designed to analyze vibration data from each of the following SSME components: high-pressure oxidizer turbopump, high-pressure fuel turbopump, low-pressure fuel turbopump, and preburner boost pump as described in Ref. 1. The pre-processor module of the software system locates and classifies peaks in the power spectral density of each 0.4-sec window of steady-state data. Peaks which represent fundamental and harmonic frequencies of both shaft rotation and bearing cage rotation are identified by the module. Based on the statistics and neural network methods, anomalies are then detected by the amplitude of each of these peaks individually.

Using the statistical method, anomalies are detected on the basis of two thresholds set individually for the amplitude of each of these peaks: a prior threshold used during the first group of windows of data in a test, and a posterior threshold used thereafter. In most cases the anomalies detected by the statistics agree with those reported by NASA.

Using the neural networks, the amplitudes of each of these peaks are selected as input training data sets including normal and abnormal samples in a single test. The reserved testing data which have not been used to training the network in the same test are applied to assess the effectiveness and feasibility of the neural network approach. The HPFTP is the selected component for the current study. The rate of correct diagnosis to identify the normal or abnormal conditions is better than 95% of the total testing cases.

Current Systems

The prototype software systems have been designed for detecting anomalies in turbopump vibration data from ground tests of SSME by using the statistics and neural networks. They are described in the following sections after the sensor data pre-processor module.

Sensor Data Pre-processor

Vibration data was provided by NASA in the form of FFT from accelerometers mounted on the oxidizer and fuel pumps. A set of Fortran programs running on the UTSI VAX 11/780 has been developed to read these data tapes in NASA binary format which is inherently machine-dependent, to swap bytes from the NASA binary format to the VAX internal binary

* UTSI Professor, CSTAR Principal Investigator
+ CSTAR Research Engineer
++ UTSI Associate Professor

representation, and to convert the data into a portable ASCII format. After initial preprocessing on the VAX, the power spectra are stored in a form which can be quickly sent to any other platform at UTSL.

The **Frequency Extractor** is designed to identify the fundamental and harmonic frequencies of both shaft rotation and bearing cage rotation in each FFT window. First, peaks representing candidates for the shaft fundamental are reliably found based on an empirical linear fit, for each type of turbopump, of shaft rotation speed to SSME power level. The actual shaft and cage fundamental and their harmonics are then identified based on the ratio of cage to shaft rotation and the required consistency among the different harmonics of both shaft and cage. Freq-Extra is also designed to detect the intermittent frequencies whose amplitudes are above a specific value i.e. noise-level.

The typical data histogram of synchronous frequency plotted as the number density distribution from 1500 to 3900 units amplitude from 110 windows during the time period of 169 sec. to 213 sec. is shown in figure 1a. The typical data histogram of 240-hz from sensor 686 & 698 is shown in figure 1b. The data from sensor 613 shown in figure 2 are synchronous and sub-synchronous frequencies. All distribution is close to a "normal Gaussian" function. The 2nd, 3rd and 4th harmonics also have the similar distribution. Thus, the statistic mean and standard deviation of the data distribution are useful as the benchmark for the anomalies detection.

Statistical Approach

Two Versions of system. The earlier operational expert system is implemented on a Symbolics 3670 LISP machine (Ref 2). While good preliminary results have been obtained with this implementation, the LISP machine platform and the proprietary LISP language available on this platform both severely limit the portability of the expert system software. Also, the LISP language does not produce run-time code as efficiently as that produced by compilers of procedural languages.

In order to maximize the portability of the expert system software and improve the user interface, a

re-implementation of its logic in the ANSI standard version of the C programming language has been accomplished on a PC (Ref 3). By employing ANSI standard C with the standard C I/O library and making few changes on machine-dependent portion, the software system can run on any platform which has sufficient memory and disk space for the operation of the software and for the data files it requires.

The statistic module is built in a **Anomaly Detector**. Anomalies are detected in a Anomaly Detector on the basis of thresholds (prior & posterior) and sequential criteria set individually for the amplitude of each fundamental and harmonic frequency of both the shaft and the cage. A prior threshold is used during the first few windows of data in a test, while data is first being accumulated for that test. Based on the accumulated data, a posterior threshold is then determined and used for the remainder of the test. Values for the prior threshold of 300% of the amplitude observed in the first window of data, and values for the posterior threshold of **5 standard deviations** above the running average of nominal data have been found to give good results for each of the ground tests analyzed to date. For the threshold criteria, anomaly of any identified frequencies is detected when its amplitudes is above its threshold. For sequential criteria, anomaly of any identified frequency is detected when anomalies keep showing in more than three consecutive windows.

The **User Interface** is graphics-oriented and mouse-driven. It provides users several windows to actively select as screen or hardcopy display, such as Process Status, Single FFT Window, Multiple FFT Windows, Waterfall plots, FFT Recall Windows and Output Files. With a mouse and simple pulldown menus, users can switch among these windows instantly anytime during processing. A sample of an interactive (or simulated on-line) session is given in Ref 3. The output files save detailed records for further examining of anomalies.

Results of Anomaly Detector. The results of anomalies detected by the system for the data from the ground tests 902-473, 902-501, 902-519 and 904-097 are summarized in Tables 1, 2, 3 and 4, respectively. Results obtained from NASA reports are also listed in a separate column for comparison. The exact time of detection of these anomalies by

NASA experts was not given in the documentation presently available from NASA, but will be pursued. The expert system results agree with those stated in the NASA reports, with two exceptions: (1) In test 902-519, HPFTP 50% Sub-synchronized frequency was not detected; and (2) In test 904-097: HPOTP second cage frequency was not detected by the system. These discrepancies require further investigation. The overall results assure us that the current strategy for detecting anomalies works reasonably well for most cases tested.

Neural Networks Diagnosis

For a specific turbopump component, the fundamental frequency and harmonics for the normal and abnormal conditions have their distinct characteristics as shown in Figures 3 and 4. The neural networks algorithm is a powerful pattern recognition method. Thus, the application of the neural nets techniques to the HPFTP's data from test 501 and 519 allows us to examine the feasibility in diagnosing the anomalies.

Neural Network Algorithm Description. A three-layer Back-Propagation (BP) Neural Network has been selected for the present study. Multilayer BP networks have been studied extensively and are widely used for pattern classification. Multilayer networks are able to classify non-linearly separable classes. In the present case, a three layer network is utilized including input layer, hidden layer and output layer. A 3-layered (input, hidden, output), fully connected, feed-forward network as shown in Figure 5. The normalized data sets are utilized. Both input and output are continuous-valued (between -0.5 and 0.5) vector. The outputs generated by the network are compared with the desired or target outputs. Errors are computed from the differences, and the weights are changed in response to these error signals as dictated by the Generalized Delta Rule (Ref 4). Thus, a BP network learns a mapping function by repeatedly presenting patterns from a training set and adjusting the weights. A commercial neural network program named ANSim (Ref. 5) is utilized for the training process as well as the testing process.

The Training Procedure is in the iterative fashion. It loops repeatedly over the set of training patterns until the total root mean square (RMS) error for all

patterns is less than the specified value, e.g. 0.1. The Testing Procedure is forward feed processing.

Neural Network ANSim Software. SAIC ANSim 2.30 (Ref. 5) is a graphics oriented, menu-based artificial neural system (ANS) simulation program, which provides a complete complement of neural model development, allocation and analysis capabilities, including a powerful ANS creation, training, execution and monitoring tool. ANSim enables users to quickly implement and utilize ANS models using 13 paradigms such as Back Propagation (BP), Hopfield Network, etc. ANSim enables the user to configure any number of ANS neural networks. It drives each network with a sequence of training and/or input data. For each model, ANSim will (1) monitor the response, (2) capture the output, and (3) save the configuration for later re-use. ANSim is integrated under Microsoft Windows to provide an effective, easy-to-use interface.

Floating Point Processor for ANSim. A PC 386 (VGA or EGA monitor) with the SAIC's Delta Floating Point Processor, which is a 22 MFlop AT bus compatible processor, allows for high speed Neural Network Systems training and processing.

Sample Data in the Form of Spectrum Plots. The typical data sets are obtained by the pre-processor module as shown in Fig. 3, consisting of synchronous frequency samples of normal and 240-hz abnormal data sets for sensor 696 and 698. The sensor 617 for Synchronous and Sub-synch frequency data is shown in Fig. 4. The reserved testing data shown in Figures 3 & 4, which have not been used for training the network in the same test, are applied to assess the effectiveness and feasibility of the network approach.

Results of Neural Networks. The component selected for the current study is the HPFTP. The HPFTP vibration data from ground tests 902-501 and 902-915, as shown in Figures 3 & 4, are utilized for the vibration anomalies detection study. The successful detection rate is higher than 95% to identify either normal or abnormal running conditions. The results have indicated that the application of Neural Networks to the available SSME vibration data sets in diagnosing existing faults in the data is a viable method.

Moreover, the actual clock time of computer computation on a PC-386 with Floating Point Processor are less than 1 minute for the training process. The testing time of the feed-forward process is near real time in the present case. It is important to know this computation time for planning on-line or off-line operations.

Future Plan. The satisfactory results given by the neural network approach can be reassured to investigate more cases and more fault scenarios. Since the ground testing data are limited, we decided to use the data generated from a NASA/MSFC numerical simulator for the follow-on study.

Summary

Automatic detection of anomalies in Space Shuttle Main Engine Turbopumps has been implemented as a prototype software system on a Symbolics 3670 LISP machine and on a PC. The system has demonstrated its capability in detecting anomalies in turbopump vibration data earlier than the indication provided by the redline detection mechanism. The present strategy based on the statistics distribution of data in detecting anomalies for SSME turbopumps seems to work well, even though some limited cases require further study. On the other hand, the limited application of neural networks to the HPFTP has also shown the effectiveness and feasibility to diagnose the anomalies of turbopump vibrations. The further application to data from a numerical simulator is warranted.

References

1. Rockwell International "SSME Orientation (Part A--Engine), Space Transportation System Training Data," course No. ME 110(A) RIR, Jan. 1991.
2. L. Pereira and M. Ali, "Identification and Detection of Anomalies Through SSME Data Analysis," CASP, 2nd Technical Symposium Proceeding, Nov. 1990.
3. C. F. Lo, B.A. Whitehead, and K. Wu, "Automatic Detection of Anomalies in Space Shuttle Main Engine Turbopumps", AIAA paper No. 92-3329, July 1992.

4. D. E. Rumelhart, G. E. Hinton, and R. J. Williams "Learning Internal Representations by Error Propagation", Parallel Distribution Processing, vol I, 1986.

5. Science Application International Corp. "ANSim Artificial Neural Systems Simulation Program", April, 1989.

Acknowledgements

This research was supported by The Center for Space Transportation and Applied Research (CSTAR) and the Structures and Dynamics Laboratory of NASA-MSFC under Grant No. NAG 8-166. The investigators would like to thank Pat Vallely, Technical Monitor, NASA/MSFC, and Tom Fox of NASA/MSFC for their technical advice.

902-097		
NASA'S REPORT	PRESENT RESULTS	
LOX SIDE OBSERVATIONS * HPOTP: 2X CAGE PRESENT IN ACCEL DATA AT 104% & 109% (0.4 Gms MAX.). CAGE RATIO CONSISTENT THROUGH TEST AT -0.434	2X cage does appear in Sensor 637 (PBP-RAD-45-1) and 638 (PBP-RAD-45-3) around 160.0 sec., but system can not detect them now. *Analysis: Maybe 5 std. is too high and these 2X cages don't show in more than 3 consecutive windows.	
FUEL SIDE OBSERVATIONS * HPFTP: ANOM. FREQ. 1750-1800 HZ (1.0 Gms MAX). ANOM. FREQ. 560-600 HZ (7 Gms MAX)	Anom. Freq. 1750-1830 HZ presents in FASCOS-HPFP Sensors (696, 697, 698) around 97.0 sec..	
* LPFTP: "330HZ" ACTIVITY ALONG WITH "330HZ" LPFTP SYNC. MODULATION SIDEBANDS. LPFTP-RAD-240 ACCEL BAD (E/S +220 SEC.)	310HZ appears in Sensor 603 (LPFTP-RAD-180) at 393.4 sec..	

TABLE 1

902-519		
NASA'S REPORT	PRESENT RESULTS	
LOX SIDE OBSERVATIONS * HPOTP: PASS ALL GREENRUN CRITERIA/ ACCEPTABLE FOR FLIGHT.	NO ANOMALIES PRESENT IN PBP-RAD Sensors (637, 638).	
* LPOTP: ANOMALY PRESENT BETWEEN 800-900 HZ.	We don't have any LPOTP sensors.	
FUEL SIDE OBSERVATIONS * HPFTP: 50% SUBSYNC. PRESENT @109% (MAX. AMP.-1.0grams)/POSSIBLY PRESENT @104%. FURTHER ANALYSIS NECESSARY.	System couldn't detect 50% subsync. *Analysis: Lowering the 5 std. to 3 std. and dividing the white noise into two levels may help. Further work needs to be done.	
* HPFTP: HPFT RAD 180 HAS LARGE SPIKE.	Sensor 612 (HPFTP-RAD-180) shows large spike at 1730HZ at 141.0 sec.. Sensor 617 (HPFTP-RAD-180) shows large spike at 5HZ at 91.4 sec...	
* LPFTP: 330HZ PRESENT AT 104% & 109% MAX. AMP. 4.0 Grams FEEDS THROUGH TO ALL TURBOPUMPS.	We don't have any LPFTP sensors.	

TABLE 3

902-501		
NASA'S REPORT	PRESENT RESULTS	
LOX SIDE OBSERVATIONS * HPOTP: PASS ALL GREENRUN CRITERIA/ NO ANOMALIES PRESENT.	No anomalies present in HPOTP-WLD3 Sensors (705, 706, 707, 708) and ES6740 sensors (520, 522).	
FUEL SIDE OBSERVATIONS * HPFTP: ANOM. FREQ.'s PRESENT AT 109% AT 240HZ AND 950HZ (MAX. AMP. 1.9 Gms and 1.5 Gms RESPECTIVELY). ANOMALIES ARE MODULATING ABOUT SYNC.. PASSES ALL GREEN RUN CRITERIA.	Sensor 697 (FASCOS-HPFP) and Sensor 698 (FASCOS-HPFP) present Anom. Freq.'s at 109% at 240HZ around 171.0sec., but no 950HZ shows ANOM. in FASCOS sensors (696, 697, 698).	
* LPFTP: 330HZ APPEARS TO COALESCE WITH SYNC. CAUSING GREEN RUN SPEC. VIOLATION SYNC..	300HZ appears in Sensor 603 (LPFTP-RAD-180) at 91.4 sec..	

TABLE 2

902-473		
NASA'S REPORT	PRESENT RESULTS	
LOX SIDE OBSERVATIONS * SYNCHRONOUS RUNNING ON HIGH SIDE AT 100% PWL 450 HZ	PBP sensors (635, 636, 637, 638) show Anomalies of Synchronous (462.5HZ) around 360.0 sec..	
FUEL SIDE OBSERVATIONS * PSEUDO 3N AT 1725 HZ COINCIDES WITH 3N AT S +70 SEC	We don't have any FUEL SIDE sensors.	

TABLE 4

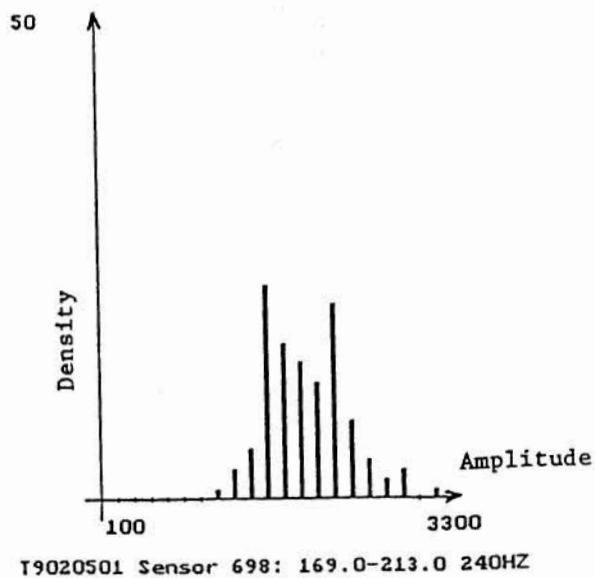
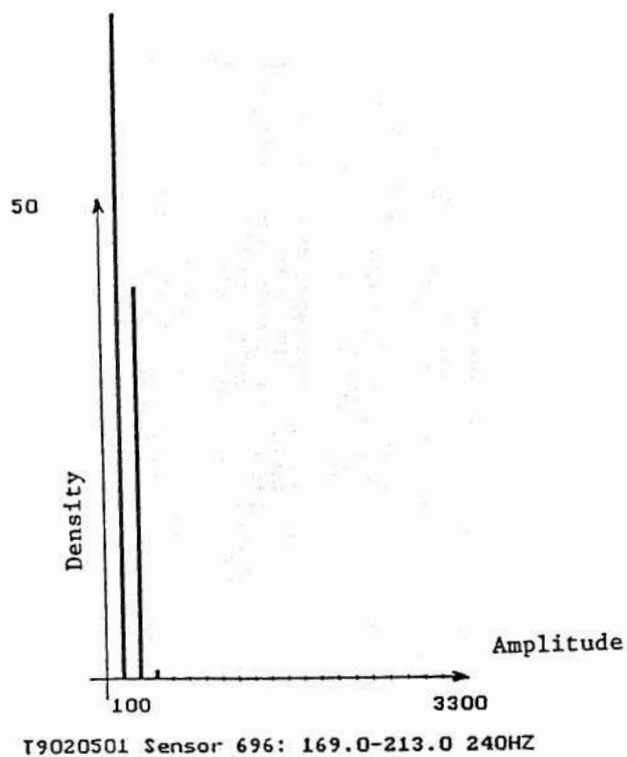
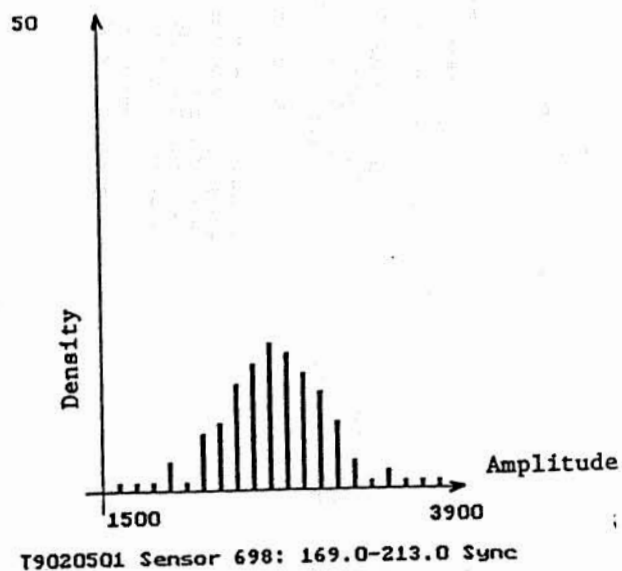
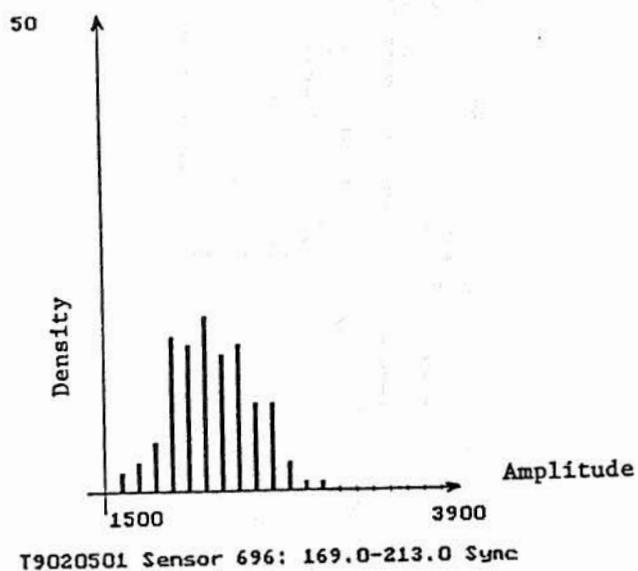
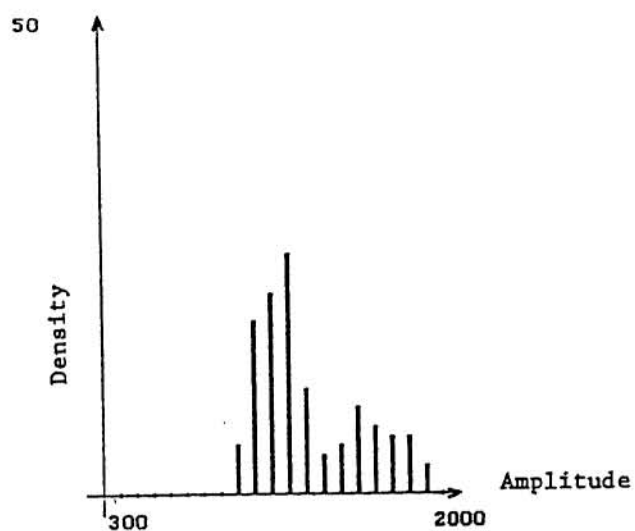
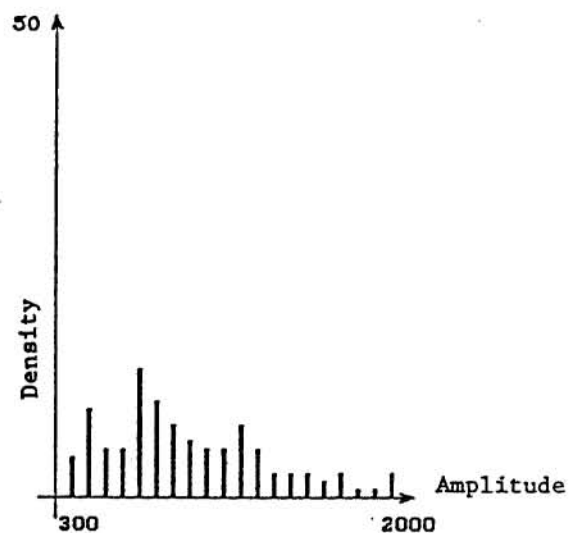


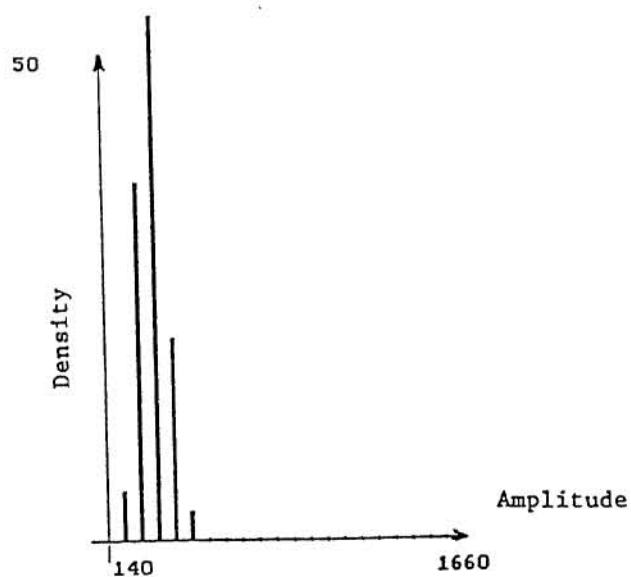
Figure 1. Data Histogram of Synchronous Frequency and 240-hz Frequency from Sensors 696 and 698.



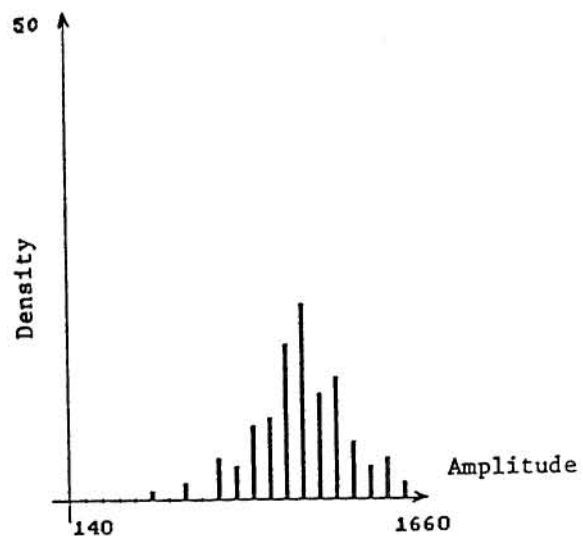
T9020519 Sensor 613: 72.2-119.4 Sync



T9020519 Sensor 613: 396.2-444.2 Sync



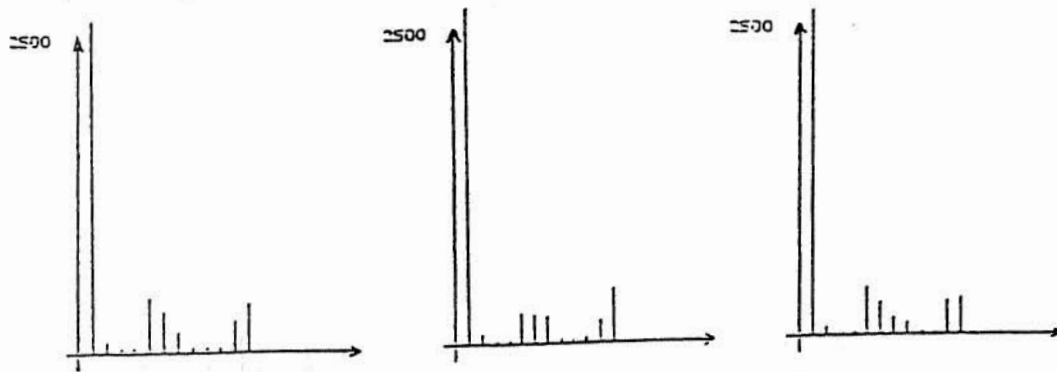
T9020519 Sensor 613: 72.2-119.4 Sub-S



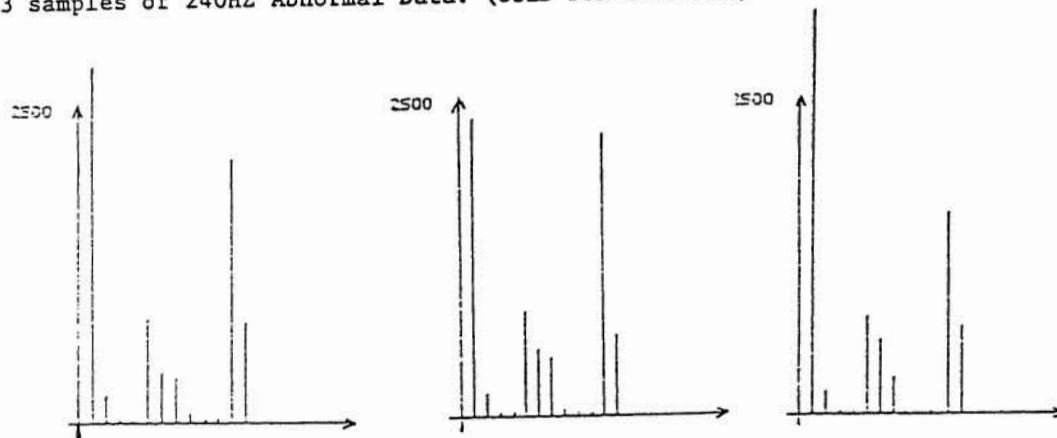
T9020519 Sensor 613: 396.2-444.2 Sub-S

Figure 2. Data Histogram of Synchronous Frequency and Sub-synchronous Frequency from Sensor 613.

3 samples of Normal Data: (USED FOR TRAINING)



3 samples of 240HZ Abnormal Data: (USED FOR TRAINING)



3 Samples of Testing Data: (Sensor 697 FASCOS-HPFP of Test 9020501 at 109%)

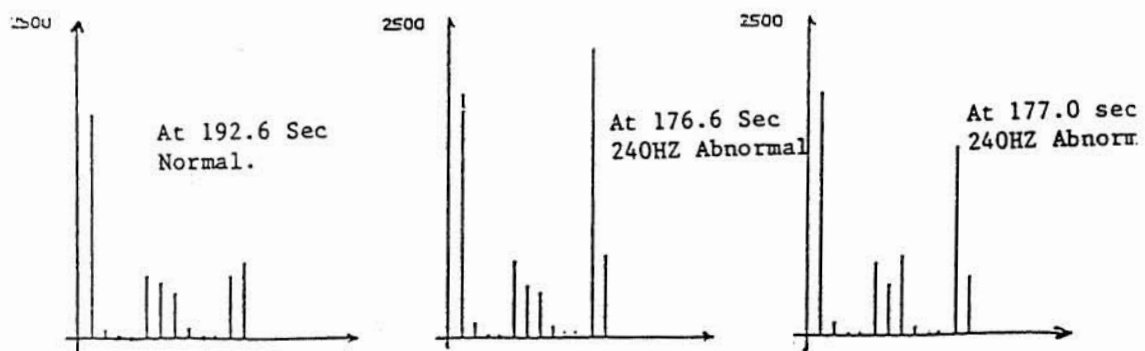
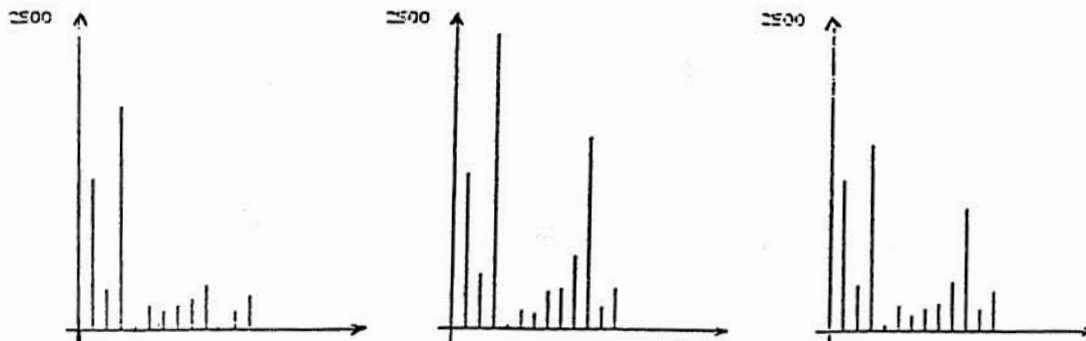
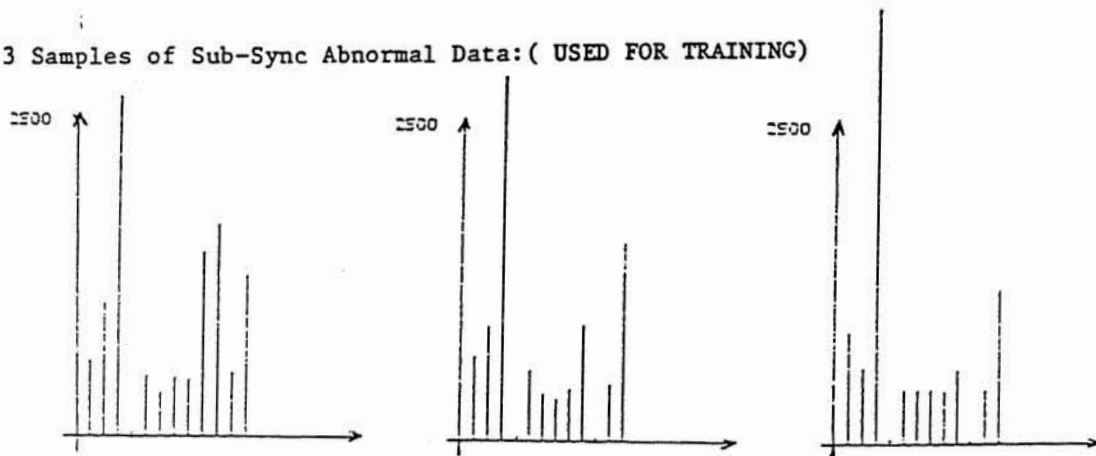


Figure 3. Samples of Normal and 240-hz Abnormal Data from HPFTP Sensors of Test 902-501 at the Thrust-level 109%.

3 Samples of Normal Data :(USED FOR TRAINING)



3 Samples of Sub-Sync Abnormal Data:(USED FOR TRAINING)



3 Samples of Testing Data:(Sensor 617 HPFP-RAD-180 of Test 9020519 at 109%)

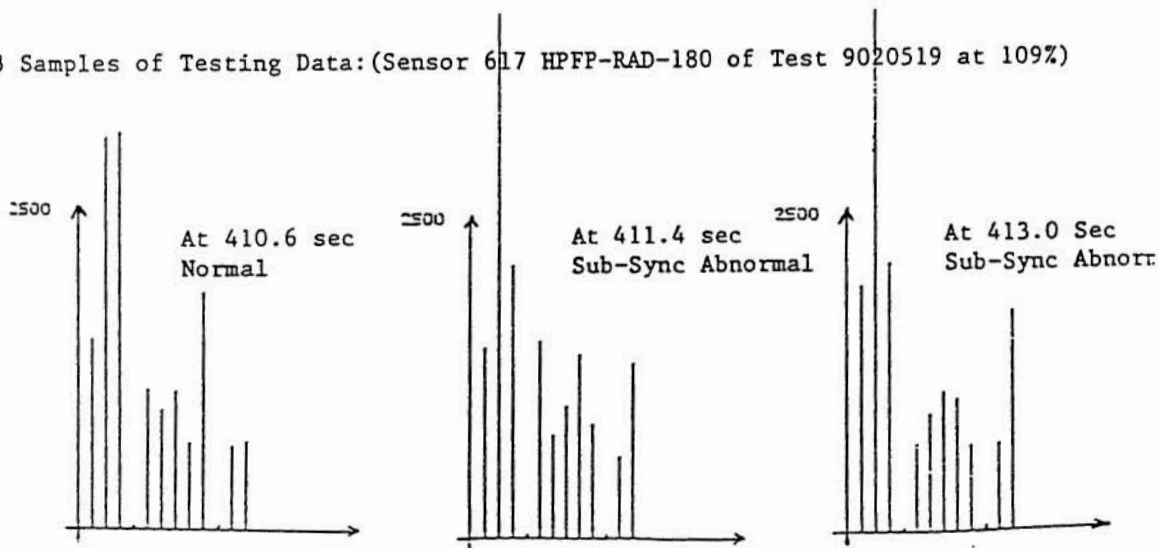


Figure 4. Samples of Normal and Sub-synchronous Abnormal Data from HPFTP Sensors of Test 902-519 at the Thrust-level 109%.

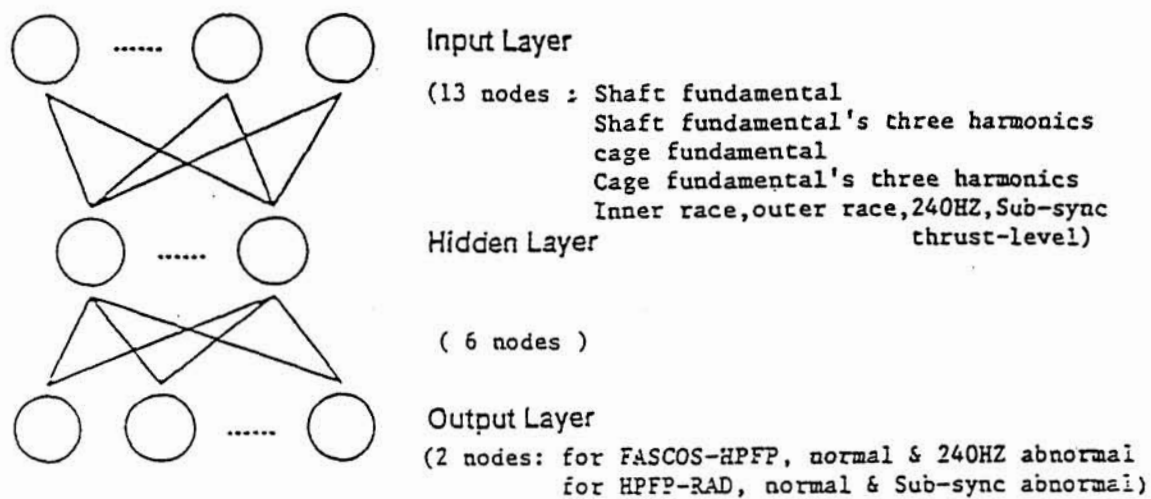


Figure 5. Three-layer Back-propagation Neural Network Architecture.

92A 14310

An Integrated Knowledge System for the Space Shuttle Hazardous Gas Detection System

Ching F. Lo¹, George Z. Shi²,
Carl Bangasser³, and Connie Fensky³

The University of Tennessee-Calspan
Center for Space Transportation and Applied Research
UTSI Research Park
Tullahoma, TN 37388-8897

Abstract

A computer-based Integrated Knowledge System (IKS), the Intelligent Hypertext Manual (IHM), is being developed for the Space Shuttle Hazardous Gas Detection System (HGDS) at the Huntsville Operations Support Center (HOSC). The IHM stores all HGDS related knowledge and presents them in an interactive and intuitive manner. The IHM's purpose is to provide HGDS personnel with the capabilities of: enhancing the interpretation of real time data; recognizing and identifying possible faults in the Space Shuttle sub-systems related to hazardous gas detections; locating applicable documentation related to procedures, constraints, and previous fault histories; and assisting in the training of personnel.

1. Introduction

Space Shuttle hazardous gas leakage monitoring is a complicated process which involves a large collection of hardware, documents, and experts' knowledge. There is a pressing need to improve the Hazardous Gas Detection System's (HGDS) data interpretation, fault recognition, and corrective action assistance. A computer-based integrated knowledge system, the Intelligent Hypertext Manual (IHM), may provide just the right tool to accomplish this task.

The IHM is a hypermedia system designed to store information related to the HGDS and to present it in an interactive and intuitive manner. The IHM has a friendly user-interface, a set of system accessories, and a knowledge base which consists of many information and knowledge elements. The fundamental principle of the IHM is the efficient organization, representation, and utilization of its knowledge. The system architecture of the IHM is

shown in Fig. 1. The basic design idea is to construct the IHM using commercial software shells, which are well developed and available for all potential users, so the developer can concentrate on developing the knowledge-elements and integrating them into the IHM. The IHM is built with an open architecture so that the new knowledge-elements can be easily integrated into the system. This greatly simplifies the task of maintaining and updating the IHM.

The IHM will also assist users in the decision-making process; it provides "quick and easy" access to appropriate information for fault detection with action options. It may also supply a large volume of accessible material in specific areas of space shuttle hardware for assistance in training personnel.

In short, the IHM has the potential to increase productivity and the quality of service for fault detection from the HGDS. It eliminates most

¹Principal Investigator-CSTAR, Professor of AE/ME, UTSI

²Research Engineer, CSTAR

³Graduate Research Assistants, CSTAR/UTSI

human errors and reduces the required resources including manpower and material cost to achieve the same specified goal.

2. Hypermedia Technology

The basic technology which makes the information presentation of the IHM possible is hypermedia. Hypermedia incorporates information in an enriched environment that complements text with high quality pictures, full motion video, and sound. More importantly, hypermedia allows the reader to browse through linked, cross-referenced, annotated, and layered information quickly in a non-sequential manner. Figure 2 is an illustration of hypermedia. Information within a hypermedia document contains facts (such as notes, papers, books, diagrams, photos, full motion video and sound, and other software packages) and the relationships between those facts. By following the relationships between facts, the reader has the ability to find and display information in an intuitive and interactive manner. The hypertext, which is used for the IHM, is one branch of hypermedia that deals mainly with text and graphics (Ref. 1 - 3).

Hypermedia is a very flexible tool that can be applied to a wide range of applications. Essentially any information that can be presented electronically can benefit from hypermedia. Theoretically, hypermedia systems have no size limitation; therefore, they can be expanded to link every piece of electronic information available. A few areas in which hypermedia is often used are technical reference materials, maintenance manuals, and policies and procedures manuals.

3. Implementation

The IHM currently operates on the IBM PC platform. The Microsoft Windows 3.1 (Ref. 4) graphical environment was selected to be the working environment and the user-interface was built using ToolBook (Ref. 5) and Guide 3 (Ref. 6). Other application software included are an expert system shell and a plotting program.

4. IHM's User-Interface

The design of the user-interface is one of the most

important aspects in developing the IHM because the user relies on it for information retrieval. The IHM's user-interface is constructed to provide easy access to all knowledge-elements such as hypertext documents, databases, expert systems, etc., and to allow the user to navigate through the system. Therefore, the interface must be simple to use and easy to understand.

The layout and operation of the IHM's user-interface is consistent throughout the entire system to promote user familiarity. The information in the IHM is formatted in distinct, screen-size pieces (or "pages") so that it can be instantly available and easily assimilated by the user. The main elements of the user-interface are buttons or other types of instant command objects which carry out pre-defined actions. The IHM's user-interface has two types of these objects, navigational and special function buttons. The navigational buttons provide quick and easy access to any piece of information within the IHM. These type of buttons are consistent in their location and function throughout the IHM. The special-function buttons are specific to a certain page or page-type. They carry out the operational needs of the page in which they are contained.

During the second year of this research program, the IHM's user-interface has been re-built using ToolBook. ToolBook has been chosen to succeed Guide 3 because:

- 1) ToolBook has more functions and is more flexible than Guide 3.
- 2) a ToolBook interface not only appears more professional, but is easier to use and understand.
- 3) the scripting language used by ToolBook is easier to program than that used by Guide 3.

Guide 3 may still be used to present longer text documents such as technical papers, but it will be called up from the ToolBook interface.

5. Knowledge-Elements and Organization

Related information or knowledge is grouped into knowledge-elements or objects in the object-oriented environment of the IHM, as illustrated in the second

layer of Fig. 1. The knowledge-elements may be built using different software shells, each according to their own usage and nature. Each knowledge-element is linked to other knowledge-elements both by the user-interface and by the links within the elements. These links are made during system construction and are implicit to the users.

The knowledge-elements of the IHM contain all the critical information related to the HGDS, including information from applicable manuals, procedures, criteria, and data. The information included in the IHM are selected based on the access requirement priority in the hazardous gas leakage monitoring process and their availability.

5.1 Hypertext Document

The hypertext documents are constructed from existing computerized and/or printed documents. The hypertext documents were built using ToolBook, an application construction software, and Guide 3, a hypertext software package. Both are designed for use in the Microsoft Windows graphical environment. Figure 3 shows the overall structure of the IHM knowledge base. The specific documents that have been included in the IHM are the following:

1. Launch Commit Criteria (LCC) documents:

The LCC documents are the most important documents used during the launch monitoring. The sections of the LCC/HAZ and LCC/GSE have been implemented into hypertext form and arranged in such a way that the user can easily access any single document either by clicking on its name or by the situation it covers during the launch, e.g. launch period, gas type, and sensor location. Figure 4 shows the hypertext form of a LCC document.

2. MPS/Flight Measurement Location Document:

The MPS/Flight Measurement Location Document had been built into hypertext document format. The original Rockwell, Inc., documents were converted to Windows-readable graphic-image files. Hypertext buttons facilitate movement either sequentially through the document, or directly to a pertinent section via menus. An automatic feature is included to easily update the document by incorporating new graphics images when desired.

3. Operations and Maintenance Requirements and Specification Document:

These documents include information pertaining to events occurring before External Tank loading, during the T-6 to T-4 hr time frame, and during the T-10 to T-1 minute time frame.

4. Quick-Look Reviews:

The Quick-Look Reviews for several launches have been incorporated into the IHM. These hypertext documents include the written prefaces and tables as well as the graphs that make up the bulk of these reports. The hypertext Quick-Look Manual allows users to navigate quickly to the portion they want to review. Figure 6 shows an example of a hypertext Quick-Look preface.

5.2 Expert System for Data Retrieval

The information of hazardous gas leakage measurements for all shuttles' loading operations has been built into a dBASE file for easy access. For future updates of this information, only this database need be changed. The ToolBook interface is designed to retrieve the data intelligently from the database file. The user can quickly retrieve the data sorted in several ways, such as by the launch vehicle, date, launch I.D., or by the data limit. The retrieved data is written into an ASCII report file and can be read, printed, or plotted as the user chooses.

6. IHM System Accessories

System accessories, such as Help, Index, Glossary, and Map are designed to increase the IHM's efficiency and make it more user-friendly. Because of the nature of the IHM, these accessories are in hypertext format and the user may access these accessories from anywhere within the IHM.

The Index is an alphabetical list of topics contained within the IHM. The hypertext nature of the Index allows the user to navigate directly to the topic he/she wishes to see by clicking on the topic. A Map is another such navigational aid, except that it shows a graphical representation of the system and allows travel to different locations within the system. The context-sensitive Help provides assistance depending on where the user is in the

system. Users can easily get the specific help they need rather than search through long help-menu screens.

7. IHM Plotting Upgrade

The IHM's plotting ability has been upgraded with Origin (Ref. 7), a new Windows-based scientific and technical graphics software package by MicroCal, Inc. The user is able to: zoom to portions of the graph, view the numerical data, print portions of the plot, and manipulate the data with curve-fitting, statistics, arithmetic, etc. The user can also pre-program the tasks they desire using Origin's macro capability.

This upgrade was performed for a number of reasons. The transition from the IHM into Origin is much smoother because it stays in Windows and does not need to shell to DOS. Origin's user interface is much more "friendly" and supports the use of a mouse. Origin also allows for pre-programming, which reduces the amount of input and learning required for the user to plot data in the IHM.

The IHM has been set up to run Origin directly when plotting the data sorted by the expert system. Upon choosing the plot command in the IHM, Origin is launched and the data is automatically loaded. A plot is then automatically produced and scaled for that data. Figure 7 is a screen-print of a plot of sorted data from an expert system session.

The IHM also allows the user to plot off-line, time dependent gas concentration data for a single launch. This gives the user a quick way of reviewing this form of the gas concentration data.

8. Hypermedia Incorporation

The possibility of incorporating full motion video and sound into the IHM has also been studied. A VideoLogic DVA-4000 video board and MIC System software (Ref. 8) have been installed on our IBM PC-386 computer. A laser-disc player is used to retrieve video images from pre-made laser discs. The command-buttons, which launch the player and call the related video images to the computer screen, are placed within the text documents so the user can

view these images while reading the documents by simply clicking the buttons. This would give the IHM the capability of demonstrating a particular task to the user visually, rather than attempting to relate the task strictly with words. A photograph of a sample screen display is shown in Fig. 8. We believe that by incorporating the hypermedia technology into the IHM would greatly increase its user-friendliness and efficiency.

9. Concluding Remarks and Future Work

Integration of computer and Artificial Intelligence technologies, in the form of the Integrated Knowledge System, holds much promise in improving the efficiency of personnel and increasing the productivity in aerospace applications. A well-designed IKS does more than merely present its stored knowledge to a user, it will: (1). Store information and present it quickly and efficiently. (2). Filter that information down to the essentials. (3). Help the user make a good decision. The rich knowledge-base of the Space Shuttle Hazardous Gas Detection System included in the IHM will provide HGDS personnel with a useful tool.

A functional IHM will be installed at HOSC, where its operational capabilities will be tested. The feedback from the NASA personnel will provide ideas for further improvement and expansion. Utilities which automatically incorporate new data will be added into the system to simplify the maintenance procedure.

Acknowledgements

This work was supported under NASA Marshall Space Flight Center Grant NAG8-835. The authors would like to thank R. D. Bachtel, H. Campbell, G. Lyles, and J. R. Redus of NASA/MSFC for identifying the present topic and providing technical advice. Rockwell Inc. personnel are also appreciated for their technical support.

References

1. Conklin, J., "Hypertext: An Introduction and Survey," IEEE Computer, September, 1987.

2. Special Issue - "Hypertext" - communications of the ACM, July 1988.
3. Special Issue - "Hypertext-In-Depth Review", BYTE, October 1988.
4. Microsoft Windows 3.1, Microsoft Corp., 1992.
5. ToolBook 1.5, Assymetrix Corporation, 1989.
6. Guide 3 Professional Hypertext System, Owl International, Inc., 1990.
7. Origin 1.2. MicroCal, Inc., 1992.
8. DVA-4000 Full Motion Digital Video Adapter and Mic System 3.0 software, VideoLogic Limited, 1988.

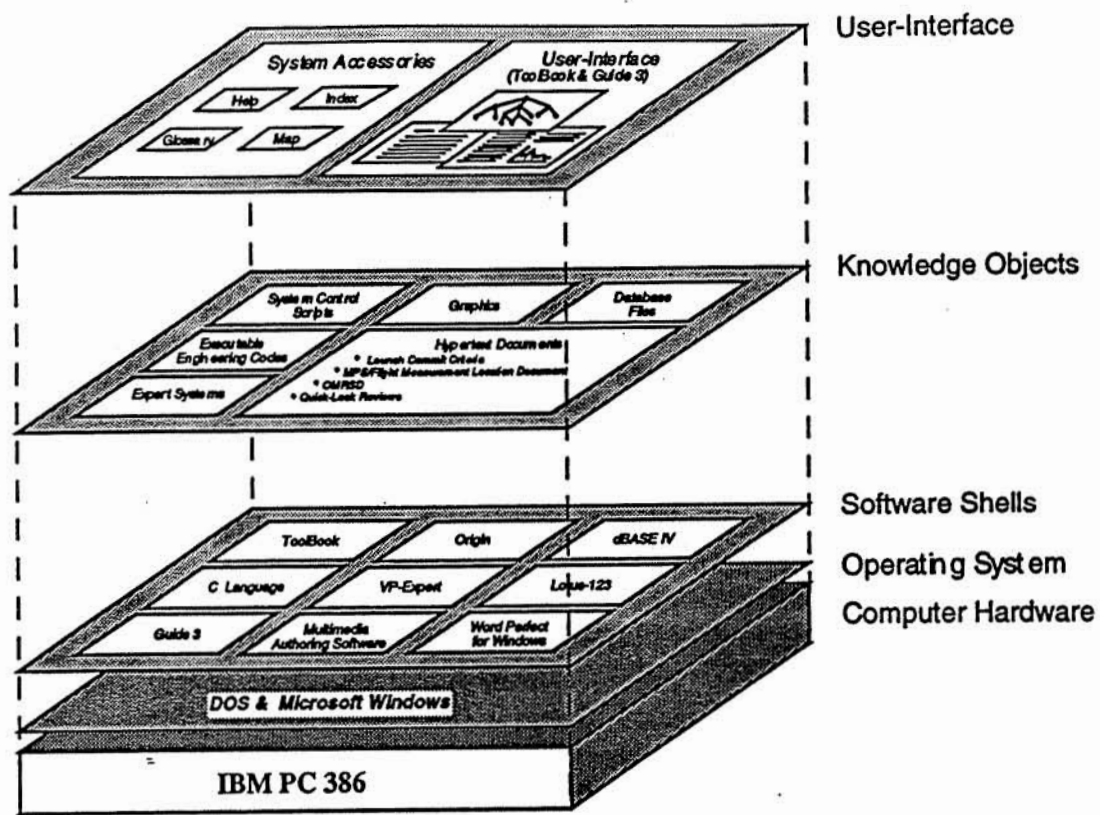


Figure 1. System architecture of the Intelligent Hypertext Manual.

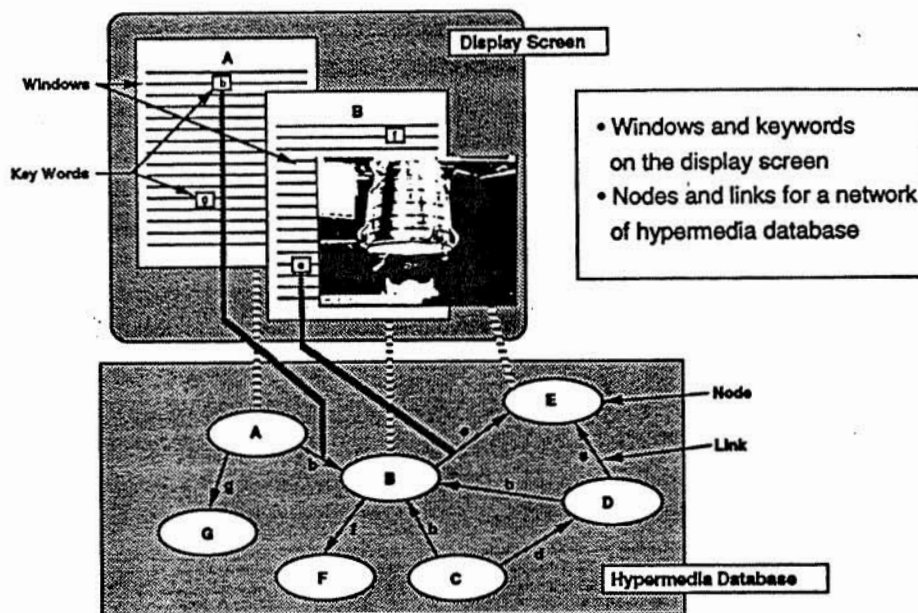


Figure 2. An illustration of hypermedia.

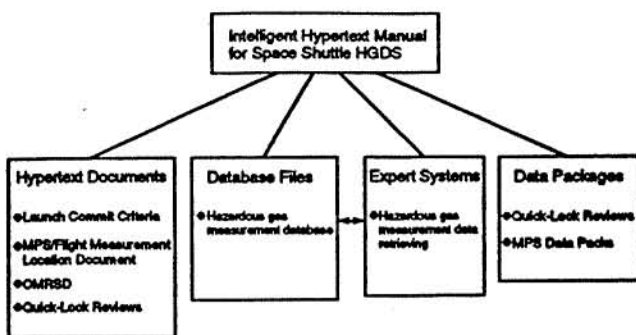


Figure 3. The knowledge-base of the Intelligent Hypertext Manual (IHM).

Figure 6 shows a screenshot of a "Quick Look Review" window titled "I. Hazardous Gas Detection System" and "C. Maximum Observed HAZGAS Readings". It contains a table with two columns: "Compartment - Gas" and "Launch".

Compartment - Gas	Launch
Alt - Hydrogen	298/283 PPM
Alt - Oxygen	48 PPM
Alt - Helium	11,188 PPM
ET/IT - Hydrogen	86 PPM
ET/IT - Oxygen	68 PPM
ET/IT - Helium	258 PPM

NOTE: Numbers in Table are Flow/Corrected

The window also features a menu bar (File, Edit, Text, Page, Help) and a sidebar with buttons for "Launch Menu", "Contents Menu", and navigation arrows.

Figure 6. An example preface from the hypertext Quick-Look Reviews.

Figure 4 shows a screenshot of a "Launch Commit Criteria (LCC)" window. It displays various parameters and requirements for a launch.

STS 10887 LAUNCH COMMIT CRITERIA AND BACKGROUND SSID: HAZ-04

LCC VIOLATION CALL: Excessive Hydrogen Concentration Anomaly EMERG COND: Yellow

MEAS. NO.	MEASUREMENT DESCRIPTION	CAT	MINIMUM	MAXIMUM	UNITS	CODE
66DR21211	H2 Concns #2 AR fuselage Hi Range, -500 to		200 (1)		ppm	
66DR21211	2000 ppm		200 (1)		ppm	
66DR22211	H2 Concns #2 AR Fuselage Hi Range		200 (1)		ppm	
66DR22211			500 (2)		ppm	
66DR22211			500 (2)		ppm	

TIME PERIOD: From Start of ET Cys Tanking (T-5 hours) to start of Replenish.

REQUIREMENTS: DRAWING:

(1) 200 ppm indicates positive out-of-spec leakage and requires a hold for leak evaluation.

(2) 10,000 ppm is the redline for ground safety during evaluation.

(3) 500 ppm indicates positive out-of-spec leakage and requires a hold for leak evaluation. For

Figure 4. A screen display of LCC.

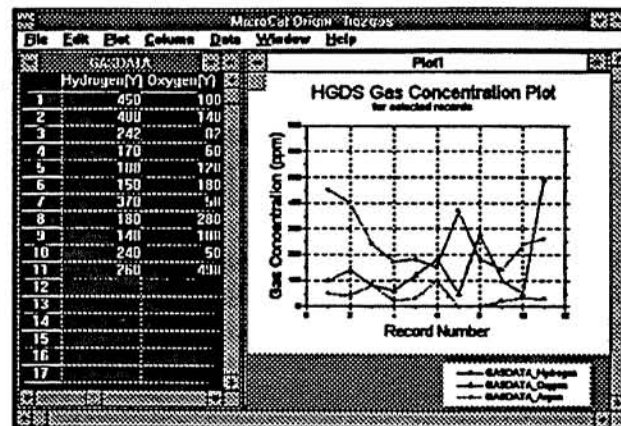


Figure 7. A Plot of sorted data from an expert system session.

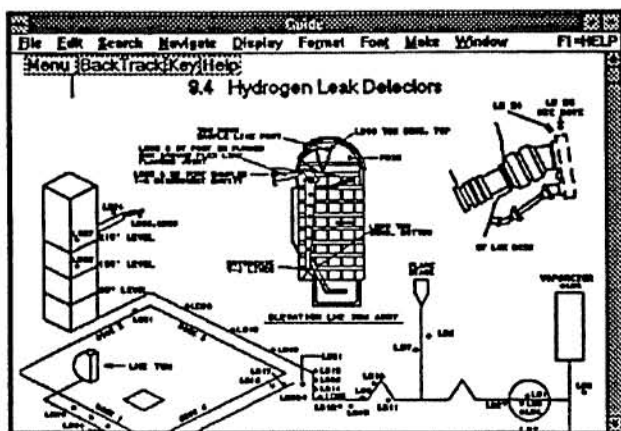


Figure 5. Display of an MPS/MLD document (Location of Hydrogen Leak Detectors).

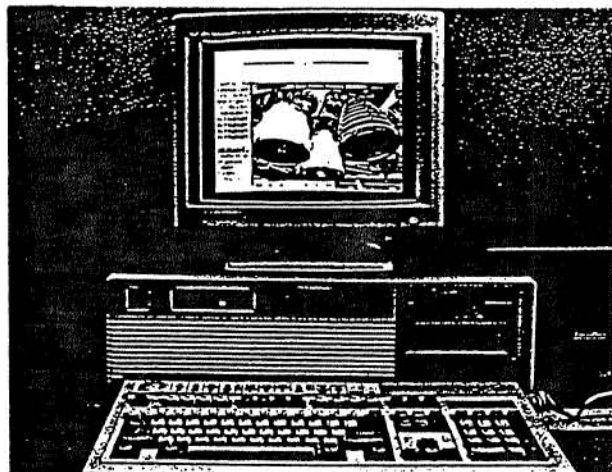


Figure 8. A sample hypermedia screen display.

FLUID MECHANICS COMPUTER BASED LAB SIMULATOR

(CBLS)

Ahmad D. Vakili* and Edward M. Kraft**

CSTAR
UTSI Research Park
Tullahoma, Tennessee 37388-8897

ABSTRACT

This paper describes a novel concept to develop computer based multimedia simulators for engineering laboratories. An important part of education is the hands-on experience of various fundamental science subjects, normally taught within a laboratory environment. Because of overcrowding, deteriorated lab equipment, cost of supplies, maintenance and replacement, laboratory education in most educational systems is highly overburdened and in need of major renovations. Recent progress in personal computers/ workstations, expert systems, video capture and replay, mass storage, and local area network technologies have made computer based laboratories practical. Multimedia is the combination of information technologies that incorporate full-motion video presentations with the personal computer's capabilities to process data. A multimedia system can be designed to use text, still images, animation, video, audio, and special effects to improve understanding of concepts and to increase retention. Such systems can be designed to be interactively controlled by the user. Benchmark laboratory experiments will be conducted in selected research and laboratory facilities under carefully controlled environments. These will be fully documented and recorded on videotape or other media, and along with data acquired by selected instruments, will be incorporated into the interactive video computer based lab software. Interactive lab sessions will be developed based on the integration of the various recorded information. Actual images recorded will be digitally stored and used in conjunction with audio, text and graphic overlays necessary to recreate the experiments in individual modules. Each module will be designed as a specific lab session. The modules will be replayable on inexpensive customized small desktop computer systems such as an IBM PC. All system software will be menu driven, and written so that routine interactions with such systems will not require extensive computer knowledge or experience. Instruction and tutoring will be in the intelligent hypermedia format. The resulting innovative software systems of lab problems and their solutions will significantly improve the students understanding and retention. In addition, laboratory education will become more cost effective, more efficient, and available to an increased number of students.

I. Introduction and Technical Discussion

Description of Problem Addressed and Approach

Throughout higher education and education in other environments such as government, industries, and the high schools, there are a number of programs,

courses, and degrees that require hands-on exposure as experienced in laboratory instructions. Laboratory instruction is an integral part of the most successful education curriculums.

The large number of students and the cost of the laboratory facilities, make it impossible for all the schools and organizations to acquire the sophisticated equipment, instruments and computers needed for a complete lab. Even when available, access to the labs and utilization of the labs' equipment can be quite time-consuming and

* Professor, The University of Tennessee Space Institute

** Deputy Director, Arvin Calspan AEDC operation

@ Copyright A.D. Vakili and E.M. Kraft

expensive to maintain. As a result labs are frequently poorly equipped and under-utilized.

Replacement of rapidly aging university laboratories has become prohibitively expensive and many major universities cannot afford the large investment necessary to upgrade their facilities (Ref. 1). A survey by the National Science Foundation in 1989 found that universities and colleges had identified \$11.7 billion worth of renovation or new construction needed for lab facilities. However, because of budget constraints, schools had only planned for \$3.1 billion worth of work. In addition, lack of funding and the high maintenance cost for the existing labs force some of these labs to become outdated, not used and deteriorated.

Goals and Objectives Recent developments in the area of digital video and audio processing such as Digital Video Interactive (DVI) technology have made new approaches in the area of computerized simulation possible. Using personal computers or workstations, computer simulation of laboratory experiments is readily becoming feasible.

The objective of this effort is to develop highly realistic and interactive Computer Based Lab Simulator (CBLS) for fluid mechanics engineering students. Detailed experiments will be conducted in selected universities, government or industrial labs under the supervision of engineers and scientists, expert in the areas of interest. Careful and high quality flow visualization results obtained during the experiments will be first video recorded and then digitally stored on laser disks. Video sequence of various characteristic flow conditions will be incorporated into the interactive computer based experiment. The results will be edited to enhance the educational objectives and integrated into individual computer modules.

Each module will incorporate realistic video experiences that are encountered in the labs while performing realistic experiments. Analytical and computational solutions will also be obtained as necessary to complement the experimental results for completing the description of each problem under investigation. All the steps which a student must follow to conduct an experiment in a laboratory will be incorporated in the simulation. In addition, the results of theoretical and analytical prediction

techniques will be used and displayed both for instructional and comparison purposes.

The real images to be used from actual observations, in the selected labs, would allow students to run experiments, as if they were performing it within the laboratory setting, themselves. The reality of an actual image in comparison with computer generated images makes a significant difference in the attention span and the interest shown by the participants (Ref. 2). performing it within the laboratory setting, themselves. The reality of an actual image in comparison with computer generated images makes a significant difference in the attention span and the interest shown by the participants (Ref. 2). In addition to the events in the experiment, the students will be able to access other related information. These are incorporated in the design of each module to improve comprehension of the science in the experiment. The additional information can be selected based on the experience of the authors of any of the specific module topics.

If some events are too fast to be observed in real time, the students will have the choice of selecting a time-lapsed or even frame-by-frame mode of observing that event. For example, in the case of supersonic flow over a body with shock boundary layer interaction, shock is not stationary at a fixed location. The only way to observe this is through fast motion photography. The replay of which at slower speeds will enable a student to observe the moving shock in detail.

In 1961, the National Committee for Fluid Mechanic Films (NCFMF) was established to develop a series of films to be used for supplementing texts and classroom education in fluid mechanics. They were convinced that through visual observation of the fluid dynamic principles, students will develop a better understanding of the physical principles involved. In addition students will develop their physical intuition and a better "feel" for ways fluids behave. The NCFMF was concerned about the effectiveness and the popularity of the films that they were about to produce. They justified the high cost of the project with the high quality of the films and that it may be one generation, at least, before improvements on these films would be attempted.

Even though the films are mainly silent, they have become a success story throughout educational and

scientific communities. The films have received numerous awards in various categories and have been credited with the improved understanding of fluid mechanics by students all over the world. We believe it is time for the next generation of the film to be developed, using the newest technology available. With the advancement of computer technology, the obvious base medium is naturally the personal computer.

This paper describes the fundamental mechanism and the detailed procedures to be considered in the development of the new medium. Similar efforts are under way in other scientific communities, but without the attention to details proposed here.

In chemistry, Interactive Video (IV) has been used at the University of Illinois Urbana Champaign (UIUC) by Dr. L. Jones and Prof. S. Smith, (Refs. 3,4, & 5). They have developed approximately thirty modules for the freshman chemistry lab. They have also conducted studies of the effectiveness of their course material. The results are very positive and encouraging. The results indicate that the implementation of their system leads to increased lab experimentation time without increased instructors' time. Some issues like safety, time, and expense, which are normally major concerns in the labs, limiting the experimentation and the frequency experiment may be repeated, are not present in the IV labs. They conclude that the combination of labs and the IV labs has resulted in superior retention of the information by students.

A major effort has been pursued at Massachusetts Institute of Technology (MIT) to enhance fluid mechanics education with workstation based software, under project ATHENA, (Ref. 6). They have not used the developments in multimedia technologies. Several modules in the area of fluid mechanics are available from the MIT's group under the title of TODOR. It is our understanding that MIT's TODOR is designed for more powerful workstations with computer generated graphics and no video footage from lab experiments. Various information is computed by the machines and displayed as graphical images. The purpose of MIT's work is to augment classroom instruction through computer interactions rather than to simulate labs. Professors Redish and Wilson have been developing similar computer based approaches for

teaching Physics (Refs. 7&8). Artificial intelligence techniques have also been used for developing Computer-Assisted Instruction systems (Refs. 9-11).

Procedures and Methods To create a realistic simulation of lab experiments, many steps are to be meticulously designed, prior to the production for each of the simulation modules. A text describing the experiment and the basic science it conveys to students must be prepared. For selected experiments such information is available and requires some modification. It must be determined as to what type of instrumentation, flow conditions and facilities are needed. Fundamentals of fluid mechanic similarity and modeling rules must be available to the students in the form of tutorial or theoretical support. Additional tutorial and background materials, as applicable to each specific module are to be prioritized and documented. Equipment to be used must be identified and fully described with video, pictures, and words.

Other details to be evaluated are: profile identification and description of primary and secondary users, and hardware requirements including installation. The detail design process will then consider the criteria stated in the following steps: Preparing an application design document for presentation methods and approaches, structure and sequence, motivational techniques, media selection, interactions, adult learning principals, assessment and evaluation techniques.

Based on the results of analysis from the application design document, production documentation for modules will be drawn up. Video storyboard, audio scripts, and graphics renditions are to be sequenced in the production document.

The production document will be the basis for pre-production, production, and post production work. Pre-production includes activities such as casting, set design, and preparation for them. Production includes the conducting of each experiment and the creation of the graphics, and analytical and computational aspects of the module. Post production consists of editing, creation of special effects, and addition of audio. The above process will be implemented for each module. Following assessment and validation, the final products will be transferred to a master tape to be sent to the videodisc manufacturers for mass production.

It is the objective of this effort to develop highly realistic and interactive computer based lab simulation. As stated earlier, almost all the steps in a complete lab experiment will be documented. In the process of navigating the interactive lab simulation, each of many carefully selected items will be presented in a menu on the interactive computer screen displays. Each menu will contain a list of items to be read, evaluated, and responded to by using an input device such as a mouse. The user will also have the option of seeking help, if desired. The user has to navigate the steps by reading, responding, and if needed, by inquiring. All the questions will center on the primary purpose of the specific module. The title of each module will be descriptive of the module contents.

A path mechanism will be in place to display images of the experiment's equipment under consideration from the menu screens. For example, if we are selecting facilities, photographic images or video of the selected national or local facilities and their capabilities, it would be addressable by multi-level questions. The level of detail provided will be dependent on the user selected level of interaction such as introductory, intermediate, and advanced.

Specific Considerations: The topics initially selected are: 1. Flow around bluff bodies. 2. Flow over airfoils. 3. Laminar, Transition, and Turbulence. The experimental segments of the three modules are being developed using the facilities in the Gas Dynamic Laboratory of The University of Tennessee Space Institute. The IBM Corporation has awarded a developer package which will be used for the software development and the integration of the various segments such as text, video, graphic overlays, etc.

Assessment and validation of the effectiveness for the modules developed in this effort are also to be made. A study will be performed at the undergraduate level at The University of Tennessee, Knoxville within laboratories as an integral part of fluid mechanics and solid mechanics education. It is essential that a comparison be made between students conducting experiments in the lab, students who are conducting simulations, and those students who are doing both.

We are developing software packages to standardize the simulation development process. It is obvious

that there will be other authors who will be interested in developing their own simulators. Therefore, availability of standardized software will ensure elimination of redundant efforts for software development.

The overall organization of the lab simulation depends upon the authors and concept constraints of the courseware. Standardized formats for instructional strategies will be followed so that experiments and educational materials follow consistent development paths, taking into consideration adult learning principles and instructional methodologies. A mechanism to track the student's progress will be established by evaluating feedback from the student's responses to screen inquiries, help screens accessed, and frequency of responses. In addition, the organization of the material presented will allow both students and instructors to control their pace and path during the interaction with the system.

A mechanism for dissemination of the various simulators will be setup through a network for those with interest in furthering the state of the art in this area and possibly with support by the National Science Foundation or another source. Various consortiums may then be formed to share their resources towards developing a large number of modules on other fundamental subjects. Modules must be standardized to ensure compatibility with hardware and uniformity of their contents.

II. A Walk Through a Generic Module

The design of each Computer Based Lab Simulator (CBLS) module will be based on the requirements of the particular experiment and the characteristics of the selected facility. The following outline lists the various steps which are incorporated in a fundamental experiment. In this module, flow over a circular cylinder at different Reynolds numbers, is discretized as an example with a wide level of fundamental educational potential. The following is an example menu that would be provided to guide the student through the experiment.

I. Introduction to the module

- review of the module's operation?
- theoretical introduction?
- experimental introduction?

II. Design Considerations

- instrument Selection
 - . pressure probes
 - . total-, static- surface pressures
 - . pressure transducers
 - . hot wire/film
 - . laser velocimeter

- instrument Characteristics
 - . size
 - . range
 - . frequency response
 - . accuracy

- Experimental Setup
 - . facility
 - . key flow parameters
 - . Velocity, Reynolds number, Mach number, etc.
 - . test matrix specification

III. Calibration

- pressure transducers
- hot wire/film settings and procedures using known calibration methods

IV. Experiment

- flow visualization
 - . surface flow patterns
 - . laser sheet, vapor screens, dye or smoke injection
- conduction of specific tasks such as pressure, temperature, hot-wire or laser velocimeter measurements.

V. Analysis

- forces: lift, drag, moments
- unsteady events; Strouhal no., wake stability/spacing, structure,

....

VI. Theory and Comparison

- boundary layer theory
- von Karman vortex street theory
- Reynolds/Oseen drag at low Reynolds no.

VII. General Discussion on Results

- data accuracy/error band
- flow quality/uniformity, turbulence level, etc.
- wall interference
- limitations and Strength

VIII. Conclusion

- report
- comments

III. Evaluation

A brief description of the individual sub-topics listed above are discussed in the following pages.

Introduction to the Module: Flow over cylindrical bodies are simulated in this module. Basic understanding of fluid mechanics at the levels of introductory, intermediate, and advanced in relation to the topic of this module is available. The student may choose any of the options. Flow parameters may be selected by the student based on a selected diameter and or geometry for the cylinder, fluid properties, velocity, and any other parameter which the student wishes to take into account. In the event that there are insufficient or redundant parameters, then the artificial intelligence in the program will guide the student to identify the essential ones for a given experiment. If the need is there, the tutorial help files will be recommended to be interactively reviewed.

Design Considerations: In the previous step the student selected the parameters for the problem to be

studied in this simulation session. Once the experiment is defined, then the student must identify what sort of measurements must be made to obtain the needed information for desirable quantitative or qualitative description of the phenomenon involved. Whether we are dealing with a steady state problem or an unsteady one, the types of instruments employed, must be appropriately selected.

Here also, if either too few or too many parameters are selected, the AI software will guide the student through the tutorials for a better understanding of the measurements needed.

Calibration: Each of the instruments selected to be used for measurements will be displayed in realistic pictures. Depending on the level of the interaction, identified at the beginning of each session by the user, some of the instruments must be validated through calibration. Calibration procedures will be interactively conducted by the user and tutorial help will be available if needed by the user. Typical calibration curves of realistic instruments with known properties will be used for the simulated environment.

Experiment: After successful completion of the earlier steps, the selected facility will be used to conduct the experiment. First the model must be instrumented, if applicable. Some experiments do not need this step. The facility instrumentation and any additional instruments will be installed in desired locations and viewed in a realistic image of the facility. Facility operating conditions will be set and the student will have to record the data as identified earlier for each tunnel operating condition. Students will have an option for flow visualization to study the physical features of real experiments under similar conditions.

Images of the real experiments are recalled from the CD ROM, and are prerecorded by the authors of each module as explained earlier. Since these images are digitally stored, they can be rapidly recalled and manipulated for additional probes or repositioning of a transducer.

Analysis: The data obtained in the previous step can be recalled and post processed to obtain information such as forces and moments and other information relevant to the understanding of the problem under consideration.

Theory and Comparison: Theoretical information relevant to the data and the problem under study are discussed in this segment. Students have access to this information either by direct request for help on theory or indirectly through the AI. The purpose of this information is to provide the students with the theoretical help without having to refer to a book and be side tracked.

General Discussion on Results: This segment contains a typical outline for a report on a study of this type of problem. This is to be used by a student as a guide for the lab report. The information for the report may be typed at the end of this segment and then printed for submission as the lab report.

Conclusion: A summary of the main observation is to be presented in this segment. The material in this segment will also be in the lab report.

Evaluation: The student's progress will be tracked by evaluating the student's responses to screen inquiries, help screen accessed, and frequency of responses. Another evaluation mechanism will be based on the report submitted by the student at the conclusion of the simulation session. A successful interactive simulation will be followed through a module without significant help from the module itself. A selection of typical screens from a module developed as a proof of concept are shown in Figure 1.

IV. Applying Innovation in Course and Curriculum

Computer Based Laboratory Simulation: This project incorporates information technology into one computer system which will be the platform for the development of the computer based laboratory simulator. Computer based laboratory simulation will be designed around the laboratories used to augment engineering classroom lectures. The development system will be a microcomputer equipped with specialized boards and software that will be used to incorporate motion video, audio, graphics, and texts into an educational courseware. The courseware developed will be the computer based laboratory simulator, the vehicle by which the fluid mechanics lab sessions are presented to the students.

The computer based laboratory simulator is a computer-aided learning system that can be used to augment classroom instruction with laboratory instruction. It is an excellent tool for experiment simulation where laboratory testing can be dangerous and expensive to replicate. The simulator can become an exceptional tool for educational purposes. The intended use for the computer based laboratory simulator at the Center for Space Transportation and Aerospace Research (CSTAR) is to develop courseware for the engineering curriculum for first and second year engineering students. Laboratory equipment, time and personnel expenses can be minimized by building a library of computer based lab simulations which encompass the common body of knowledge for the engineering disciplines.

The laboratory study of fluid mechanics introduces students to large amounts of visual data. Capturing, storing, and editing visual data is paramount to the effectiveness of the computer based lab simulator. Capturing visual images, which will be incorporated into the simulator, requires special hardware and software configuration considerations. Providing access to artificial intelligence and an expert system for additional information also requires special hardware and software. The physical equipment and the information technologies chosen for the simulator have been researched and examined for availability, compatibility, flexibility and affordability. Every measure has been taken to assure that the selected systems, products and methodologies are appropriate for the computer based lab simulator.

The selected hardware platform for the application development system is a product equal to, but not limited to, the IBM PC. The specialized board is the ActionMedia products developed by Intel in cooperation with IBM for use in educational software development. The software and authoring languages selected are industry standards and are readily available from their respective vendors along with adequate technical support. The simulator will also employ Digital Video Interactive Technology, Artificial Intelligence, Hypermedia and MultiMedia methodologies to develop each courseware module. This information technology provides access to visual data, allows construction of the hypermedia sub-structure for access to additional information and integrate the different media required for a

successful simulation of laboratory experiments and their associated instructive values.

Organization of Laboratory Simulator Data and Theory: The overall organization of the lab simulation depends upon the authors and concept constraints of the courseware. Standardized formats for instructional strategies will be followed so that experiments and educational materials follow consistent development paths, taking into consideration adult learning principles and instructional methodologies. A mechanism to track the student's progress will be established by evaluating feedback from the student's responses to screen inquiries, help screens accessed and frequency of responses. In addition, the organization of the material presented will allow both students and instructors to control their pace and path during the interaction with the system.

V. Anticipated Results

The main outcome of this proposed effort is a **Computer Based Laboratory Simulator (CBLS)**. The simulator will be designed for interactive use by various laboratory educational programs, especially for undergraduate education. Such a system is expected to be easily adapted for other areas and groups. As a result of the lab simulator, laboratory education will be significantly enhanced. The chronic lab shortages and lack of adequate facilities and equipment will be relieved. Improved understanding of the fundamental scientific principles in the labs will help broaden understanding of the subjects in classrooms as well. This is an essential element for better education in many classrooms.

The lab simulator will be available so that students may run their simulated experiments as many times as it takes for them to learn the topic and to master the experiment. This is not an option in the real labs, due to many of the limitations mentioned earlier.

The laboratory simulator will be developed using the existing experimental facilities in different university labs and some government research centers. Each lab has certain facilities and measurement equipment which would make it better suited for particular experiments.

Assessment and Evaluation: Short term assessment and validation will be performed through a limited time process of testing the application of the modules with a group of its intended users - both the students and the instructors. The test objective will be to identify the extent to which the objectives of the simulator are met. The assessment process will be designed to measure, analyze and report on the following topics:

1. Accuracy and completeness of the content.
2. How closely the application reflects the anticipation.
3. How it influences the users' performance.
4. How well the application is accepted by the users.
5. How does it improve retention.

Findings as a result of the assessment process will be integrated in the revisions to improve the modules.

Long time assessment will be through upgrading of the content based on availability of new material and input from the broad base users in various locations. It may also be possible to allow students to conduct typical additional experiments to be integrated as part of each module, depending on the educational value of the outcome as determined by the authors. If a student makes a mistake during the experiment, the mistake itself will become an educational segment piece of the module. This will be done with the aid of AI guiding the interaction through questions and answers. It is anticipated that students should be included in the design and evaluation of the various modules. Students will be asked to conduct the experiment in the lab and record the interactions for several cases. The different approaches and difficulties encountered by the students will be added to the system as alternate options the simulator would support. That is, if a student selects a wrong approach which has been attempted before, he/she may proceed.

The artificial intelligence aspect of the simulator will prompt a warning message depending on the

severity of the mistakes. We would like to create a documented effort that will be stored for possible upgrading as more advances in the 22nd Century technology enable the next generation computer interactive devices to become more economically feasible.

Dissemination of Results: The implementation of the computer based lab simulator will consider the computing environment of the university, engineering school or client. In order to make widespread use of the computer based simulator, development will be based on the relatively inexpensive, readily available hardware and software. In addition, the simulator and its knowledge base will be portable among as many computer platforms as possible, since the client environment is likely to involve various kinds of computer hardware. This concept of portability supports the usage of a common interface and compatibility with local area networks (LAN).

The Computer Based Laboratory Simulator, once developed will, at least, partially solve the problems associated with undergraduate laboratory education. The IBM corporation has provided equipment support toward the development of this program. In return the software developed will be compatible with the IBM hardware and software technologies. In addition, we believe the quality of the modules will be such that they will be adopted for use by universities in large numbers. To ensure this is going to be the case, we have plans to ensure hardware and software are thoughtfully selected and developed.

Acknowledgement

The assistance by Dr. C.F. Lo, Mr. Rick Clippard and Mrs. Pamela Clippard on the aspects of Artificial Intelligence, programming, hardware and software related to this work is gratefully acknowledged. This work was supported by the CSTAR IR&D Proposal Development Efforts.

Bibliography

1. Education Column "Can Stanford Build Labs for the New Millennium ?" Business Week, Dec. 4, 1989.

2. Chen, Allan "DVI Technology: Bringing Desktop Computing to Life," Microcomputer Solution, Sept/Oct. 1989.

3. Jones L. L. and Smith, S. G., "Lights, Camera, Reaction! The Interactive Videodisc: A Tool for Teaching Chemistry," T.H.E. Journal, Vol. 17, No. 7, March 1989, pp. 78-85.

4. Jones L. L. and Smith, S. G., "Using Interactive Video Courseware to Teach Laboratory Science," Tech Trends, No. 35, 1991, pp. 22-24

5. Smith, S.G. and L.L. Jones, "The Acid Test: Five Years of Multimedia Chemistry." special issue supplement, T.H.E. Journal Sept. 1991

6. Murman, M., R. LaVin, C. Ellis, "Enhancing Fluid Mechanics Education with Workstation Based Software," AIAA Paper No. 88-0001.

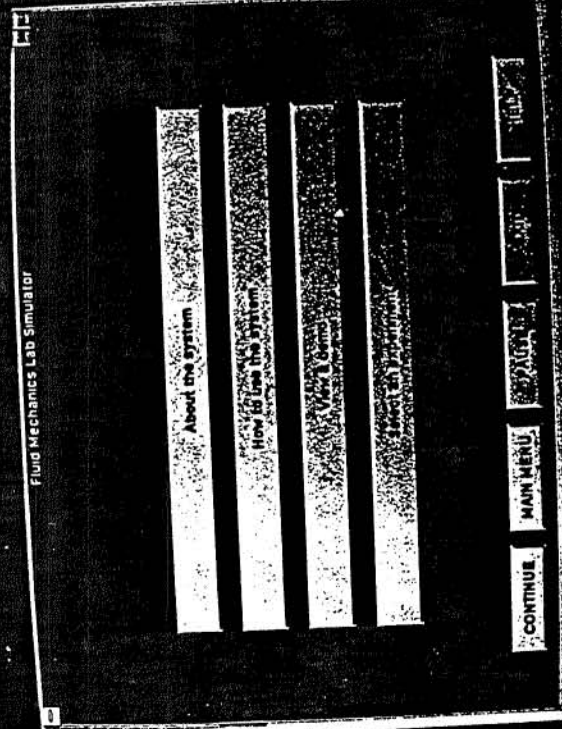
7. Wilson, J.M. and E.F. Redish, "Using Computers in Teaching Physics," Physics Today 42(1) 34(January 1989).

8. Wilson, J.M. and E.F. Redish, "Couple: The Comprehensive Unified Physics Learning Environment," private communication.

9. Jaffe, C. C. "Hypermedia for Education in the Life Science," Academic Computing, Sept. 1989.

10. Lo, C.F. and Steinle, F.W., "Application of Intelligent Systems to Wind Tunnel Test Facilities," AIAA Paper No. 88- 0193, Jan. 1988.

11. Duchastel, P. " Intelligent Computer-Assisted Instruction Systems: the Natural of Learner Control," Journal of Educational Computing Research. 2:3 (1986) pp. 379-393



You will be asked to set-up a fluid mechanics experiment by selecting a model, the instruments, flow parameters and the facility.

Facility

Parameters

Velocity =
Type =
Other =

Instruments

Model

Press any key to continue

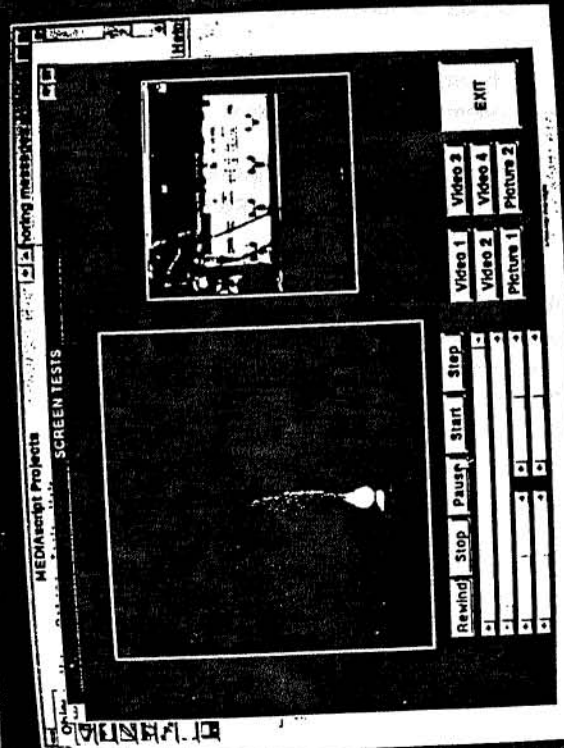


Figure 1. Four typical screens from a proof of concept module depicting text, audio and video combined in an interactive presentation of a Lab experiment.

omit

CSTAR FOCUS AREA:

LASER MATERIALS PROCESSING

·The Space Applications Industrial Laser System

Dr. Robert Mueller
Mr. Brice Bible
Dr. Mary Helen McCay
Mr. Michael Sharp
Dr. T. Dwayne McCay

·Laser Industrial Partnership Program

Mr. Michael Sharp
Dr. Robert Mueller
Dr. T. Dwayne McCay
Dr. Mary Helen McCay
Mr. Brice Bible

·WELDER-LWP: A Fast-Transient, Three Dimensional Computational Model for Continuous and Pulsed High-Energy-Density Welding Processes

Dr. Arsev Eraslan, ERAS, Inc.
Dr. T. Dwayne McCay